UNIVERSITY OF TRENTO
Department of Physics

Atomic dynamics in glass-forming liquids during the Johari-Goldstein relaxation

Supervisor:
Prof. Giulio Monaco

PhD Candidate :
Federico Caporaletti

Doctoral Program in Physics
XXXII cycle

Contents

Chapter 1

Introduction

If a liquid is cooled down below its melting temperature rapidly enough to avoid crystallization, it enters a meta-stable state and becomes a supercooled liquid. A supercooled liquid can be further cooled down and, on lowering its temperature, its viscosity increases of many orders of magnitude and its molecular dynamics slows down. When the glass-transition temperature, T_g, is reached, the liquid has become so viscous that it appears to be frozen on the observation time-scale: a glass has been obtained.
The microscopic origin of the dynamic arrest occurring at the glass-transition is one of the most intriguing open questions in condensed-matter physics and its understanding requires the study of the dynamics of supercooled liquids while approaching T_g [1–4].
The molecular dynamics in supercooled liquids is described in terms of relaxation processes. These are the microscopic mechanisms by which a liquid can restore equilibrium after an external perturbation or a spontaneous fluctuation. In a scattering experiment, they appear as time decays in e.g. the intermediate scattering function (ISF), the auto-correlation function of the microscopic density fluctuations probed at a certain exchanged wave-vector, q. Each relaxation process is characterized by two main parameters: the relaxation time, τ, (i.e its characteristic timescale) and the relaxation strength, f_q (i.e the fraction of molecules that participate to that process). Studying how τ and f_q evolve as a function of q and of the temperature T provides invaluable information about the microscopic mechanisms underlying the relaxation.
One of the main issues in dealing with the glass transition problem is that the investigation of relaxation processes during the dynamic arrest is extremely challenging. For instance, several experimental techniques are required as the dynamics of supercooled liquids stretches over a very wide time window ranging from the fast liquid dynamics in the sub-picoseconds domain to the very long times ($\simeq$ 1000s) characteristic of the glassy state.
Two main slow relaxations govern the microscopic dynamics of ultra-viscous liquids: the well known structural or α-relaxation [3], directly involved in the dynamic arrest occurring at T_g, and the secondary, Johari-Goldstein or β_{JG}-relaxation [5]. While the former has been extensively studied and modeled

[3], the latter is still not completely understood.
The β_{JG}-relaxation usually decouples from the structural one below a temperature where the structural relaxation time is in the μs - ms range and shows a milder temperature dependence than the structural process. In fact, the β_{JG}-process is faster than the structural rearrangements due to the α-relaxation and surprisingly remains active even in the glassy state.
Since its discovery in 1970 by Johari and Goldstein [5], the β_{JG}-relaxation process has attracted an increasing attention because of its strong relationship with the α-relaxation and of its influence over many relevant material properties. For example, when the β_{JG}-relaxation is pronounced, metallic glasses display a high tensile plasticity [6, 7], and amorphous pharmaceuticals [8] show a higher tendency to crystallize, which implies a reduction of the solubility of the medicine. Still, its role in the process of dynamic arrest at T_g is largely unknown.
Even though this secondary process has been at the focus of a large number of theoretical, experimental and simulation studies [4] the problem is still open. Most of what is known about this relaxation process comes from techniques sensitive to molecular re-orientations such as Nuclear Magnetic Resonance (NMR) and Dielectric Spectroscopy (DS). Information about the associated center-of-mass motion (CM) is instead scarce and the atomic dynamics involved in the β_{JG}-relaxation has not been clarified yet. In fact, addressing the microscopic dynamics at the μs timescale, when typically the β_{JG}-process decouples from the α-relaxation, is extremely difficult and only recently experiments and simulations have started to provide some insights. As a consequence, a complete microscopic description of the phenomenon is still missing and only phenomenological models, able to partially account for some of the properties of β_{JG}-process, are available at the moment. Several fundamental questions remain therefore open:

1. The structural relaxation is the main process which leads to the dynamic arrest. Why do glass-formers then show a universal, faster time scale? What is it special with that time-scale?

2. How can we label the molecules participating to the β_{JG}-process? They are clearly expected to be more mobile than the others on a timescale shorter than the structural relaxation, but what does this mean in detail?

3. Is the β_{JG}-process rather homogeneous or heterogeneous, and to what extent?

4. Do the molecules participating in the β_{JG}-process move in groups in a cooperative way or do they rather move independently of the others?

5. Do they diffuse away from the initial position in the characteristic timescale of the process or can they rather be imagined as rattling in the cage of the nearest neighbors?

All in one question:

6. Which are the microscopic mechanisms governing the β_{JG}-relaxation?

New information at the microscopic length-scale are clearly needed in order to provide some answers.
To this aim, in this Thesis we exploit recent advancements in a synchrotron-radiation based technique known as nuclear γ-resonance time-domain interferometry (TDI) to take a *microscopic look* at this old problem of the Johari-Goldstein relaxation with new eyes. We focus our attention on two mono-hydroxyl alcohols, 5-methyl-2-hexanol (5M2H) and 1-propanol. The choice of investigating these two mono-alcohols is motivated by the fact that 5M2H and 1-propanol display a rather different dynamical behavior though both are H-bonded liquids. In 5M2H the β_{JG}- and the α-relaxation are already well separated in time above T_g, while in 1-propanol the two processes are much closer in the supercooled state. So these two samples allow characterizing the microscopic features of the β_{JG}-relaxation in two very different regimes.
Concerning the experimental technique, TDI was selected as it can access the atomic dynamics in the crucial 10 ns-10 μs time window where typically the β_{JG}-process decouples from the α-one.
TDI exploits the first excited state of ^{57}Fe, which lies at an energy of 14.412 keV and has a lifetime of 141.1 ns, to implement the probe and reference arms of an interferometer in the time-domain [9, 10]. More in detail, two identical single-line nuclear absorbers containing ^{57}Fe are placed upstream and downstream of the sample. The upstream absorber is driven at constant velocity so that its excitation energy is slightly shifted with respect to that of the downstream one. The upstream or probe absorber acts as a split and delay line [10]: when a hard X-ray photon impinges onto it, it can either coherently excite the nuclear resonance or be simply transmitted. These two scattering paths are coherently coupled and recombine, after having interacted with the sample, at the second absorber which acts instead as a phase-sensitive analyzer. As a result, a pattern of quantum beats, modulated by the dynamics of the sample, emerges and from its analysis the intermediate scattering function of the sample can be obtained.
TDI was conceived and implemented for the first time in 1997 by Baron *et al.* [9] and since then its application to the study of glass-forming liquids and of the β_{JG}-relaxation has been established [11–13]. However, further developments of the technique are required. In fact, standard TDI set-ups suffer of low count-rates and do not allow for a direct estimation of the relaxation strength of the process [14]. Therefore, part of this Thesis work has been devoted to study how to improve the TDI scheme to make it even more informative in the investigation of relaxation processes in glass-forming liquids.

Structure of this work

My Thesis is composed of 7 Chapters that are organized as follows.

- Ch. 2 provides a general overview of the glass-transition and reviews its thermodynamical aspects.
  The concept of relaxation process, central in the study of the glass-transition, is also introduced within the formalism of the linear response theory. The main features of the relaxations of interest for the glass-transition are then discussed, with a particular focus on the β_{JG}-relaxation. Eventually, the main models proposed to describe the β_{JG}-relaxation are critically reviewed and compared.

- Ch. 3 describes the theoretical background for nuclear γ-resonance time-domain interferometry.
  The Mössbauer effect is initially introduced and then the basic principles of nuclear resonant scattering (NRS) of synchrotron radiation are described in view of its application to TDI. Finally the working principles of TDI are extensively discussed along with its application to the study of microscopic relaxation processes.

- Ch. 4 is devoted to the experimental setup used for the TDI investigations reported in this Thesis.
  After a quick overview of the beamline ID18 of the European Synchrotron Radiation Facility, where the TDI measurements were performed, the experimental set-up is described in detail along with the main optical elements required to carry out TDI experiments. Some methodological aspects of TDI are then reviewed, with a particular attention to the issue of momentum-resolution.

- Ch. 5 is dedicated to the investigation of the β_{JG}-relaxation in 5-methyl-2-hexanol and 1-propanol. The properties of these two mono-hydroxyl alcohols are briefly reviewed along with the data-analysis strategy I developed. The remaining part of the Chapter is focused on the experimental results. A detailed microscopic characterization of the β_{JG} is obtained from the study of the length-scale and temperature dependence of the microscopic dynamics of the samples. These new insights are then combined with the information available in the literature and a unifying picture for the microscopic dynamics within the β_{JG}-relaxation is proposed.

- Ch. 6 explores the potentialities offered by TDI experimental set-ups based on the use of absorbers with multi-line energy spectra instead of the single-line ones as in standard TDI experiments. More precisely, a new experimental scheme, based on 3-lines beating patterns, is introduced, characterized and tested on the prototypical glass-former o-terphenyl. The advantages of this new set-up are finally discussed.

- Ch. 7 draws the conclusions of this work along with an outlook for future studies necessary to extend the results here reported to more glass-formers.

Chapter 2

Relaxations in supercooled liquids and the glass-transition

In this chapter the phenomenology of the glass-transition is reviewed along with its thermodynamic aspects. The concept of relaxation process, central in the study of supercooled liquids and glasses, is also introduced and discussed in the framework of the linear response theory. Finally the main features of the two slow relaxation processes involved in the glass-transition, that is the structural and the Johari-Goldstein relaxations, are presented with a particular focus on the latter one.

2.1 Phenomenology of the glass-transition

A glass is a liquid which is no longer able to flow [1]. It is clear that this definition reflects the usual procedure by which glasses are obtained, that is by the fast quench of a liquid across its glass-transition temperature T_g. The cooling-rate should be rapid enough that crystallization is avoided on crossing the melting temperature (T_m). Below T_m the liquid enters the supercooled state and it can be further cooled down. As the temperature decreases the liquid passes across the liquid-to-glass transition region and its viscosity (η) increases of many orders of magnitude while the molecular dynamics slows down [1–3]. The glass-transition temperature T_g is conventionally defined as the temperature at which η has reached a value of 10^{12} Pa·s or, equivalently, the characteristic timescale for molecular dynamics is of 100s [1–3]. In fact, at T_g, the supercooled liquid is not able anymore to "flow" and appears to be rigid on the timescale of the experimental observation: a glass has been obtained [1–3]. To appreciate how viscous is a supercooled liquid at T_g we recall that the viscosity of water at room temperature is 2×10^{-3}Pa·s, that is $\simeq 15$ orders of magnitude smaller.
Before proceeding, it is important to stress that the glass-transition is not a phase-transition as, for example, crystallization, since T_g is only empirically defined and depends on the cooling-rate (i.e history) of the system [1–3] (more details in Sec. 2.2). In fact, T_g is simply that temperature below which the

supercooled liquid is not able to equilibrate on the experimental time scale and appears macroscopically as rigid. At the microscopic length-scale a glass displays moreover a disordered structure resembling that of a liquid [3].

2.1.0.1 Kinetic fragility

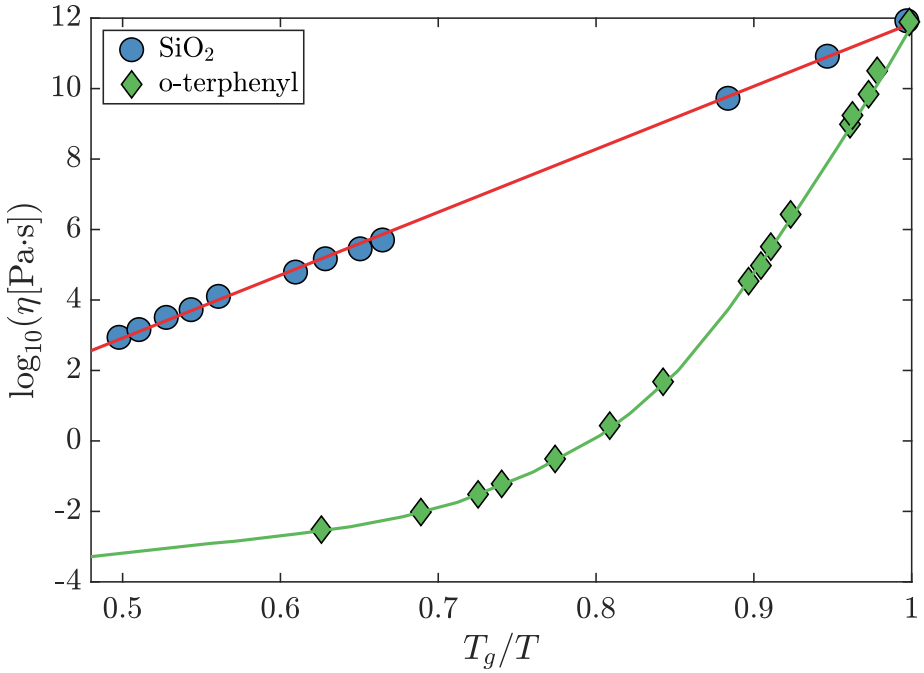

Figure 2.1: Logarithm of the viscosity of SiO_2 (blue cirlces) and o-terphenyl (green diamonds) as a function of the inverse temperature, rescaled by their glass-transition temperature T_g. Red-solid line: Arrhenius fit to the T-dependence of the SiO_2 viscosity. Light green solid line: curve obtained from fitting the VFT law to the o-terphenyl data. *Data taken from [1].*

The T-dependence of the viscosity (or of the characteristic timescale of the molecular dynamics) varies from one system to another and is usually used to classify glass-forming liquids. This can be easily seen on the so-called *Angell plot* [1–3], where the viscosity of a liquid is reported on a logarithmic scale as a function of its inverse temperature, typically re-scaled with respect to T_g. Depending on the shape of the $\eta(T)$ curve on the Angell plot a liquid can be classified as either being "strong" or "fragile". These terms do not refer to the mechanical properties of the glass but rather to the sensitivity of the liquid to changes in temperature [1–3]. A glass-former is strong if the T-dependence of η in the Angell-plot is described by a straight-line, i.e it displays an Arrhenius-like dependence [1–3]:

$$\eta = \eta_0 \exp\left(\frac{E}{k_B T}\right) \tag{2.1}$$

where η_0 is a phenomenological parameter, E an effective activation energy and k_B the Boltzmann constant. Network glasses are typically strong glass-formers as it can be observed in Fig. 2.1 where the viscosity of SiO_2 (blue circles) is plotted along with its Arrhenius T-dependence. On the contrary a "fragile" glass-former is characterized by a super-Arrhenius T-dependence as in the case of o-terphenyl (green diamonds in Fig.2.1). A super-Arrhenius temperature dependence indicates that the activation energy increases on approaching T_g. So glass-formation in fragile glasses is accompanied by large changes in the energy barriers [1, 3]. The T-dependence of η, for fragile liquids, is usually described using the phenomenological Vogel-Tammann-Fulcher (VFT) equation [1–4]:

$$\eta = \eta_0 \exp\left(\frac{DT_0}{T - T_0}\right) \tag{2.2}$$

where η_0,D and T_0 are phenomenological parameters. The fragility of a liquid can be quantified by the *fragility index*, defined as the slope of $log_{10}(\eta)$ in the limit of $T \to T_g$ [4]:

$$m = \lim_{T \to T_g} \frac{\partial \log_{10}(\eta)}{\partial T_g/T} \,. \tag{2.3}$$

2.2 Thermodynamic aspects of the glass-transition

After this brief description of the phenomenology of the glass-transition, it is important to discuss some thermodynamic features of the phenomenon. Fig. 2.2 reports the typical behavior of the specific volume (v_s) and enthalpy (h) for both a crystal and two supercooled liquids under two different cooling rates as a function of temperature. As it was stated, if a liquid is cooled down below T_m rapidly enough to avoid crystallization, it becomes a supercooled liquid. Differently to the case of crystallization, which is a first-order phase transition, no discontinuity is observed in both the specific volume or enthalpy [2]. In the narrow temperature range where the viscosity dramatically increases and the molecular dynamics progressively slows down, the enthalpy decreases and the liquid keeps on contracting (assuming that its thermal expansion coefficient is positive) [2]. However, when the glass-transition temperature is reached, the rate of change of both the volume and enthalpy suddenly (but continuously) decreases, reaching a value which is close to that of the corresponding crystal [2]. So, an apparent discontinuity is observed in both the thermal expansion coefficient $\alpha_p = \left(\frac{\partial \ln v_s}{\partial T}\right)_P$ and isobaric heat capacity $C_p = \left(\frac{\partial h}{\partial T}\right)_P$ (see the inset in Fig. 2.2).
These observations might induce to think that the glass-transition is a proper second-order phase transition. As already anticipated, this is not the case as T_g depends on the history of the system and in particular on the cooling rate, which fixes the time a liquid has at disposal to equilibrate when T is changed (see Fig. 2.2) [2, 3]. To better understand this concept it is useful to consider

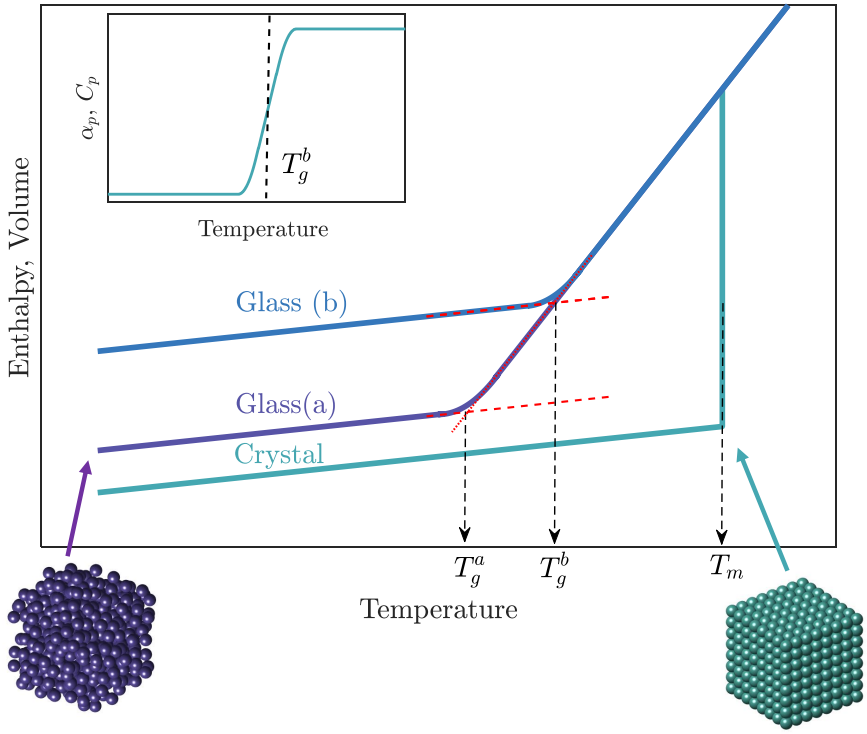

Figure 2.2: Sketch of the characteristic temperature dependence of both enthalpy and volume for a liquid undergoing the crystallization or the glass-transition. The blue and dark blue curves refer to two glasses obtained with two distinct cooling rates: glass (b) forms after a fast quenching and glass (a) after a slower one. Consequently their glass transition temperatures are different. Inset: characteristic jump in the isobaric specific heat (C_p) and thermal expansion coefficient (α_p) occurring at T_g. The sketched atomic configurations enlighten the different microscopic structures after crystallization and the glass transition. While the former displays long-range order, the latter is characterized only by the short-range one.

what happens microscopically during the quenching procedure. Every time the temperature is modified the liquid returns to equilibrium rearranging its microscopic configuration and minimizing its free-energy. The characteristic timescale for this process is the relaxation time τ (more details in Sec. 2.3.5). When T_g is approached, the molecular dynamics slows down and τ becomes very long. This naturally affects the capability of the liquid to explore the configuration space and when the time required to reach a new minimum becomes of the order of the available time imposed by the cooling rate the liquid eventually falls out of equilibrium and becomes a glass [2]. So, the higher the cooling rate, the higher the temperature at which the supercooled liquid will fall out of equilibrium [2]. Conversely, the more slowly a liquid is quenched, the longer is the time available for equilibration: the glass-transition temperature is therefore lower [2].

2.2.1 Entropy and potential energy landscape

Another thermodynamic quantity of particular interest in the glass-transition is the entropy S, and in particular the excess entropy S_{exc} of a liquid with respect to that of the corresponding crystal [1–3]:

$$S_{exc}(T) = S_{liq}(T) - S_{cry}(T). \tag{2.4}$$

The temperature dependence of S_{exc} can be followed until T_g, i.e. before the system falls out of thermal equilibrium, and shows a decreasing trend on decreasing temperature. If extrapolated below T_g, S_{exc} approaches 0 at some finite temperature T_K called Kauzmann temperature [1–3]. Below T_K the entropy of the supercooled liquid S_{liq} is then expected to become smaller than S_{cry}. This phenomenon is also known as the *entropy crisis* [1–3, 15]. The occurrence of a phase transition, or crystal nucleation, above T_K was therefore suggested by Kauzmann [15] as otherwise below T_K a disordered state of matter would have ended having a smaller entropy than the ordered phase. This paradox is of course only apparent, since no general principle forbids the entropy of a liquid to be smaller than that of a crystal [3]. Nonetheless T_K is still recognised as a crucial temperature for the glass-transition [1–3, 15]. In fact, it has been observed that T_K is generally close to 0K for network glasses and to T_0 for fragile ones, where T_0 is the temperature at which the VFT law diverges [1–3]. This intriguing coincidence observed in several glass-formers, has been interpreted as the indication of a link between excess-entropy and the diverging time-scale of supercooled liquids dynamics [1–3]. The importance of T_K is further reinforced if the excess entropy S_{exc} is identified with the so called configurational entropy (S_c) which quantifies the excess of metastable states of a glass with respect to a crystal [2, 3]. The meaning of S_c can easily understood within the *potential energy landscape* (PEL) description of the glass-transition. The PEL paradigm was originally introduced by Goldstein in 1969 [16] and actually provides a useful tool for understanding, at least qualitatively, many of the features of the glass transition that have been introduced above [1, 2, 17]. Formally the PEL, for a system composed of N particles, is the potential energy hyper-surface $U(\mathbf{r_1}, ..\mathbf{r_i}, ...r_N)$ in the $3(N-1)$ configuration space describing the system [1, 2, 16–18]. A point in the PEL defines the state of the system, which actually samples the hyper-surface with a $3(N-1)$ dimensional velocity which is temperature dependent [16]. The PEL, according to the *topographic view* introduced by Stillinger [17], can be visualised as a collection of maxima, minima and saddle points. The minima are the mechanically stable configurations for the N particles. A one dimensional schematic representation of the PEL for a supercooled liquid can seen in Fig. 2.3: the shallow minima are the inherent structures (IS) which group in metabasins, that is, deeper minima separated by larger energy barriers [2, 17, 18]. In the picture the absolute minimum due to crystallization has been omitted for clarity. The way in which a system explores such landscape defines its dynamical properties [2, 17]. At high temperatures the kinetic energy is high enough to explore the entire landscape and the majority of the sampled minima are the shallow ones [2, 17].

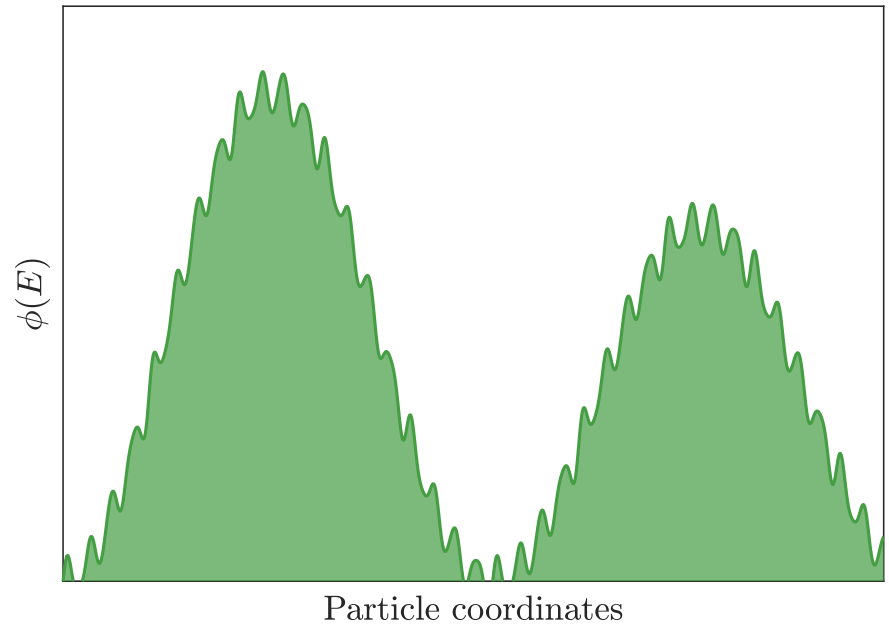

Figure 2.3: One-dimensional sketch of the potential energy landscape in the configuration state. The crystal state, corresponding, to the absolute minimum, has been omitted for the sake of clarity, whereas the different local minima associated to the glassy dynamics are shown.

As the temperature decreases, the particles are not able anymore to cross all the energy barriers and a smaller portion of the PEL can be visited: the system is therefore forced to sample the deeper and rarer "valleys" (i.e metabasin) [2]. Eventually, at sufficiently low T, that is on approaching T_g, the sample remains stuck in one of those minima, whose depth increases with decreasing cooling-rate [2].
The differences between strong and fragile glass-formers can be also rationalised in terms of PEL. In fact, as proposed in [2, 17], fragile glass-formers should be characterized by several metabasins of different depths, well separated one with respect to the other. Strong glass-formers, on the contrary, present a less rugged landscape, with a minor number of metastable minima.
Another phenomenon easy to understand within the PEL description is the aging: when a glass is trapped in an out-of-equilibrium state, it indeed tries nonetheless to move toward a more stable configuration [3]. The *physical* aging, which affects almost all physical properties of a glass [19], can then be pictured as an out-of-equilibrium process during which the system tries to reach deeper basins in the PEL, corresponding to more stable "glassy"-configurations [20].
One of the main advantages of the PEL picture is that it allows to naturally separate, at sufficiently low temperature, the molecular dynamics into vibrations and exploration of the metastable minima [2]. The latter contribution is the

one related to the configurational entropy which is indeed defined as

$$S_c = k_B log(N_{meta}) \tag{2.5}$$

where N_{meta} is the number of metastable configurations [2, 3]. Under the assumption that the vibrational entropy of supercooled liquids is similar to that of crystals, the excess entropy reduces to the configurational one [3]:

$$S_{exc} \simeq S_c \,. \tag{2.6}$$

Before proceeding, it is important to point out that such assumption has been questioned in [21, 22], since it neglects the greater anharmonicity of the potential of a liquid with respect to that of the crystal. Nonetheless, a robust proportionality between the two quantities (S_{exc} and S_c) has been found [23, 24].
Within this approximation, T_K is thus the temperature where S_c vanishes leading to a consequent jump in the specific heat and a thermodynamic phase transition [1–3]. This phase transition, hidden by the kinetic glass transition occurring at T_g, would lead to an *ideal glass* characterized by null configurational entropy. According to this view, the laboratory glass transition would be a manifestation of this underlying thermodynamic phase-transition [2, 3, 25].
A connection between kinetics and thermodynamics is provided by the well-known Adam-Gibbs relation [25]:

$$\eta = B \cdot exp\left[\frac{A}{TS_c}\right] . \tag{2.7}$$

The dramatic increase in the viscosity (and molecular slowdown) would then be due to the reduction of the configurations accessible to the system [2, 25]. The derivation of Eq. 2.7, relies on the concept of cooperative rearranging regions (CRR): at sufficiently low temperatures re-arrangements should involve the cooperative motion of an increasingly high number of particles [25].
Adam-Gibbs's theory, and in particular the idea of a thermodynamic driven, hidden "ideal glass transition", are also at the basis of the so-called Random First Order Theory (RFOT) [26, 27] of the glass-transition. The ROFT is a mean-field theory, inspired by the theoretical framework of spin-glasses, which has been able to further expand and investigate the connections between thermodynamics and dynamics in the glass-transitions [26–28]. In the RFOT such connection is established first showing, with thermodynamic arguments, that the decrease in configurational entropy is accompanied by a growing *point-to-set* static correlation length-scale ξ_{pts} [30, 31] over which molecules re-arrange cooperatively. The connection to dynamics is then made through the assumption that at sufficiently low temperature (i.e below the mode-coupling cross-over temperature T_c [32]) relaxations occur via thermally activated events, which are correlated over ξ_{pts} [26, 29, 30]. From these two considerations a generalised version of the Adam-Gibbs's relation arises [26, 27]:

$$log(\eta) \propto \frac{1}{S_c^{\alpha} T} \tag{2.8}$$

where α is an exponent which can be derived by first principles. In the ROFT picture a central role is played by the concept of *mosaic state*: the liquid, between T_c and T_K, consists of CRRs (or entropic droplets) with a linear size equal to ξ_{pts}. The size of these domains is expected to grow on lowering the temperature [3, 27, 29]. It is important to remark that, in the framework of the RFOT, T_c is regarded, in analogy to regular first-order transitions, as a spinodal temperature [3, 27, 29, 33, 34]. In fact, T_c, in the mean-field limit, signals the limit of stability of the mosaic state which, as said before, is a collection of metastable, contiguous glassy structures. For instance, on approaching T_c the barriers between the different CRRs soften and not-activated events become more and more important until the liquid becomes again uniform [27, 29, 34]. The RFOT has been proven to quantitatively describe many properties of the glass-transition [3, 26–28] such as the kinetic fragility [33] or the emergence of secondary relaxation processes [35] (more details in Sec. 2.5.5.4) just to name a few. However, as it has been pointed out in several reviews [3, 28] the RFOT, besides its successes, presents issues which should be further addressed and tested. This topic, along with a more detailed description of the ROFT, is beyond the purpose of this work and the interested reader is referred to the literature [3, 27, 28].
It is finally important to spend few words about the assumption of the glass-transition as an entropy-driven transition. As mentioned above, the existence of an ideal glassy state is hinted by the correlation between the diverging time-scale of the VFT law and the Kauzmann temperature. However both quantities depend on extrapolations performed above the glass-transition temperature and estimates might be affected by pre-asymptotic effects. It has also been suggested that the relation between T_K and T_0 might not depend on S_c [36]. The Adam-Gibbs's relation too has been recently put to test combining simulations and new experimental data [31]. It was observed that while the Adam-Gibbs relation fails, its generalised version (Eq. 2.8) can reproduce both experimental data and simulated ones in a wide temperature range [31]. The obtained values for the exponent $\alpha < 1$ might however suggest that entropy is not the only cause of the dynamic arrest [31].
It is also important to underline that there are also theories according to which the configurational entropy S_c might be only a spectator of the glass-transition [37].

2.2.1.1 Other approaches to the glass-transition problem.

In the previous paragraph (Sec. 2.2.1) several models based on the entropic origin of the glass transition have been discussed. However, other viewpoints are also present.
One of them is the free-volume approach [38–40], widely used in the description of polymeric systems [39]. The main idea behind free-volume models is that a molecule in a liquid requires free volume in order to re-arrange. Upon cooling, the liquid contracts and the free volume reduces accordingly. The glass-transition occurs when the free-volume available is not sufficient anymore

for molecular movement. A problem of free-volume models is that a rigorous definition of the free-volume itself is difficult [40].
Elastic models represent a further approach to the problem of the glass transition. The main idea underlying the elastic models is that the solid-like character is one of the most defining features of the glassy state [40]. The relaxation properties of liquids are therefore controlled by their short time elastic properties ($\simeq$ 1 ps) [40]. In particular the activation energy for transport is expected to grow with the shear modulus [40]. So, the slow-down of the molecular dynamics is caused by the increase of the high-frequency elastic constants of the material [40]. For further details the interested reader is refereed to the literature [38, 40].

2.3 General theory of relaxation processes

After this far from complete review of the phenomenology of the glass-transition, it is time to introduce one of the key concepts in the study of the glass-transition, that of relaxation processes. During a relaxation process, the system irreversibly evolves (in time) from a thermodynamic (or physical) state to another and dissipates energy [4]. Relaxation processes are thus those microscopic mechanisms by which a liquid can reach an equilibrium configuration after a spontaneous fluctuation or an external perturbation. It is clear that investigating relaxations on approaching T_g allows to get a picture of the microscopic mechanisms that intervene in the glass transition and in particular in the process of dynamic arrest [3, 4]. For this reason it is important to provide some general remarks about the formalism of relaxation processes, starting from the linear response theory.

2.3.1 The linear response theory

The linear response theory for irreversible processes was introduced for the first time by Kubo [41] and establishes a fundamental link between the response of a system to a weakly external field and the spontaneous fluctuations of that system at equilibrium, that is without the external perturbation. In this section only the main features of the linear response theory are discussed along with some practical examples, with an approach similar to that in [4] and [43]. A more complete treatment of the involved formalism can be found by the interested reader in several textbooks [42, 43] and reviews [44, 45].
Before introducing the main results of the linear response theory, it is necessary to recall few important concepts of statistical mechanics. Let us first of all consider an isolated system consisting of N spherical particles with mass m and occupying a volume V. Classically, the state of such system, at a certain time t, is defined by the 3N coordinates $\mathbf{q}^N = (\mathbf{q}_1, ..., \mathbf{q}_N)$ and 3N momenta $\mathbf{p}^N = (\mathbf{p}_1, ..., \mathbf{p}_N)$ that identify its position in the $6N$-dimensional phase-space.

The trajectory of the system is instead governed by Hamilton's equations [43]:

$$\dot{\mathbf{q}}_\mathbf{i} = \frac{\partial \mathcal{H}}{\partial \mathbf{p}_\mathbf{i}} \tag{2.9}$$

$$\dot{\mathbf{p}}_\mathbf{i} = -\frac{\partial \mathcal{H}}{\partial \mathbf{q}_\mathbf{i}} \tag{2.10}$$

where $\mathcal{H}$ is the Hamiltonian operator of the system.
It is also important to introduce the phase-space probability density $f(\mathbf{q}^N, \mathbf{p}^N, t)$. This concept is strictly related to the Gibb's formulation of statistical mechanics where the expectation values of an observable are calculated performing averages over an ensemble of replica of the system [43]. In this context $f(\mathbf{q}^N, \mathbf{p}^N, t) d\mathbf{q}^N d\mathbf{p}^N$ is the probability that at a certain instant t the system is in a microscopic state represented by a point in the infinitesimal neighbourhood $d\mathbf{q}^N d\mathbf{p}^N$. So, the ensemble average of a dynamical variable S at time t is given by

$$\langle S(t) \rangle = \int S(\mathbf{q}^N, \mathbf{p}^N, t) f(\mathbf{q}^N, \mathbf{p}^N, t) d\mathbf{q}^N d\mathbf{p}^N \,. \tag{2.11}$$

$f(\mathbf{q}^N, \mathbf{p}^N, t)$ evolves in time according to the Liouville equation:

$$\frac{\partial f}{\partial t} = -i\mathcal{L} f \tag{2.12}$$

where $-i\mathcal{L}$ is the Liouville operator:

$$-i\mathcal{L} = \sum_{i=1}^{N} \left(\frac{\partial \mathcal{H}}{\partial \mathbf{q}_\mathbf{i}} \frac{\partial}{\partial \mathbf{p}_\mathbf{i}} - \frac{\partial \mathcal{H}}{\partial \mathbf{p}_\mathbf{i}} \frac{\partial}{\partial \mathbf{q}_\mathbf{i}} \right) = \{\mathcal{H}, \} \,. \tag{2.13}$$

Here $\{\}$ indicates the Poisson bracket between H and f.
The aim of the linear response theory is to calculate how the ensemble average of a variable S is modified by the application of an external field $E(t)$ to the conjugated variable W. $E(t)$ is supposed to couple weakly to the system and is applied on the system while at thermal equilibrium, that is, starting from "infinite past" $t = -\infty$ [4, 43]. The new Hamiltonian of the system is then re-written including the effect of the field:

$$\mathcal{H}' = \mathcal{H} - E(t) W \,. \tag{2.14}$$

The time evolution of f, according to Eq. 2.12, is

$$\frac{\partial f}{\partial t} = \{\mathcal{H}, f\} = -i\mathcal{L} f - \{W, f\} E(t) \,. \tag{2.15}$$

Since the regime of linear response is here considered, the terms in Eq. 2.15 that are not linear in $E(t)$ can be disregarded, and f can be split in two terms, one accounting for the equilibrium probability distribution (f_{eq}) and another for the change Δf, up to the first order, induced by $E(t)$. So Eq. 2.15 reduces to:

$$\frac{\partial \Delta f}{\partial t} = -i\mathcal{L} \Delta f(\mathbf{q}^n, \mathbf{p}^n, t) - \{W, f_{eq}\} E(t) \,. \tag{2.16}$$

Δf can then be readily obtained integrating Eq. 2.16:

$$\Delta f(t) = \int_{-\infty}^{t} e^{-i(t-t')\mathcal{L}}\{-W(\mathbf{q^N}, \mathbf{p^N}), f_{eq}(\mathbf{q^N}, \mathbf{p^N})\}E(t')dt' \,. \tag{2.17}$$

The effect of the external field $E(t)$ is to change the phase-space distribution function and in turn the expectation value of S. The ensemble averaged modification of $\langle S\rangle$ results to be equal to [4, 43]

$$\langle \Delta S(t)\rangle = \int\int d\mathbf{q}^n d\mathbf{p}^n S(\mathbf{q}^n, \mathbf{p}^n)\Delta f(\mathbf{q}^n, \mathbf{p}^n) = \int_{-\infty}^{t} \Psi_{SW}(t-t')E(t')dt' \,, \tag{2.18}$$

where $\Psi_{SW}(t-t')$ is the response function [4, 43].

$$\Psi_{SW}(t-t') = \beta\langle S(t)\dot{W}(t')\rangle \,. \tag{2.19}$$

In Eq. 2.19 β is the Boltzmann factor $1/k_BT$ (k_B is the Boltzmann constant). $\Psi_{SW}(t-t')$ is simply the ensemble averaged response of S at the time t after that an impulse $\delta(t)$ (δ is the Dirac's delta) has perturbed W at t'.
In the case of $E(t)$ being an oscillating field of the type $E(t) = E_0e^{-i\omega t}$, Eq. 2.18 can be re-written as [4, 43]:

$$\langle S(t)\rangle = E_0e^{i\omega t}\int_0^{+\infty} e^{-i\omega t'}\Psi_{SW}(t')dt' \equiv E_0\chi_{SW}(\omega)e^{i\omega t} \,. \tag{2.20}$$

$\chi_{SW}(\omega)$ is the complex dynamic susceptibility, which is related to the response function via

$$\chi_{SW}(\omega) \equiv \chi'_{SW}(\omega) - i\chi''_{SW}(\omega) = \int_0^{+\infty} \psi_{SW}(t)e^{-i\omega t}dt \,, \tag{2.21}$$

where χ'_{SW} and χ''_{SW} are the real and imaginary parts of the dynamic susceptibility. What discussed up to now obviously applies also to the special case when S=W:

$$\Psi_{WW} = -\beta\langle \dot{S}(t)S(0)\rangle \,. \tag{2.22}$$

2.3.2 The fluctuation dissipation theorem

The linear response theorem allows us to relate the microscopic response of a system to an external field. At this point another important ingredient should be introduced: the fluctuation dissipation theorem. The fluctuations dissipation theorem, whose general formulation is due to Callen and Walton [46] and Kubo [41], essentially connects the response of a system to an external perturbation to its fluctuations at thermodynamic equilibrium. In fact a system at equilibrium, even in absence of an external perturbation, shows the presence of spontaneous fluctuations.
The fluctuations of a dynamical variable W that varies from its average value $\langle W\rangle$ by $\delta W = W(t) - \langle W\rangle$ are characterized by the time auto-correlation function of δW:

$$C_{WW} = \langle \delta W(0)\delta W(t)\rangle \tag{2.23}$$

and by its power spectrum

$$S_{WW} = \frac{1}{2\pi}\int_{-\infty}^{+\infty} C_{WW}(t)e^{i\omega t}dt\,. \tag{2.24}$$

S_{WW} is a real and even function of ω and, according to the dissipation fluctuation theorem, is related to the dynamic susceptibility χ_{WW} by [4, 41–43, 46]:

$$S_{WW}(\omega) = \frac{k_B T}{\pi\omega}\chi''_{WW}(\omega)\,. \tag{2.25}$$

Eq. 2.25 essentially tells us that the relaxation processes affecting a certain dynamical variable can be equivalently studied i) applying and external field and probing the response function or ii) directly looking at its fluctuations at thermal equilibrium. In the following two practical examples of interest to this work are treated in some details, namely dipole re-orientations and density fluctuations.

2.3.3 Dipole reorientations

In this section the linear response formalism is applied to the case of dielectric spectroscopy (DS) in order to show the connection between the measured macroscopic response and the microscopic properties of the system.
In a typical DS experiment, the reorientation of permanent molecular dipoles is probed by applying a weak electric field $E(t)$ and studying the evolution of the time-dependent polarization $P(t)$ [4, 47].
In what follows the electric field is assumed to be oriented along the z axis and to be applied to the system starting from time $t = 0$ and the system to be isotropic. The resulting dielectric displacement $D_z(t)$ is equal to [4]:

$$D_z(t) = \epsilon_v\epsilon_\infty E_z(t) + P_z(t)\,. \tag{2.26}$$

Here P_z is the polarization in the z-direction because of E_z, ϵ_v is the vacuum permittivity and ϵ_∞ is the permittivity at $t \to \infty$. Concerning P_z, it can be written as [4]:

$$P_z(t) = \epsilon_v(\epsilon_0 - \epsilon_\infty)\int_{-\infty}^{t} E_z(t')\psi(t-t')dt' \tag{2.27}$$

with ϵ_0 being the dielectric response at $t = 0$ and ψ is the macroscopic response of the system. If the external field is oscillating $E(t) = E_0 e^{i\omega t}$ and taking into account Eq. 2.27, Eq. 2.26 becomes [4]:

$$D_z(t) = \epsilon_v[\epsilon'(\omega) - i\epsilon''(\omega)]E_0 e^{i\omega t} \tag{2.28}$$

where ϵ' and ϵ'' are the real and imaginary parts of the complex permittivity ϵ^*:

$$\epsilon^* = \epsilon_\infty + (\epsilon_0 - \epsilon_\infty)\int_0^\infty e^{-i\omega t}\psi(t)dt\,. \tag{2.29}$$

$\psi(t)$ is connected to the microscopic properties of the system since the macroscopic polarization P_z is related to the dipole moment of the system $M_z(t)$ (along z) [4]:

$$P_z = \frac{\langle M_z \rangle}{V} \,. \tag{2.30}$$

In an ensemble with N dipoles, $\mathbf{M}$ is given by the sum of the microscopic dipole moments $\mu_\mathbf{i}$ in the volume V [4]:

$$\mathbf{M} = \sum_i^N \mu_i \,. \tag{2.31}$$

Using Eq. 2.18, it is then easy to calculate the time evolution of $\langle M_z(t) \rangle$ [4]:

$$\begin{aligned} \langle M_z(t) \rangle &= -\frac{1}{k_B T} \int_{-\infty}^{t} E_z(t') \langle \dot{M}_z(t-t') M_z(t') \rangle dt' \\ &= -\frac{\langle \mathbf{M}(0) \cdot \mathbf{M}(0) \rangle}{3 k_B T} \int_{-\infty}^{t} E_z(t') \dot{J}(t-t') dt' \end{aligned} \tag{2.32}$$

In Eq. 2.32 $\langle \dot{M}_z(t-t') M_z(0) \rangle$ has been replaced by the corresponding scalar product and $\dot{J}$ is the derivative of the time autocorrelation function of the dipole moments [4]

$$J = \frac{\langle \mathbf{M}(t) \cdot \mathbf{M}(0) \rangle}{\langle \mathbf{M}(0) \cdot \mathbf{M}(t') \rangle} \,. \tag{2.33}$$

So, if P_z is expressed in terms of Eq. 2.32, it is readily obtained that the complex permittivity $\epsilon(\omega)$, probed in DS experiments, bears information on the autocorrelation function of the dipole moments [4]:

$$\frac{\epsilon^*(\omega) - \epsilon_\infty}{\epsilon_0 - \epsilon_\infty} = 1 - i\omega \int_0^\infty \frac{\langle \mathbf{M}(t) \cdot \mathbf{M}(0) \rangle}{\langle \mathbf{M}(0) \cdot \mathbf{M}(0) \rangle} e^{i\omega t} dt \,. \tag{2.34}$$

2.3.3.1 Molecular re-orientational correlation functions

Techniques sensitive to orientational degree of freedom such as DS are strictly connected to molecular reorientational correlation functions. More precisely, J is strongly related to the single molecule reorientational correlation function [4, 48]:

$$C_1 = \langle \mathbf{u}(t) \cdot \mathbf{u}(0) \rangle \tag{2.35}$$

where $\mathbf{u}$ is the unit vector along the molecular dipole. C_1 is usually expressed in terms of the first-order Legendre polynomial P_1 [4]

$$C_1(t) = \langle cos(\theta) \rangle = \langle P_1[cos(\theta)] \rangle \,. \tag{2.36}$$

Another important example worthwhile mentioning is depolarized dynamic light scattering (DDLS). In this case, differently from DS, the observable is not a vector but a tensor: the anisotropic polarizability [4, 48]. Molecular

re-orientations are then probed via the C_2 correlation function which is instead linked to the second-order Legendre polynomial [4, 48]:

$$C_2(t) = \left\langle \frac{1}{2}\left(3cos^2\theta - 1\right)\right\rangle . \tag{2.37}$$

For these reasons, comparing the results between the two techniques as pointed out in [48] and demonstrated in recent studies on mono-alcohols [49, 50], can provide important information on the underlying microscopic motion. For further details on this topic the interested reader is referred to [48].

2.3.4 Density fluctuations

This section will be dedicated to microscopic density fluctuations. This dynamical quantity is usually studied by probes able to access dynamics at the atomic and molecular level, such as X-rays and neutrons.
Let us consider a uniform system consisting of N particles with coordinates $\mathbf{q}^N = \mathbf{r}^N = (\mathbf{r}_1, \mathbf{r}_2, .., \mathbf{r}_i, ...\mathbf{r}_N)$. Their instantaneous spatial distribution is expressed by the microscopic particle density [43]:

$$\rho(\mathbf{r}, t) = \sum_i^N \delta[\mathbf{r} - \mathbf{r}_i(t)] . \tag{2.38}$$

Eq. 2.38 indeed counts the number of particles that at time t are in a neighborhood of r. The corresponding correlation function is the Van-Hove correlation function [43, 51]:

$$\begin{aligned} G(\mathbf{r}, t) &= \frac{1}{N}\left\langle \sum_i^N \sum_j^N \delta[\mathbf{r} - \mathbf{r}_j(t) + \mathbf{r}_i(0)]\right\rangle \\ &= \frac{1}{N}\left\langle \sum_i^N \sum_j^N \int \delta[\mathbf{r}' + \mathbf{r} - \mathbf{r}_j(t)]\delta[\mathbf{r}' - \mathbf{r}_i(0)]d\mathbf{r}'\right\rangle \\ &= \frac{1}{N}\left\langle \int \rho(\mathbf{r}' + \mathbf{r}, t)\rho(\mathbf{r}', 0)d\mathbf{r}'\right\rangle = \frac{1}{\rho}\langle\rho(\mathbf{r}, t)\rho(0, 0)\rangle \end{aligned} \tag{2.39}$$

where ρ is the average density of the system. The physical meaning of the van Hove function can be easily understood if it is considered in terms of a probability distribution. In fact $G(\mathbf{r}, t)d\mathbf{r}$ is the number of particles j in an infinitesimal neighborhood $d\mathbf{r}$ of $\mathbf{r}$ at the time t, provided that a particle i was at the origin at time 0 [43]. The van Hove correlation function is usually split in two terms, the *self* and *distinct* parts

$$G(\mathbf{r}, t) = G_s(\mathbf{r}, t) + G_d(\mathbf{r}, t) \tag{2.40}$$

respectively defined as [43]

$$G_s(\mathbf{r}, t) = \left\langle \sum_i^N \delta[\mathbf{r} - \mathbf{r}_i(t) + \mathbf{r}_i(0)]\right\rangle \tag{2.41}$$

and

$$G_d(\mathbf{r},t) = \left\langle \sum_i^N \sum_{j\neq i}^N \delta[\mathbf{r} - \mathbf{r}_j(t) + \mathbf{r}_i(0)] \right\rangle . \tag{2.42}$$

G_s and G_d separately account for the possibility that i and j are the same particle or not. It is crucial to notice that, in the limit $t \to 0$, the distinct part $G_d(\mathbf{r},0)$ reduces to $\rho g(\mathbf{r})$, where $g(\mathbf{r})$ is the so-called pair distribution function. $g(\mathbf{r})$ is a static correlation function that describes the average distance between particles in the system [43].
In the opposite limit, $t \to \infty$, both G_s and G_d become instead independent of $\mathbf{r}$ [43]:

$$\begin{aligned} \lim_{t\to\infty} G_s(\mathbf{r},t) &= \frac{1}{V} \\ \lim_{t\to\infty} G_d(\mathbf{r},t) &= \rho. \end{aligned} \tag{2.43}$$

Density-density correlation functions provide a direct picture in real space of the microscopic motions of atoms and molecules within a relaxation process. Scattering experiments can probe microscopic dynamics only in the reciprocal space. In this case the observable that is usually accessed is the *intermediate scattering function* $F(\mathbf{q},t)$. $F(\mathbf{q},t)$ is the correlation function of the Fourier components $\rho(\mathbf{q},t) = \sum_i^N e^{i\mathbf{q}\cdot\mathbf{r}}$ of the density function $\rho(\mathbf{r},t)$ [43]:

$$F(\mathbf{q},t) = \frac{1}{N} \langle \rho(\mathbf{q},t)\rho^*(\mathbf{q},0)\rangle . \tag{2.44}$$

Here $\mathbf{q}$ indicates the wave-number of the Fourier component.
Density fluctuations with different $\mathbf{q}$ can be experimentally accessed selecting the momentum $\hbar\mathbf{q}$ exchanged by the probe (typically X-rays or neutrons) with the system during the scattering process. $F(\mathbf{q},t)$ is connected to the van Hove correlation function [43] via

$$F(\mathbf{q},t) = \int G(\mathbf{r},t) e^{-i\mathbf{q}\cdot\mathbf{r}} d\mathbf{r} , \tag{2.45}$$

and its power-spectrum is the so-called *dynamic structure factor*:

$$S(\mathbf{q},\omega) = \frac{1}{2\pi} \int_{-\infty}^{+\infty} F(\mathbf{q},t) e^{i\omega t} d\omega . \tag{2.46}$$

Another important static correlation function which should be introduced is the static structure factor $S(\mathbf{q})$, defined as [43]:

$$S(\mathbf{q}) = \int_{-\infty}^{+\infty} S(\mathbf{q},\omega) d\omega = F(\mathbf{q},0) \tag{2.47}$$

Similarly to the pair correlation function, the static structure factor $S(\mathbf{q})$ provides information about the average particle distance, but in reciprocal space. $S(\mathbf{q})$ can be seen as the density response of the system to a perturbation of wave-length $\frac{2\pi}{\mathbf{q}}$ [43]. In neutron or X-ray scattering experiments the total

diffuse intensity is indeed connected to $S(\mathbf{q})$, whose peak q_{max} is usually related to the average intermolecular distance by $r_p \simeq \frac{2\pi}{q_{max}}$. In the macroscopic limit, that is for small $\mathbf{q}$, the static structure factor is proportional to the isothermal compressibility χ_T [43]

$$lim_{\mathbf{q}\to 0} S(\mathbf{q}) = \rho k_B T \chi_T \,. \tag{2.48}$$

$F(\mathbf{q},t)$ is usually normalized to one at $t=0$ using $S(q)$:

$$\phi(\mathbf{q},t) = \frac{F(\mathbf{q},t)}{S(\mathbf{q})} = \frac{\langle \rho^*(\mathbf{q},0)\rho(\mathbf{q},t)\rangle}{\langle |\rho(\mathbf{q})|^2\rangle} \,. \tag{2.49}$$

$\phi(\mathbf{q},t)$ is the so called *normalized intermediate scattering function* and typically, in liquids and glasses, it is a decreasing function of t which evolves from 1 at $t=0$ to 0 at $t=\infty$. As it will be clarified in Ch. 3, the normalized intermediate scattering function is the observable accessed in nuclear γ-resonance time-domain interferometry experiments.
To conclude, it should be noted that for isotropic systems, such as liquids and supercooled liquids, all the aforementioned correlation functions depend only on the module of $\mathbf{q}$.

2.3.5 Which parameters characterize a relaxation?

After having introduced the correlation functions probed in dielectric spectroscopy and scattering experiments, it is worth discussing which parameters actually define a relaxation process. The relaxation time τ and the relaxation strength f can be recognised as the main ones. τ is the characteristic time-scale of the processes, that is the time necessary to restore equilibrium after an external perturbation. In the case of the normalized intermediate scattering function, the relaxation time τ_q, relative to density fluctuations with wave-vector q, can be identified as the time required for the particles of the system to move (on average) over a distance $\delta_r \simeq \frac{1}{q}$.
f instead quantifies the amount of decorrelation experienced by the considered dynamical variable (for example density fluctuations or dipole orientations) because of the relaxation process. If several relaxations are present, as in the case of supercooled liquids approaching T_g, it is interesting to characterize the relative contributions of each of them. Regarding density fluctuations, the relaxation strength can also be directly interpreted as the average number of atoms/molecules participating to the relaxation process.
To properly characterize a relaxation it is therefore crucial to study how these parameters (τ and f_q) vary as a function of the temperature and, in the case of $\phi(\mathbf{q},t)$, as a function of q. Investigating the q-dependence of τ and f_q is essentially equivalent to probe how relaxations affect the molecular and atomic dynamics at different length-scales, identified by $r = \frac{2\pi}{q}$. For example in the case of simple diffusion the intermediate scattering function is an exponential function [4, 43]:

$$\phi(\mathbf{q},t) = \exp\left[-\frac{t}{\tau_q}\right] \tag{2.50}$$

and the q-dependence of τ is described by

$$\tau_q = \frac{1}{Dq^2} \tag{2.51}$$

where D is the diffusion coefficient. In simple diffusion τ is thus proportional to q^{-2} and the mean-square displacement of the particle, defined as:

$$\langle r^2(t) \rangle = \langle |\mathbf{r}(t) - \mathbf{r}(0)|^2 \rangle \tag{2.52}$$

grows linearly in time [4, 43]. If a deviation from this behavior is observed, we are in presence of anomalous diffusion. A ballistic motion is characterized by a sub-quadratic q-dependence ($n < 2$), formally with $n = 1$ [52], whereas in presence of a sub-diffusive dynamics a super quadratic q-dependence appears ($n > 2$) [53, 54]. An example of the former regime can be found in colloidal glasses and gels, where a ballistic motion (i.e. $\langle r^2(t) \rangle \propto t^b$ with $b > 2$) is a signature of the presence of internal stresses in the system. The latter regime is instead a signature of restricted dynamics (i.e. $\langle r^2(t) \rangle \propto t^b$ with $b < 2$) and has been observed, for example, in polymers [53] or in colloids close to the colloidal glass-transition [55].
Clearly the wave-number dependence of τ provides valuable information on the underlying microscopic motions.
As it will be clarified in the next paragraphs, such characterization is not an easy task as supercooled liquids close to T_g are characterized by several relaxations processes that stretch over several decades in time. Many experimental techniques, sensitive to different degrees of freedom and with different dynamic ranges, are therefore required.

2.4 Relaxations in glass-forming liquids

The dynamics of a supercooled liquid close to T_g is rather complex and covers almost 14 decades in time (see for instance the sketch reported in Fig. 2.4). In the following the properties of the main relaxation processes are reviewed, with a particular attention to the structural (α) and the Johari-Goldstein (β_{JG}) processes.

2.4.1 Fast relaxations

At the ps and sub-ps timescale the dynamics is dominated by the so-called fast-processes [56, 57]. Microscopically, fast relaxations are pictured as a fast "rattling" occurring in the transient cages which are defined by the nearest neighbors and prevent the molecules from free diffusion [4]. The length-scale of this rattling motion, i.e the associated mean square displacement $\langle r^2 \rangle$, is usually obtained from the measurement of the Debye-Waller factor in incoherent elastic neutron scattering.
Their characteristic relaxation time displays a rather weak temperature dependence whereas their strength decreases on lowering T [56, 57]. Concerning

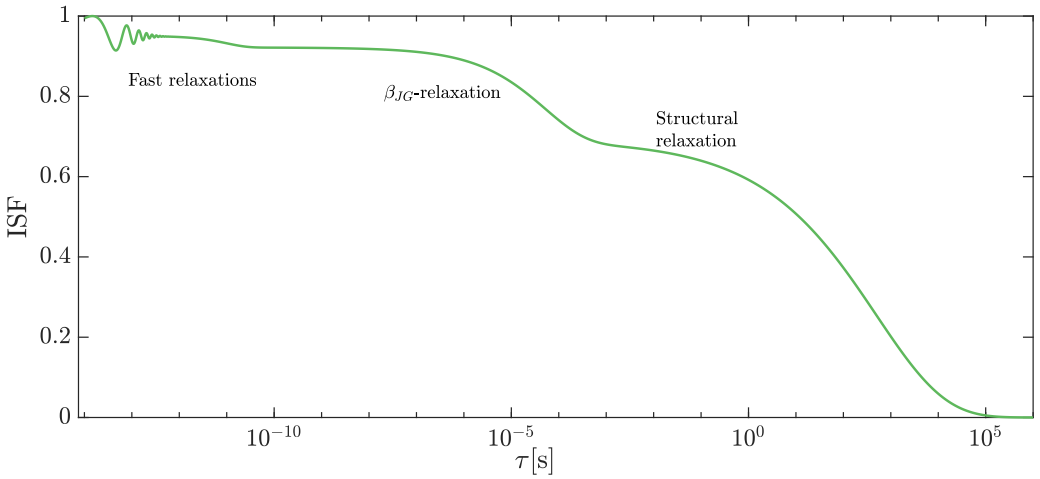

Figure 2.4: Sketch of the intermediate scattering function for a supercooled liquid close to its glass-transition temperature. The main relaxation processes are labeled.

density fluctuations, f_q decreases close the maximum of the $S(q)$, that is, on approaching the average intermolecular distance. In dielectric spectra fast relaxations are characterized by a susceptibility of the type [4]:

$$\chi''(\nu) = B(T)\nu^{-\lambda} \tag{2.53}$$

with $B(T)$ weakly dependent on temperature and $\lambda \ll 1$. This part of the susceptibility spectra is usually called *nearly constant loss* because of its weak power-law dependence on frequency [4].
The interested reader can find further information in the literature [4].
Fast-relaxations, close to T_g, are followed by a plateau after which two slower relaxation processes take place: the Johari-Goldstein (β_{JG}) and the structural (α) relaxation process.

2.4.2 α-relaxation

The structural or α-relaxation can be regarded as the main relaxation process for supercooled liquids and its characteristic time is directly related to the viscosity via the Maxwell relation [1, 3, 4]:

$$\eta = \tau_\alpha G_\infty \,. \tag{2.54}$$

where G_∞ is the infinite shear modulus. The α-process, that is thus related to the response of the system to shear stress, is the principal mechanism by which a liquid relaxes its internal structure [3].
The α-relaxation is directly involved in the process of dynamic arrest occurring during the glass-transition and its relaxation time (τ_α) dramatically slows down on approaching T_g, where it becomes $\simeq 100s$. An example is shown in Fig. 2.5, where the τ_α of the monohydroxyl alcohol 5-methyl-2-hexanol is reported

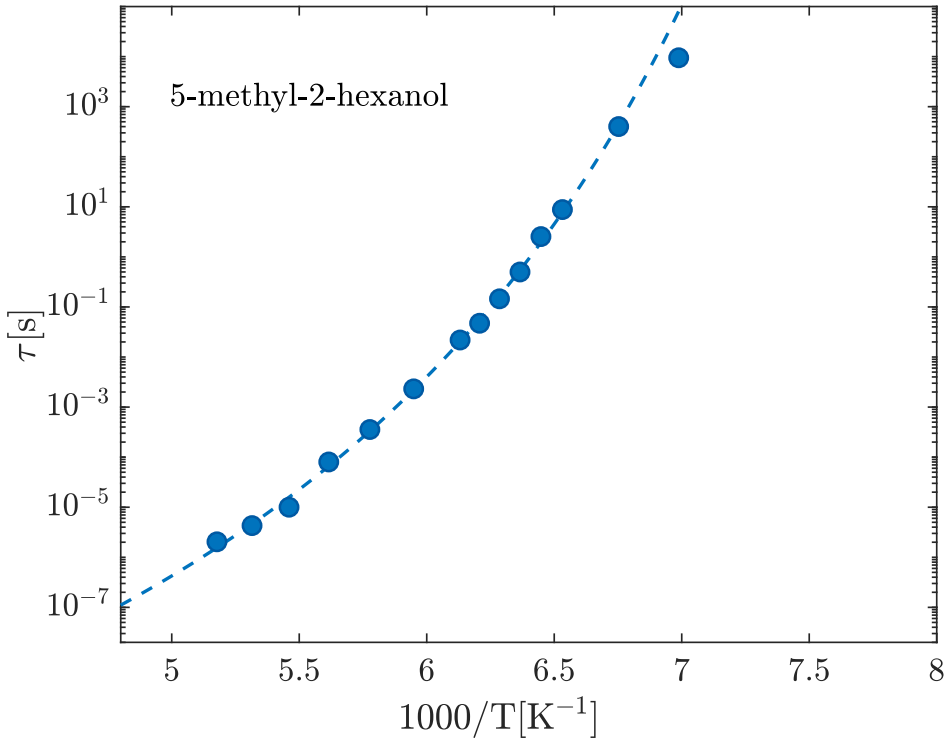

Figure 2.5: Structural relaxation time of 5-methyl-2-hexanol probed by dielectric spectroscopy as a function of the inverse temperature $1000/T$ (blue dots). The dashed line is the curve obtained from the fit of Eq. 2.2 to the experimental data. *Data taken from [134].*

as probed by DS. 5M2H is a fragile liquid and therefore τ_α displays a super-Arrhenius VFT T-dependence (Eq. 2.2). Concerning the time-evolution of the α-relaxation, this cannot be simply described in terms of free-diffusion, i.e using Eq. 2.50, in the supercooled state. The strong deviation from the simple exponential behavior is well described by the Kohlrausch-Williams-Watts (KWW) model [4]

$$\phi(\mathbf{q},t) = f_\mathbf{q} \exp\left[-\left(\frac{t}{\tau_q}\right)^{\beta_{KWW}}\right] \tag{2.55}$$

where β_{KWW} is the so-called stretching parameter and for supercooled-liquids is usually < 1. Fig. 2.6 shows the time-evolution of the structural relaxation of under-cooled lithium-metaborate ($LiBO_2$) close to its T_g: it is clear that Eq. 2.55 is required in order to reproduce the "stretched shape" of the auto-correlation function. Typically, on lowering the temperature, β_{KWW} becomes increasingly smaller than 1. The dispersion of the structural relaxation, which is phenomenologically accounted for by the stretching parameter β_{KWW}, is a hint, among others, of its many-body nature governed by intermolecular interactions [4, 58]. The α-relaxation is indeed strongly related to the microscopic structure of the system. In fact, when density fluctuations are considered, it is possible

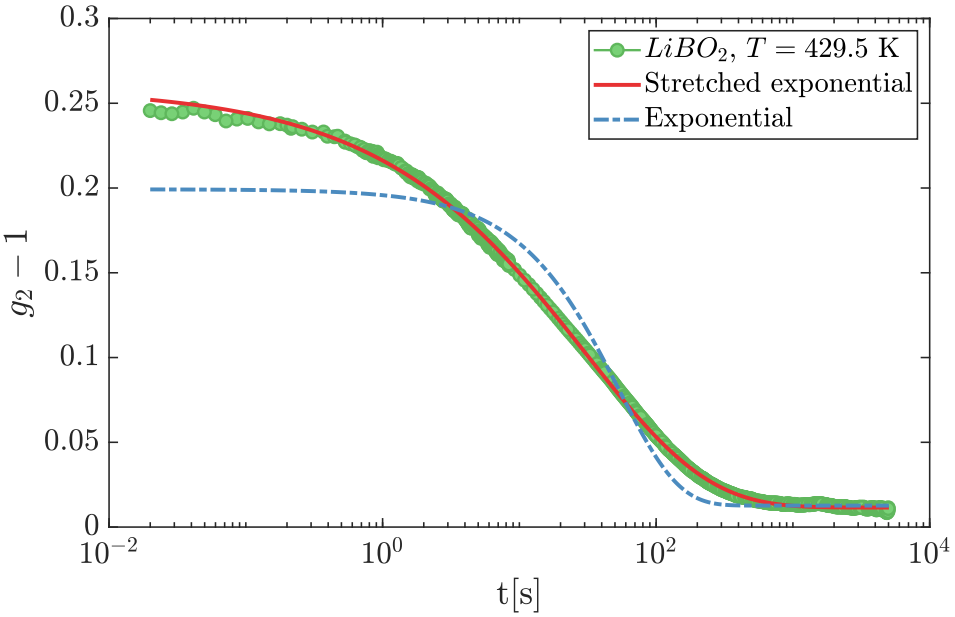

Figure 2.6: Time-evolution of the $|F(\mathbf{q},t)|^2$ auto-correlation function of a lithium meta-borate glass at $T = 702$K (green circles) as measured by visible photon correlation spectroscopy ($q = 0.0167\text{nm}^{-1}$). Red-solid line: curve obtained from fitting Eq. 2.55 to the experimental data. Blue dashed-dotted line: fitting curve obtained considering a simple exponential decay for the g_2 function.

to observe that the relaxation parameters (f_q, τ_q and β_{KWW}) oscillate in phase with the static structure factor of the system. This is the so-called De-Gennes narrowing and it has been observed both in simulations [59, 60] and in experiments [56, 61]. This phenomenon, and in particular the slow-down of τ_α at q_{max} is explained by the fact that relaxations over inter-molecular distances are more difficult: the molecules have indeed to move to positions which are likely already occupied by the nearest neighbours.
Another important aspect concerning the KWW expression is that it can be written as a superposition of exponentials with different relaxation times, weighted over a suitable distribution:

$$\phi(\mathbf{q},t) = \int_0^{+\infty} G(\tau) e^{(-\frac{t}{\tau})} d\tau \,. \tag{2.56}$$

The stretching exponent β_{KWW} can thus be interpreted as a sign of the heterogeneity of the glassy dynamics: different regions relax with different rates [62]. This interpretation, nowadays widely accepted, has been however challenged by the so-called *homogeneous scenario*. According to this last one, the relaxation time is the same in any region of the sample and the stretched shape arises from the local disordered structure of the glass [62]. However, it is known both from simulations [3, 63, 64] and experiments both on colloids and structural glasses [55, 65–71] that the dynamics close to the glass transition is genuinely

heterogeneous.
As already pointed out in Sec. 2.2, the concept of CRR and *dynamical heterogeneities* is central for the understanding of the process of dynamic arrest. This spatio-temporal fluctuations can be quantified by four-point correlation functions [3]. In the case of density fluctuations the G_4 function is defined [3]:

$$\begin{aligned} G_4(\mathbf{r},t) =& \langle \rho^*(0,0)\rho(0,t)\rho(\mathbf{r},0)^*\rho(\mathbf{r},t)\rangle - \\ & \langle \rho(0,0)^*\rho(0,t)\rangle\langle \rho(\mathbf{r},0)^*\rho(\mathbf{r},t)\rangle \,. \end{aligned} \tag{2.57}$$

So G_4 specifically accounts for spatial correlations in time fluctuations of the microscopic density. The physical origin of this heterogeneous dynamics can be traced back to the disordered structure of glass-forming liquids: molecules relax with different rates depending on their environment. Since above T_g the internal structure of the supercooled liquid is still able to re-arrange, these heterogeneous regions will have a finite lifetime. In analogy with critical phenomena, dynamical hetereogenities can be expected to be correlated over a certain length scale ξ. ξ thus quantifies the extension of this correlated fluctuations in the liquid [3] and, according to the already discussed concept of an ideal glass transition, ξ is expected to grow on lowering T and on approaching T_K [3]. It is still debated whether and how this dynamical correlation length is related to the static point-to-set one which defines the boundaries of the mosaic state within the RFOT [3].
It is extremely difficult to experimentally access dynamical hetereogenities, especially in structural glasses and looking at density fluctuations. In fact the dynamics needs to be investigated over small volumes, comparable to the size of the spatial fluctuations and at the atomic level: average over many CRRs will greatly reduce the visibility of dynamical hetereogenities (see for instance the discussion in [72]). Since for molecular liquids the size of dynamical heterogeneities is expected to be around $\simeq$ 1nm [66, 71], a comparable scattering volume should be studied. For microscopic probes able to access bulk samples such as X-rays achieving these small scattering volumes is still out of reach.

2.4.2.1 TV^γ scaling

Another important property of the α-relaxation worthwhile discussing is its thermodynamic scaling. In fact, it has been observed in several glass-formers that the evolution of τ_α under different combinations of T,P and V can be effectively described by a single variable TV^γ (or equivalently $\frac{\rho^\gamma}{T}$), where γ is a system-dependent parameter [58, 73–75] related to the apparent repulsive part of the inter-molecular potential [58, 75, 76].
Another intriguing aspect concerning the thermodynamic scaling of the α-relaxation is that its dispersion (or stretching parameter β_{KWW}) is constant under combined variations of pressure and temperature that keep τ_α constant [58, 73, 75]: this is the so-called isochronal invariance. In other words the dispersion of the structural relaxation is invariant along lines in the phase-diagram corresponding to fixed τ_α [58, 73, 75]. It is relevant to point out that

both of the aforementioned observations nicely hold for liquids which do not present directional bonding, whereas in systems with H-bonds and covalent bonds they tend to fail [73, 75]. Both the TV^{γ} scaling and the isochronal superposition are rationalised within the isomorph theory. The main idea behind this theory is that two states are isomorphic if, after a proper scaling of the atomic coordinates, they display an identical PEL [75]
Further details about isomorphs, isochronal superposition and density scaling are beyond the purpose of this work and the interested reader is referred once again to the literature [73, 75].

2.4.2.2 The connection between the α-relaxation and the fast-processes

In this paragraph we briefly review another intriguing feature of the α-relaxation, that is, its connection with the fast processes occurring at the ps timescale.
This connection was initially proposed by Hall and Wolynes (HW) within the framework of the RFOT [77]. In aperiodic crystal structures (i.e. in glasses) the viscous flow occurs through thermally activated processes over free energy barriers $\Delta E \propto \frac{k_b T d^2}{\langle r^2 \rangle}$ [77]. $\langle r^2 \rangle$ is the amplitude of the rattling motion occurring during the fast processes and d is the critical displacement required to overcome the barrier. τ_α and $\langle r^2 \rangle$ are then related by the following rate equation [77]:

$$\tau_\alpha \propto exp\left[\frac{d^2}{\langle r^2(t) \rangle}\right] . \tag{2.58}$$

Experimental evidences of such connection between τ_α and $\langle r(t)^2 \rangle$ were found for the first time by Buchenau and Zorn [78].
Over the years, this correlation has been widely investigated and quantitatively described by more refined analytical models [40, 79, 80]. Furthermore the scaling between τ_α and $\langle r^2 \rangle$ has been verified both in real and simulated systems and for timescales ranging from $\simeq$ 1ps up to 100s [79, 80].
The physical origin of such scaling has been widely debated. First of all it is important to observe that $\langle r^2 \rangle$ is connected with the local molecular free volume [79]. So the scaling between the rattling amplitude at the ps timescale and the much slower α-process can be understood in terms of free-volume models [79]. At the same time $\langle r^2 \rangle$ can be regarded as a measurement of the local stiffness as it is related to the high frequency shear modulus [81]. So this scaling can be also rationalised in terms of the emergent elasticity characterizing the glass-transition (see Sec. 2.2.1.1) [80, 81]. Finally, as pointed out in [80], a connection with the cooperative motions envisaged by entropic-based models can also be found.

2.4.2.3 The glass-transition and the Lindemann criterion

Another important feature emerging from the study of the scaling between τ_α and $\langle r^2 \rangle$ is that the glass is stable until $\langle r^2 \rangle$ reaches a critical amplitude (d in Eq. 2.58) [79]. This observation is naturally reminiscent of the well-known

Lindemann melting criterion for crystals [82–85] which states that a solid starts to melt when the vibrational amplitude (MSA) of the atoms, defined as [83–85]:

$$MSA = \sqrt{\langle |\mathbf{r} - \langle \mathbf{r} \rangle)|^2 \rangle} \tag{2.59}$$

reaches $\simeq 10\%$ of the inter-molecular distance. The mean-squared displacement $\langle r^2(t) \rangle$, under the hypothesis that $\mathbf{r}(t)$ and $\mathbf{r}(0)$ are uncorrelated, is proportional to the MSA [84]:

$$\sqrt{\langle r^2(t) \rangle} = \sqrt{2} MSA \,. \tag{2.60}$$

The extension of the Lindemann criterion to glasses is central in many models of the glass-transition [33, 40, 79, 81, 86, 87] as it universally defines, analogously to the case of crystalline solids, the "stability" of the amorphous phase.

2.4.2.4 The α-relaxation in the PEL

To conclude this short overview of the properties of the structural relaxation, its description in terms of PEL should be discussed. The α-process, being the main process thorough which a liquid relaxes its internal structure, has been naturally associated to transition between metabasins [2, 17, 18], that is, to motions between the deepest minima of the PEL. This would be consistent also with the high energy barriers involved in the structural process. For example, in the case of OTP the effective activation energy extrapolated from its Angell plot (see Fig. 2.1) passes from $\simeq 20$ kcal/mol at T_m to $\simeq 100$ kcal/mol at T_g [88]. These numbers are much higher than the characteristic bond energy of two OTP molecules $\epsilon \simeq 1.24$ kcal/mol [89] (OTP is a Van der Walls glass-former) and indicate that the structural relaxation indeed requires the rearrangement of several particles.
It has also been argued, on the basis of molecular dynamics simulations of Lennard-Jones systems [90], that the α-relaxation should involve several, subsequent transitions between metabasins.

2.5 The Johari-Goldstein relaxation

Glass-forming molecules are usually characterized by secondary or β relaxation processes, active even below the glass-transition temperature. All these processes were used to be considered of intra-molecular nature and therefore not related at all to the glass-transition which is instead governed by inter-molecular interactions [4]. Motions of pendant groups in polymers can be regarded as an example of this kind of secondary relaxations.
In 1970 Johari and Goldstein discovered the existence of slow, secondary relaxation processes also in rigid and small molecules [5] and therefore not caused by internal degrees of freedom. These first studies [5, 91, 92, 94, 95] performed using DS provided some intriguing insights on these intermolecular secondary processes. For instance it was noticed that [5, 91, 92, 94, 95] i) they occur also in supercooled liquids, that is above the glass-transition temperature; ii) their

dielectric relaxation strength $\Delta\epsilon$ depends on the thermal history of the system and iii) they are present also in the relaxation spectra of polymers with features similar to those of rigid molecules.
These secondary relaxation processes have been named Johari-Goldstein (β_{JG}) relaxations in order to distinguish them from the others due to the internal degrees of freedom of the glass-forming molecules.
Since these pioneering studies the β_{JG} relaxation has drawn increasing attention as a genuine and fundamental feature of the glass-transition [4, 58]. In fact, it is nowadays accepted that the β_{JG} relaxation occurs through the motion of the molecular unit as a whole [96] and that it is strictly linked to and acts as a precursor of the slower and more cooperative α-relaxation [4, 58, 97].
The β_{JG} process is ubiquitous as it has been observed in a large number of materials, ranging from molecular liquids, ionic liquids, polymers, metallic glasses and orientantional glasses as well [4, 98]. Even though nearly universal, there are some systems where the presence of β_{JG}-relaxation is still debated [4]. For example, in strong network glasses the β_{JG}, if present, is expected to have a timescale very close to that of the α-process and therefore not easily resolvable in susceptibility spectra [4]. Furthermore, measurements on network glasses are also challenging because of their high T_g. Despite the scarce information available, some observations of secondary processes with characteristics compatible with those of the β_{JG}-relaxation have been reported also for these systems [4, 99, 100].
The β_{JG} is also claimed to play a crucial role in a number of properties of relevance for material science. For example, metallic glasses with a pronounced β_{JG} relaxation show a high tensile plasticity [6, 7], and amorphous pharmaceuticals easily crystallize, which is regarded as being a problem as it implies a reduction of the solubility of the medicine [8].

Therefore, disclosing the microscopic mechanism governing the β_{JG} process is crucial for both a complete understanding of the glass transition and of importance for technologies and practical applications. Consequently the β_{JG}-relaxation has been at the center of a large number of phenomenological, theoretical and experimental studies [11–13, 35, 48–50, 58, 96–135].

2.5.1 Some properties of the β_{JG}-relaxation

The β_{JG} relaxation typically decouples from the structural one when the glass-forming liquid is cooled down below a temperature where the relaxation time is in the μs-ms timescale [1, 2, 4, 5]. The corresponding temperature is usually close to the mode-coupling cross-over temperaure $T_c \simeq 1.2T_g$, where the characteristic features of the glass-transition start to show up [2, 3]. The β_{JG} process is faster than the structural one, remains active also in the glassy state and is typically characterized by a milder Arrhenius temperature dependence with respect to that of the structural relaxation [4]:

$$\tau_{\beta_{JG}} = \tau_0 \cdot \exp\left[\frac{E_{\beta_{JG}}}{k_B T}\right]. \tag{2.61}$$

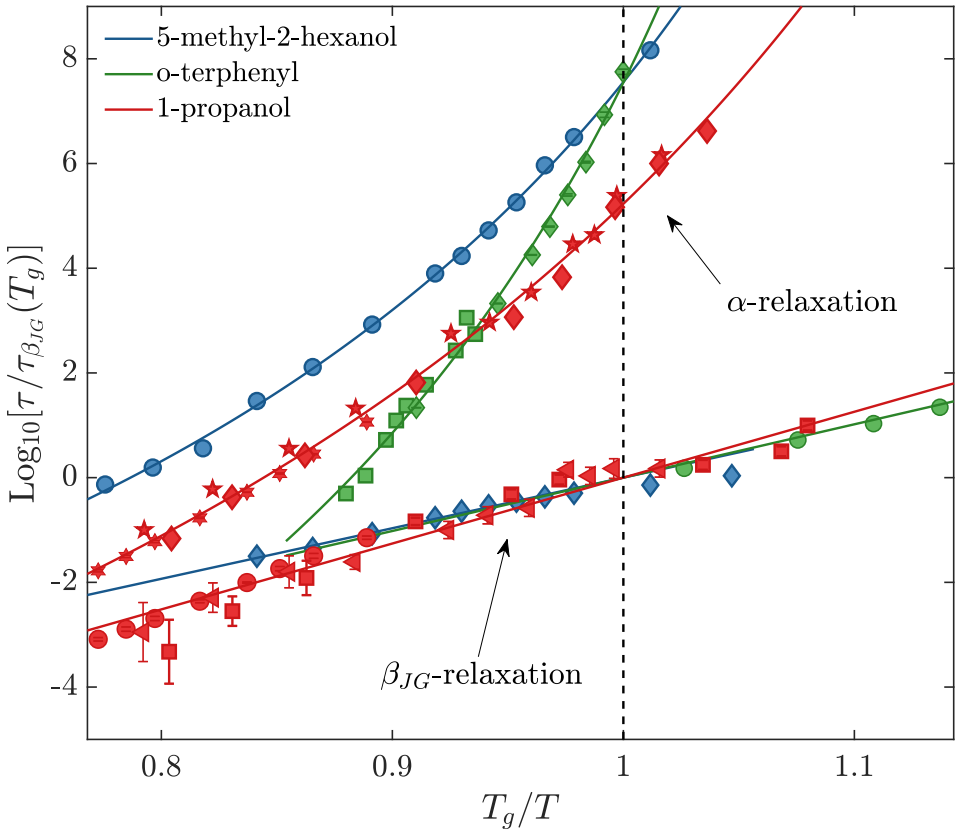

Figure 2.7: $\frac{T_g}{T}$-dependence of the β_{JG} and α-relaxation time as measured by DS and/or PCS for 5-methyl-2-hexanol [134] (blue symbols), 1-propanol (red circles [135], triangles and squares [49]) and o-terphenyl (green circles [5], squares [102] and diamonds [135]). To facilitate the comparison the relaxation times have been normalized with respect to the value of the corresponding $\tau_{\beta_{JG}}$ at T_g.

Typical values for its activation energy $E_{\beta_{JG}}$ are in $\simeq$ 0.2 eV-1 eV range both for organic and metallic glass-formers [98, 104, 111]. Fig. 2.7 shows, as an example, the relaxation time of the β_{JG} process $\tau_{\beta_{JG}}$ along with the slower α-relaxation for three systems : the two mono-alcohols 5-methyl-2-hexanol and 1-propanol and the van der Walls liquid o-terphenyl. The $\tau_{\beta_{JG}}$'s in Fig. 2.7, measured by means of DS and PCS, have been normalized to their values at T_g and the inverse temperature rescaled with respect to T_g to favor the comparison between the three systems. It is easy to observe that their activation energies are very similar.

A secondary relaxation can either appear, in susceptibility spectra, as a distinct peak or as an excess wing departing from the high-frequency side of the structural relaxation, as sketched in Fig. 2.8. Excess wings are typically observed in strong glass-formers, whereas in fragile liquids the β_{JG}-relaxation is usually more separated from the structural process [4]. Some glass-formers even display both an excess wing and a distinct peak and it is in that case necessary to discriminate whether any or which can be recognised as a genuine

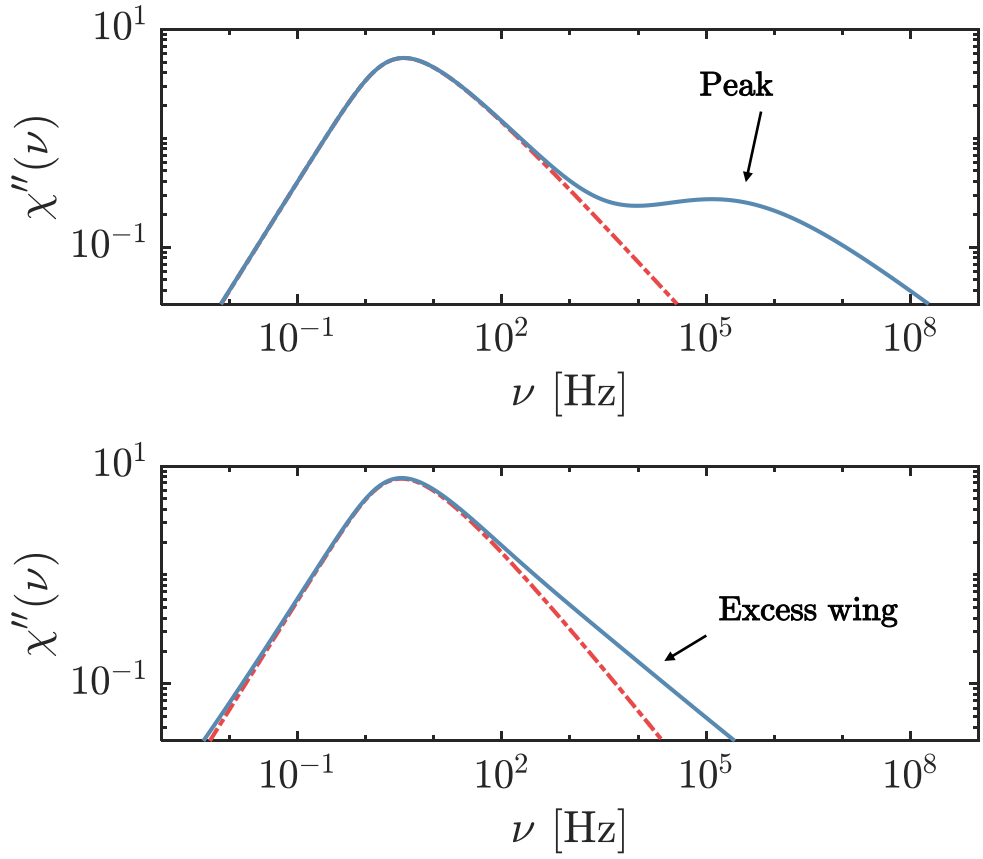

Figure 2.8: Typical appearance of the β_{JG}-relaxation in susceptibility spectra. It can either arise as a well separated peak (upper pannel) or as an excess wing on top of the structural relaxation (lower pannel).

β_{JG}-process [96]. As it will be elucidated in Sec. 2.5.2 there are several ways to do so.
The spectrum of the β_{JG} relaxation, when it is well separated from the structural process, is typically symmetric (in a log-log plot) and characterized by a broader dispersion with respect to that of the α relaxation [4, 104]. Fig. 2.9-(a) reports the dielectric loss spectra of 5-methyl-2-hexanol while 2.9-(b) shows only the β_{JG}-relaxation obtained after the subtraction of the other contributions coming from the α and the Debye processes. This last relaxation is a characteristic feature of mono-hydroxyl alcohols and reflects the formation of transient supramolecular structures by H-bonding (more details in Sec.4.1.3).
The shape of the β_{JG}-relaxation is usually well described by the Cole-Cole expression [47] in susceptibility spectra (see the solid line in Fig. 2.9):

$$\chi_{\beta_{JG}}(\omega) \propto \frac{1}{1+(-i\omega\tau)^a} \tag{2.62}$$

where a is a shape parameter. Other models can also be effectively used [104]. Independently of the expression chosen to fit the susceptibility of the

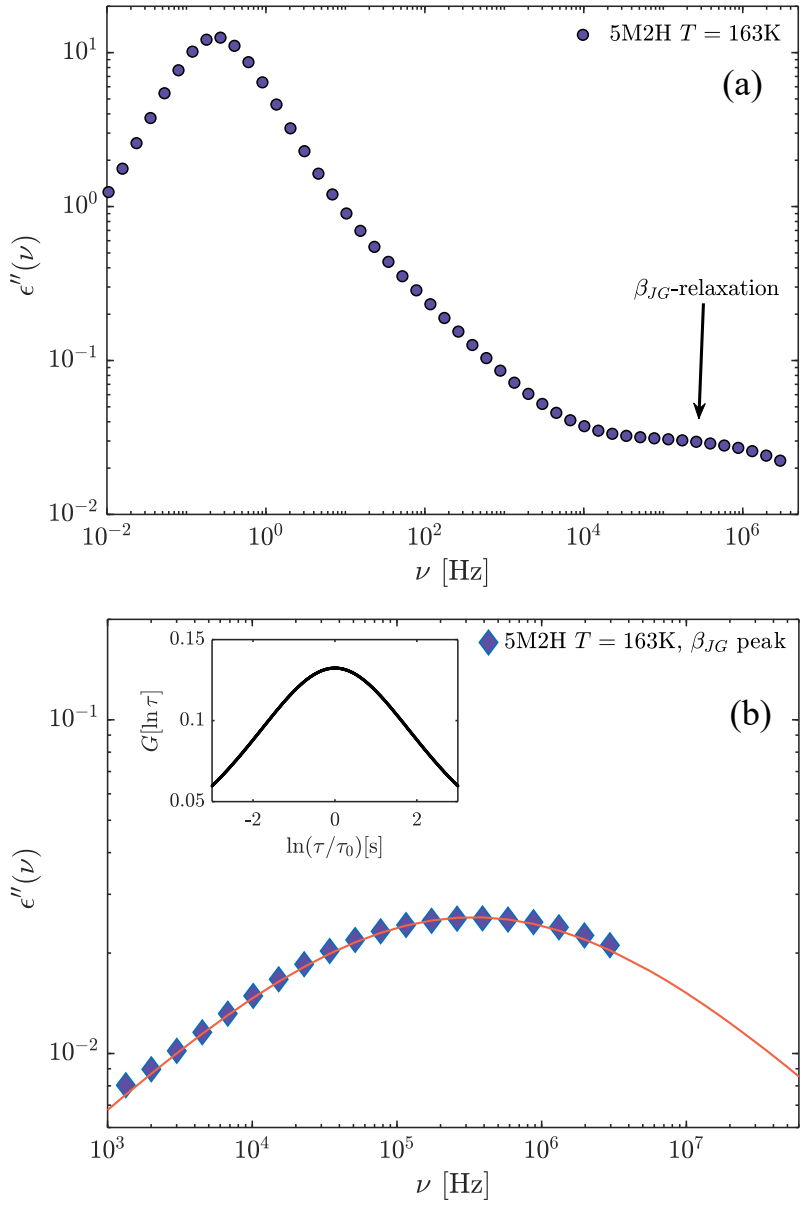

Figure 2.9: (a): Dielectric loss-spectra of 5M2H at 163 K (blue diamonds). (b): The β_{JG}-peak, obtained after subtraction of the contributions of the α and Debye relaxations. The curve obtained from the fit of the Cole-Cole model to the experimental data is also reported (red solid line). The corresponding distribution of the logarithm of relaxation times (G(lnτ)) is plotted in the inset. *Data taken from [134].*

β_{JG}-process the underlying distribution of relaxation times $G(\ln\tau)$, which can be obtained decomposing the β_{JG} relaxation in terms of exponential elementary processes (Eq. 2.56), is clearly very broad with tails extending over many decades (see the inset in Fig. 2.9). Such a large distribution suggests the

heterogeneous nature of the β_{JG} process which has been directly observed in dielectric hole burning experiments [106, 109], deuteron NMR measurements [105] and in simulations as well [123, 128, 131]. The dispersion of the β_{JG}-relaxation becomes even broader on lowering the temperature [4, 104].
Regarding the strength of the β_{JG}-relaxation, most of what we know comes from macroscopic techniques such as DS and DDLS which can provide information only about its relative strength with respect to the α-process. In this case it has been shown that it typically decreases on decreasing T towards T_g, below which it becomes only weakly T-dependent [104].

2.5.2 The role of the β_{JG}-relaxation in the glass-transition

Another important characteristic of "genuine" β_{JG} relaxations is their strong relationship with the structural process. This connection has been extensively investigated in many experimental works [4, 58, 96, 97] and in the following we will review some of the most important results.
A first hint of such connection was found in the correlation, for a large number of systems, between dispersion of the α-process, described by the Kohlraush exponent β_{KWW}, and the characteristic time of the β_{JG}-relaxation evaluated at T_g [97]. In detail, the broader is the dispersion of the α-process, the larger is the separation between the time-scales of the α and the β_{JG}-relaxation [97].
Other proofs can be found in the properties of its activation energy $E_{\beta_{JG}}$. It has indeed been observed that the following empirical relation [98, 104, 111] between T_g and $E_{\beta_{JG}}$

$$E_{\beta_{JG}} \simeq 24RT_g \tag{2.63}$$

holds for several glass-forming materials including metallic glasses. Here R is the gas-constant. Even though Eq. 2.63 is an approximation and some systems deviate from it, the correspondence is still striking and suggests a strong connection of the β_{JG} relaxation to the glass-transition [111].
Another intriguing observation is that the β_{JG} changes its activation energy on crossing T_g: above T_g, $E_{\beta_{JG}}$ is larger than below it [110]. An example of this behavior can be observed for 1-propanol and 5M2H in Fig. 2.7, since for these two glass-formers $\tau_{\beta_{JG}}$ is reported also for $T > T_g$.
In other words, the β_{JG}-relaxation is sensitive to the glass-transition and to the corresponding change in the temperature dependence of the density of the sample [4, 96]. Above T_g the temperature dependence can be non-Arrhenius [96] because of the larger coupling between the α and β_{JG} process. One more fundamental property of the β_{JG}-relaxation is that it responds to the application of pressure. For example, increasing P might enhance the separation between the α and β_{JG}-process if accompanied by a broadening of the dispersion of the α-process [110]. Application of high pressure can even transform an excess-wing into a well-separated peak in relaxation spectra, provided that the system posses a genuine β_{JG}-relaxation [118]. This actually reflects the inter-molecular nature of the β_{JG} relaxation [4, 96].
Furthermore, it has been observed in many glass-formers that the separation

between the time-scales of the α and the β_{JG}-relaxation is approximately invariant to large changes of P and T that leave τ_α and β_{KWW} constant (isochronal condition). This co-invariance of τ_α, $\tau_{\beta_{JG}}$ and β_{KWW} holds even when accompanied by large changes in the thermodynamic properties of the system, such as entropy and volume [4, 58].
As initially enlightened by the first works of Johari and Goldstein [5, 94], the β_{JG}-relaxation is influenced by the thermal history of the system. Moreover when aging takes place the $\tau_{\beta_{JG}}$ becomes slower mimicking again the behavior of the structural process which slows down while approaching a more stable configuration in the PEL [4, 96].
All the aforementioned results can be rationalised and explained within the *Coupling model* proposed by K. L. Ngai [4, 97] and the identification of $\tau_{\beta_{JG}}$ with the primitive relaxation time τ_0 of the theory. This is discussed in more details in Sec. 2.5.5.2.
In addition to the evidences presented above, mainly obtained by means of macroscopic techniques such as DS, there are also microscopic proofs of the link between the α and the β_{JG}-process. In fact, spin-lattice relaxation weighted stimulated-echo spectroscopy has shown that the inhibition of some sub-ensembles of the molecules participating to the β_{JG}-relaxation modifies the α-relaxation as well [115].

2.5.3 Microscopic dynamics within the β_{JG}-relaxation

As it emerges from the last paragraph, most of what is known about the β_{JG} relaxation comes from DS and nuclear magnetic resonance NMR studies. For this reason the re-orientational dynamics occurring within the β_{JG}-relaxation has been characterized in great detail. Large-angle molecular re-arrangements are expected to be dominant at high temperatures [104], and to become more and more restricted on approaching T_g from above. 1D and 2D NMR studies on small, organic molecules and polymers [107] show indeed that below T_g the β_{JG} relaxation is characterized by small-angle ($< 10°$), hindered reorientations. Accordingly, reorientational diffusion is restricted across T_g [107].
On the contrary we have less information on the microscopic center of mass (CM) motion, highly required to e.g. extract the typical length-scale and degree of cooperativity of the β_{JG} process. It is indeed extremely difficult to probe this relatively slow process at the microscopic scale both employing numerical simulations and experimentally.
For what concerns experiments, only few studies have been conducted up to now with the aim of addressing the CM motion involved in the β_{JG} relaxation at the Ångström scale. Neutron scattering experiments performed on the polymer polybutadiene (PB) revealed the presence of the β_{JG} relaxation only at the intra-molecular scale [101, 103] and a model with a strong wave number (q) dependence for the β_{JG} relaxation strength was introduced. More recent nuclear γ-resonance time-domain interferometry (TDI) experiments on PB [13] and on the molecular glass-former o-terphenyl (OTP) [11, 12] corroborate

the presence of the β_{JG} relaxation at the intra-molecular scale. In the case of OTP it is also been observed that the $\tau_{\beta_{JG}}$ is characterized by an anomalous, super-quadratic q-dependence, indicative of a restricted, sub-diffusive dynamics [11, 12].
Incoherent elastic and inelastic neutron scattering experiments on propylene carbonate [132], analysed applying an heterogeneous dynamics model introduced in [124] (more details in Sec. 2.5.5.5), provide a characteristic length-scale for the β_{JG}-relaxation of about 0.5 Å. The β_{JG}-process should therefore be associated to metabasin transitions in a PEL description of the supercooled liquid dynamics [132]. This conclusion should be naturally generalized to more glass-formers, possibly recurring to experimental schemes based on fewer, or at least different, model hypotheses. It is intriguing to notice that this length-scale is consistent with the molecular excursions which can be estimated i) assuming the local validity of the Stokes-Einstein relation and ii) considering the typical angular exploration within the β_{JG}-relaxation as provided by NMR [107].
On the numerical simulations side, studies performed on a specially designed model, consisting of mixtures of asymmetric dumbbell molecules with short bond lengths, suggest that, well below T_g, the β_{JG} relaxation occurs via large reorientations of otherwise immobile molecules [129]. In the simpler case of metallic glasses, computer simulations with atomistic potentials have became able to sample long-enough atomic trajectories to observe the β_{JG}-relaxation [128, 131]. These investigations indicate cooperative rearranging regions with string-like shape to be the origin of the β_{JG}-process [128, 131]. The distinctive length-scale of the process is thus here identified with the inter-molecular distance as atoms jump from one atomic side to another in a cooperative way [128, 131]. The relationship between the β_{JG} relaxation in metallic glasses and string-like rearranging regions is also suggested by the observation that alloys constituted by atoms with similar negative enthalpy of mixing show pronounced β_{JG}-relaxation peaks in mechanical loss spectra: in this case the formation of molecule-like structures is favored [122]. This is consistent with the picture of the β_{JG}-relaxation proposed in Ref. [58] as a distribution of processes with increasing participation of molecules and longer length scale with increasing time.
Another remarkable aspect evidenced by the atomistic simulations on MGs is that the string-like configurations and thus the β_{JG}-relaxation are favored by cage-breaking events [131]. Cage-breaking tendency is also suggested to discriminate between the appearance of the β_{JG}-process as an excess-wing or a well-separated peak in relaxation spectra. If cage-breaking events do not occur before the emergence of the structural relaxation, strings cannot develop.
It is important to recall that a connection between fast cage-dynamics and the β_{JG}-relaxation has also been previously suggested in the framework of the Coupling model and in view of several experimental evidences of the sensitivity of the fast processes to the "glass-transition" temperature for the β_{JG}-process (i.e the temperature at which $\tau_{\beta_{JG}} = 1000$ s) [125–127]. In the coupling mode picture of the glassy dynamics, the fast caged-dynamics is indeed terminated

by the onset of β_{JG}-relaxation [125–127].
This short overview clearly shows that a new picture is emerging from the study of the center-of-mass motion within the β_{JG}-relaxation. However some pieces of the puzzle are still missing, as we will discuss in the following.
The β_{JG}-relaxation, according to dynamical mechanical measurements [122] and MD simulations on MGs [128, 131], should consist of cooperative hops leading to string-like excitations. As already said, the distinctive scale of this process is thus the inter-molecular one. However, the intermediate scattering functions from the MD simulations do not show any clear sign of the β_{JG}-process at the peak of the $S(q)$ [128, 131]. Also neutron and X-ray scattering experiments suggest that the β_{JG}-relaxation occurs rather at the intra-molecular scale [11–13, 101, 103]. The first question which arises is then: *i) why doesn't the β_{JG}-process contribute to relax density fluctuations at q_{max}, especially in MGs where collective jump-dynamics is observed?* A further, related question concerns the characteristic length-scale of the process: *ii) is the β_{JG}-relaxation a local process or does it involve also large motions extending over the nearest-neighbors distance?* In fact the super-quadratic q-dependence [11, 12] of the β_{JG}-relaxation observed in organic glass-formers is the signature of a rather local, restricted process. This is clearly at odds with what suggested by the observations on MGs. Another important piece of information we lack is its absolute relaxation strength. In other words: *iii) how many molecules participate to the β_{JG}-relaxation?*. An additional crucial point to address concerns the cooperativity of the β_{JG}-relaxation. As discussed in Sec. 2.5.1 the β_{JG}-relaxation is heterogeneous, however it is still debated whether it also displays dynamical heterogeneities in a similar way as the structural relaxation. Clearly the results on MGs as well as the presence of dynamical correlations indicate that the β_{JG}-relaxation is highly cooperative [128]. However, molecular dynamics simulations on asymmetric dumbbell molecules suggest that dynamical correlations within the β_{JG}-relaxation are rather weak, or however, weaker than in the α-relaxation case [123]. Therefore, *iv) is the β_{JG}-relaxation cooperative? v) Does it display dynamic heterogeneities? vi) Are its dynamic correlations related to those of the α-process?*.

2.5.4 PEL description of the β_{JG}-process

A further aspect of the β_{JG}-relaxation to address is its description in the PEL formalism. The β_{JG}-relaxation, differently to the α-process, has been usually attributed to transitions between inherent-structures within the same meta-basin [17]. MD studies on Lennard-Jones systems also identify the β_{JG}-relaxation with series of transitions between inherent-structures leaving the system inside the same basin [90].
However, as questioned in [18, 119], the known activation energies for the β_{JG}-process are too high to be compatible with this interpretation ($E_{\beta_{JG}} \simeq 24RT_g$). As pointed out in [119], the activation energies of the β_{JG}-relaxation may be similar or slightly lower to those of the structural process and therefore also in

this case metabasin (MB) transitions should be involved. As a consequence dynamic heterogeneities might play a role in β_{JG}-relaxation as well [119]. This conclusion might be seen to be at odds with the the two processes displaying rather different T-dependence. However, as it has been argued in [119], the slope of the Arrhenius plots of fragile liquids might overestimate the actual activation energy of the α-relaxation (see the discussion in [119]).
It is important to notice that the activation energies calculated by the RFOT theory for the β_{JG}-process (stringy CRRs) result to be close to those obtained for the α one (compact CRRs) [35].
It is also recalled that the identification of the β_{JG} relaxation with metabasin transitions has been proposed in the light of the aforementioned incoherent scattering experiment on PC [132].

2.5.5 Models for the β_{JG}-relaxation

In this paragraph some of the models and interpretations regarding the β_{JG}-relaxation, some of them already mentioned in the previous sections, are briefly reviewed.

2.5.5.1 Participation: islands of mobility vs. Williams-Watt picture

Since its discovery, two rather different pictures have been proposed for the β_{JG}-relaxation. In one of them the β_{JG}-process is assumed to be related to the motion, either translational or orientational, of groups of loosely packed molecules located in so-called *islands of mobility*, that is regions of lower density randomly and heterogeneously distributed in the glassy-matrix [5, 94, 95].
According to the other viewpoint the β_{JG}-process should instead consist of hindered orientations involving all the molecules of the supercooled liquid/glass [93]. The β_{JG}-relaxation would therefore be spatially uniform [93]. The structural relaxation would then occur through a larger and complete reorientation of the whole molecule.
A uniform participation to the β_{JG}-process is suggested by NMR [107] and dielectric hole-burning [106] measurements. In a recent paper by Johari it has been instead objected, invoking an entropic argument and reviewing the available literature, that the β_{JG}-relaxation, in the glassy state, should occur in randomly dispersed regions which are locally in equilibrium within the glass structure, thus supporting the *islands of mobility* picture [133]. It is important to underline that an indirect evidence of the presence of the *islands of mobility* within the glassy structure and of their connection with the β_{JG}-relaxation can be found in the work of Ichitsubo and collaborators [114, 117]. They investigated metallic glasses utilizing ultrasonic waves and observed that they could induce partial crystallization of the sample below T_g using ultrasonic vibrations in resonance with the atomic motions ($\simeq$ MHz) associated with the β_{JG}-relaxation [114, 117]. In fact the annealed samples presented amorphous regions separated by crystallized walls and they interpreted such results as an

evidence of the heterogeneity of the glassy structure. Moreover, they inferred from the crystallized patterns the presence of "weakly bounded regions" (WBR), characterized by a higher atomic mobility and more prone to crystallize, and "strongly bounded regions" (SBR), frozen instead on the timescale of the ultrasound excitation [114]. Since the induced crystallization is strongly related to the β_{JG}-relaxation, they concluded that this last one should occur within the WBR [114].
More details and a more complete discussion of the two different perspectives on the molecular participation to the β_{JG}-relaxation can be found in [108] and [133].

2.5.5.2 Coupling model

Another important model to discuss is the coupling model [4, 97] by Ngai, able to successfully account for the connection of the β_{JG}-relaxation to the α-process and also to provide criteria for identifying genuine β_{JG}-relaxations. The first ingredient of the CM is the existence of a T-independent time t_c, which is of the order of $1-2$ps [4, 97] for molecular systems. At times $t < t_c$ the molecule relaxes independently from the others via a simple exponential with a characteristic *primitive relaxation time* τ_0. At times longer than t_c many-body effects and inter-molecular interactions start to play an increasingly important role and the correlation function assumes the characteristic KWW shape. The primitive relaxation is therefore the precursor of the cooperative α-relaxation and, while being a local process, it involves all the atoms of the molecule [4, 97]. τ_0 and τ_α are related by the following relation in the CM [4, 97]:

$$\tau_\alpha = (t_c^{-n}\tau_0)^{(\frac{1}{1-n})} \tag{2.64}$$

where n is the complement to one of the stretching parameter $\beta_{KWW} = 1 - n$ and provides an indication of the inter-molecular coupling.
In the framework of the coupling model the β_{JG}-relaxation has the same characteristics, i.e. is a local process involving all the atoms of the molecule, and is approximately related to the primitive relaxation [4, 97] by:

$$\tau_{\beta_{JG}}(P,T) \approx \tau_0(P,T)\,. \tag{2.65}$$

Remarkably Eq. 2.65, with τ_0 calculated from Eq. 2.64 holds in a large number of glass-former with genuine β_{JG}-relaxations [4]. The condition prescribed by Eq. 2.65 has been indeed proposed to discriminate between secondary relaxations involved in the glass-transitions ("genuine" β_{JG}-process) and the ones due to intra-molecular degrees of freedom [96] and not related to the α-relaxation. Under the condition $\tau_\alpha \gg \tau_{\beta_{JG}} \gg t_c$, commonly verified in experiments, the following approximate equation can also be derived [4, 58, 97]

$$\log\left(\frac{\tau_\alpha}{\tau_{\beta_{JG}}}\right) \approx n \log\left(\frac{\tau_\alpha}{t_c}\right)\,. \tag{2.66}$$

It is clear that the experimental results presented in Sec. 2.5.2 are rationalised by Eq. 2.66. For example, with application of high pressures, if an enhancement of the inter-molecular coupling (i.e. n increases) takes place, then the separation between τ_α and $\tau_{\beta_{JG}}$ increases, as indeed observed in [110, 118]. On the basis of the coupling model and the observed co-invariance between τ_α and $\tau_{\beta_{JG}}$ under isochronal conditions, it has also been argued that the TV^γ-scaling discussed in Sec. 2.4.2.1 should originate from the more local β_{JG}-relaxation, which is the initiator of the many-body dynamics, and then inherited by the α-relaxation [58, 130]. A further aspect of the coupling model to be discussed is the molecular participation to the β_{JG}-process. Within this model all molecules are expected to be able to relax via the primitive/β_{JG}-relaxation but not all can succeed at the same time as a consequence of the many-body effects governing the inter-molecular interactions [96]. So, not all molecules simultaneously take part in the β_{JG}-process [96]. However, all molecules will eventually end up relaxing via the β_{JG}-process. Therefore, if the dynamic evolution is followed over long enough time, essentially all molecules will contribute to the process [96]. This interpretation partially reconciles the two different visions discussed in Sec. 2.5.5.1, at least above T_g.

2.5.5.3 Local orientational fluctuations

Another description for the β_{JG}-process is the one proposed by Tanaka within the two-order-parameters model (TOP) of the glass-transition [112, 113] . The main idea underlying the TOP is that any liquid is characterized by two competing tendencies: density ordering which advocates for crystallization and bond ordering which instead favours local symmetries usually not compatible with the crystallographic ones [113]. The corresponding order-parameters are respectively the density and the bond order-parameter [113]. In the TOP model the onset of cooperative dynamics occurs around a temperature T_A, which is close to T_m and is accompanied by the presence of "metastable islands" [113] with a lifetime $\approx \tau_\alpha$. In the densely packed island, molecular re-orientations are hindered and restricted [112, 113]. While inside such metastable islands a molecule cannot translationally escape or fully reorient, only small amplitude angular fluctuations or re-orientations can take place [112, 113]. The β_{JG}-relaxation consists then of multi-step, non-cooperative small rotational jumps over an energy barrier $E_{\beta_{JG}}$ whose corresponding attempt frequency is given by $\tau_{\beta_{JG}}$ [112, 113]. A molecule finally succeeds in escaping from its cage and fully reorient as the metastable island re-organize at about τ_α [112, 113]. The β_{JG}-relaxation is expected to decouple from the structural one as cooperative dynamics onsets, consistently with the formation of metastable islands [112, 113]. Concerning participation, also in this model all molecules are envisaged to contribute to the β_{JG}-process with an amplitude depending on the tightness or looseness of the cage [112, 113]. The distribution of metastable islands, which can be interpreted as the presence of dynamic heterogeneities, should cause heterogeneity in the stiffness of the cages and in the β_{JG}-relaxation as well [113]. It is also argued that the relation between the size of the metastable

islands and the size of the local-cage mainly controls the decoupling between the α and β_{JG}-relaxation (i.e. appereance of the β_{JG}-process as either an excess wing or a distinct peak in susceptibility spectra) [112].

2.5.5.4 RFOT

A universal origin for the β_{JG}-process is also proposed in the framework of the RFOT [35]. As argued in [35], in the RFOT secondary relaxations should be governed by string or percolation-like ramified clusters of particles while the α-relaxation should involve more compact, nearly spherical clusters of particles. Such string-like cooperative re-configuring regions are stabilized by disorder and are embodied in the fluctuations of the local configurational entropy [35]. Here secondary relaxations, differing from the structural one because of the underlying geometry of CRRs, appear as a tail on the low energy side of the calculated distributions of activation energies. At the kinetic glass-transition temperature the shape of the CRR is mainly compact and ramified clusters are scarce. On the contrary, at higher temperatures the contribution of stringy re-configuring regions becomes larger, that is the relative strength of the secondary process increases [35]. Fragile glasses with larger fluctuations in the configurational entropy [33] are also expected to present a more intense β_{JG}-relaxation [35]. The energy barriers from the two processes eventually merge at T_c above which string configurations become dominant. The theory predicts string-like CRRs to be dominant also in the ageing regime, that is below the kinetic glass-transition temperature T_g. Most of the these features clearly resemble the ones of the β_{JG}-relaxation that have been presented in Sec. 2.5.1.
It is also clear that here the β_{JG} process is visualized as being cooperative. This is at odds with the TOP model while more consistent with the idea of a process with a length-scale and participation increasing in time as proposed by the coupling model [58]. Furthermore, it is also important to recall that string-like re-configuring regions have been observed also in MD dynamics simulations in MG glasses [128, 131], as discussed in Sec. 2.5.3.

2.5.5.5 Loosely caged-tightly caged exchange

The last model which is here presented is the one proposed by Cicerone *et al.* in [124]. Their incoherent scattering measurements on several molecular glass-formers are compatible with the existence of two dynamical states at the ps timescale, corresponding to molecules either tightly confined or able to perform large excursion [124]. Thus fast processes present two distinct components: one due to more localized, tightly caged (TC) molecules, and the other due to molecules that instead are more loosely caged (LC) [124]. Cicerone *et al.* suggested a structural origin for these two dynamic states such as frustrated packing [124] and they demonstrate that these two populations exchange over time. A simple picture for relaxations in supercooled liquids based on the existence of TC and LC molecules is then provided. Namely, the

α-relaxation occurs within the TC state, whereas fast-processes take place in the LC one. The β_{JG}-relaxation is instead the mechanism allowing the exchange of population between TC-LC dynamic states. The β_{JG}-process, i.e the TC-LC exchange, is expected to facilitate the α one [124], as a LC domain might locally increase mobility near TC molecules. The characteristic timescales of the two processes are proposed to be related by a relation of the type

$$\log(\tau_\alpha) \approx \log(\tau_{\beta_{JG}})/\gamma \tag{2.67}$$

with $\gamma < 1$ because of the spatial correlations in the structural relaxation [124]. The β_{JG} process is also assumed to be only weakly cooperative and describable as a simple activated process [124]. The merging of the α and β_{JG} relaxations at T_c is explained by the exchange time becoming comparable or shorter than the relaxation time of the TC domains. Several simple equations to calculate both relaxation times and diffusion constants from the TC and LC properties obtained from their QENS measurements are eventually proposed [124]. In particular the equation describing the relaxation time of the β_{JG}-equation is given by:

$$\tau_{\beta_{JG}} = \tau_0 \exp\left[\frac{\delta}{\sigma_{TC} k_B T}\right] \tag{2.68}$$

where σ_{TC} is the characteristic length-scale of the fast-dynamics ($\simeq 1ps$) in TC states as extracted by QENS while τ_0 and δ are parameters extracted from fitting.
Within this model the length-scale of the β_{JG}-relaxation coincides with that of the motions occurring in LC-domains which is of the order of 20% of the hydrodynamic radius of the molecule [132].

2.5.5.6 Models at comparison

In this final paragraph we briefly compare the presented models, focusing on the different aspects/proprieties of the β_{JG}-relaxation that they address and that can be rationalised.

Decoupling from the α-relaxation. Each one of the models presented above are able to explain the decoupling of the β_{JG}-relaxation from the α one close to the mode-coupling temperature T_c. However, they propose rather different microscopic mechanisms.
In the framework of the coupling model, T_c is the temperature at which many-body effects become relevant for the liquid dynamics and consequently the timescales of the α-process and that of the primitive (β_{JG}) relaxation separate [4].
In the TOP model, instead, the β_{JG}-relaxation appears only at T_c as a consequence of the emergence of the metastable islands [112].
Within the RFOT, T_c is the temperature where the energy barriers of the string CRRs merge with those of the more compact reconfiguring regions. Indeed above T_c strings/percolation like clusters become dominant as the dynamics is

no longer activated [35].
Concerning the TC-LC exchange model [124], the β_{JG} relaxation separates from the α one as a consequence of the depletion of LC domains below T_c.

The relation between the α and the β_{JG}-relaxation. As discussed in Sec. 2.5.2, the β_{JG}-relaxation is strongly connected to the α-one.
In the coupling model this relationship is explained by the identification of the β_{JG}-process with the primitive relaxation of the model. Eq. 2.66 is indeed able to explain the experimental observations reported in Sec. 2.5.2
Also the TC-LC exchange model envisages a strong connection between the α and β_{JG}-process: TC-LC exchange events are indeed required in order to facilitate the α-process. It is noteworthy that the equation linking the α- and β_{JG}-relaxation timescale (Eq.2.67) is a power law function similar to that predicted by the coupling model (Eq. 2.66).
According to the TOP model instead the β_{JG}-relaxation is not a precursor of the structural one. The coupling between the two processes is rather controlled by the properties of the metastable islands within which the β_{JG}-relaxation occurs.
For what concerns the RFOT, no particular connection is envisaged for the α and β_{JG}-relaxations as the two involve excitations with rather different geometry [35].

Cooperativity. The degree of cooperativity of the β_{JG} relaxation is still debated. In fact, all the presented models, while agreeing on the fact that the β_{JG}-relaxation is highly heterogeneous, propose rather different pictures for what concerns its cooperativity. However, a comparison among these models is not straightforward as the concept of cooperativity itself is declined in different ways within the considered models. The TOP model describes the β_{JG}-relaxation as a non-cooperative, local process.
Also according to the coupling model the β_{JG}-relaxation is essentially local, even though [4, 58, 96, 97] it is foreseen to become more cooperative and involve more molecules with increasing time, until it eventually evolves into the α relaxation. So in this case collective motions are a natural consequence of the evolution of the microscopic dynamics toward the complete relaxation of the internal structure of the liquid.
In the TC-LC exchange model [124] the cooperativity of the β_{JG}-relaxation is not described in details apart from the fact that the process is assumed to be weakly cooperative and approximated as a simple activated process. Within the RFOT [35] the β_{JG}-relaxation is instead intrinsically cooperative as it involves the collective rearrangement of particles through the reconfiguration of string-like regions.

Activation energy and PEL description The activation energy of the β_{JG}-relaxation, as anticipated in Sec. 2.5.2, is roughly equal to $24RT_g$ (Eq.

2.63). It has also been discussed in Sec. 2.5.4 that this rather high value for $E_{\beta_{JG}}$ might be an indication that, in the PEL formalism, the β_{JG}-relaxation should be identified with a transition between metabasins (MB) [119]. First of all we notice the Eq. 2.63 is readily explained by the coupling model [111], which is actually able to account also for the those systems which deviate from the empirical rule.
Concerning the PEL description, it has already been discussed that the TL-LC exchange model links the β_{JG}-relaxation to transitions between metabasins [132].
A hint of this connection, even if not directly discussed, can be also found in the RFOT [35]. Indeed the activation energies calculated by the model for the β_{JG}-process (stringy CRRs), though smaller, are of the same of order of magnitude of those obtained for the α-relaxation (compact CRRs) [35]. An activation energy similar to that of the α-process, as argued in [119], is indeed a strong hint that the two processes should be able to explore similar features of the PEL and therefore the β_{JG} relaxation should be associated to metabasin transitions as well.
In the TOP model the PEL origin of the β_{JG}-relaxation is not addressed [112]. However, the description of the β_{JG}-relaxation as due to local, small-angle molecular re-orientations, is hardly compatible with the high energy barriers required for transitions between two MB.

Chapter 3

Nuclear resonant scattering and and nuclear γ-resonance time-domain interferometry: theoretical background

In this chapter the main aspects of the nuclear resonant scattering of synchrotron radiation (NRS) and of nuclear γ-resonance time-domain interferometry (TDI) are introduced. To this aim, the Mössbauer effect is initially reviewed as it is at the basis of both NRS and TDI. The fundamentals and the formalism of NRS are then briefly discussed along with the main properties of the Mössbauer nucleus ^{57}Fe. The last section is instead devoted to TDI. Here the working principles of this technique are described in detail along with the theoretical formalism required to model the time-evolution of a TDI beating pattern. Finally the possible experimental schemes for TDI, involving both single-line and multi-line absorbers are presented.

3.1 The Mössbauer effect

The Mössbauer effect (ME), discovered in 1958 by Rudolf Mössbauer [136], is the recoil-free emission or absorption of a γ-ray by a nucleus bound in a solid. In what follows the relevance of this phenomenon is briefly reviewed.
The absorption or the emission of a photon by a nucleus is generally accompanied by recoil to ensure both energy and momentum conservation. If E_0 is the energy of the excited nuclear state, then the energy of an emitted/absorbed photon is $E_\gamma = E_0 \mp E_R$, where E_R is the recoil energy. E_R is equal, in the case of a free nucleus, to [137]:

$$E_R = \frac{E_\gamma^2}{2Mc^2} \ , \tag{3.1}$$

where M is the mass of the nucleus and c is the speed of light in vacuum. As a consequence of the recoil, the probability distributions associated to the absorption and emission of a photon are shifted by $\Delta E = 2E_R$. So a γ-ray

emitted by the de-excitation of a nucleus can be *resonantly* absorbed by another nucleus only if the gap ΔE is smaller than the natural line-width Γ_0 of the nuclear excited state (see fig.3.1-(a)). Γ_0 is related to the lifetime of the excited

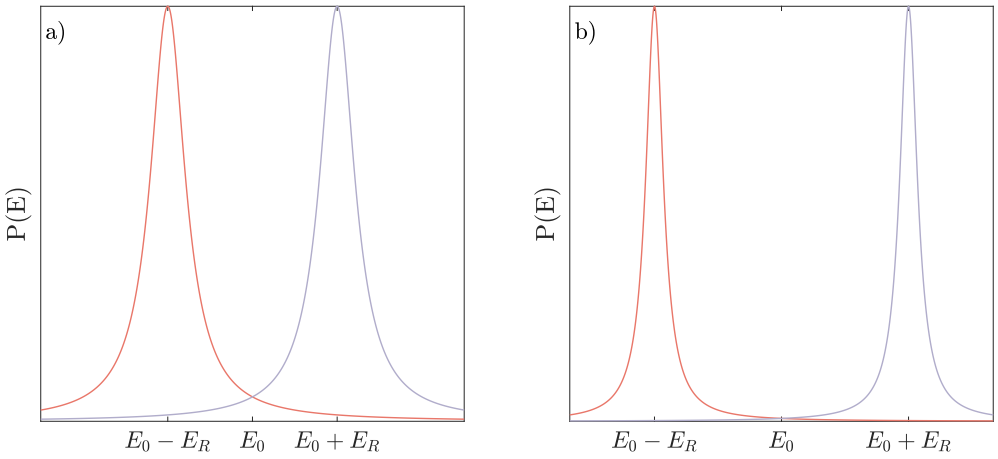

Figure 3.1: Sketches of emission (red solid line) and absorption probability (grey solid line) of a given transition E_0 as a function of the energy of the absorbed/emitted photon. If the shift of the two probabilities, due to the recoil energy E_R, is small enough that the two partially overlap, resonant absorption can take place (a), otherwise no-resonance is possible (b)

nuclear state via the Heisenberg's uncertainty principle

$$\tau_0 = \frac{\hbar}{\Gamma_0} \tag{3.2}$$

where $\hbar = 1.054571800(13) \times 10^{-34} J \cdot s$ is the reduced Planck constant and typical values for τ_0 range from 10 ns up to 1000 ns. So the bandwidth for these nuclear transitions is of the order of 10^{-7}eV-10^{-9}eV, while the excitation energies E_γ are typically of several keV, as it can be observed in Fig. 3.2. At such large E_γ, the role of the recoil energy becomes more and more critical. If we consider, for example, the case of ^{57}Fe whose first excited state lies at E_0=14.413 KeV, we have that, according to Eq. 3.1, $E_R \simeq 2 \times 10^{-3} eV$. This value is much larger than the linewidth of its transition $\Gamma_0 = 4.66$ neV and therefore it is impossible to observe resonant absorption for free nuclei. The situation is different if the nucleus is embedded into a solid [137]: in this case, since the binding energies involved are of the order of few eV, free recoil cannot occur and phonons must be created or annihilated. From the quantum-mechanics point of view there is a certain probability that a γ-quantum is absorbed or emitted without exciting phonons [137]. As a consequence there is a certain probability that the crystal recoils as a whole [137]. In this situation resonant absorption and emission can occur since $E_R \to 0$ and consequently $E_\gamma = E_0$. The probability of a recoil-less absorption/emission events is quantified by the Lamb-Mössbauer factor f_{LM}

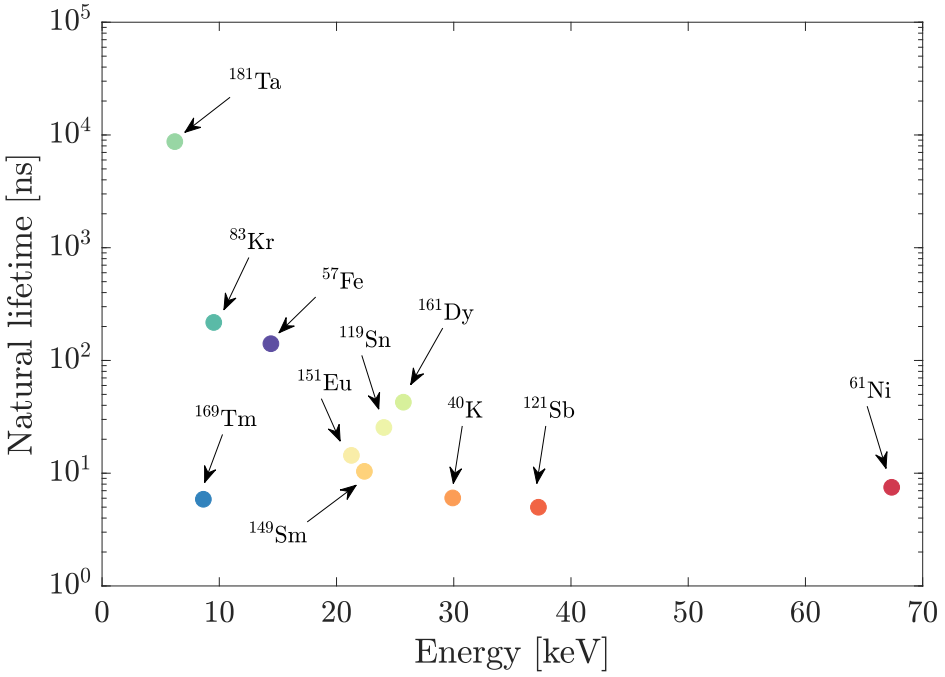

Figure 3.2: All Mössbauer isotopes investigated in nuclear resonant scattering experiments with synchrotron radiation. Each isotope is reported as a function of its resonance energy and lifetime. *Data taken from [10]*

which, in the case of a harmonic crystal can be expressed as [137]:

$$f_{LM} = e^{-\frac{\langle x_k^2 \rangle \cdot E_\gamma^2}{(\hbar c)^2}} \tag{3.3}$$

Here $\langle x_k^2 \rangle$ is the projection of the nuclear mean-square displacement along the direction $\hat{k}$ of the emitted/absorbed photon. f_{LM}, because of its dependence on the mean-squared displacement, is extremely sensitive to both the temperature and the chemical bonds characterizing the solid.

3.2 Nuclear Resonant Scattering

The ME is at the basis of the Mössbauer absorption spectroscopy: recoil-less resonant absorption and emission indeed allow probing the hyper-fine interactions at the nucleus and thus provide information about the local environment of the absorber. In this technique all the nuclei in the ensemble are seen as independent and no information about their collective behavior or relative phase is extracted. However, already early scattering experiments, performed using traditional Mössbauer sources, revealed strong coherent effects in the interaction of a resonant γ-quantum with an ensemble of Mössbauer nuclei, showing that collective excitations were also possible (for a review see [138]). The study of these coherence properties of the resonant scattering of photons

by a nuclear ensemble, also called Nuclear Resonant Scattering (NRS), was greatly boosted by the advent of the synchrotron radiation (SR) [10], much brighter than the conventional Mössbauer sources.
In fact, after the first experiments performed in Laue and Bragg geometry, nuclear scattering experiment in transmission geometry, also known as nuclear forward scattering (NFS), started to be performed.
As it will be shown in the following paragraphs, the exceptional coherence of NFS is a valuable tool for investigating slow dynamics in liquids at microscopic length-scale, especially if used to implement time-domain interferometers.

3.2.1 Nuclear Exciton

The concept of the *nuclear exciton* [10, 139, 140, 142] is crucial to understand nuclear resonant scattering. In a typical NRS experiment performed with SR, a single γ-photon at a time interacts with the nuclear ensemble. The energy of this γ-quantum would be sufficient to resonantly excite only one nucleus, however the experimental observation of collective phenomena such as total reflection requires the coherent excitation of the whole ensemble. These two apparent contradictory observations can be rationalized by the physical picture of a delocalized nuclear excitation, i.e the nuclear exciton [10, 139–142]. In the case of coherent scattering, indeed, it is not possible to identify the nucleus that has interacted with the γ-photon, as the initial and final state of the nuclear ensemble are identical: each nucleus has a certain probability amplitude to interact with the incoming photon while the others remain in their ground state [10, 142]. The sum of all these amplitudes give the total probability of a photon to interact resonantly with all the nuclei. If the duration of the incident pulse is shorter than the lifetime of the resonance, the temporal phases of these amplitudes are equal and consequently a single excitation coherently distributes over the whole ensemble of nuclei [141]. The wave-function of this collective and non-localized excitation is then given by [10]

$$|\phi\rangle = \sum_i e^{i\vec{k}\cdot\vec{r_i}} |g\rangle |e_i\rangle \ . \tag{3.4}$$

Here $|g\rangle |e_i\rangle$ is the state where the i-th nucleus is in its excited state $|e_i\rangle$ whereas the others are in their ground state and r_i is its position. This state, as it will be elucidated in the following, has an exceptional optical coherence.

3.2.2 Time-evolution of Nuclear Forward Scattering

In introducing the formalism to describe coherent nuclear resonant scattering we will focus on the case of Nuclear Forward Scattering (NFS). Indeed in most atomic systems, especially in presence of disorder, the forward direction, i.e. the same direction as the incident beam, is the only one where constructive interference takes place yielding to coherent NRS [142].
The starting point to describe the response of a nuclear ensemble under coherent

excitation, as already stressed in the previous section, is the concept of nuclear exciton. This strong collective excitation can be seen as a nuclear polariton [10], where the radiative field and the nuclei are strongly coupled and an effective description of its properties can be obtained in terms of index of refraction [10, 142].
Having in mind this concept, the theory of NFS can be derived according to what reported in [10, 142] and summarized in [143]. We can start considering the amplitude of the field scattered by a nuclear absorber, which is given, in the frequency domain, by the product of the incident field ($E_{in}(\omega)$) with the frequency response of the absorber ($R(\omega)$):

$$E(\omega) = E_{in}(\omega)R(\omega)\,. \tag{3.5}$$

$E_{in}(\omega)$ is here assumed to impinge perpendicularly onto the resonant target. In typical NFS experiments the incident radiation is uniformly distributed within the very narrow bandwidth of the nuclear resonance so that we can assume $E_{in}(\omega) = E_{in}$. $R(\omega)$, instead, is a function of the refractive index $n(\omega)$ [10, 142] and consequently of the nuclear susceptibility $\eta(\omega)$ [142].
If the nuclear absorber is assumed to be an isotropic, plane plate, condition typically verified in a NFS experiment, $\eta(\omega)$ is a complex scalar [142] which, in the case of N resonances, can be written as:

$$\eta_0(\omega) = \sum_{j=1}^{N} \frac{\mu_j}{2k_0} \frac{\Gamma_j}{\hbar(\omega - \omega_j) + i\frac{\Gamma_j}{2}}\,. \tag{3.6}$$

In Eq. 3.6 μ_j is the nuclear absorption coefficient of the j-th resonance, k_0 is the wavevector of the incident radiation in vacuum and at the frequency ω, Γ_j is the linewidth of the *j-th* transition and ω_j is its angular frequency. Since $n(\omega) \simeq 1 + \eta(\omega)$, it is finally possible to write $R(\omega)$ as:

$$R(\omega) = e^{-ik_0 n(\omega)L} = e^{-ik_0\left(1+\sum_{j=1}^{N}\frac{\mu_j}{4k_0}\frac{\Gamma_j}{\hbar(\omega-\omega_j)+i\frac{\Gamma_j}{2}}\right)L}\,. \tag{3.7}$$

So, once $R(\omega)$ is evaluated via Eq. 3.7, the intensity resonantly scattered by the nuclear absorber at a given instant t can be calculated from the square modulus of inverse Fourier transform of Eq. 3.5:

$$I(t) = \left|\int_{-\infty}^{+\infty} E_{in}R(\omega)e^{-i\omega t}d\omega\right|^2\,. \tag{3.8}$$

Single-line absorber. For a nuclear absorber with a single resonance ($N = 1$) Eq.3.8 can be analytically calculated [10, 142, 144] and the scattered field is

equal to

$$E(t,T) = E_{in}\exp\left[-\frac{\mu_e L}{2}\right]\left\{\delta(t) - \frac{T_{eff}}{2}e^{-i\omega_0 t-\frac{t}{2\tau_0}}\left[\frac{J_1\left(\sqrt{\frac{T_{eff}t}{\tau_0}}\right)}{\sqrt{\frac{T_{eff}t}{\tau_0}}}\right]\right\} = \\ = \exp\left[-\frac{\mu_e L}{2}\right]\left(\delta(t) + G(t,T_{eff})e^{-i\omega_0 t}\right), \tag{3.9}$$

where $T_{eff} = \mu_1 L$ is the *effective thickness* of the absorber and J_1 is the Bessel function of first order and first kind and accounts for multiple scattering within the target [10, 142]. The term $\exp\left[-\frac{\mu_e L}{2}\right]$ has been added to account for electronic photon-absorption within the target and μ_e is the corresponding absorption length. So, the scattered intensity will be simply given, neglecting the prompt scattering and the absorption from the electrons, by

$$I(t) = \frac{T_{eff}^2}{4}e^{\frac{-t}{\tau_0}}\left[\frac{J_1\left(\sqrt{\frac{T_{eff}t}{\tau_0}}\right)}{\sqrt{\frac{T_{eff}t}{\tau_0}}}\right]^2 \tag{3.10}$$

As it can be easily inferred from Eq. 3.10, the time evolution of the scattered intensity by an ensemble of nuclei is dramatically different from the one we will expect from an isolated nucleus (that is $I(t) \propto e^{-\frac{t}{\tau_0}}$). Fig. 3.3 reports the calculated time-evolution for the NFS arising from absorbers with increasing effective thicknesses (that is with an increasing density of nuclei) ranging from 0.001 to 40. As it is possible to observe the constructive interference in the forward direction gives rise to an enhancement of the overall scattered intensity proportional to T^2. Furthermore, $I(t)$, for the larger values of T, shows also an aperiodic modulation of the exponential decay known as *dynamical beats* (DB), described in Eq. 3.10 by J_1. This time-domain pattern has a characteristic signature also in the energy-domain, consisting in the "double-hump" profile (see the inset in Fig. 3.3). Multiple nuclear resonant scattering in the forward direction, occurring in extended samples, is at the basis of the observed DB [142]: the larger is sample and the higher is the density of nuclei, the more beats will be present in a fixed time-span. Another effect of these multiple interactions between the propagating field and the nuclear ensemble is the speed up of the initial decay of the scattered intensity [142]. This effect can be easily observed if Eq. 3.10 is expanded for $t < 3.8\tau_0 \cdot T$ [142]:

$$I(t) \simeq T_{eff}^2 e^{-\frac{t}{\tau_0}\left(1+\frac{T_{eff}}{4}\right)}. \tag{3.11}$$

In fact, Eq. 3.11 clearly shows that at early times, the effective lifetime of excited state is $\frac{\tau_0}{\left(1+\frac{T_{eff}}{4}\right)}$

Two-lines absorber. Another remarkable case is the one represented by an absorber with several nuclear resonances. This scenario typically arises when

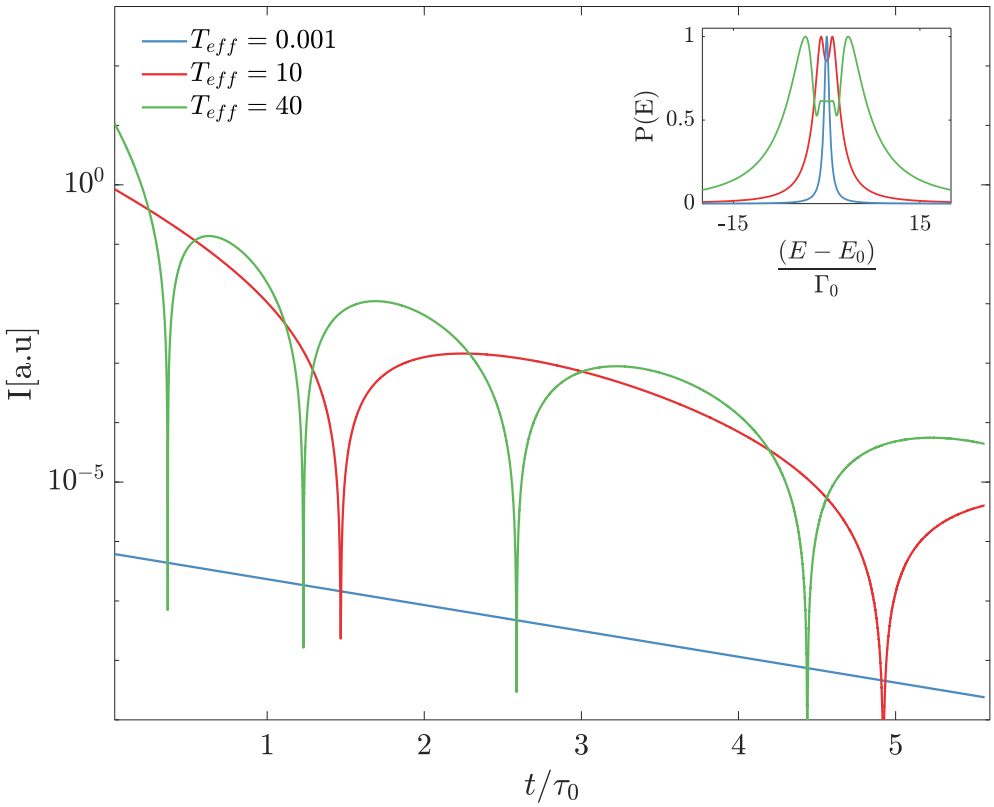

Figure 3.3: Calculated NFS intensity from absorbers with different effective thicknesses as a function of the reduced time t/τ_0: $T_{eff} = 0.001$ (blues solid line), $T = 10$ (red solid line) and $T_{eff} = 40$ (green solid line). The corresponding energy spectra are reported in the inset as a function of the reduced energy $\frac{E-E_0}{\Gamma_0}$.

the nuclei are subjected to hyper-fine interactions that remove the degeneracy of the nuclear levels. If these sub-levels are excited instantaneously and coherently, the resonantly scattered intensity will be modulated by the presence of *quantum beats* as the indistinguishable scattering paths corresponding to different resonances will interfere coherently. In the following an absorber with two resonances at energy $\hbar\omega_1$ and $\hbar\omega_2$ and with an equal linewidth Γ_0 is considered. Its full frequency response is again described by Eq. 3.7 with $N = 2$. However, differently from $N = 1$, Eq. 3.8 (and therefore the time-response of the target) cannot be calculated analytically. However, a simple expression can still be found in the approximation of two resonances sufficiently distant in energy [10, 142, 143], that is, if the radiative coupling between the scattering channels is negligible:

$$I(t) = |E_{in}|^2 |G(t, T_{eff})|^2 \cdot \{1 + \cos[(\omega_1 - \omega_2)t]\} \ . \tag{3.12}$$

The parameters controlling the validity of this approximation are i) the effective thickness of the absorber, which affects the width of the nuclear resonance (see

the inset of Fig. 3.3) and ii) the frequency separation $\Omega = \omega_1 - \omega_2$. When these conditions are not fulfilled the interplay between QB and DB becomes more complex along with the time-evolution of the scattered intensity. This can be observed in Fig. 3.4 where the $I(t)$ numerically calculated via Eq. 3.8 at fixed $\Omega = 50\Gamma_0$ and for two different $T = 10, 100$ is reported.

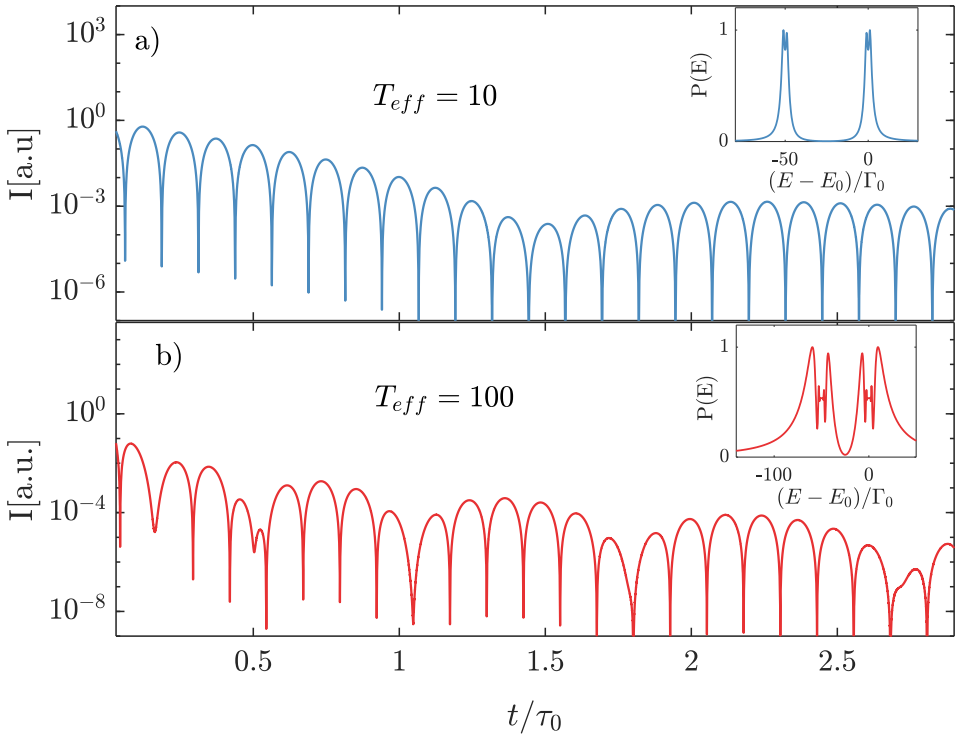

Figure 3.4: Calculated time evolution for the intensity scattered by a two-line nuclear absorber with an effective thickness of $T = 10$ (blue solid line in panel a))and of $T = 100$ (red solid line in panel b)). The insets report the correspondent energy spectra.

3.2.3 Separated targets

In this subsection the concept of separated-targets, crucial for the implementation of time-domain interferometers with the aid of NFS, is briefly introduced. As already pointed out in the previous paragraphs, a SR pulse impinging onto a nuclear absorber generates a nuclear exiciton and its evolution can be described as the one of two coupled sub-systems, the nuclear current and the propagating γ-field [142]. What is interesting to notice is that a nuclear exciton can develop in the space occupied by the nuclear ensemble even if this last one is split into several spatially separated targets [10, 142]. A SR pulse while traversing different targets containing Mössbauer nuclei, can indeed create spatially and temporally phased excitons thanks to the longitudinal coherence of the nuclear

resonance. So a target divided in different slices that are spatially separated behaves exactly as an unsplit target and thus all the coherence properties previously described are preserved [142]. Using separated targets allows to act on different parts of the nuclear ensemble and consequently to modify in a controlled way the properties of the nuclear exciton [142]. As an illustrative

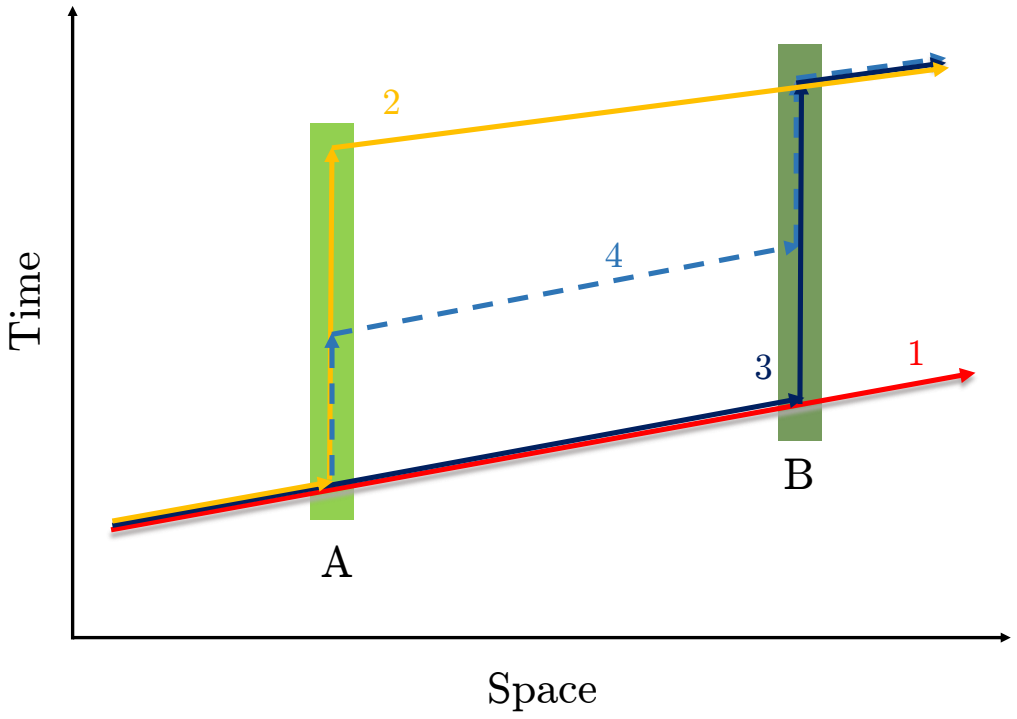

Figure 3.5: Space-time diagram of the resonant scattering process occurring in a nuclear ensemble split into two targets. The main scattering paths are reported using different colors.

example let us consider a system composed by two separated targets as for the scheme reported in Fig. 3.5. An efficient way to analyze this kind of separated systems, as demonstrated by Smirnov [142], is to consider the main scattering paths of the system, accounting for both the response of the single components and their radiative coupling.

Scattering paths approach. In the time-domain, a SR pulse can be approximated as a Dirac's delta

$$E_{in}(t) = E_{in}\delta(t) \tag{3.13}$$

This assumption, equivalent to consider constant $E_{in}(\omega)$ within the linewidth of the nuclear resonance, can be justified considering the time properties of the typical SR pulses used in NFS experiments. The incident SR pulse is typically

monochromatized down to few meV around the energy of the nuclear resonance, in order to reduce as much as possible the non-resonant electronic scattering. So the SR pulse has a time duration of $\simeq 1 \times 10^{-12}$ s, much shorter than the lifetime of the excited nuclear levels involved ($t \simeq 10^{-7}$ s-10^{-9} s). For the same reason the time the incident SR takes to travel from one target to the other can be neglected. Under all the previous assumptions we have that the frequency response of a system of the type of the one reported in Fig. 3.5 is given by:

$$E(\omega) = E_{\omega_0} \cdot R_A(\omega) R_B(\omega) \tag{3.14}$$

where R_A and R_B are the response of target A (effective thickness T_A) and target B (effective thickness T_B) respectively. In the time domain the response of such a system is thus traduced, under the previous premises and according to Ref. [142], into the sum of the scattering amplitude of the main scattering paths of the system. In the case shown in Fig.3.5 four main scattering paths can be easily identified:

- the incident pulse does not excite the first nor the second foil (scattering channel (1) in Fig. 3.5): the impulse of SR is simply transmitted. The time-domain response of this path is simply a Dirac's delta $\delta(t)$.
- The incident pulse interacts only with one of the two foils individually (scattering paths number $(2) - (3)$ in Fig. 3.5). The two scattering paths are described by the response of the single foils R_A and R_B.
- The incident pulse excites the first foil and then the resonantly scattered photons interact with the second one. The two resonances are therefore radiatively coupled and *cross-scattering* takes place. This scattering channel is be described by the term

$$R_{AB} = \int R_A(t) R_B(t - t') dt' \tag{3.15}$$

Finally, the total scattered field is obtained accounting for all the possible channels [10, 142]:

$$E(t) = E_{\omega_0} R(t) = E_{\omega_0} (\delta(t) + R_A(t) + R_B(t) + R_{AB}(t)) \ . \tag{3.16}$$

As it will be elucidated in the following section, the possibility of splitting a nuclear ensemble in several targets is crucial for the implementation of time-domain interferometers based on NFS.

3.3 Time-domain interferometry

A two-target system as the one shown in Fig. 3.5 can be regarded as a time-domain interferometer (TDI), with the absorbers A and B providing its probe and reference arms, respectively. TDI was implemented for the first time by

Baron in 1997 [9] and its working principle can be summarized as follows. Synchrotron radiation photons impinging onto the probe absorber can either coherently excite the nuclear resonance or be simply transmitted. The probe absorber can therefore be regarded as a *split and delay line* [9, 10, 145] These two paths result to be coherently coupled and, after having interacted with the sample, recombine at the reference absorber which is usually chosen to have a different energy spectrum with respect to the probe one in order to avoid the radiative coupling between the two. The reference absorber, since it has a slightly different excitation energy, behaves as a phase-sensitive analyzer [9, 10] and is sensitive to changes in the relative phase of the two paths. The interference between the scattering paths at the output of the reference absorber produces a pattern of quantum-beats. Since the coherent superposition of the paths is mediated by the scattering from the sample placed in between the two absorbers, when quasi-elastic scattering takes place a loss of phasing occurs because of the energy exchange and consequent damping of the beating pattern contrast is observed. The time evolution of the beating patterns is therefore modulated by the sample dynamics and, if properly modeled, allows to extract detailed information on the relaxation processes [9, 14]. If the radiative coupling between the probe and reference absorber is negligible, i.e the excitation energies of the nuclear resonances of the two absorbers are sufficiently apart compared to their linewidths, a simple expression for the field $E_s(t, \mathbf{q})$ emerging from the TDI sketched in Fig. 3.5 can be extracted [14]. Negligible radiative coupling means that the scattering path number 4 in Fig. 3.5 has a very small probability to occur and, indeed, under this assumption $E_s(t, \mathbf{q})$ results to be equal to [14]:

$$E_s(t, \mathbf{q}) = E_{in}(t) \otimes [R_A(t, T^A_{eff})\rho(t, \mathbf{q}) + R_B(t, T^B_{eff})\rho(0, \mathbf{q})] \,. \tag{3.17}$$

Here $\rho(t, \mathbf{q})$ is the time-response of the sample, which is proportional to the Fourier transform of the electron density $\rho(t, \mathbf{r})$ [9]

$$\rho(t, \mathbf{q}) \propto \int \rho(t, \mathbf{r}) e^{-i\mathbf{q}\cdot\mathbf{r}} dr \,. \tag{3.18}$$

Before continuing in the derivation of the models describing TDI data, it is important to point out that the approximation reported in Eq. 3.13 is no longer valid when we consider the scattering path number 3 in Fig. 3.5, i.e. the incident beam is transmitted by the first absorber and impinges onto the sample before exciting the nuclear resonance.
In a typical TDI experiment the incident beam has a bandwidth of $\simeq 1meV$, i.e $E_{in}(t)$ has a duration of $\Delta t_{E_{in}} \simeq 1 \times 10^{-12} s$. While $\Delta t_{E_{in}}$ can be approximated as $\delta(t)$ when compared with the lifetime of the nuclear-fluorescence, this is not the case for the scattering from a supercooled liquid [14]. Supercooled liquids are indeed characterized by various dynamical processes occurring at the ps timescale [57] which can produce an additional loss of coherence in the scattering path number 3. Following the procedure reported in [9, 14, 143], it can be demonstrated that time evolution of the intensity emerging from the TDI, if we neglect the prompt electronic scattering (scattering path 1 in

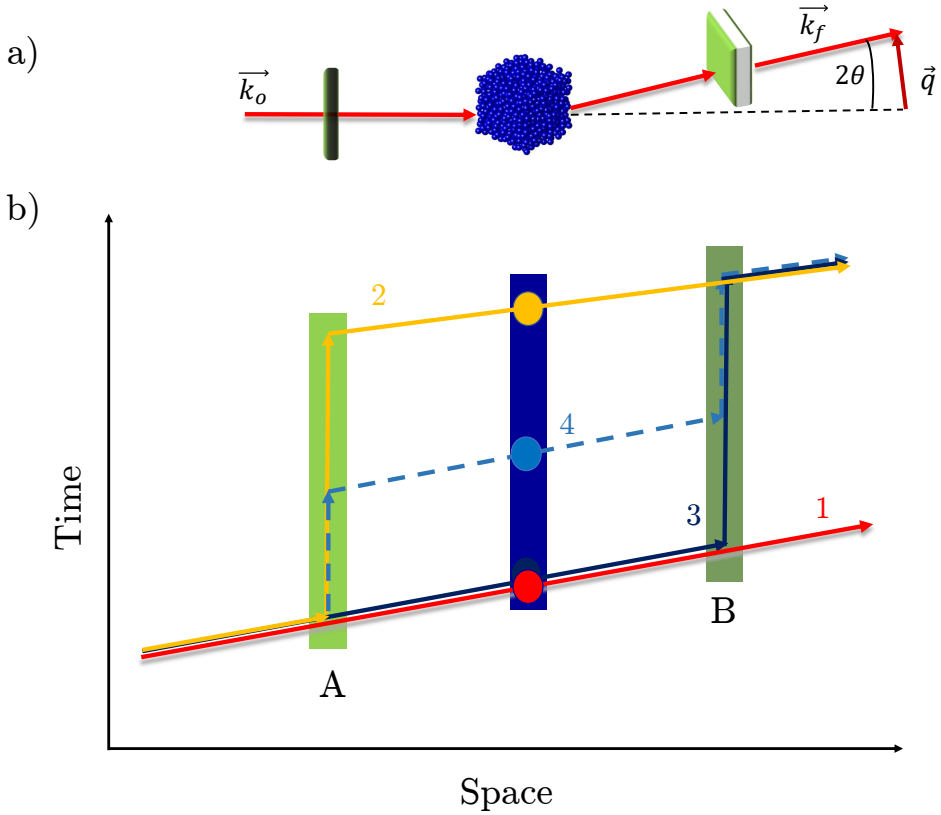

Figure 3.6: Space-time diagram of a nuclear γ-resonance time-domain interferometer (TDI). (a): sketch of the typical experimental set-up for TDI. The incident ($\vec{k}_i$), scattered ($\vec{k}_f$) and exchanged (($\vec{q}$)) wave-vectors are reported along with the scattering angle (2θ). (b): Space-time diagram of a TDI. The main scattering paths are shown in different colors.

Fig.3.5) and we assume that the beating pattern is time-averaged ($\langle\cdot\rangle_t$) over many SR pulses, is described by

$$\begin{aligned}\bar{I}(t,\mathbf{q}) = \langle|E_s(t,\mathbf{q})|\rangle_t = |R_A(t,T^A_{eff})|^2 + |R_B(t,T^B_{eff})|^2 \cdot f_{\Delta E}(\mathbf{q}) \\ + 2Re\{R^*_A(t,T_{eff}) \cdot R_B(t,T_{eff})\}\phi(\mathbf{q},t)\,.\end{aligned} \tag{3.19}$$

Here $\phi(t,\mathbf{q})$ is the normalized intermediate scattering function, introduced in Sec. 2.3.4 and here reported again for the sake of clarity,

$$\phi(\mathbf{q},t) = \frac{\langle\rho(\mathbf{q},0)\rho(\mathbf{q},0)\rangle}{\langle|\rho(\mathbf{q})|^2\rangle}\,, \tag{3.20}$$

and $f_{\Delta E}$ is the fraction of the dynamic structure factor $S(\mathbf{q},\omega)$ which overlaps with the bandwidth of the incident SR [14]:

$$f_{\Delta E} = \frac{\int_{-\infty}^{\infty} S(\omega,\mathbf{q})I(-\omega)d\omega}{\int_{-\infty}^{\infty} S(\mathbf{q},\omega)d\omega}\,. \tag{3.21}$$

In Eq. 3.21, $I(-\omega)$ is the area-normalized energy spectrum of the incident SR pulse.

3.3.1 Two-lines scheme

In the first implementation of TDI described in [9], two identical single line absorbers are used to provide both the probe and reference absorbers. The upstream absorber is driven at constant velocity v using a transducer. In this way the excitation energy of its nuclear resonance is shifted with respect to the one of the downstream absorber by $\hbar\Omega = \frac{v}{c}\hbar\omega$ and the probability of radiative coupling is reduced. Under these conditions Eq. 3.19 can be re-written as [14, 134]:

$$\bar{I}(t,\mathbf{q}) = |E_{in}|^2 |G(t,T_{eff})|^2 \cdot \left[1 + \frac{2}{1+f_{\Delta E}}\cos(\Omega t)\phi(\mathbf{q},t)\right] . \tag{3.22}$$

In this configuration, the loss of coherence induced by the quasi-elastic scat-

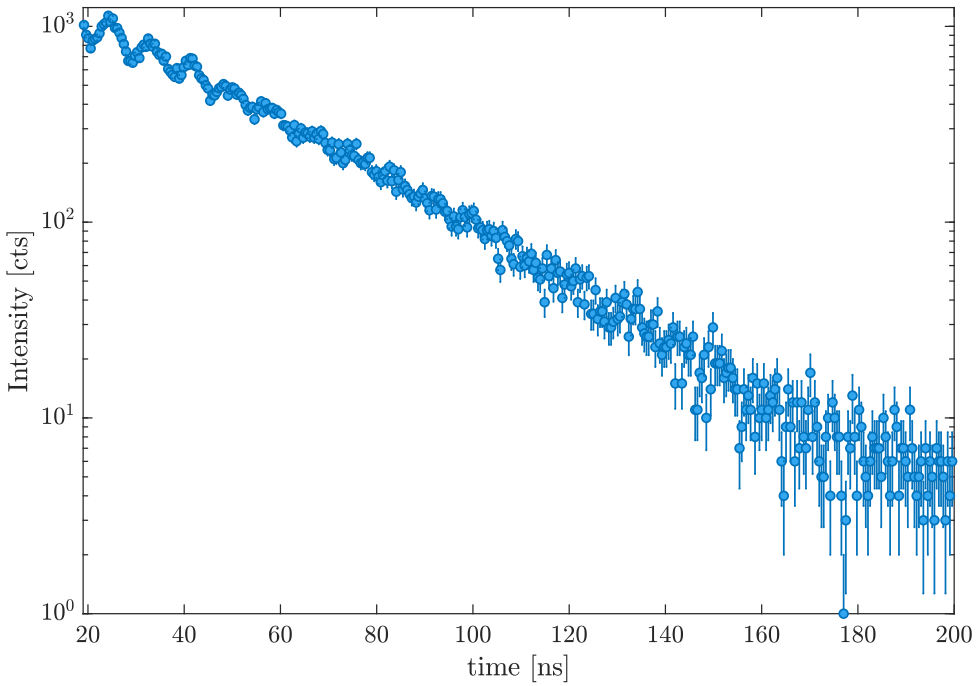

Figure 3.7: Time-domain interferometry pattern as a function of time (points with errorbars) measured from the mono-hydroxyl alcohol 5-methyl-2-hexanol at a wave-numbers q=13nm^{-1} and at the temperature T=206.7 K in the undercooled liquid state

tering from the sample produce a clear decay in the contrast of the beating pattern described by the oscillating term $\cos(\Omega t)$. This can be clearly observed in the beating pattern reported in Fig. 3.7, which was measured from the mono-hydroxyl alcohol 5-methyl-2-hexanol at $T = 206.7$K, i.e will above its $T_g = 155$K . However, this configuration does not allow to disentangle $f_{\Delta E}$, which depends both on the sample dynamics in the meV range and on the

experimental set-up, from $\phi(t, \mathbf{q})$ and therefore biases the estimation of the relaxation strength [14]. Indeed, what is probed, instead, is the contrast function [14, 134] $\phi'(t, \mathbf{q})$:

$$\phi'(t, \mathbf{q}) = \frac{2}{1 + f_{\Delta E}} \phi(t, \mathbf{q}) \tag{3.23}$$

3.3.2 Multi-lines scheme

Recently, new TDI schemes [14, 143], involving the use of absorbers with multi-line energy spectra and different effective thicknesses has been proposed in order to improve both efficiency and directly measure $f_{\Delta E}$. In fact, using absorbers with different responses R_A, R_B (see Eq.3.19) $f_{\Delta E}$ can be easily disentangled from f_q. So these new schemes allow measuring the absolute strength of relaxation processes and reduce the acquisition time. This is possible, however, only at the price of a more complex interferogram to analyze. A more detailed discussion about a TDI experiment based on nuclear absorbers with multi-line energy spectrum is postponed to Ch. 6, where the technical aspects and the possibilities offered by the use of a three-lines scheme recently introduced in [143] will be described and analysed.

3.3.3 A remarkable isotope for TDI: ^{57}Fe

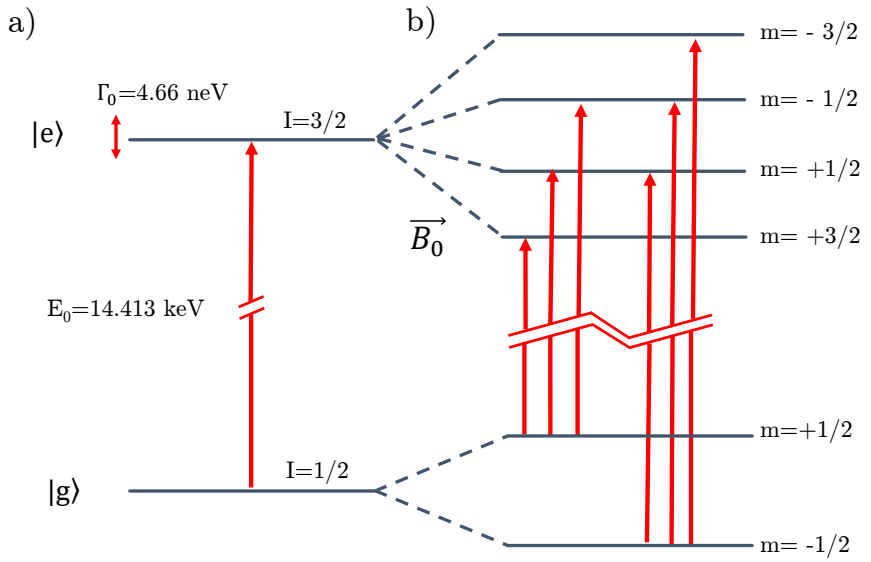

Figure 3.8: a): sketch of the ground and first excited states of ^{57}Fe. b): Zeeman's splitting of the ^{57}Fe energy levels. The red-solid lines represent in both cases the allowed magnetic dipole transitions.

The first nuclear resonance of ^{57}Fe is one of the most studied and is also the one typically used to to generate the reference and the probe beam in a TDI experiment.
Its first excited state $|e\rangle$ lies at an energy of 14.413 keV, has a natural linewidth

of 4.66 neV and a nuclear spin $I = \frac{3}{2}$. The ground-state $|g\rangle$ is characterized instead by spin $I = \frac{1}{2}$ and the transition between the two $|g\rangle \leftarrow |e\rangle$ is a magnetic dipole one (see Fig.3.8-(a)). In presence of hyperfine interactions the structure of the energy levels is of course more complex. Fig.(3.8)-(b) shows, for example, the splitting of the ^{57}Fe ground and excited states in presence of an external magnetic field, along with all the allowed nuclear transitions. There are many reasons behind the choice of this particular Mössbauer isotope. First of all, ^{57}Fe has one of the largest resonant cross-section $\sigma = 246.40 \cdot 10^{-24}$ m^2. Secondly, its lifetime $\tau_0 = 141.1ns$ is more than suitable for investigating slow relaxations in the 10ns-10μs time window. Finally, its transition energy $E = 14.4keV$ is high enough to study dynamics at the Ångström and sub-Ångström length-scale. In fact TDI with ^{57}Fe nuclei has been already effectively applied to the study of slow dynamics in supercooled liquids [9, 11–13, 134], providing the access to an otherwise precluded dynamic-range.

Chapter 4

Nuclear γ-resonance time-domain interferometry: experimental details

The purpose of this chapter is to introduce the technical aspects of nuclear γ-resonance time-domain interferometry. Initially a quick overview of the beamline ID18 of the European Synchrotron Radiation Facility, specialized in the excitation of nuclear resonances, is given. Then the experimental set-up is discussed in detail and the main optical elements required to perform TDI experiments are described. Particular attention is also paid to the issue of momentum resolution. Finally, the models introduced in Ch. 3 for analysing the TDI data are revised accounting for i) the finite time-response of avalanche photo-diode detectors, ii) the loss of coherence induced by fictive relaxations and iii) the use of nuclear absorbers with a distribution of thicknesses. All these topics are discussed in view of the experiments reported in Ch. 5 and Ch. 6.

4.1 Beamline ID18 of the ESRF

The beamline ID18 of European Synchrotron Radiation Facility (ESRF) in France is one of the few laboratories able to effectively excite and study the nuclear resonances of Mössbauer nuclei using synchrotron radiation. As it can be observed in Fig. 4.1, the layout of the beamline ID18 consists of an undulator stage providing SR and of five hutches. The first two house the X-ray optics necessary to properly monochromatize the SR for NRS experiment. The last three hutches are instead dedicated to the installation of the experimental equipment and of various sample environments. The TDI investigation reported in this thesis were performed in the first experimental hutch (E1 in Fig. 4.1)

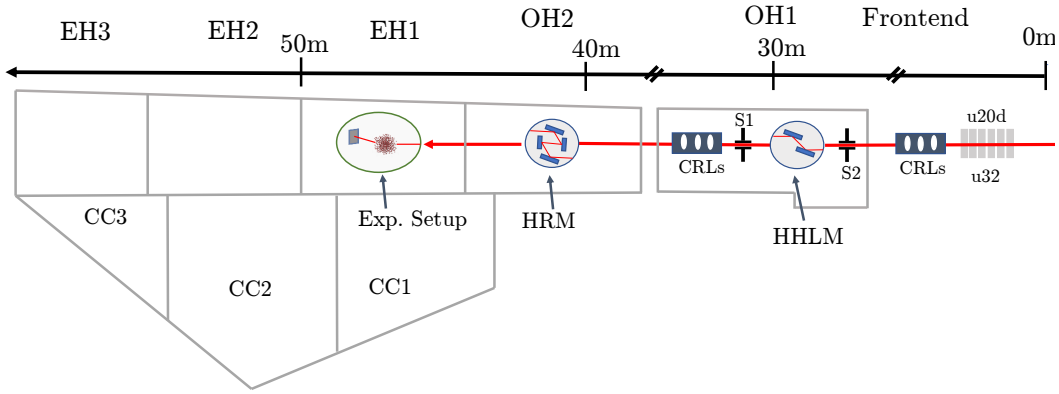

Figure 4.1: Layout of the Nuclear Resonance beamline ID18. ID18 consists of an the undulator stage, providing the primary X-ray source, two optical hutches ($OH1 - OH2$) where the beam is monochromatized and three experimental hutches ($EH1 - EH2 - EH3$) controlled by dedicated control cabins ($CC1 - CC2 - CC3$). HRM and HHLM stands for high-resolution monochromators and high-heat load monochromator respectively. CLR are compound refractive lenses and S1, and S2 labels the slits used to cut the beam tails at input and output of the HHLM. The TDI experiments were performed in the first experimental hutch. Only the elements of interest for the experiments reported in this thesis are shown for the sake of clarity. Further details and the complete layout can be found in [146].

4.1.1 The accumulation ring of the ESRF

Before proceeding in the description of the beamline ID18 it important to briefly review some of general properties of the ESRF.
The ESRF consists of a storage ring with a circumference of 884 m where electrons are injected after having being accelerated to an energy of 6GeV by a linear accelerator (LINAC) and a booster synchrotron. While traveling around the storage ring these relativistic electrons pass through different magnetic structures (insertion devices) where they are radially accelerated and emit SR. One of the peculiar properties of the SR is its time structure. In fact the electrons in the storage ring are grouped in "bunches" that are then distributed along the circumference according to different filling modes. Pulses of SR radiation are therefore emitted with a time structure which reflects the particular filling mode of the ring. In NRS and TDI experiments the time-separation between the electron bunches should be long enough to enable the observation of the time-evolution of the intensity resonantly scattered by Mössbauer nuclei. For what concerns the measurements described in this Thesis, they were performed while the synchrotron was operating in the 4-bunch filling

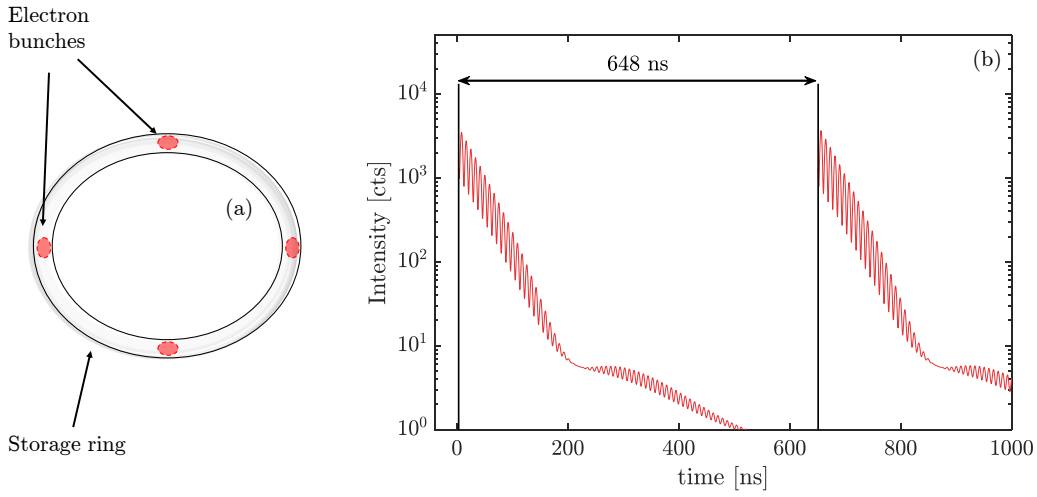

Figure 4.2: (a): In the 4-bunch filling mode, the storage ring is filled with 4 groups of electron spaced by 648ns. (b) The time window between two SR radiation pulses is, accordingly, 648ns.

mode. In this configuration the storage ring is filled with four electron bunches separated in time by $\Delta t = 648$ns (see Fig.4.2-(a)). Accordingly the time interval between two SR pulses is of 648ns (see Fig.4.2-(b)). Such a long time window is more than suitable for TDI experiments based on the first excite state of ^{57}Fe.

4.1.2 Undulators

Undulators are the most common insertion devices that can be found in 3rd generation synchrotron radiation facilities. Undulators consist of magnetic periodic structures, placed along the storage ring, that force the orbiting electrons on sinusoidal trajectories around the forward direction (see Fig. 4.3). More specifically, undulators are designed so that the radiation emitted by an electron at a given oscillation and at a specific energy results to be in phase with the radiation produced during the successive wiggles. In this way the radiated waves constructively interfere and high fluxes are achieved. Another important consequence is that the energy spectrum of the radiation produced by undulators is characterized by the presence of sharp harmonics. The main parameter characterizing an undulator is the so called *deflection coefficient* K defined as [147]:

$$K = \frac{e}{2\pi m_e c}\lambda_0 B_0 \,. \tag{4.1}$$

Here B_0 is the amplitude of the magnetic field between the upper and lower arrays of magnets and depends on the gap between the two, m_e is the mass of the electron and λ_0 is the period of the magnetic structure. The parameter K determines the energy of the radiation emitted by an undulator. The energy of

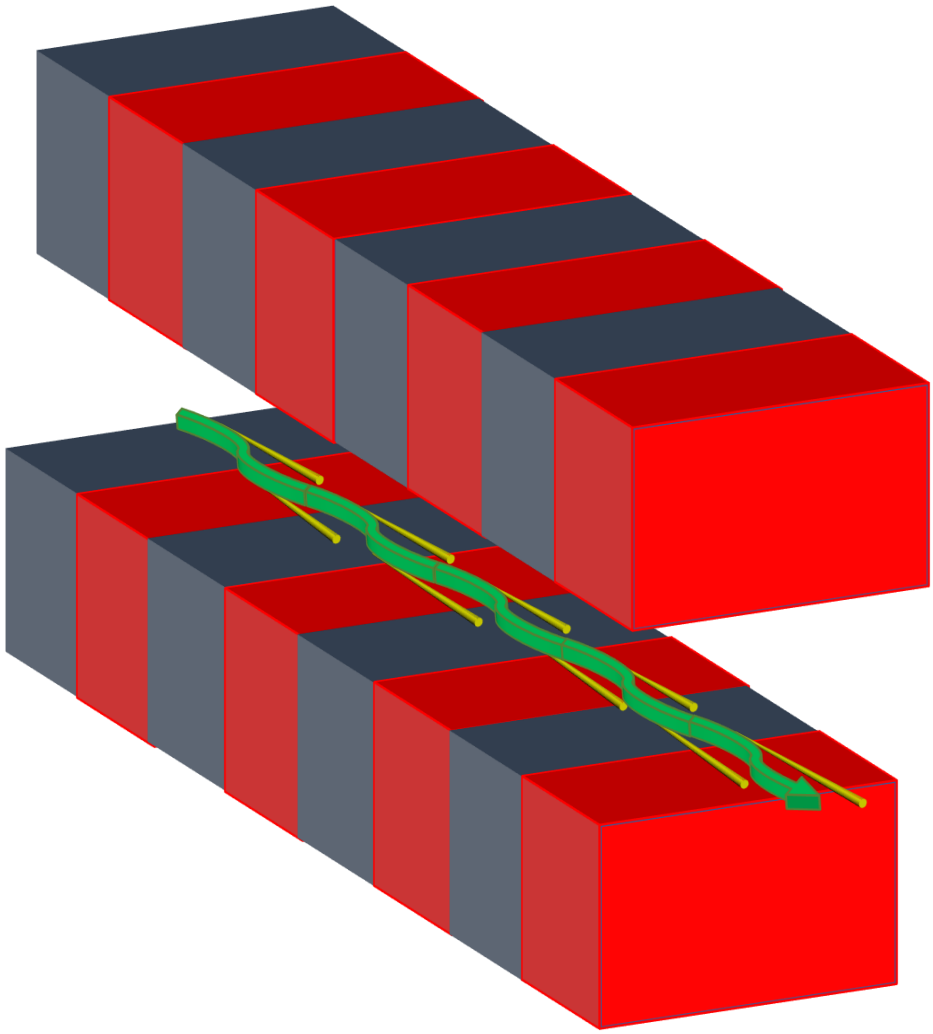

Figure 4.3: Typical structure of an undulator.

the m-th harmonic is indeed given by [147]:

$$E_m(\theta) = m\frac{2c\gamma^2}{\lambda_0}\frac{1}{1+\frac{1}{2}K^2+\gamma^2\theta^2} \tag{4.2}$$

where θ is the angle of observation of the beam and γ is the Lorentz factor

$$\gamma = \frac{c}{\sqrt{c^2-v^2}} \tag{4.3}$$

As it can be easily grasped from Eq. 4.2, the frequency of the produced SR can be tuned changing the gap between the two sets of periodic magnets. For the interested readers further remarks about undulators can be found in reference [147].
ID18, as already stated, is an undulator beamline and the SR radiation is there produced by three "revolver" undulators (i.e with double interchangeable periodic structures) with a period of $\lambda_0 = 27$mm and $\lambda_0 = 20$mm, respectively,

and each 1.6m long. These undulators can cover energies ranging from 8keV to 80keV, allowing to probe a large number of Mössbauer isotopes. In particular the 20mm undulators are optimized to excite the first nuclear transition of ^{57}Fe, which lies at $14.413keV$. The shape of the harmonics at the resonance energy of ^{57}Fe for the two different undulators are reported in Fig. 4.4. The SR radiation

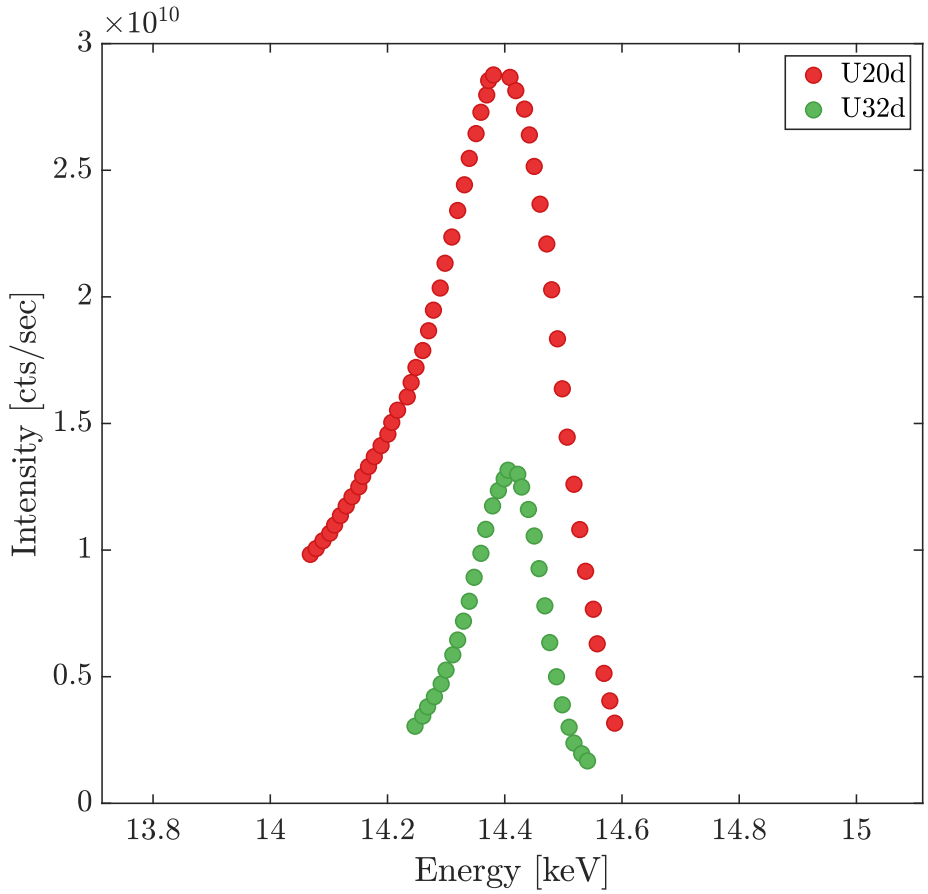

Figure 4.4: Radiation fluxes at the energy of the first resonance of ^{57}Fe produced by two different undulators. The fluxes were measured setting the exit slits of the undulator to $20\mu m \times 200\mu m$ and with an electron current in the storage ring equal to $100mA$. *Data taken from [146]*

.

at the exit of the $\lambda = 20$mm undulator is characterized by a bandwidth of $\simeq 290eV$ at $E_\gamma = 14.413keV$, and by a cross section of $\sigma_U = 900 \times 10\mu$m^2 (H×V).

4.1.3 OH1 and OH2

The photons coming from the undulators require to be further monochromatized before being used in a NRS experiment. It is indeed necessary to reduce as much as possible the amount of non-resonant photons impinging onto the absorber to avoid an overload of the detector system and radiation damage on the sample. To this aim, a high heat-load (HHLM) and a high resolution monochromator (HRM) are typically used in cascade.

4.1.3.1 HHLM

The HHLM consists of two separate, cryogenically cooled Si crystals in (111) reflection [148]. These two crystals, mounted on two separate movements and operating in ultra-high vacuum conditions are characterized by high and long-term angular stability ($\simeq 34$ μrad)[146, 148]. This is required to reduce as much as possible the thermal angular drift that be caused by the high fluxes at the output of the undulators. The time-evolution of the intensity at output of the HHLM is also characterized by a large stability and it is able to steadily adapt to fluctuations in the incident intensity (i.e electron current in the storage ring) without drifts (see Fig.4.5). The HHLM reduces the bandwidth of the

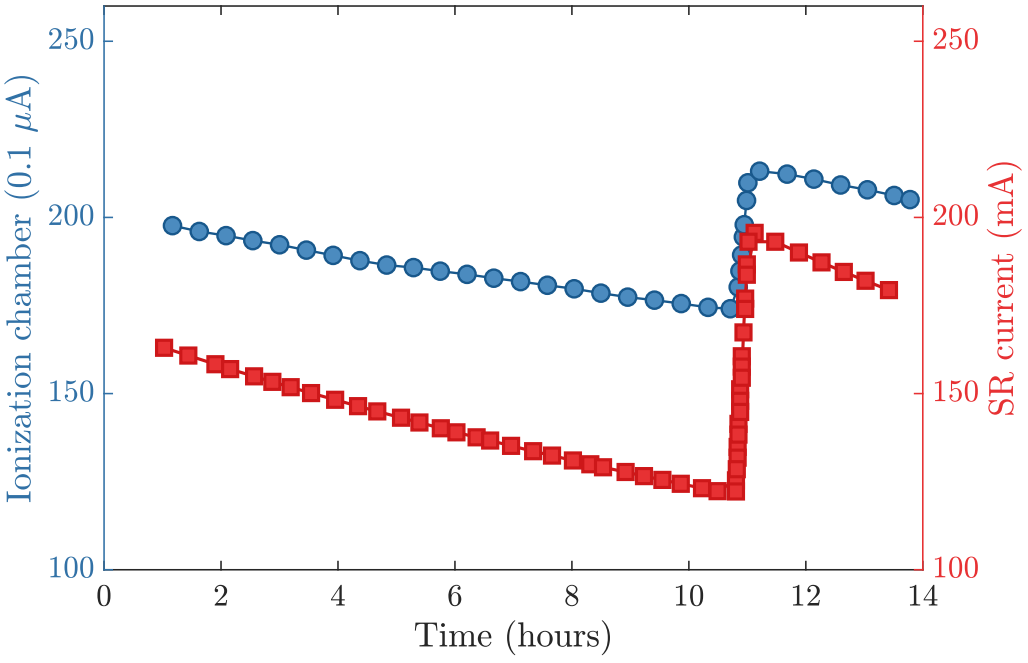

Figure 4.5: Blue circles: time-evolution of the x-ray intensity at output of the high heat-load monochromator as measured by a ionization chamber. Red squares: electron current in the synchrotron. The discontinuity at 10 hrs is due to the refill of electrons in the storage ring. The intensity at output of the HHLM readily responds to the new incident current. *Data taken and adapted from [146].*

incident radiation down to 2.1 eV.

4.1.3.2 Collimating lenses

After the HHLM a set of 7 cylindrical beryllium compound refractive lenses (CRLs) with the radius of curvature of 1.0 mm and focal distance of 43.5m at 14.4 keV radiation can be inserted at 39 m from the undulators in order to reduce the vertical divergence of the beam. This is often required, in presence of further monochromatization stages, to match the angular divergence of the beam to the acceptance of successive monochromators and increase their throughput. The configuration of lenses described above allows to reduce the vertical divergence of the beam down to 1.6 μrad.

4.1.3.3 HRM

The incident SR needs to be further monochromatized after the HHLM, since its bandwidth is still too large to perform NRS experiments. This is usually done using the HRM located at the second optical hutch (OH2) of ID18. There, several HRMs specialized for the nuclear transitions of various Mössbauer nuclei are present.
The HRM monochromators which can be used for NRS experiments on ^{57}Fe consists of four asymmetrically cut Si-crystals in a configuration similar to the one described in [149]. The main idea underlying this design is to exploit the combined diffraction from four crystals to obtain the wanted energy resolution. The sequence of Bragg reflections indeed reduces the angular spread of the incident beam and provides a smaller spectral spread. These monochromators have typically an in-line configuration, that is, the direction of the beam at the output of the crystals is the same as the incident one. The first couple of crystals, in a non-dispersive configuration, collimates the beam, whereas the final bandwidth is selected by the second couple (also in a non-dispersive configuration) that operates at a higher order reflection. Another important feature of these HRM is that the crystals are asymmetrically cut. This means that the crystal surface is cut so that it is not parallel to the diffracting atomic planes. In this way the Bragg reflections can be engineered, increasing or decreasing the angular dispersion and acceptance [150]. The properties of a such crystal reflections are encoded in the asymmetry parameter b which is defined as [150]:

$$b = -\frac{\sin(\theta_{in})}{\sin(\theta_{out})} \tag{4.4}$$

where θ_{in} and θ_{out} are respectively the angles of the incident and exit beams with respect to the crystal surface. The HRMs employed in the two different experiments described in Ch. 5 and Ch. 6 were both based on the (4 0 0) and (12 2 2) reflections of Si. However, since they were made of crystals with different b-values, the provided beams were characterized by two different bandwidths: 2.5meV and 0.75meV respectively (see Fig. 4.6-(b) and (c)). It is important to remark that in NFS experiments the bandwidth of the incident

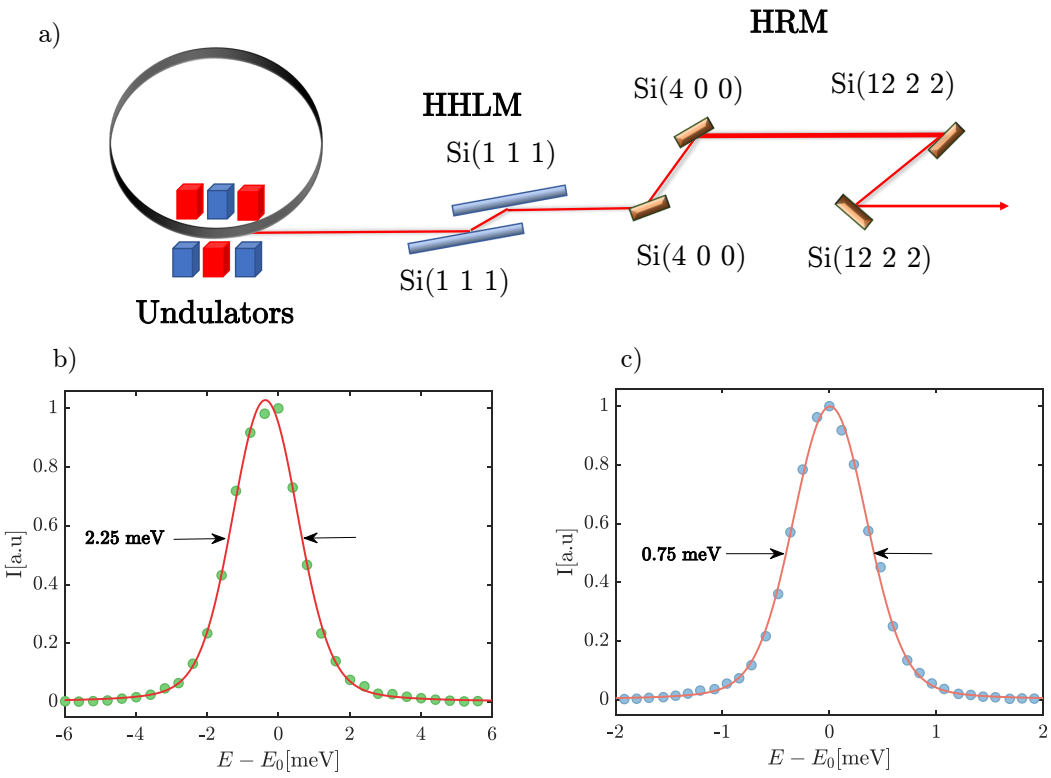

Figure 4.6: (a): Schematics of the HHLM and HRM used in cascade to provide the monochromatic beam used in NRS experiments at ID18. (b) Energy spectrum used in the experiment reported in Ch.5. Green dots: experimental data. Red solid line: curve obtained from fitting a Voigt-profile to the measured energy spectrum. (c): Energy spectrum used in the experiment reported in Ch.6. Gray dots: experimental data. Red solid line: curve obtained from fitting a Voigt-profile to the measured energy spectrum.

beam does not play a crucial role as long as it has been sufficiently reduced so that overload of the detector system is prevented (more details on the detectors in Sec. 4.2.1). On the contrary in TDI measurements, as already clarified in Ch. 3, the spectral width of the SR directly influences the value of $f_{\Delta E}$. We indeed recall that $f_{\Delta E}$ depends on the fraction of the dynamics structure factor of the sample which is comprised within the energy spectrum of the exciting radiation (see Eq. 3.21 in Ch. 3).
All the steps described up to now and required to suitably reduce the SR bandwidth for TDI measurements are summarized by Fig. 4.6.

4.2 Scattering geometry and signal detection

A sketch of the typical experimental set-up for TDI experiments is reported in Fig. 4.7. As already discussed in Ch. 3 the probe and reference absorber are respectively placed upstream and downstream with respect to the sample. A photon-counting detector is placed right after the reference absorber and collects, at a certain scattering angle θ, the radiation diffused by the sample . It is important to remark that in X-rays scattering experiments θ completely defines the probed exchanged wave-vector q according to the relation:

$$q = 2 \cdot k_0 \sin\left(\frac{\theta}{2}\right) \tag{4.5}$$

where k_0 is the wave-number of the incident beam. In the following the main technical aspects of the TDI will be reviewed paying particular attention to i) the signal detection (Sec. 4.2.1), ii) the optimal sample thickness (Sec. 4.2.2) and iii) the design of the scattering geometry and q-resolution (Sec. 4.2.3). For what concerns the nuclear absorbers used in the TDI experiments discussed in this Thesis the reader is refereed to Sec. 5.1.1 of Ch. 5 and Sec. 6.1.1 of Ch. 6.

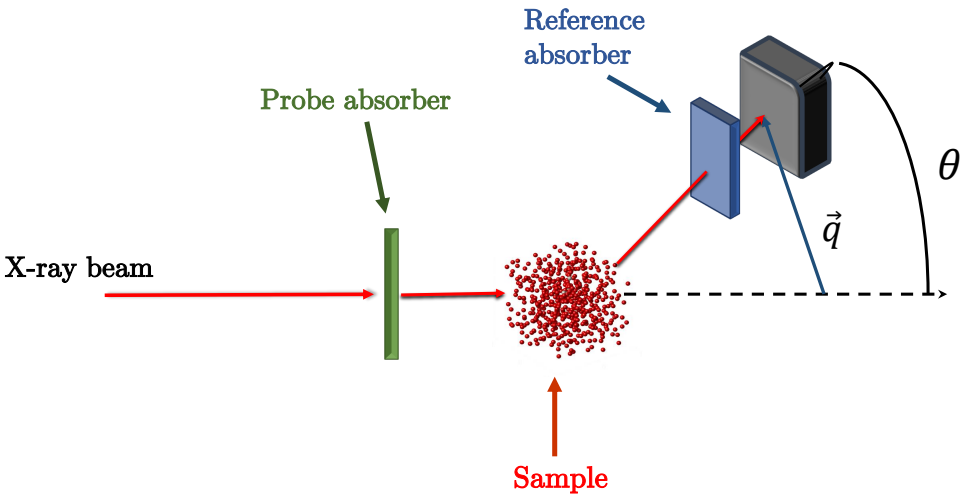

Figure 4.7: Sketch of the typical experimental set-up for TDI. The red-line indicates the pattern of the SR before and after being scattered by the sample. The black dashed line shows the direction of the transmitted beam. θ and $\vec{q}$ are the scattering angle and the exchanged wave-vector respectively.

4.2.1 Avalanche photo-diode detectors

In NRS experiments high dynamical range, ns time-resolution and fast recovery time are mandatory requirements for a detector. The detector must indeed be able, after few ns (typically 5ns-10ns) from the prompt and intense electronic

scattering, to detect the single photon events related to the excitation of the nuclear resonance. To this aim avalanche photo-diodes (APD) are typically used. The measurements reported in this thesis were all performed using double avalanche photodiode (APD) detectors manufactured by the EG&G Optoelectronics and characterized by 10×10 mm^2 active area and an efficiency of 66% (see Fig. 4.8-(a)). The typical time-response for such APD detectors is shown in Fig. 4.8-(b). As it can be noticed the time-resolution is usually $\simeq 1ns$.

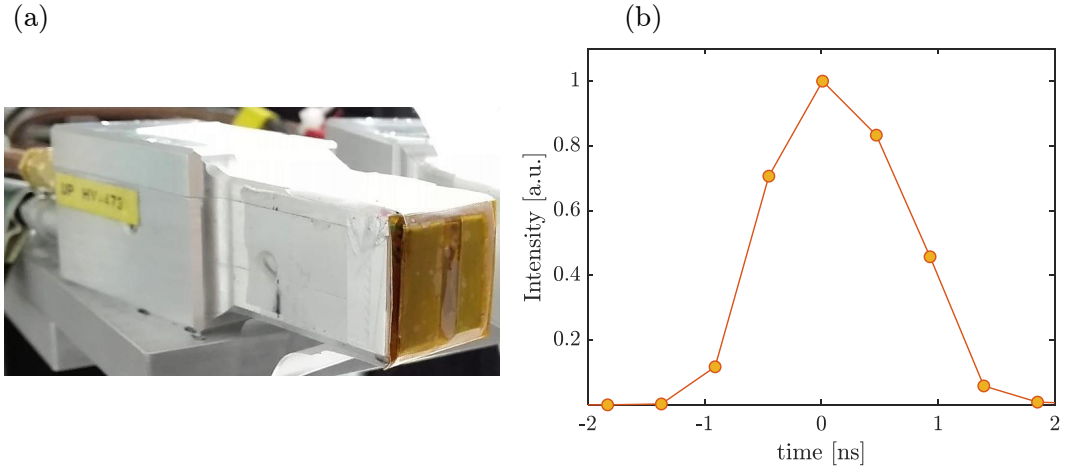

Figure 4.8: (a): Photo of a avalanche photodiode detector (APD) of the EG&G Optoelectronics. (b): Characteristic time-response of this APD.

4.2.2 Optimal sample thickness

In any X-ray scattering experiment, it is important to select the correct sample thickness, so that the scattering intensity is maximized. It goes without saying that the thicker is the sample the larger is the probability that a photon will interact with an atom while traveling across it. However, X-rays are also strongly absorbed by condensed-matter systems and therefore if a sample is too thick, a relevant fraction of the radiation will be absorbed.
To calculate the optimal sample thickness we can proceed as follows. Let us consider an incoming X-ray beam with initial intensity I_0, propagating along the x-direction and which is then scattered at an angle θ. If the material has an absorption coefficient μ, we have that the diffuse intensity coming from an infinitesimal portion of the scattering volume can be written as [151]:

$$dI = I_0 e^{-\mu x} s e^{\frac{W-x}{\cos(\theta)}} dx \,, \tag{4.6}$$

where s is the isotropic scattering factor and W is the thickness of the sample. If Eq.4.6 is integrated over W, the scattering intensity coming from the sample

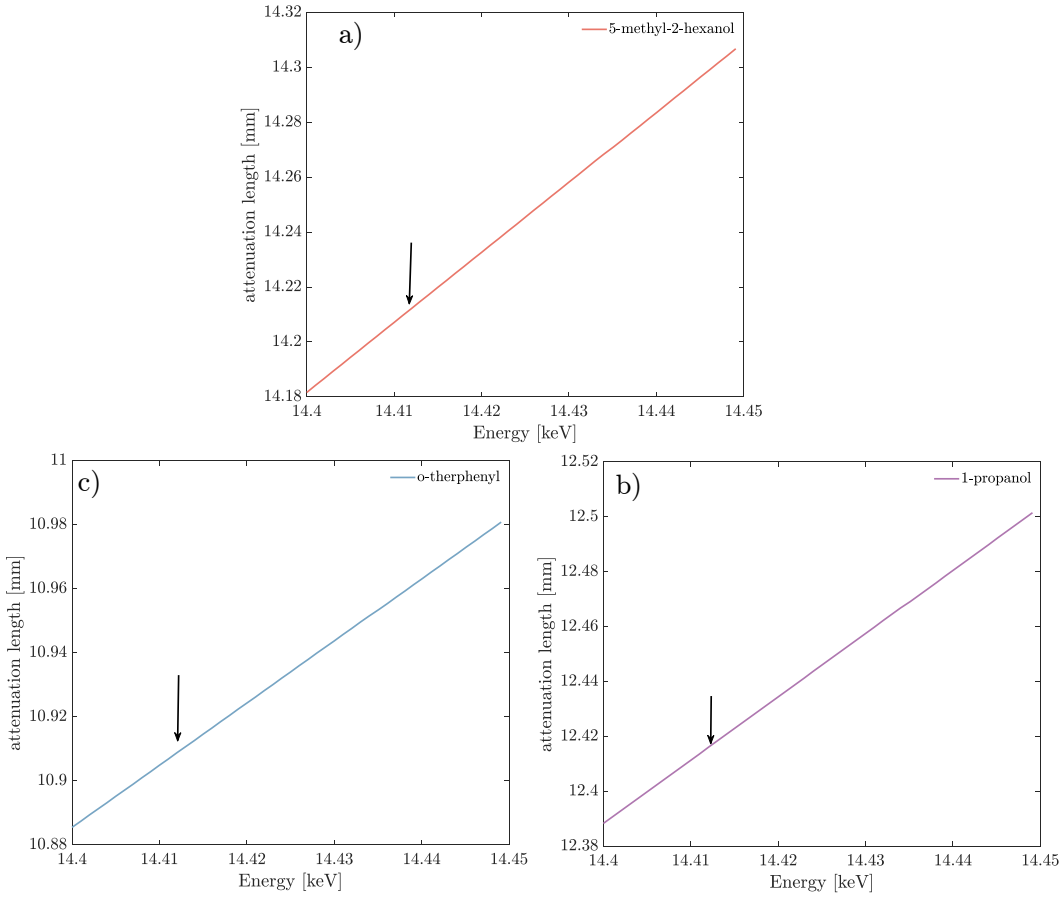

Figure 4.9: Calculated attenuation lengths at the energy of the first nuclear excited state of ^{57}Fe for 5-methyl-2-hexanol (a), 1-propanol (b) and o-therphenyl (c).

is obtained [151]:

$$I = \int_0^W dI = I_0 s \frac{e^{\frac{-\mu W}{cos(\theta)}}}{\mu\left(1 - \frac{1}{\cos(\theta)}\right)} \tag{4.7}$$

Then, it is not difficult to demonstrate the value of W that maximises I is equal to:

$$W = \frac{\ln(cos(\theta))}{\mu\left(1 - \frac{1}{cos\theta}\right)}\,. \tag{4.8}$$

If expanded for $\theta \to 0$, Eq. 4.8 reduces to:

$$W \simeq \frac{1}{\mu}\,. \tag{4.9}$$

So, the optimal sample thickness can be approximated with the attenuation length of the sample. Eq. 4.9 is accurate within 8% for the angles here considered (i.e $< 35°$).
Consequently, all the sample holders employed in the scattering experiments in

Ch. 5 and Ch. 6 were designed to match the attenuation length of the samples at the energy of the nuclear resonance of ^{57}Fe (see Fig. 4.9)

4.2.3 Scattering geometry

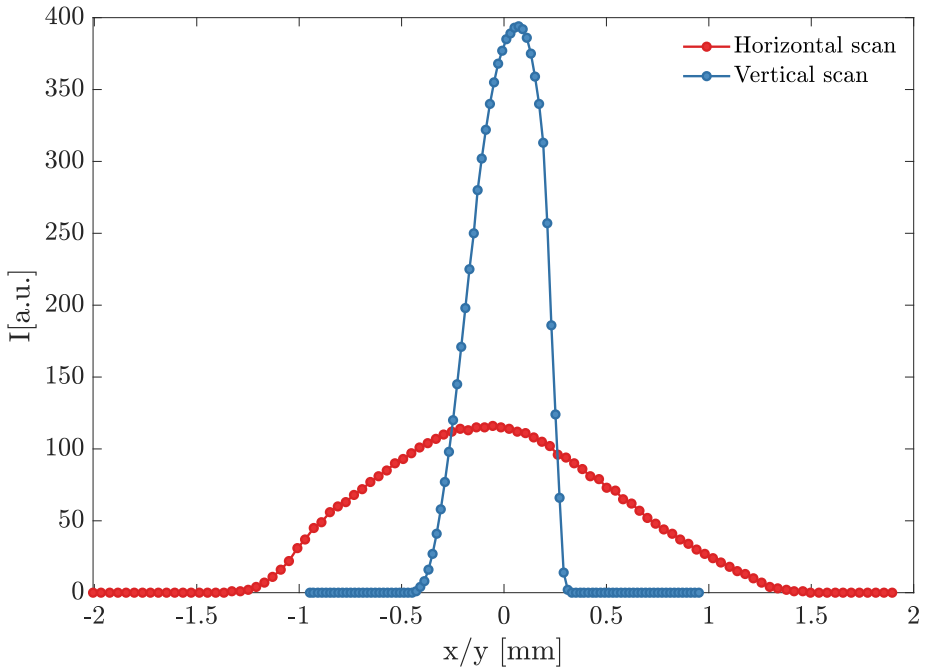

Figure 4.10: Horizontal (red dots) and vertical (blue dots) beam profile as measured at 32m from the undulators. The solid lines are a guide for the eye.

Designing the scattering geometry, as we will see in the following, is a crucial aspect of any TDI experiment.
The characteristic count-rate of a TDI measurement is low and so to reduce the collection time for a beating pattern is highly desirable. A possible way to solve this issue is to increase the fraction of solid angle covered by the detector, at the price of a worse scattering-vector (q) resolution. A compromise is typically sought, keeping in mind that the q-resolution should be high enough to study the microscopic features of a relaxation process.

Concerning the q-resolution, it is typically determined by three main parameters in a TDI experiment: i) the synchrotron radiation spot size at the sample-position, ii) the length of the sample and iii) the solid angle intercepted by the detector. The final distributions of q-values, corresponding to a certain scattering vector q, result from the convolution of these three contributions. The parameters i) and ii) are set by the X-rays optics and by the attenuation length of the sample. Parameter iii) is instead controlled by the geometry which, in turn can be designed in order to achieve the aimed q-resolution.
The calculations for the terms ii) and iii) are straightforward as all the needed parameters are easily available. The situation is different for i), since no direct

measurement of the X-ray beam profile is possible at the experimental hutch EH1 where the TDI experiments were performed, that is 47m away from the X-ray source.
In this case the beam cross-section at the sample position needs to be estimated from the original size of the X-ray source and the angular divergence of the beam.
The beam divergence can be easily calculated from the comparison of the beam size at the output of the undulator with one (see Fig. 4.10) measured by the ionization chamber placed 32m further away from it for monitoring purposes. The found values for the vertical α_V and horizontal α_H angular divergences were respectively:

$$\alpha_H = 36\mu rad \quad \alpha_V = 16\mu rad\,. \tag{4.10}$$

The beam-cross section at the sample position (FWHM) was then estimated to be:

$$\sigma_S = 1.76 \times 0.65\, mm^2\,. \tag{4.11}$$

In Eq. 4.11 the presence of CRLs at 39 m from the source (see Sec. 4.1.3.2) has been also taken into account while the small contributions from the two monochromatization stages to α_H and α_V ($\simeq 1\mu$rad) were not considered.
An example of the characteristic q-distribution under the experimental conditions of the TDI experiments described in Ch. 5 is shown in Fig. 4.11. The plotted distributions have been calculated considering a scattering angle $\theta = 18.5°$, a sample-length of 13mm, a sample-detector distance of 80mm and a detector with an active area of 6.3×10 mm^2. The contributions, i),ii) and iii) can be separately observed in Fig. 4.11-(a) , while Fig. 4.11-(b) reports the final q-distribution arising from the convolution of the three contributions. The resulting q-resolution, defined as the FWHM of the total distribution, is 4nm^{-1}, i.e $\frac{\Delta q}{q} \simeq 20\%$. This a typical value for the TDI experiments reported in this thesis.

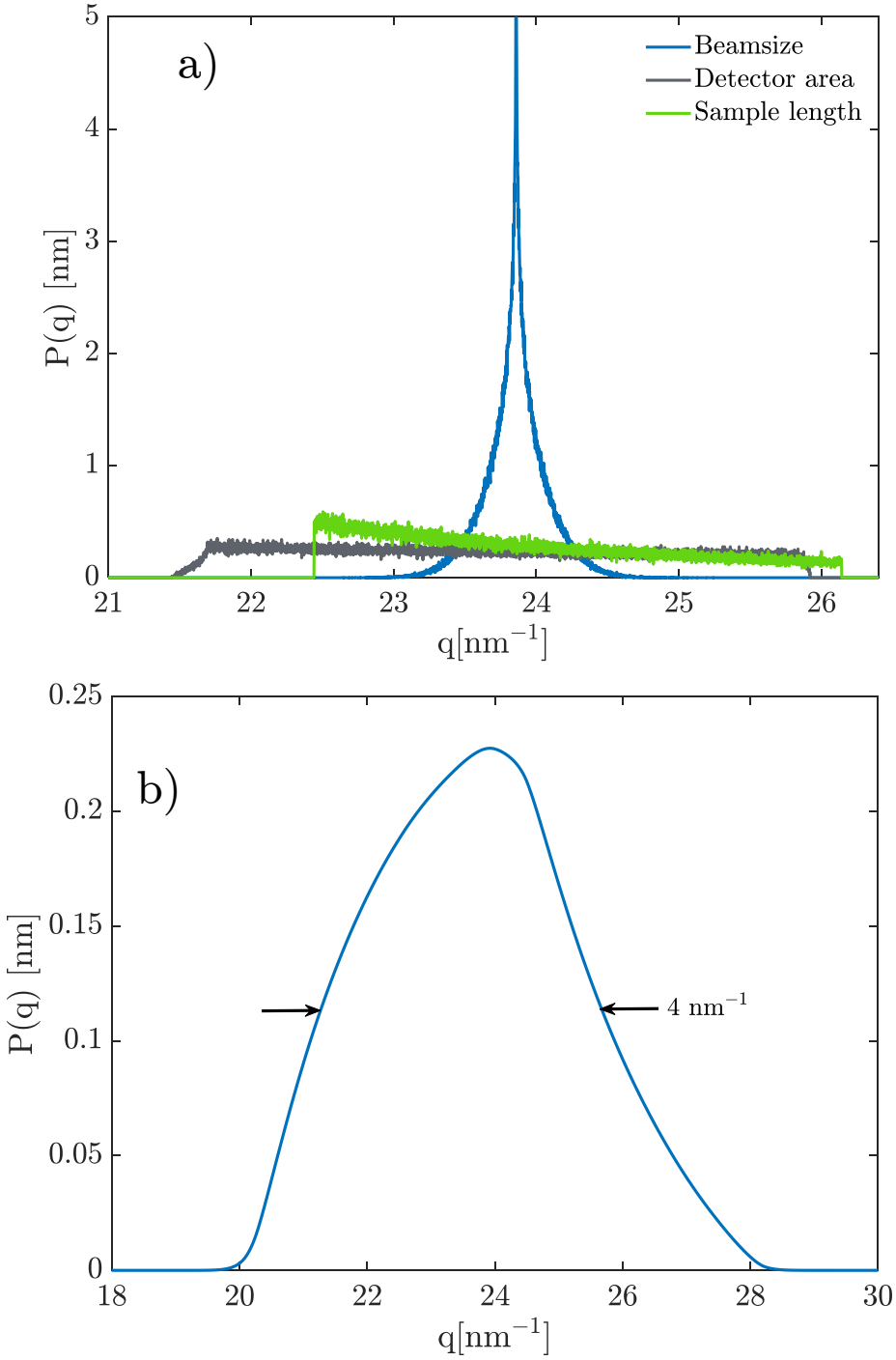

Figure 4.11: (a): calculated wave number (q) distributions due to i) beam spot at the sample (blue line), ii) sample length (green line) and iii) detector area (gray line). (b): Total q-distribution due to the convolution of the three distributions in (a). Calculations were performed considering a scattering angle $\theta = 18.5$, a beam-size of $\sigma_S = 1.75 \times 0.65 mm^2$, a sample length of 13mm and a detector area of 6.3×10 mm^2.

4.3 Methodological aspects of TDI

In this section the models introduced in Ch. 3 are revised in order to describe the influence of several experimental parameters on the TDI signal.

4.3.0.1 Finite time-response of the detector

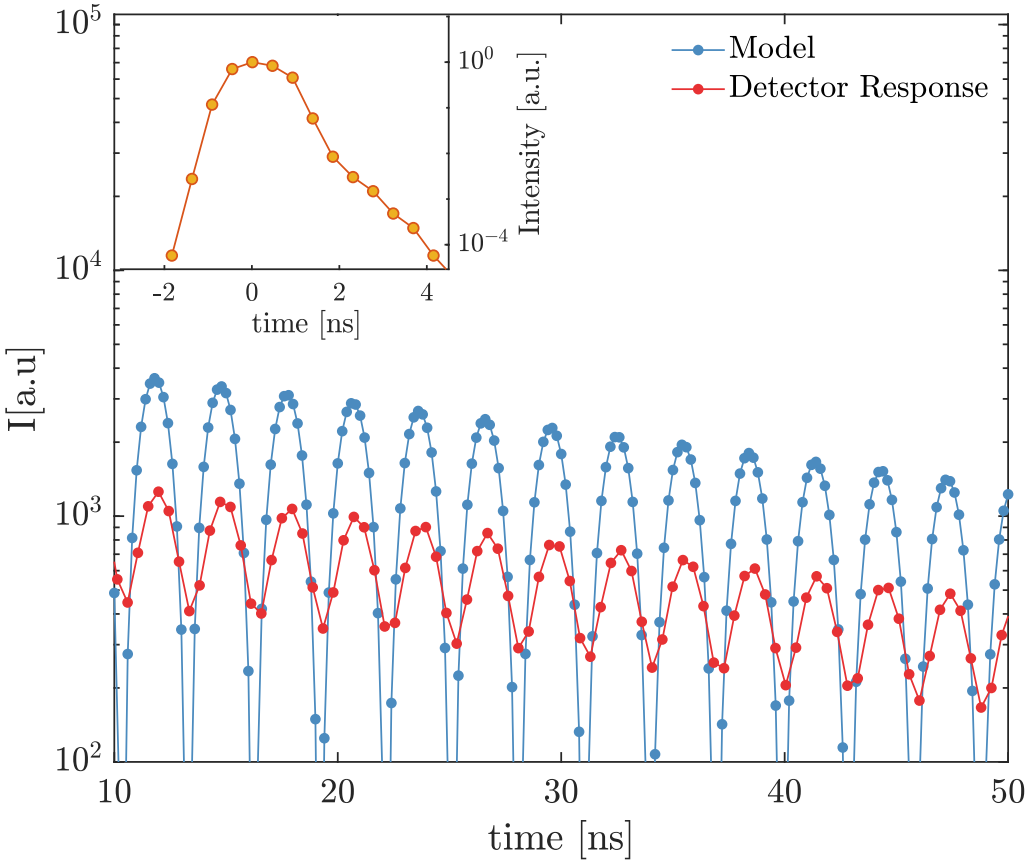

Figure 4.12: Effects of the finite time-resolution of the APD detector. Blue solid line with dots: numerically calculated beating pattern. Red solid line with dots: the same curve convolved with the detector response shown in the inset.

Properly accounting for the finite time-response of the APD detectors in crucial to extract correct information from the measured interferograms. As shown in Fig. 4.8-(b), an APD detector has a time-response $A(t)$ of $\lesssim 1ns$, and therefore it strongly influences the shape of the probed beats, which have a duration of few nanoseconds. An efficient way to deal with this issue, during the fitting procedure, is to numerically convolve the model curve calculated using Eq. 3.19 with the detector detector response ($D_A(t)$):

$$\bar{I}' = \bar{I} \otimes D_A(t)\,. \tag{4.12}$$

$D_A(t)$ can be directly measured shining the monochromatized direct beam directly onto the APD detector. In this way $D_A(t)$ also accounts for the

distribution of the arrival times for the SR, which is related to the spatial distribution of the electrons in the bunch. This distribution at the ESRF is expected to be $\simeq$ 100ps. An example of the characteristic time-response of an APD is plotted in the inset of Fig. 4.12. It can be noticed that it is characterized by a complex shape and by tails extending up to few ns.
The effect of a finite detector response is to smear the beating pattern, i.e to reduce its contrast, as it can be easily observed from Fig. 4.12.

4.3.0.2 Distribution of effective thicknesses and inhomogeneous broadening of the nuclear resonance.

Nuclear absorbers, especially the ones made out of pellets, typically present a distribution of thicknesses L and consequently of effective thicknesses T_{eff}. To take into account this aspect, the scattered field has to be averaged over the thickness distribution in the volume of the absorber illuminated by the impinging radiation. In NFS experiments the transverse coherence of the incident X-rays is usually small ($L_T = 1\mu$m) [152]. Consequently the contributions from different regions of the illuminated volume to the total scattered field add up incoherently. In other words, the total intensity emerging from the TDI results from the sum of the intensities emerging from the different regions of the absorber. To perform this average it is required to model the thickness distribution of the target. A possible approach is the one reported in [143], that is a uniform distribution $U(\langle T_{eff}\rangle, w)$ is assumed, with a mean value $\langle T_{eff}\rangle$ and half width at half maximum w. So Eq.3.19 needs to be convoluted with the distribution $U(\langle T_{eff}\rangle, w)$ associated with each of the nuclear absorbers of the interferometer:

$$\bar{I}^T(t) = \bar{I}(t, T_{eff,1}, T_{eff,2}) \otimes U(\langle T_{eff,1}\rangle, w_1) \otimes U(\langle T_{eff,2}\rangle, w_2) \simeq \sum_{j=-N}^{N} \sum_{i=-N}^{N} \bar{I}(t, \langle T_{eff,1}\rangle + \frac{i}{N} w_1, \langle T_{eff,2}\rangle + \frac{j}{N} w_1) \frac{w_1}{2N+1} \frac{w_2}{2N+1} \tag{4.13}$$

In Eq.4.13, the convolution has been approximated by a sum, expanding the integral around the mean value $\langle T\rangle$. The sums are performed over N terms of the distributions that are spaced by $w_{1,2}/(2N+1)$. The presence of a distribution of thicknesses gives rise of a smearing and modification of the dynamical beats which cannot be reproduced assuming a single effective thickness. This can be clearly observed in Fig. 4.13, where the time evolution of the intensity resonantly scattered by a thin foil of $K_2Mg^{57}Fe[CN]_6$ (1 mg of ^{57}Fe per cm^2) is reported.
Another effect which should be included to properly reproduce TDI data is the inhomogeneous broadening of the spectral lines of the absorbers due to external mechanical vibrations and defects in the absorbers. This effect can be described including a fictive relaxation function which causes an additional damping of the beating pattern contrast which is not due to the sample dynamics. To this aim usually a Gaussian damping function

$$F_D(t, \Gamma_D) = e^{(-t\Gamma_{Damp})^2} \tag{4.14}$$

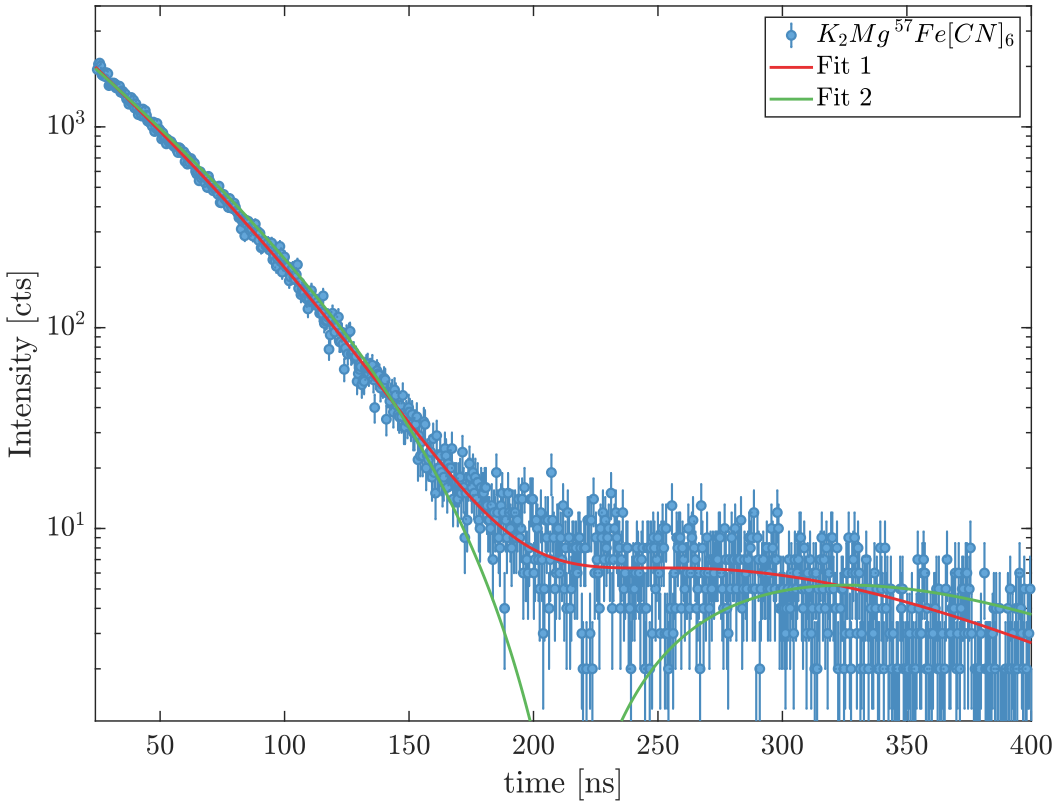

Figure 4.13: Blue dots: time evolution of the nuclear resonant scattering from a single-line nuclear absorber ($K_2Mg^{57}Fe[CN]_6$). Red solid line: curve obtained from fitting Eq.4.13 with $N = 2$ (that is considering $2N + 1 = 5$ terms in each sum) to the experimental data. A distribution of effective thicknesses with a mean-value $\langle T \rangle = 9.76(5)$ and half width at half maximum $w = 3.40(8)$ has been used. Green solid line: curve obtained assuming for the fitting procedure a single-value of effective thickness ($T = 9.80(5)$).

acting on the interference term of the radiation from the upstream and downstream absorbers in Eq. 3.19 is included [14, 134, 143]. Estimating Γ_D is fundamental if we want to detect with accuracy slow relaxation processes. This can be done, for example, analyzing the damping in beating patterns measured from samples at very low-temperatures, that is at temperatures at which the samples are expected to show no dynamics in the time window directly accessed by TDI.

Chapter 5

A microscopic look at the Johari-Goldstein relaxation in two hydrogen-bonded liquids

In this chapter the results obtained from the microscopic investigation of the Johari-Goldstein relaxation in two mono-hydroxyls alcohols are reported. After a brief discussion about the importance of this class of samples for the understanding of the glass-transition, TDI measurement performed on 5-methyl-2-hexanol and 1-propanol are shown along with dielectric spectroscopy data. The latter ones were provided in the framework of a collaboration by Prof. S. Capaccioli and S. Valenti from the Department of Physics of the University of Pisa. The results here described have been presented in [134] and [135].

5.1 Why mono-hydroxyl alcohols?

Monohydroxyl alcohols belong to one of the largest classes of glass-forming materials, that of the hydrogen-bonded liquids, and are characterized by an excellent glass-forming ability. Mono-alcohols started to be investigated already at the end of the 19th century [153] and have always drawn a lot of attention from the scientific community since they are the simplest molecules able to form H-bonds. In fact, their properties, far from being as anomalous as the ones of water, have been studied with the aim of better understanding hydrogen-bonded systems [153]. Since monohydroxyl alcohols are exceptionally polar they have been widely investigated by means of dielectric spectroscopy and the main feature of their DS loss spectra is the presence of an intense and narrow peak with Lorentzian shape (see Fig. 5.1). This is the so-called Debye peak which is typically so intense in DS spectra to partially obscure the ones due to the α or β_{JG} relaxations. The properties of this relaxation, much slower than the α and β_{JG} processes and related to transient supra-molecular structures formed by H-bonding [153], have been the main object of investigations in mono-alcohols since Debye's pioneering studies [154] .
For what concerns the relaxation processes of interest for the glass-transition

and in particular the β_{JG}-relaxation, there is instead little information. It is however known that mono-alcohols, such as the ones here studied, are usually characterized by a genuine β_{JG}-relaxation (as pointed in [155]) and are therefore perfect candidates for addressing its properties.
Most of what is known about the relaxation processes for this class of samples comes from DS and DDLS measurements. In fact, investigations of the β_{JG} relaxation at the microscopic scale have not yet been reported for mono-hydroxyl alcohols and hydrogen-bonded liquids in general. For these reasons,

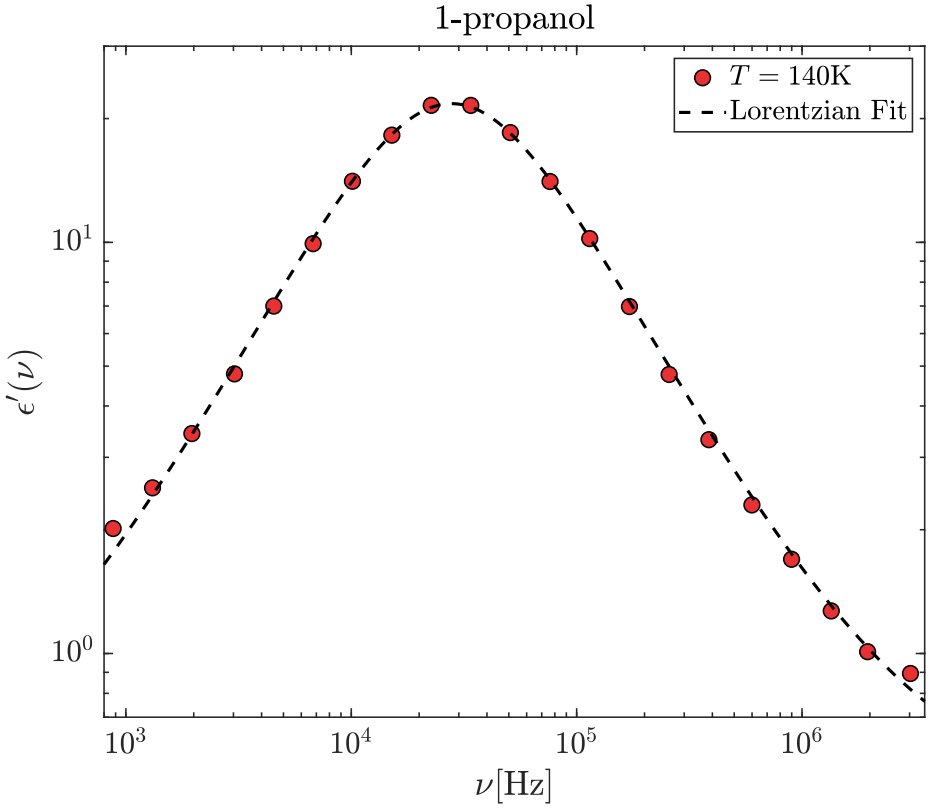

Figure 5.1: Dielectric loss spectrum of 1-propanol at $T = 140$K. Red circles: experimental data. Black dashed line: Lorentzian fit.

two mono-hydroxyl alcohols, namely 5-methyl-2-hexanol and 1-propanol were chosen for the TDI investigations here discussed. They are indeed ideal samples to study the role played by H-bonds on the Johari-Goldstein relaxation and to disentangle which features are universal and which ones depend on the underlying, system-dependent, chemical interactions. Furthermore, 5M2H and 1-propanol exhibit a rather different behavior for what concerns the separation between the timescales of the α- and β_{JG}-relaxation despite belonging to the same class of materials.

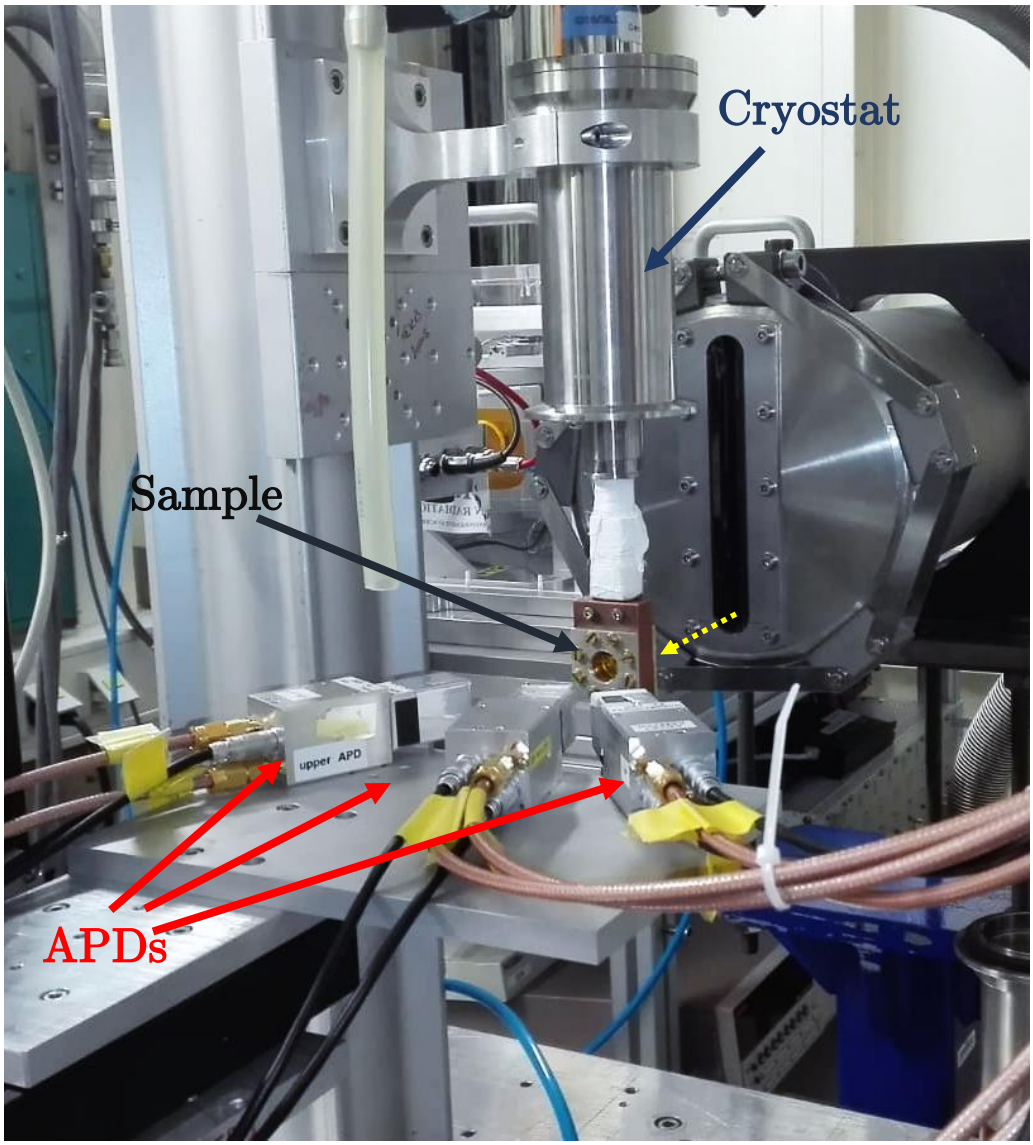

Figure 5.2: Picture of the experimental setup used to collect the TDI beating patterns from 1-propanol and 5-methyl-2-hexanol. The APDs, the sample cell and the cryostat cold-finger are labeled and pointed to by red, black and blue arrows, respectively. The yellow dashed line indicates the beam propagation direction.

5.1.1 Experimental details

The TDI measurements on 5-methyl-2-hexanol and 1-propanol were carried employing the two-lines scheme described in Sec. 3.3.1. The TDI spectra were simultaneously collected at three different scattering vectors employing three independent APDs (see Fig. 5.2). The q-resolution at each scattering angle θ was fixed to $\pm 2\text{nm}^{-1}$ (see Fig. 4.11) using appropriate lead-masks to reduce the active area of each APD. Each APD was equipped with a distinct reference absorber, attached at 1mm from the sensitive area. The single-line reference

and probe nuclear absorbers of the interferometer consisted of pellets made of $K_2Mg\,^{57}Fe[CN]_6$ powder with a surface density of 1 mg of ^{57}Fe per cm^2 ($\langle T_{eff}\rangle = 9.8$). The upstream absorber was driven at a constant velocity of 10mm/s in order to modify its excitation energy with respect to the one of the downstream reference absorbers mounted on the APDs. In this way an energy shift of $\hbar\Omega \simeq 105\Gamma_0$ was obtained. A transducer able to control the absorber motion with an accuracy better than 0.1% was used to reduce as much as possible the blurring of the quantum-beats.
The incident X-ray beam was characterized by a bandwidth of 2.3 meV centered at the energy of the first nuclear transition of ^{57}Fe (see Fig. 4.6-(b)). To this aim a HHLM and HRM were used in cascade in the same configuration as described in Sec. 4.1.3 and shown in Fig. 4.6-(a). The two investigated samples, 5-methyl-2-hexanol (purity $\simeq$ 98%) and 1-propanol (purity > 99%), were purchased from Sigma Aldrich and used without further purification. The sample holders consisted of copper cells with kapton windows, sealed tight with Teflon o-rings suitable for the low temperatures required for observing the slow dynamics of the two alcohols. The temperature of the samples was controlled using a He-flow cryostat, thus introducing the minimum possible amount of vibrations. The temperature stability was ±0.1K.
The TDI measurements were complemented by DS ones, which were performed at Department of Physics of the University of Pisa. The complex permittivity of the samples was measured in the 10mHz-10MHz frequency range employing a lumped impedance technique and the Novocontrol Alpha-Analyzer. Higher frequencies (in the 1MHz-3GHz range) were addressed employing a coaxial reflectometric technique [156] along with the Agilent 8753ES Network Analyzer. Parallel plate capacitors separated by silica spacers were used as dielectric cell and were filled by the sample in the liquid state. A dry nitrogen-flow Quatro cryostat, with a temperature accuracy of better than 0.1K, was used to change and control the sample temperature.

5.2 5-methyl-2-hexanol

5-methyl-2-hexanol (5M2H) (T_g = 154K) is a secondary alcohol (see Fig.5.3-(a)) with three methyl-groups and a OH-group located at the end of the alkyl-chain. The peak of its structure factor is at q_{max} = 14nm^{-1}, whereas at smaller q-values it is possible to observe the presence the pre-peak characteristic of mono-hydroxyl alcohols [153] (see Fig.5.3-(b)). This small molecule, as already said, has a genuine β_{JG} relaxation [155]. Its τ indeed displays a strong pressure dependence and the activation energy shows a clear change on crossing T_g [157]. As clarified in Ch. 2, both are evidences of a close connection to the α relaxation. 5M2H, differently from other already studied systems such as OTP [11, 12] or polybutadiene [13], is characterized by β_{JG} relaxation which is strongly separated in timescale from the α one already above T_g [155, 157] (see Fig. 5.4 for an example) and it is therefore suitable for the TDI dynamic range.

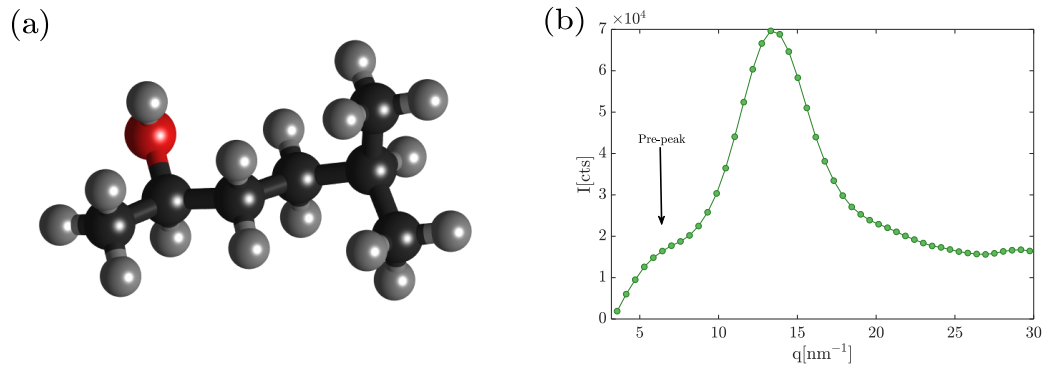

Figure 5.3: (a): chemical structure of 5-methyl-2-hexanol (5M2H). Black spheres: carbon atoms; gray spheres: hydrogen atoms, red sphere: oxygen atom. (b): diffuse scattering intensity of 5M2H measured at $T = 140.0$K as a function of q.

5.2.1 Dielectric spectroscopy data

The dielectric spectroscopy measurements were analysed simultaneous fitting the real and imaginary part of the permittivity, $\epsilon'(\nu)$ and $\epsilon''(\nu)$, where ν is the frequency. The model function employed for the fits is:

$$\epsilon(\nu) = \frac{\Delta\epsilon_D}{1 - i2\pi\nu\tau_D} + \Delta\epsilon_\alpha \mathcal{L}_{-i2\pi\nu}\left\{-\frac{d}{dt}exp\left[-\left(\frac{t}{\tau_\alpha}\right)^{\beta_{KWW}}\right]\right\} + \\ + \frac{\Delta\epsilon_{\beta_{JG}}}{1 + (-i2\pi\nu\tau_\beta)^a} + \frac{\sigma}{-i2\pi\nu\epsilon_0} + \epsilon_\infty \,. \tag{5.1}$$

Here the first Lorentzian term accounts for the Debye relaxation; the second term, i. e. the Kohlrausch-Williams-Watts (KWW) model is for the α-relaxation; the third one is the Cole-Cole function and describes the β_{JG}-relaxation. The fourth and fifth terms account for the d.c. conductivity contribution and the induced polarization dielectric constant, respectively. The dielectric relaxation strengths of the different processes are indicated by $\Delta\epsilon_{D,\alpha,\beta_{JG}}$. $\mathcal{L}_{j2\pi\nu}\{\}$ is the Laplace transform evaluated at $j2\pi\nu$. A more detailed description of these models can be retrieved in [47].
Fig. 5.4 shows an example of a dielectric spectroscopy loss spectrum of 5-methyl-2-hexanol and of the curves obtained from the fitting procedure. In addition to the best-fit (orange solid lines), the contributions of the single relaxation processes are also reported: the black dotted-dashed line is the the Debye relaxation, the blue dotted-dashed line the α relaxation and the green dotted-dashed line is β_{JG} one.

5.2.2 Analysis of the quantum-beats patterns

The time evolution of the collected TDI beating patterns was analysed according to Eq. 3.22, introduced in Sec. 3.3.1 of Ch. 3. To model the contrast function

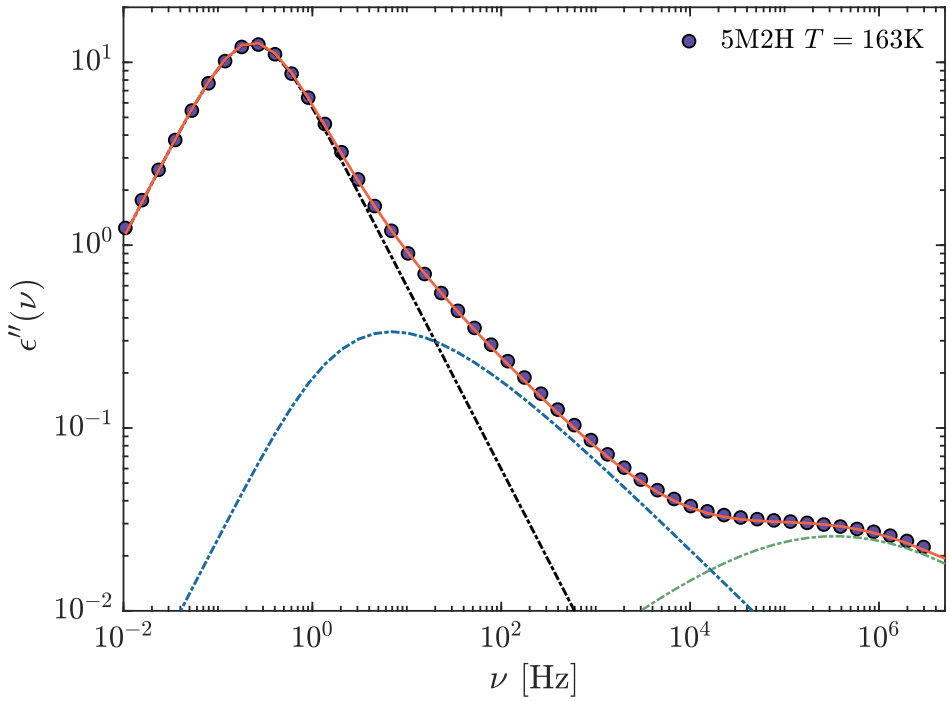

Figure 5.4: Dielectric loss spectrum of 5-methyl-2-hexanol measured at a temperature of 163 K. Blue circles: experimental data; orange solid line: curve obtained from the fit of Eq. 5.1 to the spectrum; black dashed-dotted line: Debye peak; blue dashed-dotted line: structural relaxation; green dashed-dotted line: Johari-Goldstein relaxation.

$\phi'_{\mathbf{q}}(t)$ the KWW model [4] was used:

$$\phi'(\mathbf{q},t) = f'_{\mathbf{q}} \exp\left[-\left(\frac{t}{\tau(\mathbf{q},t)}\right)^{\beta_{KWW}}\right], \tag{5.2}$$

where β_{KWW} is the stretching parameter, τ the relaxation time and $f'(q)$ is the initial beating contrast (i. e. at $t \to 0$). f'_q is related to the relaxation strength (f_q) via

$$f'_q = \frac{2}{1+f_{\Delta E}} f_q\,. \tag{5.3}$$

The parameters describing the beating patterns properties, such as the absorber thickness and the beating frequency, were fixed from the data collected at low T ($T = 25.0$, 47.8K) and at $q = 13, 24, 37\text{nm}^{-1}$. In this q-T range no sample dynamics was indeed expected in the time-window accessed by TDI and this allowed us to precisely estimate the fictive Gaussian damping, which resulted to be equal to $\Gamma_D = 0.27\Gamma_0$.
The TDI beating patterns measured at higher temperatures, that is in presence of relaxation processes, were fitted leaving as free parameters only τ and f'_q. In fact, the accuracy of the experimental data did not allow us to simultaneous

estimate also β_{KWW}: this last parameter was then fixed according to the following procedure. The stretching parameters resulting from the analysis of the DS measurements were used to represent the shape of the relaxation processes at the macroscopic ($q = 0$) length-scale. To describe instead the dynamics at larger scattering vectors, these macroscopic values were rescaled according to the results of a numerical simulation of a model hydrogen-bonded system [59] and of a model rigid molecule [60]. More precisely, the β_{KWW} was fixed to 0.51 for all scattering vectors $q > 13nm^{-1}$, that is to the value found for the α-relaxation by the DS measurements. At $q = 13\text{nm}^{-1}$, which is close to the maximum of the static structure factor in 5M2H ($q_{max} = 14nm^{-1}$), β_{KWW} was instead increased by $\simeq 20\%$ with respect to the DS value and so fixed to 0.61. In this way we accounted for De-Gennes narrowing effects occurring at q_{max}. To test this assumption, the TDI beating patterns collected at $q = 13\text{nm}^{-1}$ and

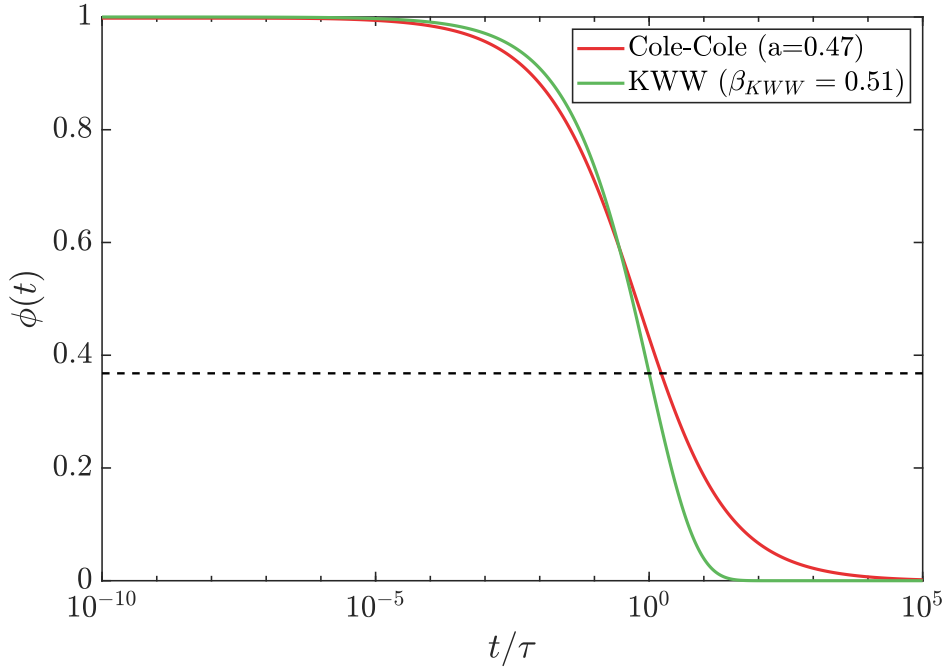

Figure 5.5: Green solid line: KWW relaxation function $\phi \propto exp[-(t/\tau)^{\beta_{KWW}}]$ with $\beta_{KWW} = 0.51$ and $\tau = 1$. Red solid line: Relaxation function corresponding to the Cole-Cole susceptibility, $\chi'' \propto \frac{1}{1+(-i\omega\tau)^a}$, with $a = 0.47$ and $\tau = 1$. Horizontal black dashed line: $1/e$.

.

206 K$> T >$ 192 K were analyzed leaving as free parameter also β_{KWW}. In fact, in this temperature range an entire decorrelation of the contrast function could be observed. Following this procedure an average value of $\beta_{KWW} = 0.7(3)$ was estimated, compatible with the assumption of 0.61 at q_{max} introduced above. It is important to stress that a stretched exponential was used in the whole investigated temperature range, including the T's where the β_{JG} process was detected (more details in Sec. 5.2.3). This approximation, common in

TDI experiments on glass-formers [11–13], was used in order to introduce a minimal amount of bias into the analysis of the experimental data. However,

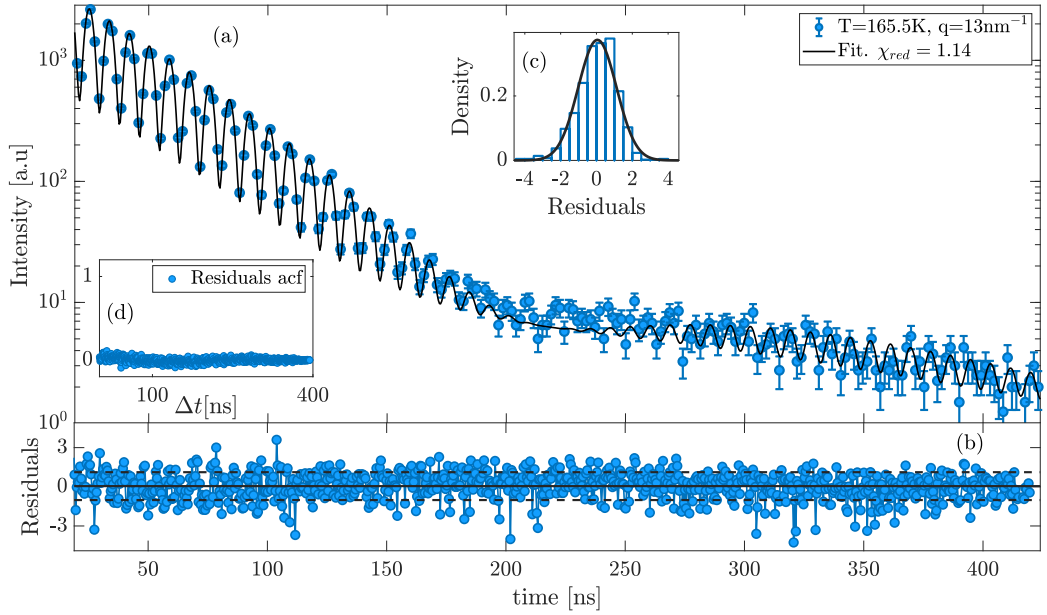

Figure 5.6: Time evolution of the TDI beating pattern of 5-methyl-2-hexanol at $T = 165.5$ K and scattering wavevector q=13 nm^{-1}. (a): blue circles with errorbars: experimental data. To improve the figure readability the data have been binned over a time range $\pm 0.7ns$. Black solid line: model curve obtained from the fitting procedure; (b). Blue circles connected by solid lines: residuals of the fit normalized with respect to the standard deviation. Black solid line: mean of the residual distribution. Black dashed lines: standard deviation of the distribution of the residuals. (c). Blue bars: histogram of the residuals normalized in area. Black solid line: curve obtained from fitting a Gaussian to the histogram of the residuals. (d). Blue circles: calculated auto-correlation function of the normalized residuals.

we also notice that even in the case in which density fluctuations within the β_{JG}-relaxation were described by a Cole-Cole susceptibility with the same shape parameter as in dielectric spectroscopy (a=0.47), the corresponding relaxation function would not differ much from the KWW one up to $t \simeq \tau$, i.e. by less than 20% (see Fig. 5.5). Two examples of TDI beating patterns, measured at two different q-values (13nm^{-1}, 24nm^{-1}) and temperatures (165.5K, 175.1K) are reported in Fig.5.6-(a) and Fig. 5.7-(a) along with the curves obtained from the fitting procedure. The normalized residuals of the fits, here defined as the difference between the experimental data and the model curve divided by the standard deviation, are instead shown in Fig. 5.6-(b) and Fig. 5.7-(b) and it can be noticed (panels (c)) that they are distributed according to a Gaussian with 0 mean and standard deviation equal to 1. The auto-correlation functions plotted in Fig. 5.6-(d) and Fig. 5.7-(d) instead clearly indicate that no correlation between the residuals is present.

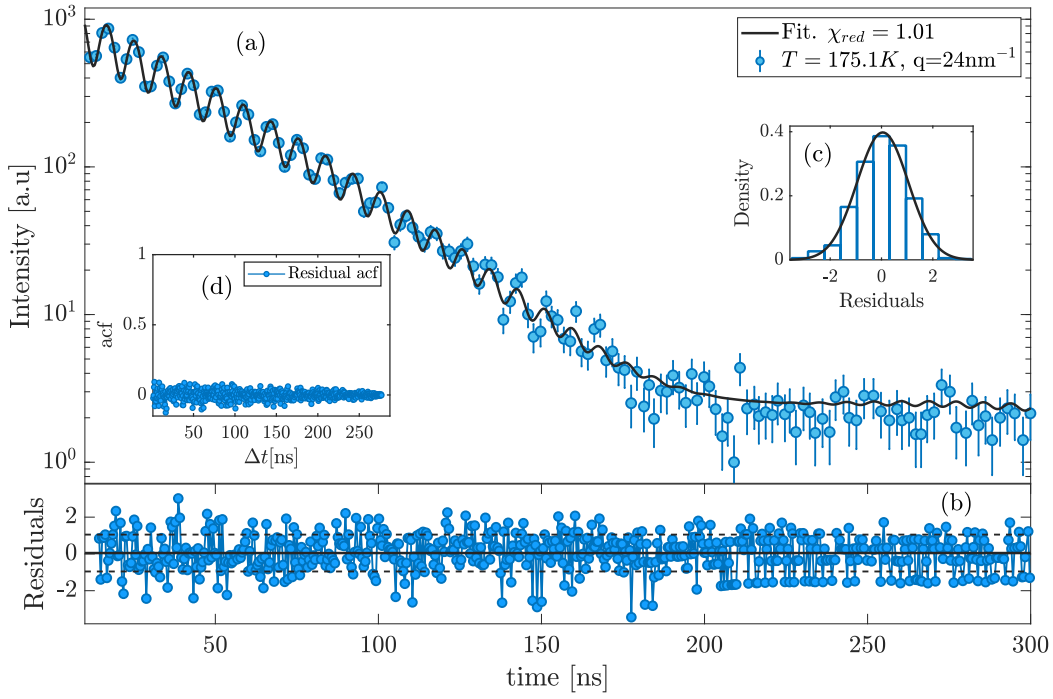

Figure 5.7: Time evolution of the TDI interferogram of 5-methyl-2-hexanol at a temperature of $T = 175.1$ K and scattering wave-vector $q = 24\text{nm}^{-1}$. Same plots and symbols as in Fig. 5.6, except for the averaging window of the experimental data, which was in this case ± 0.9ns

It can be therefore concluded that the used models and assumptions allow us to well describe the experimental data. Similar results were obtained for all the data-sets.

5.2.3 Relaxation map and initial beating-pattern contrast

The temperature dependence of the relaxation time was initially investigated. To this aim, the microscopic dynamics of 5M2H was studied in the temperature range going from 206.8K to 155K (T_g) and at three different q-values corresponding to the inter-molecular distance $q = 13\text{nm}^{-1}$ and two intra-molecular ones ($q = 24, 37\text{nm}^{-1}$). Some of the measured beating patterns are reported in Fig. 5.8 along with the contrast functions calculated from the fitting parameters (black solid line). The data in panel (a) were measured at the same temperature ($T = 175.1$K) but at different scattering vectors in the [13nm^{-1}-37nm^{-1}] range. The patterns in panel (b) were instead measured at a fixed q ($q = 13\text{nm}^{-1}$) but different T's. The contrast of the QB is clearly modulated by the sample dynamics as signaled by its sensitivity to changes in both T and q.
The extracted relaxation times are plotted in Fig. 5.9 along with the ones from DS. As an example also the distributions of the natural logarithm of the

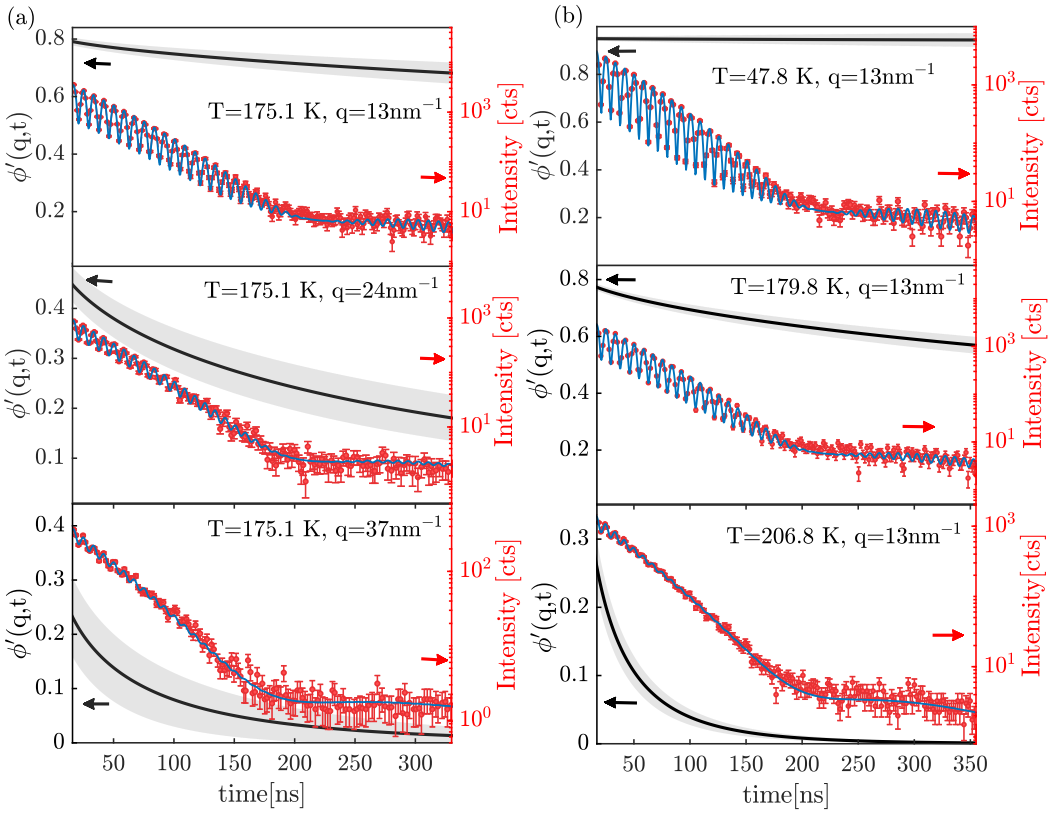

Figure 5.8: Time evolution of the TDI beating patterns as a function of time (points with errorbars) at different exchanged wave-numbers q and at the same temperature T=175.1 K in the supercooled state (a) and at different temperatures at the same q=13 nm^{-1} close to the inter-molecular distance (b). The experimental data have been averaged over a time range ±0.7 and ±0.9 ns, depending on the collected statistics, to improve the figure readability. The blue-solid lines (right y-scale) are the model curves obtained from the fitting procedure to the data whereas the black solid lines (left y-scale) are the contrast functions, calculated from the fitting parameters along with the 68% confidence intervals (gray area).

relaxation times $G(\ln\tau)$ from the DS measurements for the α and β_{JG} are shown at T =168 K (violet and red areas delimited by solid lines). The characteristic T-dependencies of the α and β_{JG} relaxation times were deduced from the DS data (violet and red diamonds, respectively). The α-relaxation characteristic time was fitted using the Vogel-Fulcher-Tammann (VFT) expression $\tau = \tau_0 \exp\left(DT_0/(T-T_0)\right)$, where τ_0, D and T_0 are phenomenological parameters (violet dash-dotted line). The found parameters (D=12(2), τ_0=$10^{-12.8(9)}$ s and T_0=112(5) K) are consistent with the ones from the literature [157]. The Arrhenius equation was instead used for the T-dependence of the β_{JG}-relaxation (red dash-dotted line). The reduced activation energy found here (E/k_B=3.3(1)×10^3 K) is in agreement with the one extracted in Ref. [50]. Concerning the TDI data, the α and β_{JG} processes were instead identified

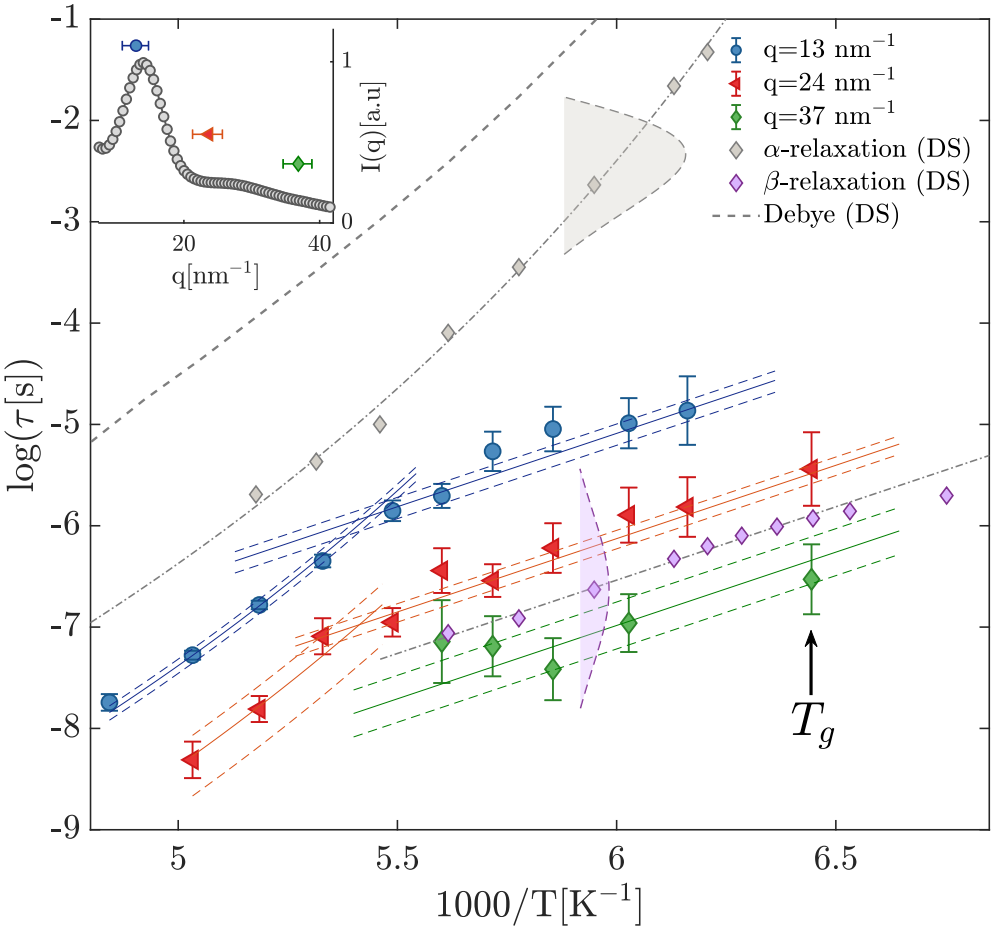

Figure 5.9: Temperature dependence of the relaxation time measured by TDI at different q-values: q=13 (blue circles), 24 (red left-pointing triangle) and 37 nm^{-1} (green diamonds) and by dielectric spectroscopy (violet and red diamonds). The fits to the DS data are reported as dotted-dashed lines (α and β_{JG} relaxation). The gray dashed line is the T-dependence of the characteristic timescale of the Debye process, detected only by DS. The solid lines are the fitting curves for the α and β_{JG} relaxations as obtained from DS and re-scaled to match the TDI data. The dashed lines are the corresponding 95% confidence intervals. The violet and red areas at $1000/T$=5.95 K^{-1} show the typical shapes of the distributions of relaxation times $G(\ln\tau)$ of the α and β_{JG} relaxations as extracted from DS spectra. The base widths of the two areas correspond to the FWHM of the two distributions. Inset: diffuse scattering pattern of 5M2H at T=187.6 K, with the indication of the q values and of the corresponding ranges covered in the TDI measurements reported in the main figure.

scaling the curves obtained from the DS measurements (solid lines in Fig. 5.9). The dashed-lines show the 95% confidence bands. It is evident from Fig. 5.9 that the α-relaxation dominates density fluctuations for $T > T_{\alpha\beta} \simeq 181$ K at q=13 and 24 nm^{-1}. At q=37 nm^{-1} the relaxations are instead too fast to be detected by TDI in such a temperature range. A change in the T-dependence

of the relaxation times occurs below $T_{\alpha\beta}$. The new temperature dependence is in close agreement with the one expected for the β_{JG}-relaxation.
It is also important to notice that after the β_{JG} process has separated from the α one, i.e below $T_{\alpha\beta}$, the dynamics of the sample at q=13 and 24 nm^{-1} is already so slow that the beating patterns do not completely decorrelate within the time-window directly accessed by TDI. As a consequence, here TDI probes only the faster of the two relaxation processes, which in this case is the β_{JG} one. Therefore the strengths of the α and β_{JG} processes cannot be separated. Naturally, the α and β_{JG} relaxations should coexist in the probed time-window close to the decoupling temperature ($T \simeq T_{\alpha\beta}$). However the accuracy of the experimental data does not allow us to disentangle the two.
At q=37 nm^{-1}, density fluctuations almost completely decorrelate even below $T_{\alpha\beta}$ (see Fig. 5.8-(a) for an example). This implies that at this large q the β_{JG} relaxation dominates the de-correlation process and its strength is much larger than that of the structural relaxation. It is also interesting that in 5M2H the β_{JG} relaxation is present also at the inter-molecular distance $2\pi/q_{max} \simeq 4.5$ Å. This is different from what has been previously observed in TDI measurements of OTP [11] and TDI and neutron scattering measurements of polybutadiene [13, 101, 103]. We can furthermore observe that the decoupling of the β_{JG} from the α process occurs at a temperature $T_{\alpha\beta} \simeq 181$ K close to 1.2 T_g: this is the typical value for the mode coupling critical temperature T_c. This is in agreement to what observed in OTP [11] and PB [13].
Another remarkable feature which can be grasped from Fig. 5.9, is that the characteristic time scales for the α and β_{JG} relaxations measured by TDI are less separated than the ones provided by DS measurements. In fact, molecular reorientations for the β_{JG} process relax almost two orders of magnitude faster than density fluctuations probed by TDI close to the average inter-molecular distance. This means that the centers of mass of two neighboring molecules barely move (one relative to the other) during the time molecular dipoles decorrelate with respect to their initial orientation. On the contrary, the α relaxation for dipole re-orientations is always slower than for density fluctuations.
The Debye relaxation [50, 153] which is much slower than the α process, was instead detected only by DS. For this reason in Fig. 5.9 only its characteristic timescale is reported. It is indeed nowadays established that the Debye relaxation is related to fluctuations of the end-to-end dipole moment of transient supramolecular structures [153] and this process, while being the predominant one in DS spectra, has little or no signature in the spectra of other experimental techniques, namely depolarized light-scattering [49, 50], mechanical spectroscopy [158], triplet solvatation state with mechanical probes [159] as well as in differential scanning calorimetry [160]. In the case of microscopic density fluctuations, neutron scattering experiments on the monohydroxyl alcohol 1-propanol have revealed that at the maximum of $S(q)$ and at the ns-timescale the relaxation dynamics is dominated by the α process [161]. Consistently with these observations, also in the present experiment no process slower than the α relaxation was detected at the probed q's. This can be clearly seen in the TDI

beating pattern measured at q=13 nm^{-1} and T=206.8 K and shown in Fig. 5.8-(b): here, after the structural relaxation has occurred, density fluctuations have completely relaxed. This implies that the Debye process has a negligible strength in the density-density correlation function of 5M2H at the probed length-scales and time-scales. It is worthwhile anticipating that also the TDI measurements on 1-propanol and discussed in Sec. 5.3.1 provide a similar picture to what described here for 5M2H and to what reported in [161].

The initial contrast of the beating pattern f'_q corresponding to the τ values

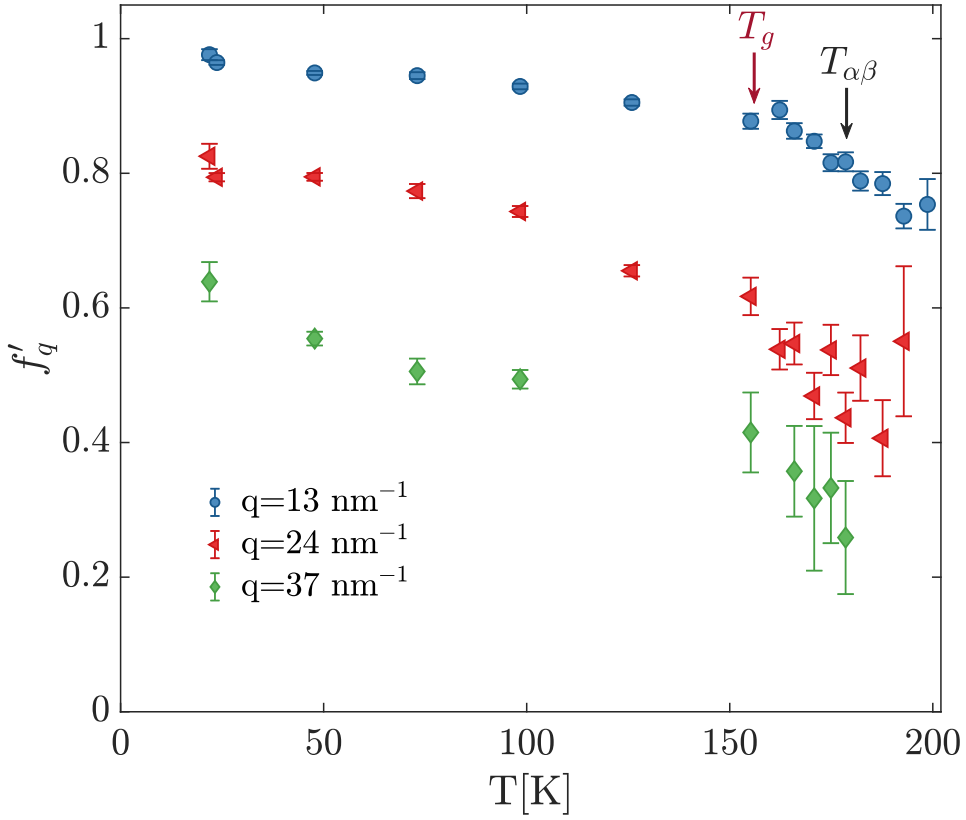

Figure 5.10: Temperature dependence of the initial contrast of the TDI interferograms, f'_q, measured at three different exchanged wave-vectors: 13 (blue circles), 24 (left-pointing red triangles) and 37 nm^{-1} (green diamonds).

shown in Fig. 5.9 is plotted in Fig. 5.10 as a function of T. The f'_q values probed below T_g, where the dynamics is too slow for TDI, are reported as well. We recall once again that the TDI measurements detect at each T and q only one relaxation process and therefore f'_q is the total strength of the α and β_{JG} processes. A clear change in the T-dependence of f'_q can be observed for all q values around T_g=154 K, that is when the glass transition takes place. Conversely no discontinuity is observed when the β_{JG}-relaxation separates from the structural one at $T_{\alpha\beta}$=181 K. This result is consistent with DS and depolarized dynamic light scattering measurements showing that the total relaxation

strength is not subjected to any discontinuity at the temperature at which the β_{JG} process decouples from the α one [49, 50]. It is important to point out that also at 37 nm^{-1}, where the β_{JG} relaxation dominates density fluctuations, the contrast changes its temperature dependence at T_g. This further confirms that the β_{JG} relaxation is indeed highly sensitive to the glass-transition, as already demonstrated for the dielectric strength of the β_{JG} process at T_g [4].
The low temperature dependence of f_q' is another interesting feature to discuss.

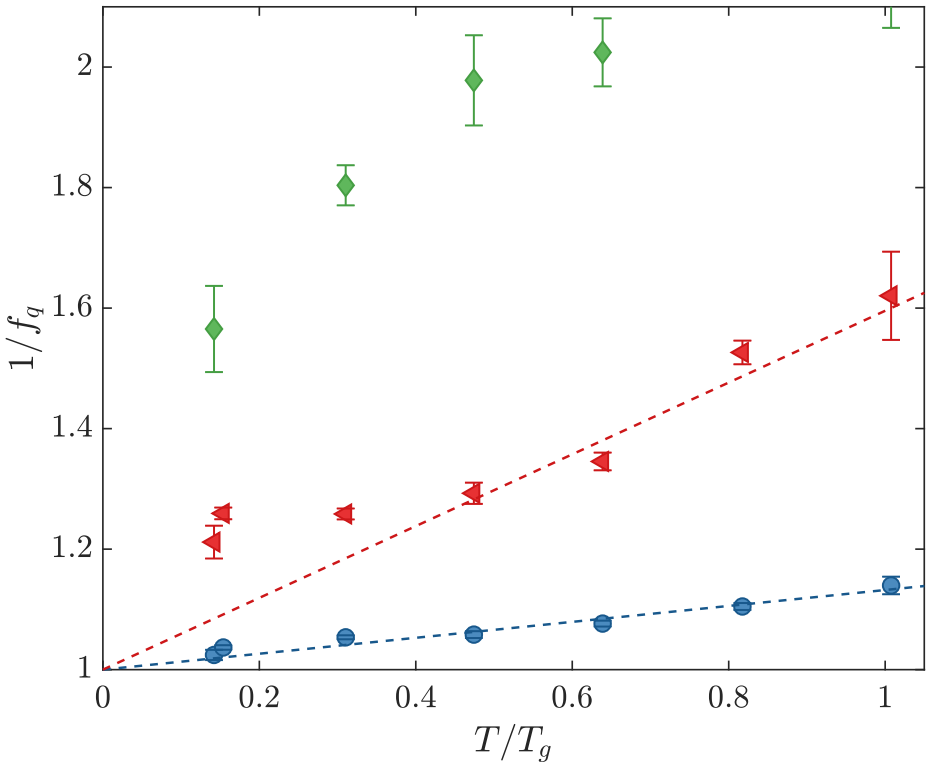

Figure 5.11: The inverse of the initial beating time contrast, f_q' is plotted as a function of T/T_g in order to enlighten its low temperature dependence. The dashed lines are linear fits with intercept at 1. The blue circles, red left pointing triangles, and green diamonds correspond to the values measured at q=13, 24, 37 nm^{-1}.

This is reported in Fig. 5.11, where $1/f_q'$ is plotted in the glassy state for the three probed q-values as a function of the reduced temperature T/T_g.
Classically, it can be demonstrated that, in the framework of the harmonic approximation, the inverse of the total relaxation strength (in this case due to the sum of the α and β_{JG} processes) should reach 1 as T goes to 0 K [162]. This is expected to hold also for $1/f_q'$. In fact $f_{\Delta E}$ should approach f_q at sufficiently low T as it is related to vibrations and fast relaxations occurring at energies of the order of few meV. The strength of these processes indeed depend at most linearly on T [56, 57, 61] and so $f_{\Delta E} - f_q$ should become quickly negligible at sufficiently low temperatures. This has been already observed for glycerol [14]

and demonstrated, within the work of this thesis, also for OTP (more details in Ch. 6).
$1/f_q'$ at $q = 13\text{nm}^{-1}$ and below T_g actually scales linearly with T. Concerning the larger q's, it can be noticed that at 24nm^{-1} the linear T-scaling holds only above 70K, whereas at 37nm^{-1} there is no temperature range where this is verified. An explanation for these observations can be found if the zero-point motions of the molecules are considered. The temperature at which zero-point vibrations start to play a role is determined by the frequency of the dominant vibrational mode, which depends on q according the characteristic dispersion relation of the system. Dispersion curves in liquids and amorphous systems typically display a sinusoidal oscillation over-imposed on a trend that increases as a function of q [163–165]. Furthermore this q-dependence usually has a first minimum at the end of the first pseudo-Brillouin zone [163–165], which here is at q_{max}=14nm^{-1}. So, above q_{max}, the larger the q the higher the temperature at which zero-point effects become important, consistently with the behavior here observed.

5.2.4 q-dependence

To gain further insights on the microscopic mechanisms underlying the α and β_{JG} processes in 5M2H, the q-dependence of the relaxation parameters was investigated at three temperatures: one (T = 187.6K) where only the α-relaxation was present and other two well below $T_{\alpha\beta} = 181$K (T=170.4 and 165.5 K) where TDI was sensitive only to the β_{JG} process. The q-dependence of f_q', plotted in Fig. 5.12, shows a shallow oscillation which is in phase with the total scattered intensity of the sample. This is consistent with what already observed by simulations [59] and experiments [56] for the α-process and indeed highlights its sensitivity to the microscopic structure.
Above q_{max}, in the q-range from 31 to 40 nm^{-1} and 181 K> T >165 K, density fluctuations relax completely within the experimental time-window and so it can be safely concluded that here the β_{JG} process dominates the slow microscopic dynamics. In that range it is then possible to measure $f_q^{'}$ for the β_{JG} relaxation. Performing an average in the aforementioned q and T intervals a value of $\langle f_q^{'}\rangle_{T,q}$=0.31(2) is found. It is important to remember that $f_q^{'}$ is not the relaxation strength and a proper estimation is possible only if the correction factor in Eq.5.3 is accounted for. To estimate $f_{\Delta E}$ it is necessary to know the integral of the dynamic structure factor of 5-methyl-2-hexanol in the energy range of the bandwidth of the incident X-rays. Since this information is not available, we can use the correction factor measured for glycerol in [14] in a similar q and τ range in order to get f_q. In this way the β_{JG} strength can be estimated and results to be $\simeq 0.25$ while that of the α relaxation is negligible. So, If we imagine to take a snapshot of the system at the intra-molecular scale, we would observe that about a quarter of the molecules relaxes, on average, through the β_{JG} process whereas the remaining fraction decorrelates because of faster processes such as the fast relaxations and vibrations, which account for

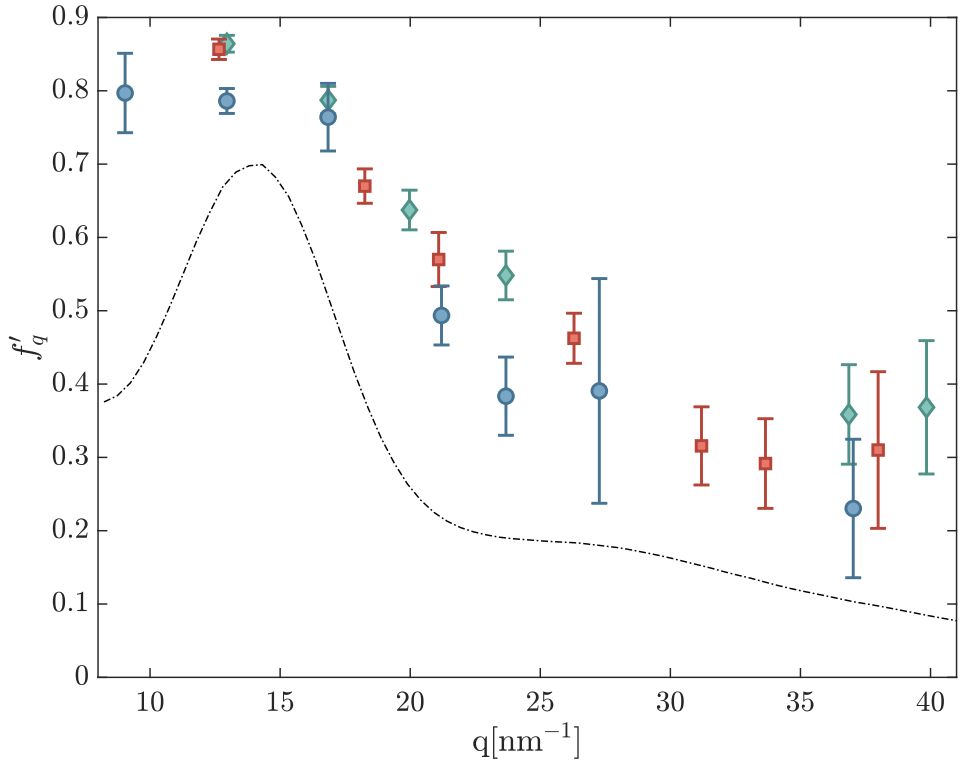

Figure 5.12: Wave-number (q) dependence of the initial beating pattern contrast at three different temperatures: T=187.6 K (blue circles), 170.4 K (red squares) and 165.5 K (cyan diamonds). The diffuse scattering pattern measured at T=187.6 K is rescaled and reported on the same axes for the sake of comparison.

the reaming strength. At that scale a negligible amount of molecules participate instead to the α-relaxation. Naturally, if the system evolution is followed over a long enough period, all molecules will eventually take part to the β_{JG} relaxation. To the best of our knowledge, this is the first time that the strength of the β_{JG} process is probed via density fluctuations, even though this is limited to only one average value in the aforementioned T and q-range.
Fig. 5.13 shows the q-dependence of the relaxation time τ at the three investigated temperatures. Fig. 5.13 reports also the relaxation times from DS (τ_{DS}), measured at the same temperature as the TDI ones and for both the α and β_{JG} processes (horizontal lines of the corresponding color). The q-dependence of τ was fitted employing a simple power-law: $\tau \propto q^{-n}$. This simple model well describes the data over the whole q-range which was investigated. It is interesting to notice that a super-quadratic, i.e. $n > 2$, dependence characterizes both relaxations with n=3.2(3) for the α and 4.5(6) and 4.3(4) for the β_{JG} relaxation at the two probed temperatures (see Fig. 5.13-(c)). This result is compatible with what already observed for o-terphenyl [11, 12]: the β_{JG}-relaxation has a distinctive sub-diffusive character.

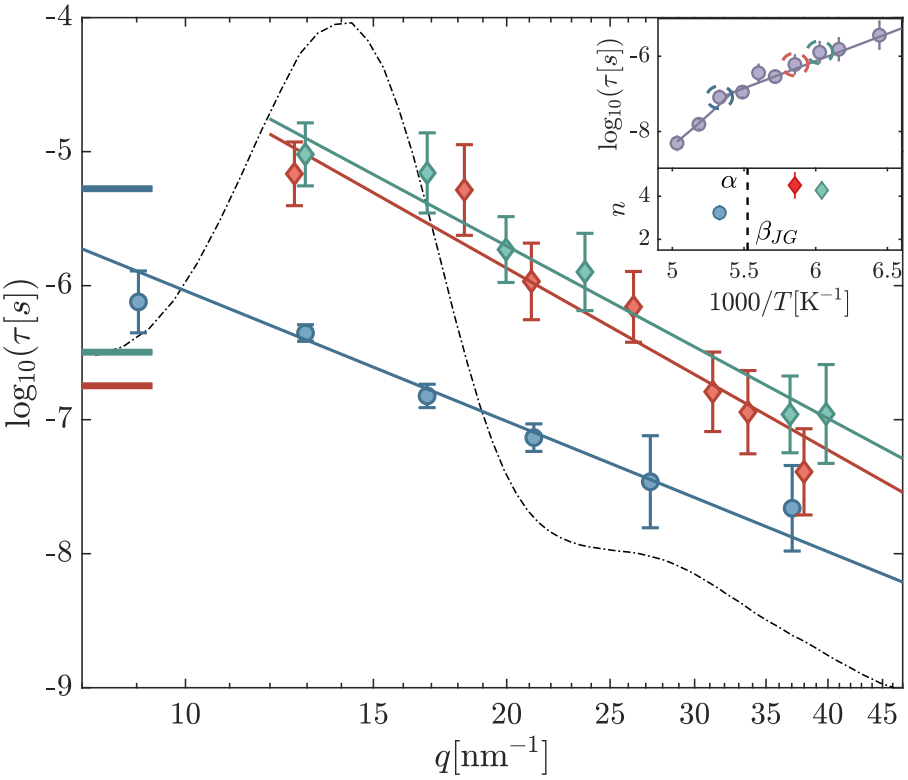

Figure 5.13: (a): Wave-number (q) dependence of the mean relaxation time at three different temperatures T=187.6 K (blue circles), 170.4 K (red squares) and 165.5 K (cyan diamonds). The diffuse scattering pattern measured at T=187.6 K is rescaled and reported on the same axes for the sake of comparison. The horizontal lines signal the corresponding relaxation times obtained from dielectric spectroscopy. The solid lines are power law fits to the data: $\tau \propto q^{-n}$. (b): Temperature dependence of the relaxation time at q=24 nm^{-1}, as in Fig.5.9. The dotted-circles show the temperatures where the q-dependencies were studied. (c): Power-law exponents, n, from the fitted power-law curves shown in (a), as a function of $1000/T$.

5.3 1-propanol

The intriguing picture emerging from the results presented in the previous paragraphs strongly motivates to extend this observations to other samples. The choice, as anticipated in Sec. 5.1, fell on propanol.
1-propanol (T_g = 97K) is a monohydroxyl alcohol whose hydroxyl group, differently from 5M2H, is located at the end of its short alkyl chain (see Fig. 5.14-(a)). 1-propanol has only one methyl-group, located at the opposite side of the chain with respect to the OH-group.
The static structure factor of 1-propanol peaks at q_{max} = 14nm^{-1} at room temperature (Fig.5.14-(b)) and shows a characteristic pre-peak around $\simeq$ 7nm^{-1}. q_{max} shifts at $\simeq$ 15nm^{-1} [166] on approaching T_g. Neutron scattering

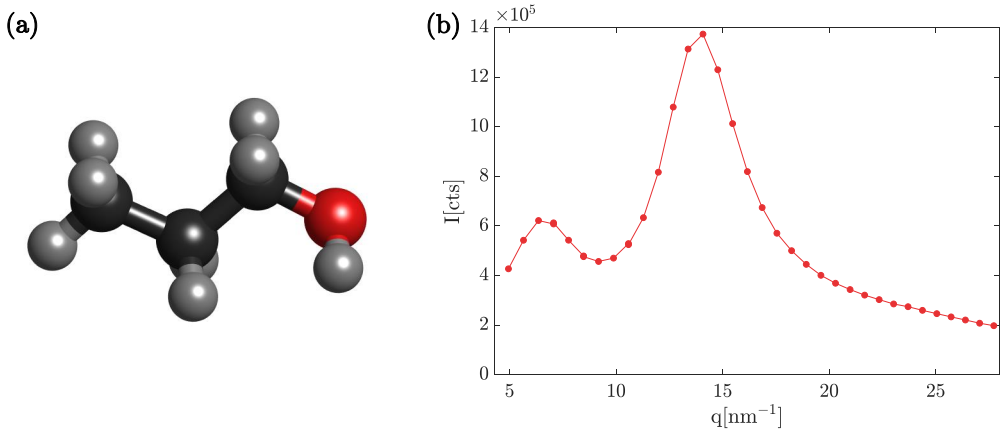

Figure 5.14: (a): chemical structure of 1-propanol. Black spheres: carbon atoms; gray spheres: hydrogen atoms; red sphere: oxygen atom. (b): diffuse scattering intensity of 1-propanol measured at $T = 300.0$K as a function of q.

experiments combined with reverse Monte-Carlo analysis have also revealed that the main peak of $S(q)$ originates from intermolecular correlations between atoms belonging to different alkyl chains [166].

1-propanol, as 5M2H, presents a genuine β_{JG}-relaxation [155] and has been widely investigated by means of several experimental techniques (even though often with a strong focus on its Debye and structural relaxations) [49, 153, 161, 167].

The α and β_{JG} processes in 1-propanol have much closer timescales than in 5-methyl-2-hexanol and the T-dependencies of the two processes are similar above T_g. This can be clearly observed in Fig. 5.15 where the relaxation map of 1-propanol probed by DS is reported in the temperature range going from $1.2T_g$ to $1.45T_g$, which is the range of temperatures where the sample dynamics was accessible by TDI. The T-dependence of the α-relaxation is well described by the VFT equation with the following parameters $D = 28(2)$, $\tau_0 = 10^{-14.4(3)}$s, $T_0 = 57(2)K$ (gray dashed-dotted line) whereas the β_{JG} process displays an Arrhenius dependence with an activation energy $E_{\beta_{JG}}/k_B = 3.86(3) \times 10^3$K (green dashed-dotted line). It is important to notice that this activation energy is larger than the one found in [49]. This difference is explained by the fact that in [49] $E_{\beta_{JG}}$ was estimated considering the relaxation time measured both above T_g, where the activation energy is expected to be larger, and below, where typically $E_{\beta_{JG}}$ becomes smaller.

An example of the DS spectra from which the relaxation times in Fig. 5.15 were estimated can be observed in Fig. 5.16 where the dielectric loss $\epsilon''(\omega)$ at 120 K is plotted. The DS data from 1-propanol were analysed using the same models and procedure as for 5M2H (Eq. 5.1). As it clearly emerges from Fig. 5.16, the spectra of the α and β_{JG} relaxations overlap much more above T_g than in 5M2H.

For what concerns the TDI measurements, they were also analysed employing the models described in Sec. 5.2.2. The β_{KWW} was fixed to 0.66 according to

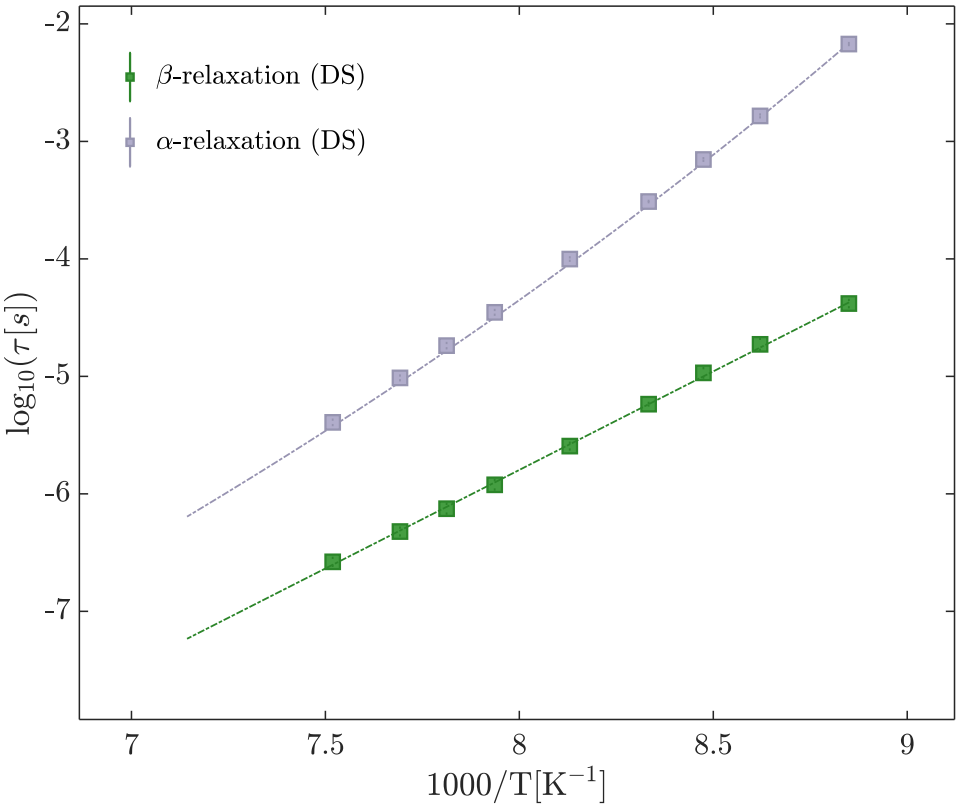

Figure 5.15: Relaxation map of 1-propanol obtained from DS measurements. The gray and green squares are the relaxation times (τ) for the α and β_{JG} process respectively. The dashed-dotted lines of the same color are the corresponding fitting curves, see text for details.

the DS spectra for $q > q_{max}$. At q_{max} the effect of De Gennes narrowing was accounted for and β_{KWW} was fixed to 0.79. As for 5M2H, low temperature TDI beating patterns ($T = 55.3$K) were used to calibrate and fully characterize the reference beating pattern. The quality of the fits was similar to those in 5M2H and some of the measured beating patterns are reported in Fig. 5.17 at different T's and q's.

5.3.1 Relaxation map and initial beating pattern contrast

The dynamics of 1-propanol was studied in the q-range from 9 to 42 nm^{-1}. For what concerns the investigated temperatures, TDI was able to probe the dynamics of 1-propanol only in the 1.45 T_g-1.20 T_g interval: below that temperature the dynamics is too slow for the dynamic range of TDI. In the relaxation map in Fig. 5.18, the τ measured by DS and TDI are both reported. Also the distributions of relaxation times for the α and β_{JG} processes as extracted from the DS spectra are plotted at $T = 133$K and $T = 128$K,

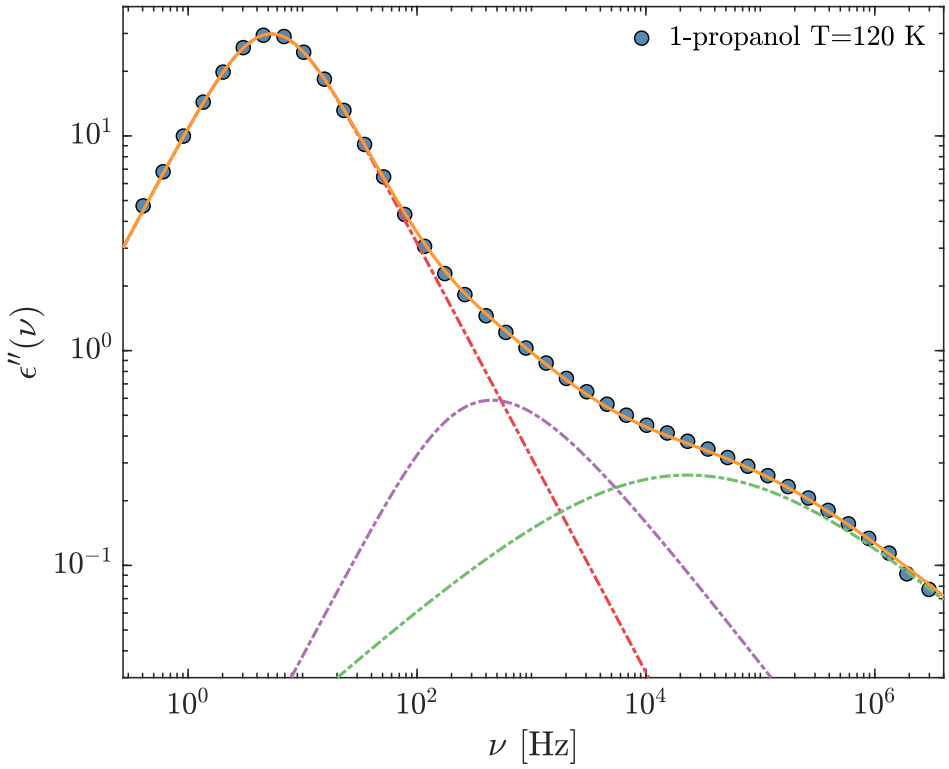

Figure 5.16: Dielectric loss spectrum of 1-propanol measured at a temperature of 120 K. Blue circles: experimental data; orange solid line: curve obtained from the fit of Eq.5.1 to the spectrum; red dashed-dotted line: Debye peak; violet dashed-dotted line: structural relaxation; green dashed-dotted line: Johari-Goldstein relaxation.

respectively. The T-dependence of the TDI data was studied at two q-values, one corresponding to the average inter-molecular distance $q_{max} = 15\text{nm}^{-1}$ (blue diamonds) and the other at the intra-molecular one $q = 25\text{nm}^{-1}$ (red diamonds). The T-dependence of the relaxation times from the DS experiment was re-scaled on the TDI data in order to identify the α and the β_{JG} processes. It is more difficult to distinguish them in 1-propanol than in 5-methyl-2-hexanol as the two process display: i) much closer time-scales and ii) more similar temperature dependencies above T_g. Nonetheless we can notice that a clear change in the T-dependence of the relaxation time occurs around $T = 131.4\text{K}$ and at $q = 25\text{nm}^{-1}$. At $q = 15\text{nm}^{-1}$ this crossover from the structural to the Johari-Goldstein process is instead weaker. Interestingly, at $q = 15\text{nm}^{-1}$ the T-dependence of τ can also be described accounting only for the β_{JG}; a similar match cannot be obtained instead accounting only for the α process. It is then clear that, at least below $T = 131.4\text{K}$, TDI is sensitive to the β_{JG} process both at the inter and intra- molecular scale.
The Debye process, as for 5-methyl-2-hexanol, was detected only by DS and no process slower than the α-relaxation appears in the TDI dynamic range. This

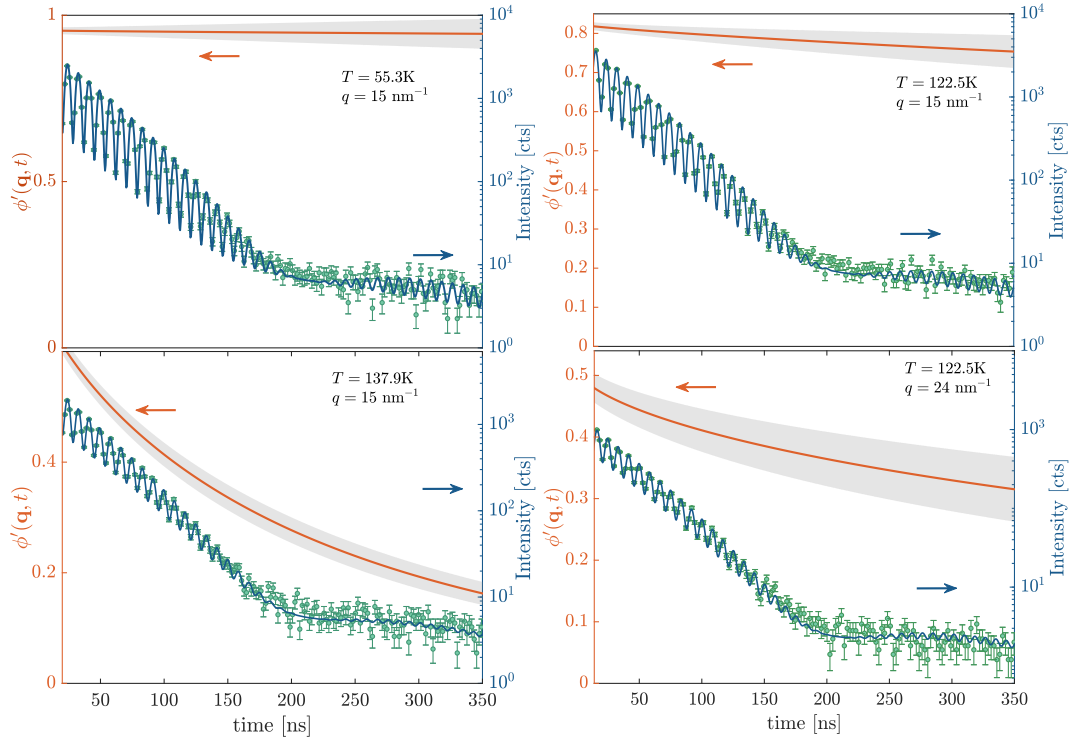

Figure 5.17: Time evolution of the TDI beating patterns as a function of time (points with errorbars) at different temperatures T and at the same exchanged wave-vector q=15nm^{-1}, close to the average intermolecular distance (a) and at different exchanged wave-vectors at the same T=122.5K in the supercooled state (b). The experimental data have been averaged over a time range ±0.7 and ±0.9 ns, depending on the collected statistics, to improve the figure readability. The blue-solid lines (right y-scale) are the model curves obtained from the fitting procedure to the data whereas the orange solid lines (left y-scale) are the contrast functions, calculated from the fitting parameters, along with the 68% confidence intervals (gray area).

observation agrees with what already observed by QENS measurements on 1-propanol performed in the same q-range as for the TDI measurements but at higher temperatures [161]. It also important to notice that the T-dependence of τ for the α relaxation resulting from such QENS experiments [161] nicely extrapolates to the one here reported (see Fig. 5.19) at the same $q = 15\text{nm}^{-1}$. As for 5M2H, it was possible to probe one relaxation process at each q and T value. Even though around $T \simeq 132$ K the two processes should coexist in the time-window of the TDI experiment, the accuracy of the experimental data was not enough to discriminate between the two. Additionally, the dynamics becomes already too slow to detect a complete decorrelation in the beating pattern at $T = 131.4$K.

It is important to point out that from the comparison between the characteristic time-scales extracted by DS and TDI a picture similar to the one observed in

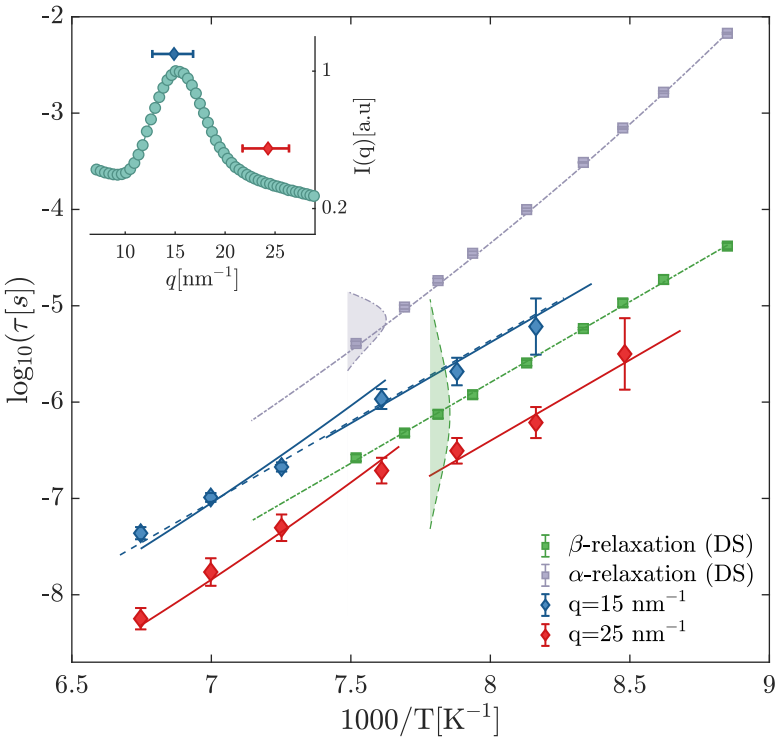

Figure 5.18: Temperature dependence of the relaxation time measured by TDI at different q-values: q=15 (blue diamonds) and 25 nm^{-1} (red diamonds). The relaxation time measured by dielectric spectroscopy are plotted as well. (gray and green squares). The fits to the DS data are reported as dotted-dashed lines (α and β_{JG} relaxation). The solid lines are the fitting curves for the α and β_{JG} relaxations as obtained from DS and re-scaled to match the TDI data. The blue dashed-line is the fitting curve obtained from the T-dependence of the β_{JG}-process rescaled in order to match the τ's at q = 15nm^{-1} over the whole temperature range. The gray and green areas at $1000/T$=7.52 K^{-1} and $1000/T$=7.81 K^{-1}, respectively, show the typical shapes of the distributions of relaxation times $G(\ln\tau)$ of the α and β_{JG} relaxations as extracted from the DS spectra. The base widths of the two areas correspond to the FWHM of the two distributions. Inset: diffuse scattering pattern of 1-propanol at T=122.5 K, with the indication of the q values and of the corresponding ranges covered in the TDI measurements reported in the main figure.

5M2H emerges. For instance, re-orientations within the structural relaxation are always slower than density fluctuations, even when probed at the maximum of the $S(q)$. On the contrary, density fluctuations within the β_{JG}-relaxation are slower than re-orientations at q_{max} and faster at 25nm^{-1}. Differently to the case of 5M2H this cross-over occurs closer to q_{max}.
The f'_q corresponding to the τ's in Fig. 5.18 are plotted in Fig. 5.20 along with the initial contrasts extracted at lower temperatures, where the dynamics

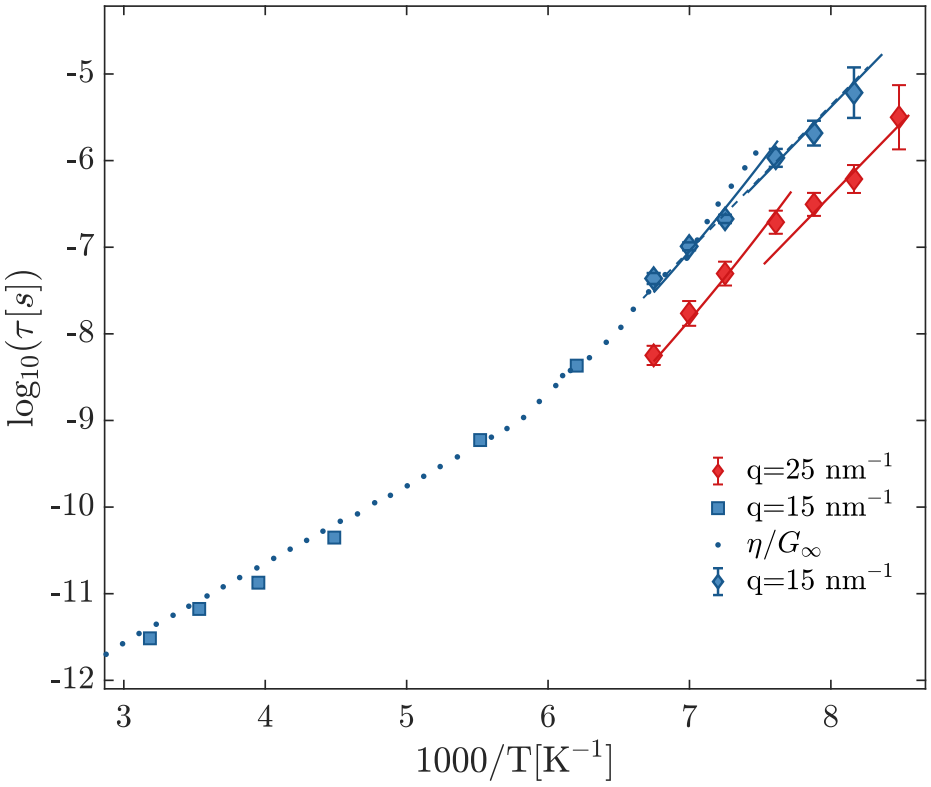

Figure 5.19: Comparison between coherent QENS and TDI data. Blue and red diamonds: same as in Fig. 5.18. Blue squares: τ measured at q_{max} of 1-propanol by QENS [161]. Blue dots: scaled shear viscosity as reported in [161].

is too slow to be probed by TDI. The f_q''s extracted from the calibration interferograms measured at 50 K are not reported in Fig. 5.20 as they were collected at slightly different q-values with respect to the ones reported in Fig. 5.20. Here, f_q' accounts for both the α and the β_{JG} processes as for 5-methyl-2-hexanol and, analogously to that case, its T-dependence shows a discontinuity at T_g but not around 131 K: the total strength, given by the sum of the two processes, is conserved. Unfortunately, in 1-propanol the β_{JG}-process separates from the structural one when its characteristic time is already too slow to observe a complete damping of the beating pattern in the time-window directly accessible by TDI, and therefore no absolute strength for the β_{JG} process was in this case estimated.

5.3.2 q-dependence

The q-dependence of the relaxation parameters was studied at two temperatures: $T = 131.4$K and $T = 122.5$K. At the former one, which is close to the decoupling temperature $T_{\alpha\beta_{JG}}$, the α-relaxation is dominant, whereas at the latter one TDI

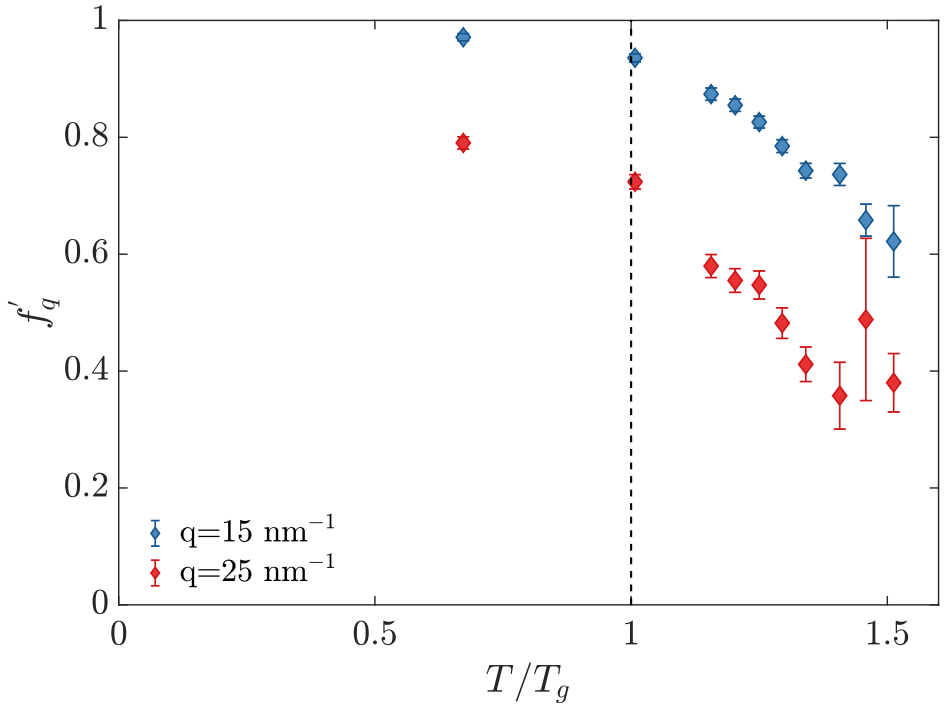

Figure 5.20: Temperature dependence of the initial contrast of the TDI interferograms, f'_q, measured at two different exchanged wave-vectors: 15 nm^{-1} (blue diamonds) and 25 nm^{-1} (red diamonds).

is sensitive only to the β_{JG}-process. The q-dependence of the initial beating contrast f'_q is reported in Fig. 5.21. We notice that in both cases f'_q displays an oscillation in phase with the $S(q)$ of 1-propanol. The De Gennes narrowing signals that, close to the peak of $S(q)$, the α-relaxation may still be present even if TDI is sensitive only to the relaxation time of the β_{JG}-process. As previously said the quality of the data does not allow us to disentangle the relative strength of the two processes.

The extracted relaxation times are plotted in Fig. 5.22-(a) along with the curves obtained from fitting a power-law $\tau \propto q^{-n}$ to the experimental data. As for 5M2H, this simple model can account for the q-dependence of the β_{JG}-relaxation at $T = 122.5$K in the whole q-range. On the contrary at $T = 131.4$K, where the α-relaxation is expected to be the dominant process, τ shows an oscillation close to the peak of the $S(q)$ (i.e. the De Gennes narrowing). The power-law is indeed able to well reproduce the experimental data only starting from $q = 18\text{nm}^{-1} > q_{max}$.

The power-law exponents n obtained from the fits, namely $n = 2.0(3)$ at $T = 131.4$K and $n = 3.9(6)$ at $T = 122.5$K, indicate that the q-dependence is quadratic (see the lowermost inset of Fig. 5.22) for the α-relaxation, and super-quadratic for the β_{JG}-relaxation. It is important to observe that the α-process in 1-propanol is still diffusive close to $T_{\alpha\beta}$ and its characteristic timescale shows the characteristic De Gennes narrowing. This is different from

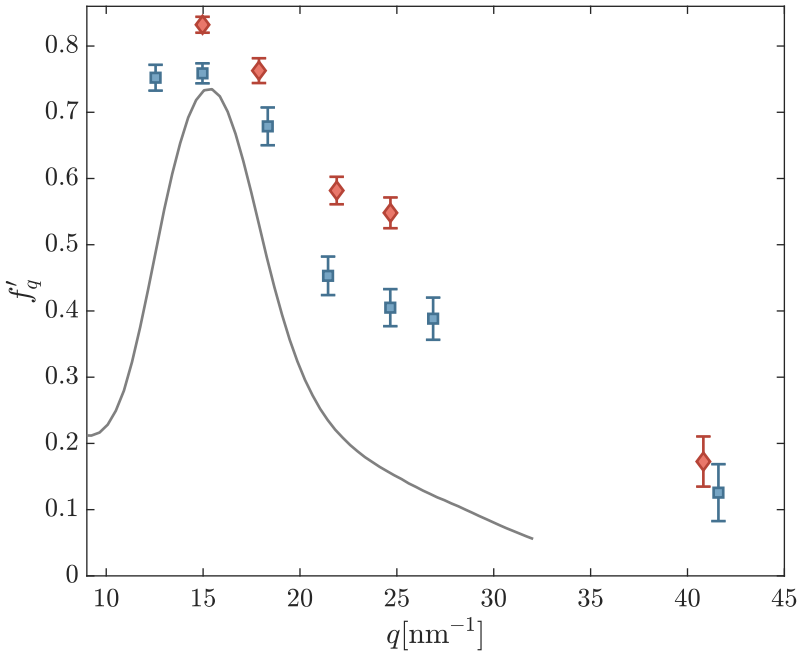

Figure 5.21: Wave-number (q) dependence of the initial beating pattern contrast at two different temperatures T=132.4 K (blue squares) and 122.5 K (red diamonds). The diffuse scattering pattern measured at T=122.5 K is rescaled and reported on the same axes for comparison.

what observed for 5M2H. A possible explanation is provided by the fact that 1-propanol was investigated at higher T with respect to T_g (131.4K=1.35T_g) than 5M2H (187.4K=1.21T_g). We recall that a quadratic q-dependence for the α-process above and close to T_c has been reported also for OTP [12, 56].
The microscopic dynamics associated to the β_{JG}-process is instead clearly restricted, compatible with the observations reported on 5M2H (see Sec. 5.2.4) and OTP [11, 12]. Interestingly the β_{JG}-process comes out to be sub-diffusive already at a relatively high T (122.5K$\simeq$ 1.25T_g). Fig. 5.22 reports also the relaxation time of the β_{JG}-relaxation as measured by DS and DDLS. Since the values of $\tau^{DS}_{\beta_{JG}}$ are not easily extracted from the DS susceptibility spectra as the α and β_{JG} peaks are partially overlapping (see Fig. 5.16), the $\tau^{DS}_{\beta_{JG}}$ data reported in Fig. 5.22 have been obtained averaging our result with the ones obtained by Gabriel *et al.* in [49] using DS and DDLS. It is important to stress that all the values resulted to be compatible within their uncertainties.

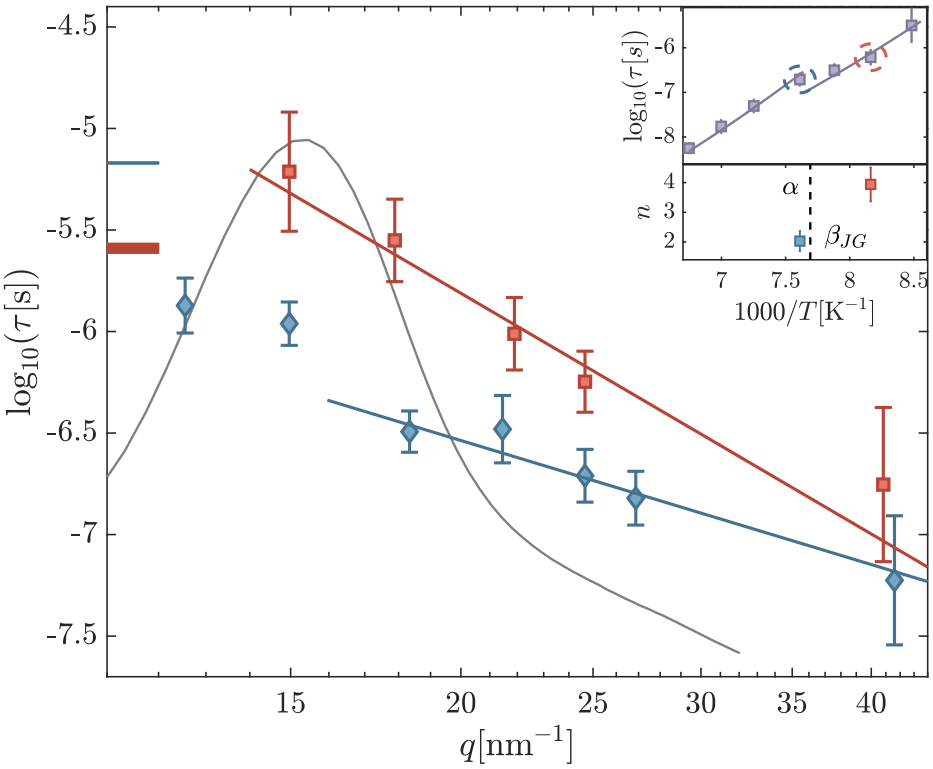

Figure 5.22: (a): Wave-number (q) dependence of the mean relaxation time at two different temperatures T=131.4 K (blue squares) and 122.5 K (red diamonds). The diffuse scattering pattern measured at T=122.5 K is rescaled and reported on the same axes for the sake of comparison. The blue horizontal bar corresponds to the relaxation time for the α process from dielectric spectroscopy at 132.5K whereas the red horizontal bar shows the relaxation time for the β_{JG}-relaxation at 122.5K obtained averaging the τ value from our dielectric spectroscopy measurements with those from [49]. The solid lines are power law fits to the data: $\tau \propto q^{-n}$. (b): Temperature dependence of the relaxation time at q=25 nm^{-1}, as in Fig.5.18. The dotted-circles show the temperatures where the q-dependencies were studied. (c): Power-law exponents, n, from the fitted power-law curves shown in (a), as a function of $1000/T$.

5.4 o-terphenyl

The results obtained on the two mono-hydroxyl alcohols combining TDI and DS data are mutually consistent and provide new information on the β_{JG}-relaxation in this class of materials. However, are our observation in agreement with the TDI data available in the literature for the prototypical glass former OTP [11–13]?

To answer this question, the results previously obtained by Saito *et al.* [11–13] on OTP are briefly reviewed in this section. Moreover, these TDI data are also compared to DS data using the same approach as for 5-methyl-2-hexanol and

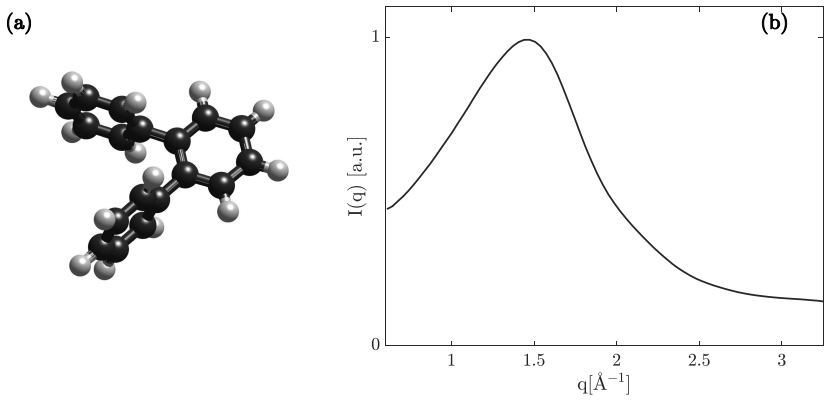

Figure 5.23: (a): 3D-structure of an ortho-therphenyl molecule. Black spheres: carbon atoms; gray spheres: hydrogen atoms. The external phenyl-rings are oriented out of the plane with respect to the central one. The two out-of-plane angles have been set equal to 54°, as expected for an isolated molecule. (b): diffuse scattering intensity of OTP measured at $T = 150$K as a function of q.

1-propanol.
OTP ($T_g = 244$K [168]) can be regarded as an archetypal fragile glass-forming liquid since it is a non-polar, compact and rigid molecule with a shape which is roughly spherical [56]. It is therefore a perfect candidate to analyze the genuine features of the glass transition. In fact, OTP is one of the most studied glass-formers and its dynamics has been investigated using many different experimental techniques besides TDI, such as neutron scattering [56], dielectric spectroscopy [5, 102, 169], NMR [107], dynamic light scattering [170, 171], Brillouin light scattering [172], inelastic X-ray scattering (IXS)[173].

An OTP molecule ($C_{18}H_{14}$) presents a central benzene ring surrounded by two lateral phenyl rings via covalent bonds (see Fig. 5.23). The side-rings are rotated out of the plane containing the central benzene ring because of steric reasons. This peculiarity is thought to be reason why it is a way better glass-former than other isomers such as m- or p-terphenyl. It has indeed been suggested that the glass-forming ability of OTP [174] is enhanced by the significant angle and out-of-plane distortions that the phenyl-phenyl bonds experience in the condensed-phase.
The TDI data from [11–13] are plotted in Fig. 5.24, along with the characteristic times of the β_{JG}-relaxation from DS [5] and adiabatic calorimetry (AC) [102] (see also the inset in Fig. 5.24). As it can be observed in Fig. 5.24, the β_{JG}-relaxation decouples from the α one around 273 K. Differently from the case of the investigated mono-hydroxyl alcohols, the β_{JG}-relaxation was observed only at the intra-molecular length-scale [11–13]. It can be easily noticed that the activation energy of the β_{JG}-relaxation as probed by the TDI data agrees with the one from the DS/AC measurements extrapolated above T_g.
From Fig. 5.24 it also emerges that molecular re-orientations within the β_{JG}-process ($\tau^{DS}_{\beta_{JG}}$) are faster than density fluctuations at $q = 18\text{nm}^{-1}$ and slightly

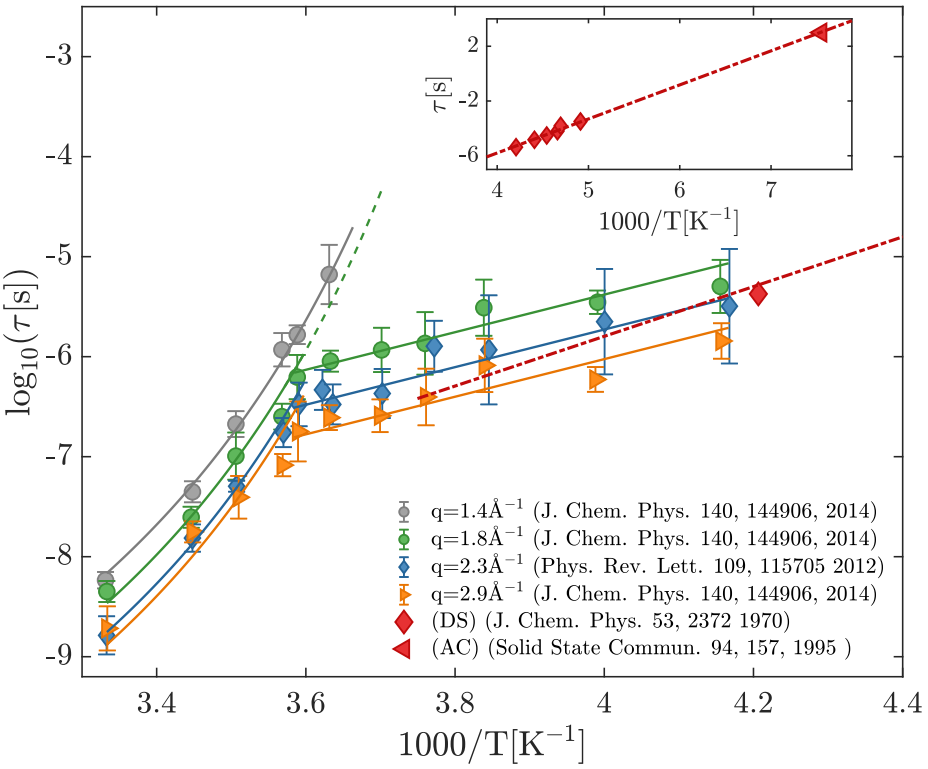

Figure 5.24: Temperature dependence of the relaxation time measured by TDI at different q-values: 14nm^{-1} [11] (grey circles), 18nm^{-1} [13] (green circles), 23nm^{-1} [11] (blue diamonds) and 29nm^{-1} [13] (yellow right-pointing triangles). The solid lines of the corresponding color show the best fitting curves using the T-dependence of the α and β_{JG}-relaxation as reported in [11, 13]. Also the relaxation time of the β_{JG}-relaxation as measured by dielectric spectroscopy (DS) [5] (red diamonds) and adiabatic calorimetry (AC) [102] (red left-pointing triangles) are reported for comparison. The red dotted-dashed line is the Arrhenius fit to the DS and AC data. Inset: extended T-dependence of the DS and AC data.

slower than those at 29nm^{-1}. This result clearly recalls what observed in 5-methyl-2-hexanol and in 1-propanol. Concerning the q-dependence of the β_{JG}-relaxation, Saito *et al.* found a super-quadratic q-dependence also in OTP [11, 12]: $n = 2.9(5)$ at 265 K and $n = 3.8(7)$ at 244K.

5.5 Which microscopic picture for the β_{JG}-relaxation?

In this section the results presented in this chapter are compared with the information available in the literature on the β_{JG}-relaxation, with the aim of possibly getting to a deeper understanding of this process.
The measurements on 1-propanol and 5M2H clearly show that the β_{JG}-relaxation

is characterized by a strong super-quadratic q-dependence, consistently with what observed in OTP [11, 12] (see also Sec. 5.4). In particular, the $\tau \propto q^{-4}$ dependence seen in 5M2H is similar to the one reported for OTP [12] below T_g. Such strong q-dependencies indicate that the β_{JG}-process is characterized by an anomalous, restricted dynamics at the investigated length-scales.
A detailed comparison between the DS and the TDI data can provide further information about the microscopic mechanism underlying the β_{JG}-relaxation. Of course, relating density fluctuations results to dipole reorientations is not always straightforward. This is exemplified by the case of PB: the characteristic time of the β_{JG} relaxation measured by DS is two orders of magnitude slower than that measured by neutron spin echo (NSE) [103]. A possible interpretation of this large difference could be found only thanks to simulations which suggested NSE and DS to be sensitive to the motion of different units in PB [175]. Here, this comparison is made easier by the fact that 5H2H, 1-propanol and OTP are small molecules. Furthermore the β_{JG} relaxation time ($\tau_{\beta_{JG}}$) of 5M2H shows a strong pressure dependence [157], evidence that it is not of intra-molecular nature. Unfortunately no information about the pressure dependence of $\tau_{\beta_{JG}}$ is available for OTP and 1-propanol. However, the timescale of the β_{JG} relaxation in 5M2H, 1-propanol [155] and OTP [176] approximately matches the prediction of the coupling model for the primitive relaxation time. As discussed in Sec. 2.5.2 this is one of the main criteria to distinguish genuine β_{JG} relaxations from secondary relaxations due to intra-molecular degrees of freedom [4, 58, 96]. In the case of OTP it has also been observed that the dielectric relaxation strength of the process, below T_g, is extremely sensitive to the changes in the sample density due to ageing [177]: also this is a sign that the process is not related to the internal degrees of freedom of the molecule, as discussed in Sec. 2.5.2.
Furthermore in both 5M2H and 1-propanol the relaxation times of the density-density correlation function, below $T_{\alpha\beta}$ and in a q-range covering both the inter-molecular and the intra-molecular length-scale, display the same T-dependence of the DS characteristic times (see Fig. 5.9 and Fig. 5.18). A similar observation holds also for OTP (Fig. 5.24), even though the β_{JG}-process was not detected at q_{max}. This result has some relevant implications.
i) The density-density correlation functions at q's in the range going to from the main peak of the $S(q)$ to $\simeq 30$ nm^{-1} couple in the same way to the same relaxation process. This entails that the density-density correlation function just describes the CM dynamics at different q's. In other terms, the considered samples can be approximated as rigid molecules in the q and time range here considered. In fact, if some kind of intra-molecular dynamics would be observed, the T-dependence of the relaxation time should be different when probed at different q's. This result is not surprising for OTP, which, as pointed out in Sec. 5.4, has a very simple and rigid molecular structure. In the case of the two mono-alcohols this conclusion agrees with the results presented in [49, 50] where a strict equivalence between the DS and depolarized dynamic light scattering data in the β_{JG} range of both 5M2H and 1-propanol was observed. This equiv-

alence indeed suggests that the symmetry axis of the molecular polarizability, which lies along the alkyl chain, and the dipole moment, which instead is oriented along the OH-bond, maintain a fixed relative orientation angle.
ii) The microscopic CM (translational) dynamics at different q's and the rotational dynamics probed by DS are coupled one to the other since they are probing the same relaxation.
iii) Because of this strong roto-translational coupling and provided that the β_{JG} process is characterized by a given length-scale, we should expect to measure the same relaxation time for CM translations and for molecular dipole reorientations if the former ones are probed at such length-scale. To be specific, the q-value at which the characteristic time measured by TDI matches the one obtained by DS ($\tau^{DS}_{\beta_{JG}}$) provides precise information about the characteristic length-scale of the β_{JG}-process at $\tau^{DS}_{\beta_{JG}}$.
On this basis, and as it can be observed from the relaxation maps presented in the previous sections (Figs. 5.9, 5.18, 5.24), the following interesting scenario emerges: at $q >> q_{max}$ density fluctuations relax faster than or in a similar way to permanent dipole reorientations. Conversely density fluctuations clearly decorrelate on a slower timescale than dipoles at q-values close to/at q_{max}, i.e closer to the average inter-molecular distance. Using the q-dependencies measured for 5M2H (Fig. 5.9) and 1-propanol (Fig. 5.22) and the ones reported in the literature for OTP [11, 12] it is then possible to find the q-value (q_{DS}) at which the relaxation time of the density fluctuations related to the β_{JG} relaxation matches the one measured by DS. Since the TDI data and the DS ones were fitted employing different models, namely the KWW equation (Eq. 5.2) for the TDI data and the Cole-Cole equation (third term of Eq. 5.1) for the DS data, we decided to perform the aforementioned comparison considering the characteristic timescales identified by the position of the maximum of the corresponding susceptibilities $\chi''(\omega)$. In fact since the TDI data do not allow for an accurate estimate of the shape of the ISF, this approach reduces as much as possible any bias introduced by the choice of a particular model for the description of the experimental data. To this aim the $\tau(\mathrm{q}, T)$ obtained from fitting Eq. 5.2 to the TDI data were used to calculate the characteristic time:

$$\tau_p(q, T) = \frac{1}{\omega_p(q, T)}, \tag{5.4}$$

where $\omega_p(\mathrm{q}, T)$ is the maximal loss angular frequency and is slightly displaced to lower frequencies with respect to $1/\tau(\mathrm{q}, t)$ (see Fig. 5.25). The values of $\tau_p(\mathrm{q}, T)$ were obtained numerically using the algorithm described in [178] since the KWW equation has no analytical Fourier/Laplace transform. In the case of the Cole-Cole expression $\tau^{DS}_{\beta_{JG}}$ is already equal to $\frac{1}{\omega_p(\mathbf{q},T)}$. The values for q_{DS} estimated from matching the characteristic times obtained from the TDI and DS experiments are reported in Tab. 5.1. It is interesting to notice that, in the case of 5M2H, q_{DS} is, not unexpectedly, in the q-range [31nm^{-1}-40nm^{-1}] where the β_{JG}-relaxation dominates density fluctuations. Unfortunately for the other samples this information is not available. As argued above, q_{DS} identifies

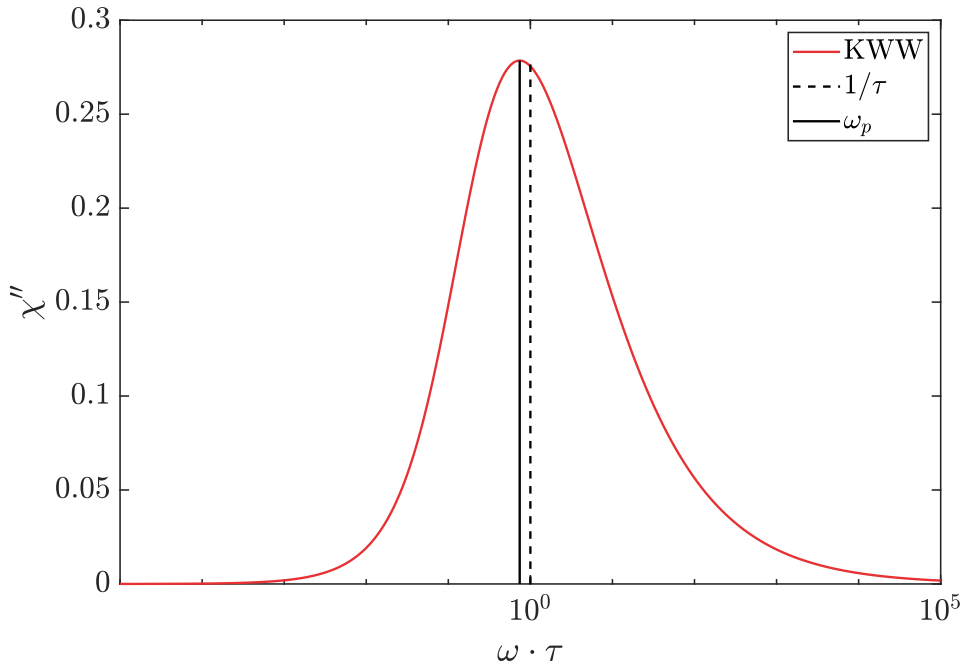

Figure 5.25: Red curve: susceptibility corresponding to the KWW relaxation function $\phi \propto exp[-(t/\tau)^{\beta_{KWW}}]$ with $\beta_{KWW} = 0.51$. Dashed vertical line: inverse of the relaxation time $\frac{1}{\tau}$. Solid vertical line: maximal-loss frequency (ω_p).

the characteristic (most probable) length scale ($\simeq \frac{1}{q_{DS}}$) for CM motion during the β_{JG}-relaxation. It is important to stress once again that there is a unique q-value satisfying the condition $\tau(q_{DS}) = \tau^{DS}_{\beta_{JG}}$.
It is possible to be more quantitative on this length-scale by relating q_{DS} to the molecular mean-squared displacement. To this aim we can resort to the anomalous diffusion model within the Gaussian approximation introduced in [53, 54] to describe sub-diffusion in polymers. In fact our experimental observations, as we will point out in the following, allow using an analogous approach as in [53], given the sub-diffusive nature of the β_{JG}-process. However, differently from what reported in [54], we here limit our comparison only to the

Table 5.1: q-value (q_{DS}) at which the relaxation time of density fluctuations matches $\tau^{DS}_{\beta_{JG}}$. Δr_{JG} is the characteristic atomic displacement at $\tau^{DS}_{\beta_{JG}}$.

Sample	T [K]	q_{DS} [Å^{-1}]	Δr_{JG}[Å]
5M2H	165.4	3.3(4)	0.75(9)
5M2H	170.1	3.4(3)	0.73(6)
1-propanol	122.5	1.9(2)	1.3(1)
OTP	244	2.2(5)	0.8(2)
OTP	265	3.1(8)	1.1(3)

most-probable relaxation time as probed by TDI and DS and the underlying distributions of relaxation times is not considered.
First of all we notice that density fluctuations within the β_{JG}-relaxation, at least in the (reduced) time-window accessible to scattering techniques based on X-rays and neutrons, are well described by the KWW model of Eq. 5.2 [11–13, 103, 134]. In particular we notice that this holds, within the experimental accuracy, also for the data collected on 5M2H in the T-range (165K$< T <$ 181K) and q-range (31nm^{-1}-40nm^{-1}) where the β_{JG}-process dominates the relaxation of density fluctuations. Another aspect to take into account is the super-quadratic q-dependence of the β_{JG}-relaxation,

$$\tau(q,T) = Aq^{-n} = \tilde{D}^{-\frac{n}{2}} q^{-n} \tag{5.5}$$

Here $\tilde{D}$ can be regarded as a generalised diffusion coefficient with dimensions $[\tilde{D}] = [L]^2[T]^{-\frac{2}{n}}$ [54, 179]. If Eq. 5.5 is inserted in Eq. 5.2, we obtain that the contrast function can be expressed as:

$$\phi'(q,t) = f'_q \exp\left[-\left(\tilde{D}^{\frac{n}{2}} q^n t\right)^{\beta_{KWW}}\right] \approx f'_q \exp\left[-\tilde{D} q^2 t^{\beta_{KWW}}\right] \tag{5.6}$$

The last approximation in Eq. 5.6 is justified by the observation that $n \cdot \beta_{KWW} \approx 2$ for all the considered samples within one or two standard deviations. It is also useful to recall that for 5M2H it was observed that around q_{DS} (25nm^{-1} $< q <$ 40nm^{-1}) the strength of the β_{JG}-relaxation (f_q) shows no q-dependence. Unfortunately this information is not available in the whole q-range where the q-dependence of τ was investigated and for the other samples. Nonetheless we can reasonably assume that around q_{DS} the relaxation strength does not show a strong q-dependence. Therefore Eq. 5.6 approximately follows a Gaussian-like behavior in q and we can therefore re-write it as [43]:

$$\phi'(q,t) \approx \exp\left[-\frac{\langle r^2(t)\rangle q^2}{6}\right] \tag{5.7}$$

and interpret $\langle r^2(t)\rangle$ as the mean-squared displacement of the molecule (MSD):

$$\langle r^2(t)\rangle = \langle |\mathbf{r}(t) - \mathbf{r}(0)|^2\rangle = 6\tilde{D}t^{2/n} \simeq 6\tilde{D}t^{\beta_{KWW}}. \tag{5.8}$$

It is important to stress that Eq. 5.8 implies that the incoherent approximation is valid for the β_{JG} process. In other words, in the q-range here considered the contribution to the intermediate scattering function describing the β_{JG}-relaxation can be approximated with its self-part, and therefore collective molecular motions can in good approximation be neglected: the β_{JG}-relaxation at times of the order of $\tau_{\beta_{JG}}$ turns out to be essentially a single molecule process. This picture, valid at least in the explored q-range and before the onset of the α-relaxation, is consistent with two other observations: 1) the q-dependence of $\tau_{\beta_{JG}}$ points to a strongly restricted character of the process and 2) no De-Gennes narrowing, hint of strong molecular correlations, was observed in the q-dependence of $\tau_{\beta_{JG}}$ and, even if present, it is not expected to play a

role at $q_{DS} > q_{max}$. Even in the case of 1-propanol, where q_{DS} is much closer to q_{max} than in 5M2H and OTP, we observed, for the more cooperative α-process, the De-Gennes narrowing to affect τ starting from $q < 18$ nm$^{-1} \lesssim q_{DS}$ (see Fig. 5.22).
From Eq.5.8 it is then possible to extract the MSD at $\tau^{DS}_{\beta_{JG}}$:

$$\langle r^2(\tau^{DS}_{\beta_{JG}})\rangle = \frac{6}{q^2_{DS}}\,. \tag{5.9}$$

We can finally use $\langle r^2(\tau^{DS}_{\beta_{JG}})\rangle$ to evaluate the CM molecular displacement occurring during the characteristic time of the β_{JG}-relaxation, i.e. $\tau^{DS}_{\beta_{JG}}$:

$$\Delta r_{JG} = \sqrt{\frac{6}{q^2_{DS}}}\,. \tag{5.10}$$

This expression gives a more solid basis to the previously used concept of typical length-scale for the β_{JG} process. It is however important to stress that Δr_{JG} has to be regarded as the most probable displacement of the molecules participating to the β_{JG}-relaxation and at $\tau^{DS}_{\beta_{JG}}$. Unfortunately, since the relaxation strength of the β_{JG}-process is not known in the whole q-range, it is not possible to determine the distribution of displacements associated to the relaxation process.
Δr_{JG} is reported for all the considered samples in Tab. 5.1 and, once rescaled by the average inter-molecular distance, is plotted in Fig. 5.26 (lower panel) as a function of the reduced inverse temperature T_g/T. The average inter-molecular distance has been estimated for all samples as $(v_{mol})^{\frac{1}{3}}$ where v_{mol} is the molecular volume. This procedure was preferred to the often-used estimation based on $\frac{2\pi}{q_{max}}$. In fact, q_{max} identifies in the reciprocal space the maximum of inter-molecular correlations which does not always reflect the average inter-molecular distance. For example in OTP the main peak of the $S(q)$ ($q_{max} = 1.4$Å^{-1}) arises from the correlations between phenyl rings belonging to different molecules while nearest-neighbors CM correlations are encoded in a pre-peak located at a lower q ($\simeq$0.85Å^{-1}) [56, 180].
On the upper panel of Fig. 5.26 the relaxation times of the three samples probed by DS and DDLS are also reported as a function of T_g/T and rescaled by the value of $\tau_{\beta_{JG}}$ at T_g to facilitate the comparison. Fig. 5.26 clearly shows that the most probable CM displacement at $\tau_{\beta_{JG}}$ for the molecules participating to the β_{JG}-relaxation is a fraction of the average inter-particle distance. In other words the β_{JG}-relaxation mainly consists of a restricted motion occurring within the cage formed by the nearest molecules. In order to have an idea of how restricted this motion is, we can use Eq. 5.8 to evaluate the CM displacement at the onset of the α-process, that is at $t \simeq \tau_\alpha$. In the case of 5M2H, a molecule participating to the β_{JG}-process will move by less than 40% of the average inter-molecular distance at $t \simeq \tau_\alpha \simeq 100\tau_{\beta_{JG}}$, clearly indicating how restricted is this motion. This is surely an approximate estimation as our model is expected to hold only around $\tau_{\beta_{JG}}$ but it gives a feeling of the

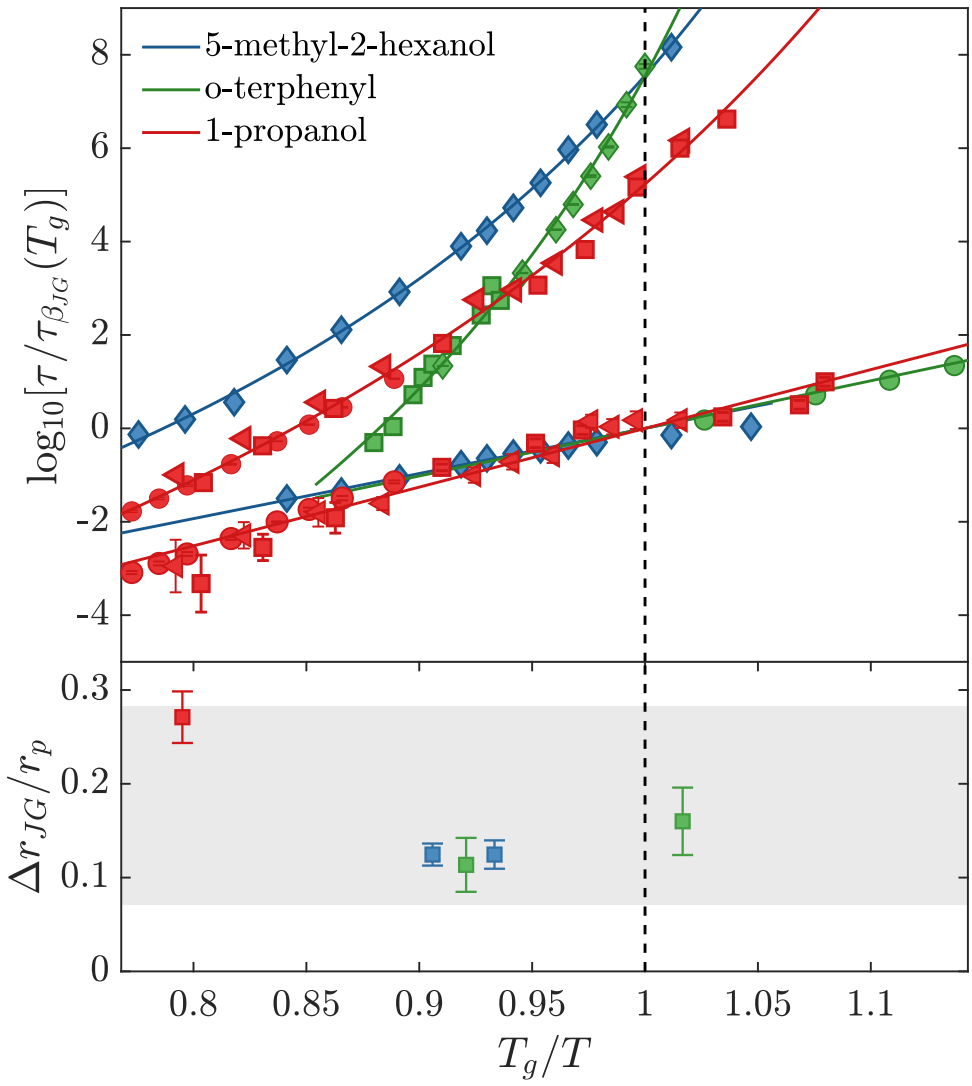

Figure 5.26: Panel (a): T_g-rescaled inverse T-dependence of the α and β_{JG} relaxation times (τ) measured by dielectric spectroscopy and/or depolarized dynamic light-scattering for 5-methyl-2-hexanol [134] (blue symbols), 1-propanol (red symbols) [49, 135] and o-terphenyl (green symbols) [5, 102, 135]. To facilitate the comparison the relaxation times have been scaled to the value of the corresponding $\tau_{\beta_{JG}}$ at T_g. Panel (b): characteristic center-of-mass displacement at $\tau_{\beta_{JG}}$ for the molecules participating to the β_{JG}-relaxation rescaled to the average inter-molecular distance. The same color code as in panel (a) has been used. The gray area in the lower panel shows the range of typical values for the Lindemann criterion in crystals (see [85] and references therein) but expressed in terms of MSD.

sub-diffusivity of the β_{JG}-process.
Another feature which can be deduced from Fig. 5.26 is that the amplitude of

these displacements is larger for 1-propanol ($\simeq 27\%$) than for 5M2H and OTP ($\simeq 12\%$). This difference can be explained by the higher reduced temperature at which the dynamics of 1-propanol was investigated i.e. at $T_g/T = 0.79$ corresponding to $T = 122.5K$. Furthermore at this temperature the timescales of the α and the β_{JG} relaxations of 1-propanol are much closer than in OTP and 5M2H and the two processes are less decoupled, see Fig. 5.26-(a).
Before proceeding, it is important to spend few words on the case of 1,4-polybutadiene (PB). As discussed above, DS and neutron scattering experiments provide rather different relaxation times for the β_{JG}-relaxation [103]. This large discrepancy was suggested to be due to the sensitivity of the two techniques to the dynamics of different units of PB characterized by distinct dynamical behaviors [175]. Intriguingly, the atomistic simulations performed by Bedrov and Smith [181] show that a complete new scenario emerges if the intra-molecular torsional barriers of PB are lowered. In their model, in fact, the relaxation time of the β_{JG}-relaxation, as probed by density fluctuations, matches that of dipole re-orientations at $q = 27\text{nm}^{-1} > q_{max} = 14\text{nm}^{-1}$ [181]. Accordingly, the CM excursions within the β_{JG}-relaxation are estimated to be roughly 20% of the inter-molecular distance [181] at $\tau^{DS}_{\beta_{JG}}$. These results clearly agree with our observations on small molecules and with the estimates provided by our simple model (Eq. 5.10).
The β_{JG} relaxation in 5M2H and 1-propanol is present up to q_{max} (see Fig. 5.9 and Fig. 5.18). This is new with respect to what observed in previous measurements in OTP and also in PB [11, 13], and evidences that, even though the β_{JG} process mainly consists of re-arrangements occurring at the intra-molecular length-scale, it is also characterized by motions extending at least up (or close) to the inter-molecular distance.
When we put together these new insights with the information from the literature, which is mainly related to molecular reorientational dynamics, the following picture emerges.
At high temperatures [104], reorientations occurs via large-angles rearrangements. As the glass transition temperature is approached, the rotational dynamics becomes progressively more and more restricted. At T_g, reorientations are characterized by angular excursions of the order of 10° [107]. The details will naturally depends on the molecular structure. Besides these restricted reorientations, a fraction of large-angle ($\gg 10°$) events also takes place. The existence of these latter ones has been found in numerical simulation studies of molecular and polymeric model systems [129]; however, the systems studied in these simulations were quenched to temperatures well below T_g and therefore a straightforward comparison to the present TDI results is not possible. From the experimental point of view, the presence of large angle reorientations emerges from combined DS and depolarized dynamic light scattering studies on 5M2H and 1-propanol [49, 50]. In fact it has been observed that the correlation functions relative to the β_{JG} relaxation probed by the two techniques are equivalent for both mono-alcohols. DS and DDLS are sensitive to the correlation functions of different Legendre polynomials ($l = 1$ and $l = 2$,

respectively) and this strict equivalence can be rationalised only if large-angle reorientations are present, at least for a fraction of the molecules, and even close to the glass-transition temperature.
The strong roto-translational coupling discussed above advocates for a parallel scenario for the CM dynamics. More precisely, it has been seen that the β_{JG} process is characterized by CM translations which are $\simeq 10\%$ of the inter-molecular distance at $\tau^{DS}_{\beta_{JG}}$ and which therefore occur within the cage formed by the first neighbours (see Fig.5.27-(a)). This is in agreement with the recent neutron scattering results on propylene carbonate [132] already discussed in Ch.2. Moreover, analogously to molecular rotations, a fraction of rearrangements will take place over a much longer length-scale. In other words, even if the β_{JG}-relaxation is mainly local at $\tau^{DS}_{\beta_{JG}}$, the characteristic lengths distribution for this process has tails for $t > \tau^{DS}_{\beta_{JG}}$ extending to longer distances, at least up to the inter-molecular one. It is important to notice that, consistently with this picture, the distribution of relaxation times $G(\ln\tau)$ extracted from DS measurements for the β_{JG} relaxation is characterized by very long tails that extend over more than two decades (see Fig. 5.9 and Fig. 5.18) reaching the characteristic timescales for density fluctuations at the inter-molecular length scale. Therefore, the restricted dynamics for both CM translations and reorientations is occasionally interrupted by longer ranged displacements accompanied by large-angle reorientations.
Interestingly these results, obtained from the investigation of organic glass-formers, are in agreement with recent simulations for model metallic glasses [128, 131] indicating that the β_{JG} relaxation is characterized by cooperative rearrangements of clusters with string-like shape. In fact, the results here reported clarify that the β_{JG} process is dominated by spatial fluctuations of molecules in the restricted environment defined by the cage formed by the nearest neighbours. At the same time, a part of the relaxation strength, corresponding to longer relaxation times, is linked to those larger spatial excursions that reach out (at least) to the intermolecular distance. This is the fraction of motions that is associated to motions beyond the cage (see Fig.5.27-(b)) and therefore likely related to the string-like dynamics observed in numerical simulations [128, 131].
Fig. 5.26 is providing even more information on the nature of the β_{JG} process. As already highlighted, the most probable center-of-mass displacement within the β_{JG}-relaxation (Δr_{JG}) corresponds to a well defined fraction of the average inter-molecular distance, namely $\simeq 12\%$ for 5-methyl-2-hexanol and OTP and $\simeq 27\%$ for 1-propanol. These values are reminiscent of the Lindemann criterion for the stability of crystalline solids [82, 83] discussed in Sec. 2.4.2.3. In fact all the estimated values for Δr_{JG} fall inside the gray band in the lower panel of Fig. 5.26 which shows the range of typical values for the Lindemann criterion in crystals (see [85] and references therein) expressed in terms of MSD. [1]

[1] The values prescribed in Ref. [85], i.e. between 5% and 20% of the average intermolecular distance, refer to the mean-square amplitude (see Eq. 2.59) so they have been multiplied by $\sqrt{2}$ in order to perform a comparison with Δr_{JG}, which is instead calculated from the MSD.

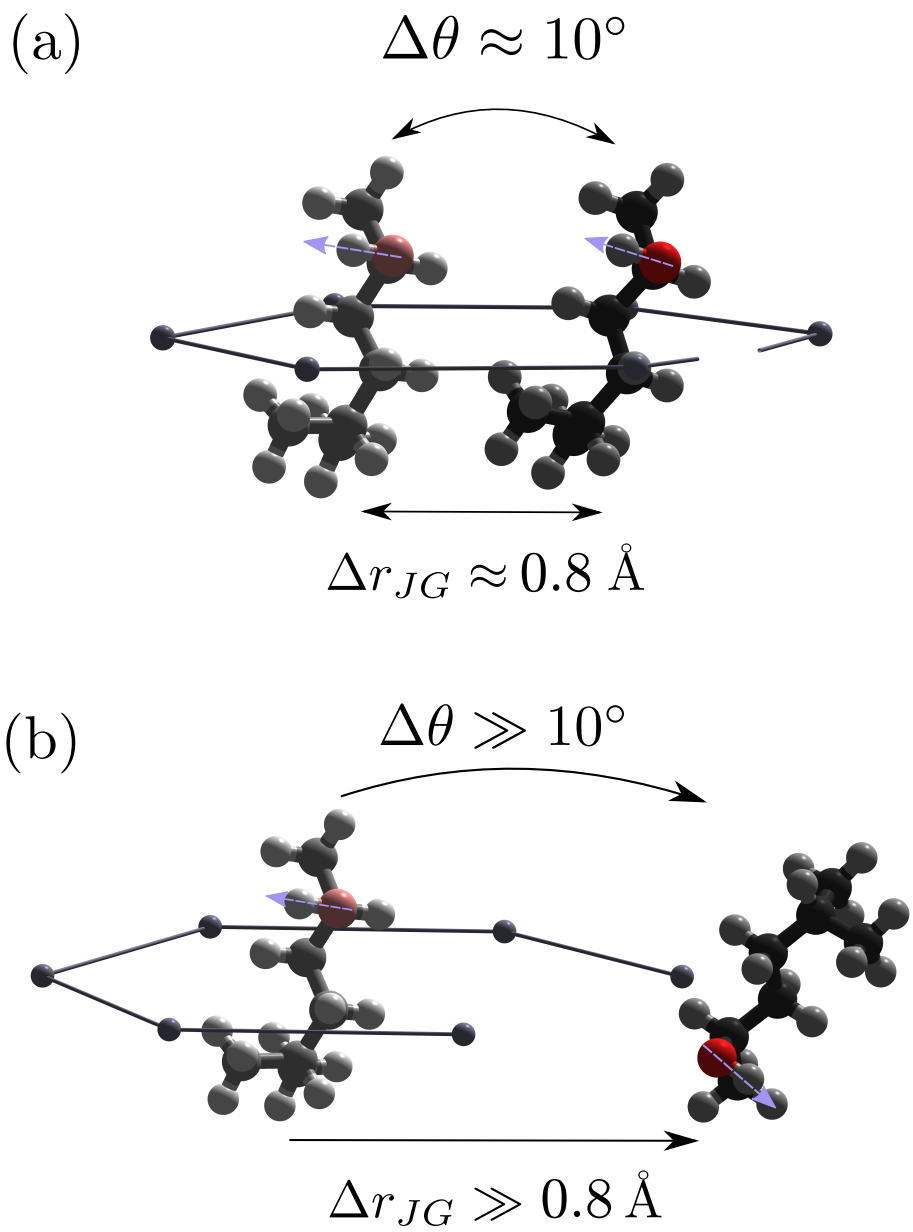

Figure 5.27: Schematic illustration of the rearrangement of a 5-methyl-2-hexanol molecule undergoing the Johari-Goldstein relaxation. The most probable microscopic dynamics consist of restricted translations and reorientations taking place in the local environment defined by the first neighbors. Because of the critical amplitude of such motion the cage is locally broken (a). Large spatial and angular excursions are also present and are likely taking place at times longer than $\tau_{\beta_{JG}}$ (b). The blue dashed lines in (a) and (b) show the dipole moment of the molecule which is oriented along the O-H bond.

In other word the restricted motion associated to the β_{JG}-relaxation corresponds to locally unstable (broken) cages, to the point that it is possible to refer to

the molecules participating to the β_{JG} process as to 'uncaged' molecules. The fraction of molecules involved in this critical displacement (25%, according to our estimate on 5M2H) at $\tau_{\beta_{JG}}$ (Fig. 5.27-(a)) is able to eventually sub-diffuse to longer distances prior to the onset of the structural relaxation. The larger CM excursions will then take place (Fig. 5.27-(b)) after the nearest-neighbors cage has been loosen. This view is consistent with the coupling model which envisages the β_{JG}-relaxation to be the terminator of the cage-dynamics [125–127]. A connection between the β_{JG}-process and cage-breaking events has been also observed in atomistic simulations of MGs: cage-breaking tendency facilitates the formation of the string-like excitations [131]. However, our results indicate that cage-breaking events rather than precursors are a fundamental parts of the β_{JG}-process. Also within the model proposed in [124], the β_{JG}-relaxation is associated to the exchange of molecules between regions of the sample where they are rigidly caged to regions where they are more loosely confined, consistently with a picture that associates the β_{JG}-process to cage-breaking events. It is interesting to notice that Yu *et al.* [87] found a similar Lindemann-like criterion for the α-relaxation. More precisely they observed in a simulated MG that the α-relaxation occurs when the most probable molecular mean-squared displacement reaches 20% of the average nearest neighbors distance [87]. Our results suggest indeed a similar scenario, but are specific to the molecules that participate to the β_{JG}-relaxation rather than to the average molecule: the β_{JG}-relaxation occurs when a fraction of the molecules (roughly one out of four according to our estimate on 5M2H) is uncaged well before that the α-relaxation completely relaxes the internal structure of the supercooled liquid. Further information concerning the structural properties of the β_{JG}-relaxation can be obtained considering the microscopic relaxation strength of this process. As discussed in Sec.5.2.4, the results obtained from 5M2H show that in a q-range around q_{DS} ($31\text{nm}^{-1} \leq q \leq 40\text{nm}^{-1}$) and above T_g ($1.07T_g < T < 1.21T_g$) the β_{JG}-relaxation has an average strength of $f_q = f_{\beta_{JG}} \simeq 0.25$ and the α-relaxation is negligible: at the intramolecular length-scale the remaining molecules are indeed involved in fast relaxation processes and vibrations. This means that roughly one molecule out of four, on average, undergoes critical CM displacements within the cage formed by the nearest neighbors. It is interesting to compare this number with the number of nearest neighbors (z) for the samples here considered. z can be easily estimated for 1-propanol and OTP integrating their radial pair distribution function, $g(r)$, up to the first coordination shell (r_{min}) [182]:

$$z = \int_0^{r_{min}} 4\pi\rho r^2 g(r) dr \,. \tag{5.11}$$

More precisely in the case of OTP we used the $g(r)$ relative to the molecular center-of-mass (see Fig. 5.28) [180], while in the case of 1-propanol, given its more complex structure, we consider the partial $g(r)$ corresponding to intermolecular correlations between the central carbon atoms of each alkyl-chain [183]. The obtained values are respectively $z \simeq 12$ [183] and $z \simeq 15$ [180]. Both estimates refer to samples at $T = 300\text{K}$. At lower temperatures we do

not expect these number to vary more than 20% according to the change in density for the two samples. Though no $g(r)$ is available in the literature for 5M2H, we can expect its number of nearest neighbors to be similar to that of 1-propanol, as they are both mono-alcohols. These coordination numbers are

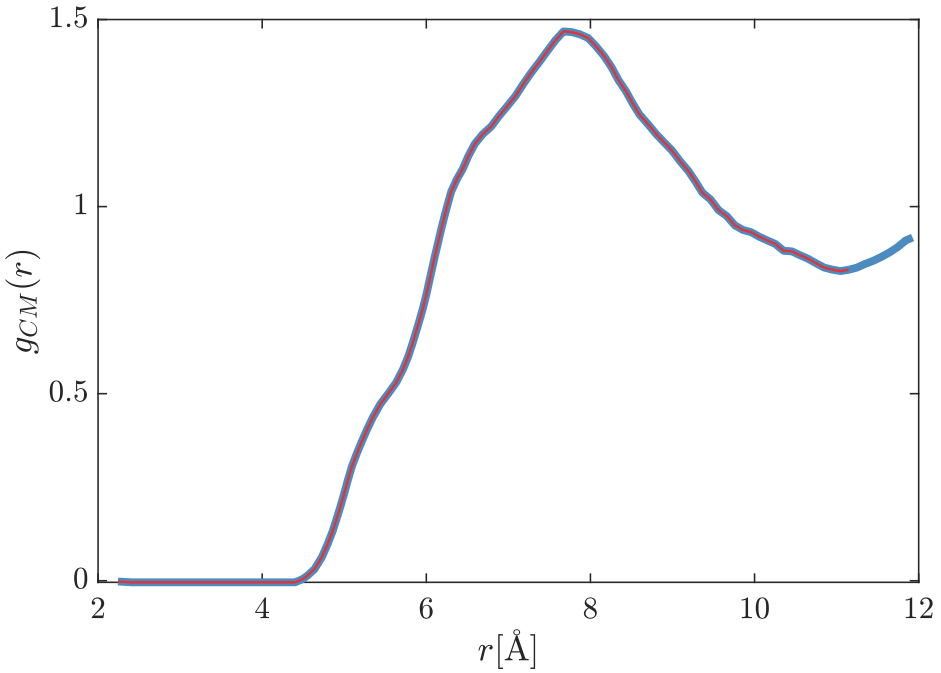

Figure 5.28: Calculated molecular center-of-mass radial pair distribution function [180] for OTP at 300K (blue solid line). The red solid-line shows the first coordination shell.

similar to that of a f.c.c lattice, i.e $z_{f.c.c} = 12$, and remarkably lattices with such connectivity present a threshold for site percolation (p_c) which is comparable with $f_{\beta_{JG}}$ ($p_c^{f.c.c} = 0.199$ [184]). This implies that the un-caged molecules participating to the β_{JG}-relaxation are spatially connected in a percolating (or close to percolation) cluster (see Fig. 5.29).

It is important to stress that this spatial connection clearly does not imply dynamical correlations among the molecules participating to the β_{JG}-process. In fact, though the β_{JG}-relaxation might be cooperative to some extent as our results from 5M2H and 1-propanol suggest, its strong sub-diffusivity clearly evidences that it is essentially local in nature. An important aspect to underline is that the percolating cluster corresponding to the β_{JG}-relaxation is clearly characterized by a higher molecular mobility with respect to the rest of the sample since it is formed by that fraction of molecules which are able to move over distances matching the Lindemann criterion on a timescale $\tau_{\beta JG}$. Intriguingly, this result is consistent with the *micro-structural* picture proposed by Ichitsubo and co-workers [114, 117]. In fact, as discussed in Sec. 2.5.5.1, they inferred from ultrasonic annealing experiments the presence of "weakly-bonded-regions" permeating the glassy structure and propose them as the

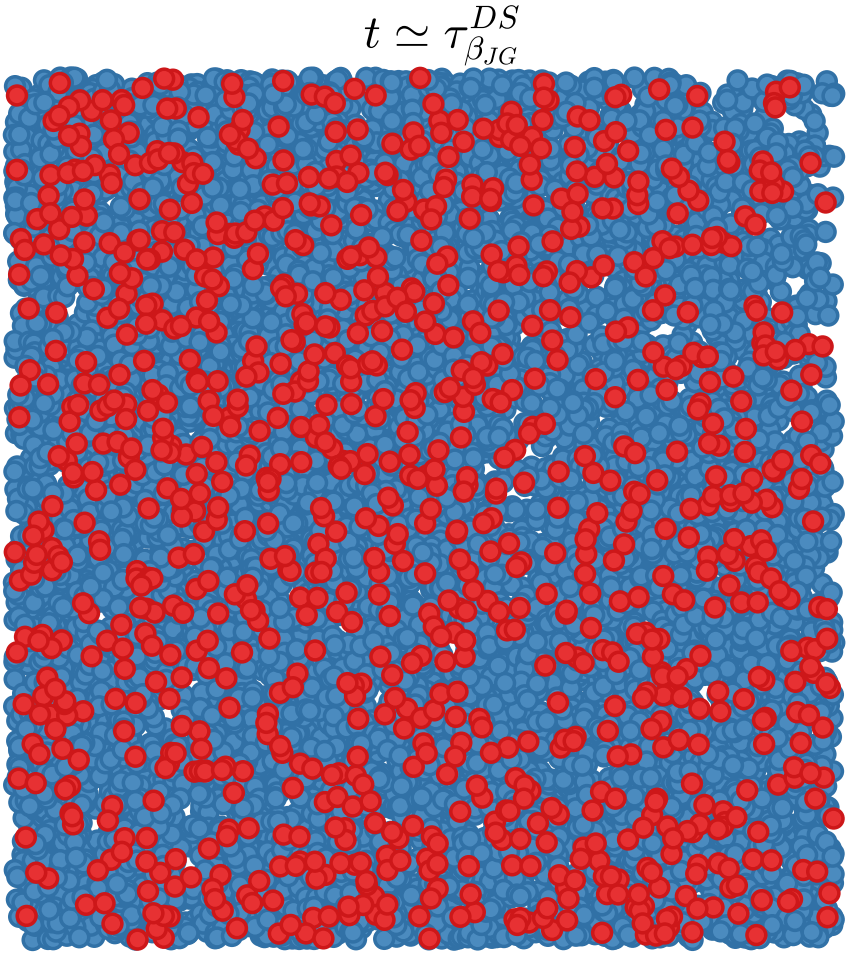

Figure 5.29: Sketch of the spatial distribution of the molecules participating to the β_{JG}-process at $\tau^{DS}_{\beta_{JG}}$. These molecules (red circles) are characterized by a higher mobility and undergo spatial excursions at $\tau^{DS}_{\beta_{JG}}$ of the order of those prescribed by the Lindemann criterion well before the onset of the structural relaxation. Such "un-caged" molecules form a (close to) percolating cluster.

structural origin of the β_{JG}-relaxation [114, 117].
It is finally interesting to make also a comparison with the results of the RFOT which also recurs to the concept of percolation for the β_{JG}-relaxation, though in a different way. In fact, we recall, the RFOT envisages the β_{JG}-relaxation to be due string-/percolation-like cooperatively re-arranging regions [35]. Clearly this dynamical perspective cannot be directly compared with our results which provide only a spatial information on the cage-breaking events within the β_{JG}-process. However, according to our findings, we can suppose such rearranging events to occur within the percolating cluster formed by the un-caged molecules since they present a similar topology. This would be consistent with our interpretation of the larger CM excursion within the β_{JG}-relaxation as string-

like dynamics which will likely occur after cage-breaking has taken place, as suggested by the simulations in [131].

Chapter 6

A new experimental set-up for γ-resonance time-domain interferometry

In this chapter the potentialities of new configurations for TDI experiments, based on absorbers with a multi-line energy spectrum, are explored. After a short discussion about the limitations posed by the standard TDI scheme with identical SL absorbers, a new set-up exploiting a 3-lines interferogram is presented and its main features and advantages described. In particular, as demonstrated by the results here obtained on the prototypical glass-former o-terphenyl, this new layout for TDI experiments is not only characterized by a larger efficiency but also allows accessing directly the absolute strength of relaxation processes, otherwise precluded in measurements with SL absorbers. Some of the work presented in this chapter has been published in [143, 185].

6.1 How to improve the standard TDI configuration?

In a typical TDI experiment the reference and probe fields are provided by two identical single-line absorbers. Despite the simplicity of this configuration, which allows to easily observe the damping of the beating pattern, some drawbacks are present. First of all, if two equal absorbers are used, it is not possible to disentangle the strength f_q of the studied relaxation process from $f_{\Delta E}$, which, as elucidated in Ch. 3, depends on the system dynamics within the bandwidth of the incident SR. This is certainly a major issue, especially in the study of the β_{JG}-relaxation. Secondly, the "standard" scheme requires the use of a velocity transducer in order to shift the excitation energy of the probe absorber with respect to the reference one via Doppler effect. Two issues are brought in by the use of a velocity transducer : i) vibrations are introduced in the interferometer, with a consequent effective increase of the broadening of the nuclear resonance and ii) the data acquisition needs to be stopped at each

change of direction of the transducer velocity to avoid blurring the beating pattern. Both effects reduce the efficiency of the TDI scheme and preclude the access to relaxation times of the order of 10μs in reasonable measuring times. To overcome all the limitations listed above, new interferometers based on more complex energy spectra have been designed [14, 143, 186]. In the alternative scheme proposed in [186], the reference and probe beams are still provided by identical SL absorbers. However, differently from the usual configuration, two probe absorbers are used instead of one. Both of them are driven by velocity transducers at the same constant velocity but in anti-phase. As a consequence a beating pattern arising from a 3-lines interference is observed. As pointed out in [186], this scheme might be up to a factor of 3 more efficient, according to simulations, than the usual 2-lines configuration. Unfortunately, the external vibrations introduced by the velocity transducers operating in anti-phase and the consequent instrumental reduction of the QB contrast limited the achieved improvements [186]. For this reason absorbers with multi-line energy spectra due to more complex hyperfine interactions started to drive more and more attention [14, 143]. In fact, multi-line absorbers do not require the use of velocity transducers and offer a higher resonant scattering probability. More channels for nuclear resonant scattering are indeed present, thus enhancing the probability of nuclear forward-scattering. Consequently the acquisition time required for collecting TDI beating patterns with satisfying statistical accuracy is greatly reduced. The price to pay is a more complicated interferogram. For example, the scheme reported in [14] is based on two α-^{57}Fe foils magnetized along the two perpendicular directions with respect to the wave-vector of the incident radiations. As a consequence the beating pattern emerges from the interference of 6 different lines.
The scheme that is presented here combines the advantages of the two aforementioned setups and avoids their drawbacks. Instead of the two driven upstream absorbers as in [186], a single absorber at rest and with a two-line energy spectrum is employed (see Fig.6.1). In this way, two goals at once are achieved: (i) vibrations due to velocity transducers are avoided and beating patterns with satisfying contrast up to 350 ns have been observed; (ii) the data analysis is simpler than the one required for the multi-line scheme in Ref. [14].

6.1.1 Some experimental features of the scheme

The experiments described in the next sections, were performed at beamline ID18 of the ESRF. The monochromatized incident radiation, with a bandwidth of 0.75meV centered at the energy of the first excited state of ^{57}Fe (14.413 keV), was obtained as described in Sec.4.1.3, i.e. through the HHLM and HRM used in cascade (see Fig.4.6-(a),(c)). A α-^{57}Fe foil vertically magnetized with a magnetic field $H_e = 0.5T$ provided the probe signal with the two-line energy spectrum.
α-^{57}Fe, because of Zeeman's splitting, allows indeed six possible magnetic-dipole transitions between the ground sub-states and the excited states, as it

can be observed in Fig. 3.8 of Ch. 3. If the α-^{57}Fe foil is magnetized along

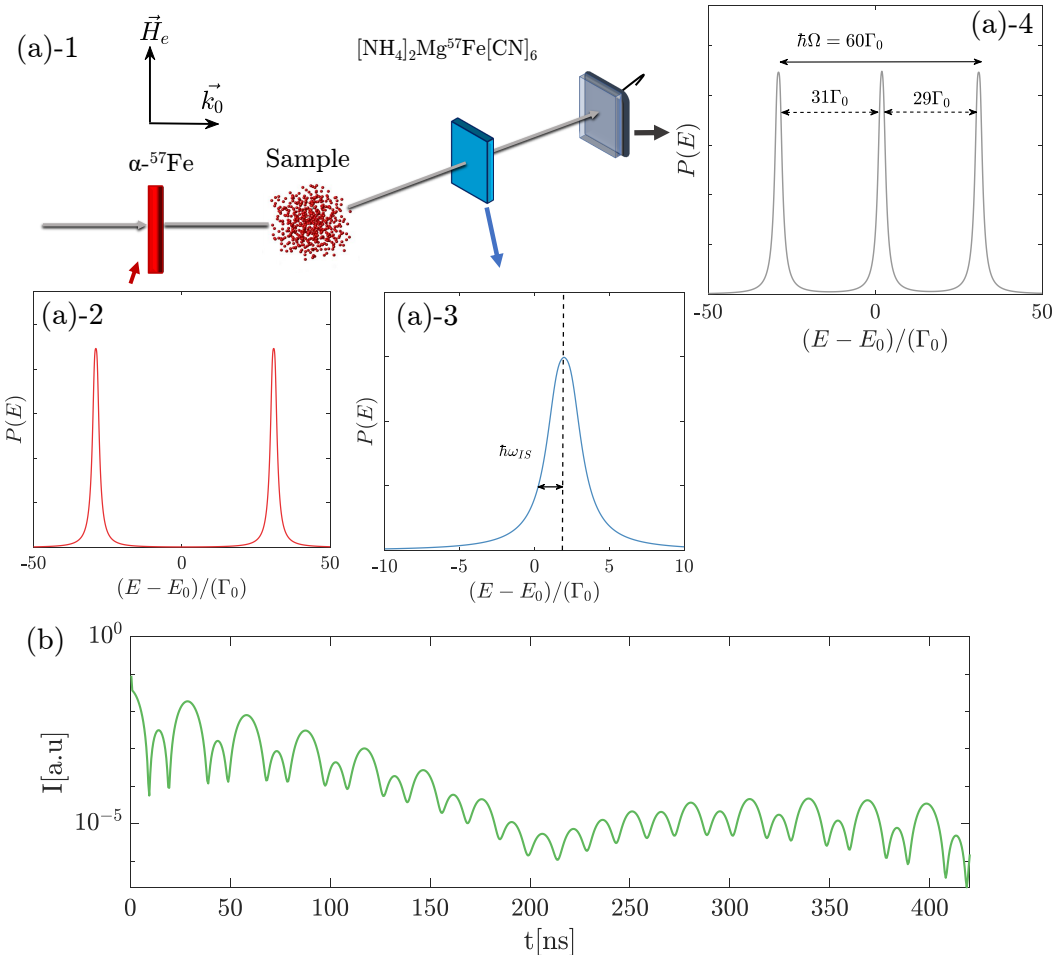

Figure 6.1: (a)-1: Sketch of the experimental setup for TDI measurements. APD stands for avalanche photodiode detector. $\vec{H}_e$ is the external magnetic field which magnetizes the α-^{57}Fe absorber, while $\vec{k}_0$ is the wave-vector of the incident SR. (a)-2 calculated energy spectrum for a magnetized α-^{57}Fe foil in the experimental conditions shown in (a)-1. (a)-3: calculated energy spectrum for the single-line reference absorber made of $[NH_4]_2Mg^{57}Fe[CN]_6$ and downstream of the sample. $\hbar\omega_{IS}$ is the isomer shift of its excitation energy. (a)-4: 3-lines energy spectrum at the output of the TDI. The distances in energy between the nuclear resonances are indicated by solid and dashed arrows. (b): simulated time spectrum corresponding to the energy spectrum in (a)-4.

the vertical direction with respect to the direction of the incident SR, only the two transition between the nuclear sub-states with $\Delta m = 0$ (m is the quantum number relative to the projection of the angular momentum along the quantization axis) are allowed. In fact, according to the selection rules for magnetic dipole transitions with $\Delta m = 0$, the polarization vector of the incident beam must have a component parallel to the direction of the magnetic field responsible for the Zeeman's splitting. Since the SR is characterized by a

magnetic field vertically polarized with respect to the plane where the emitting electron are orbiting, H_e needs than to be oriented as shown in Fig.6.1-(a)-1. If this condition is full-filled than only the two nuclear resonances listed below will be excited:

$$\begin{aligned} \left|I=\frac{1}{2},m=\frac{1}{2}\right\rangle &\rightarrow \left|I=\frac{3}{2},m=\frac{1}{2}\right\rangle \\ \left|I=\frac{1}{2},m=-\frac{1}{2}\right\rangle &\rightarrow \left|I=\frac{3}{2},m=-\frac{1}{2}\right\rangle . \end{aligned} \tag{6.1}$$

Here I is the total nuclear angular momentum. The resulting energy spectrum will be of the type reported in Fig.6.1-(b).
A pellet produced from the powder of $[NH_4]_2Mg^{57}Fe[CN]_6$ was instead used as reference absorber. The excitation energy of $[NH_4]_2Mg^{57}Fe[CN]_6$ is in between the two-lines of the upstream foil, but slightly displaced by $\hbar\omega_{IS}$ with respect to the center because of the isomer shift (IS) (Fig.6.1-(a)-3). The IS is due to the different electric monopole interaction experienced by the nuclei in the two absorbers.
The total energy spectrum for this configuration is reported in Fig.6.1-(a)-4 whereas the corresponding time-evolution of the resonantly scattered intensity is shown in Fig.6.1-(b).
The resonantly scattered photons were detected by APD detectors placed right behind the reference absorber, similarly to what shown in Ch.5.

6.1.2 Characterization of the reference beating-pattern

In order to effectively use this setup it is first of all necessary to properly characterize and model the reference unperturbed beating pattern arising from the TDI. It is important to recall that the time-evolution of the scattered intensity $\bar{I}$ is completely determined by the responses $G(t)$ of the reference and probe absorbers. Once $G(t)$ is known, $I(t)$ can be easily calculated thanks to Eq.3.19. $G(t)$ can of course be directly measured via NFS, that is removing the sample and placing the reference absorber along the forward direction.
Another important aspect that can be explored thanks to NFS is the radiative coupling between the three nuclear resonances composing the TDI. In fact, differently from the standard experimental set-up with velocity transducers, the distance between the different lines cannot be tuned. Therefore the hypothesis of negligible radiative coupling should be tested beforehand for each of the involved absorbers.

6.1.2.1 α-Fe

The α-Fe absorber, in the present scheme, presents an energy spectrum with two lines, arising from the two allowed transitions shown in Eq.6.1. The time evolution of the NRS intensity displays a beating pattern with a frequency Ω, where $\hbar\Omega$ is energy separation between the two transitions, which are expected

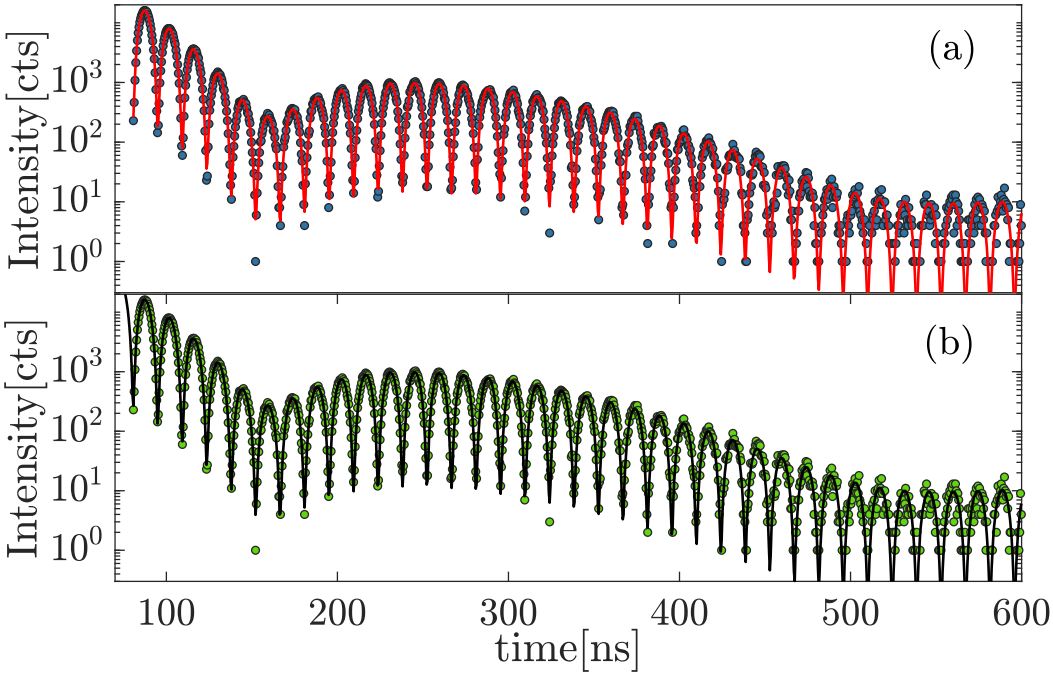

Figure 6.2: (a): Time-evolution of the Nuclear Forward Scattering for the reference magnetized $\alpha - 57^{Fe}$ foil. Blue dots: experimental data. Red solid line: fit obtained using Eq.3.8 with N = 2, i.e via the Fourier transform of the frequency response of the absorber. (b). Green data: experimental data as in (a). Black solid line: fit obtained using Eq.3.12.

to be of the order of $\simeq 60\Gamma_0$. To characterize its properties and to test if the coupling between the two resonances was negligible, the NFS data were analysed using two different approaches. Namely, i) the experimental data were initially fitted considering the inverse Fourier transform of the full frequency response (Eq.3.8) of the absorber (Fig.6.2-(a)). Then ii) an analogous fit was performed using Eq.3.12 which was derived in the approximation of $\hbar\Omega \gg \Gamma_0$ (Fig.6.2-(b)). The results from the two fitting procedures are reported in Tab. 6.1. As it clearly emerges from the parameters in Tab. 6.1, the two fits are of

Table 6.1: Parameters of the reference α-^{57}Fe absorber obtained from two different fitting procedures: fit(1) refers to Eq. 3.8 with $N = 2$ and fit(2) to Eq. 3.11. χ^2_{red} is the reduced chi-square, $\langle T_\alpha \rangle$ and w_{T_α} are the mean value and the width of the effective thickness distribution of a single resonance, respectively. $\hbar\Omega$ is the Zeeman's splitting of the nuclear resonance in units of Γ_0.

	χ^2_{red}	$\langle T_\alpha \rangle$	w_{T_α}	$\hbar\Omega/\Gamma$
fit(1)	1.39	13.19(1)	2.53(3)	61.932(3)
fit(2)	1.44	13.16(1)	2.54(3)	61.937(3)

comparable quality according to the reduced χ^2. The obtained values for the

thickness distribution ($\langle T_\alpha \rangle$, w_{T_α}) and the frequency of the Zeeman's splitting are also in agreement. The time evolution of the NFS for this absorber can be, therefore, described neglecting the radiative coupling.
The nuclear forward scattering signal from the α-Fe foil and the single-line reference absorber also needs to be characterized and the presence of radiative coupling ruled out. The central spectral line of the downstream absorber is indeed separated in energy from the α-^{57}Fe lines by only $\simeq 30\Gamma$.
The time evolution of the NFS for these two targets (in the absence of a sample) can be analytically calculated from Eq. 3.16 and, if the cross-scattering term is not considered, it results equal to:

$$\begin{aligned} I(t) \quad \propto \quad & 2|G(t,T_\alpha)|^2 + |G(t,T_{SL}) \cdot F_I(t,\Gamma_D)|^2 \\ & +4Re\{G(t,T_\alpha)G^*(t,T_S)\} \cdot F_I(t,\Gamma_D) \cdot \\ & \cos\left(\frac{\Omega}{2}t\right)\cos(\omega_{IS}t) + 2\cos(\Omega t)|G(T_\alpha,t)|^2 . \end{aligned} \tag{6.2}$$

Here $G(t,T_\alpha)$ and $G(t,T_{SL})$ are the response of a single resonance of α-^{57}Fe and of the SL absorber, respectively. The term $\cos(\omega_{IS}\ t)$ describes the effect of the isomer shift, and $F_I(t,\Gamma_D)$ is the inhomogeneous broadening of the $[NH_4]_2Mg^{57}Fe[CN]_6$ line with respect to that of α-^{57}Fe. $F_I(t,\Gamma_D)$ has been assumed to be a Gaussian with standard deviation Γ_D. The effect of $F_I(t,\Gamma_D)$ on the QB-contrast is analogous to the fictive relaxation usually introduced for the 2-lines experiment. However, here $F_I(t,\Gamma_D)$, differently from the previous analysis in Ch. 5, acts also on the reference absorber response. This term is indeed necessary to properly describe the time-evolution of the NRS from $[NH_4]_2Mg^{57}Fe[CN]_6$. No additional inhomogeneus broadening of the spectrum is instead required for α-^{57}Fe, as it can observed in Fig.6.2.
It is important to notice that in this scheme, differently from the standard implementation with SL absorbers, the coherent super-position of the probe and reference fields causes the appearance of QB with frequency $\Omega/2$ in addition to the ones coming from the magnetized α-Fe. So, the quasi-elastic scattering and de-phasing introduced by the sample act only on the components of the beatings with frequency $\Omega/2$.
As for the reference absorber, the NFS scattering was analysed using both the Fourier transform of the full frequency response (Eq. 3.8 with $N = 3$) and the separated targets approach described by Eq. 6.3. The fits were performed fixing the thickness distribution of the α-Fe foil and leaving all the other parameters as free: $\langle T_{SL} \rangle$, w_{SL}, ω_{IS}, Γ_D and Ω. The obtained curves along with the NFS data are shown in Fig.6.3-(a) and Fig.6.3-(b) respectively, whereas the best-fit parameters are listed in Tab. 6.2. As it can be observed from Tab. 6.2, apart from some small differences in $\langle T_{SL} \rangle$, the estimated parameters agree within their experimental error. It is however interesting to point out that the value of the Zeeman's splitting for the upstream foil here extracted differs by $\simeq 0.1\%$ from the one previously estimated from the α-^{57}Fe foil. This small discrepancy, however larger than the statistical error, may suggest that

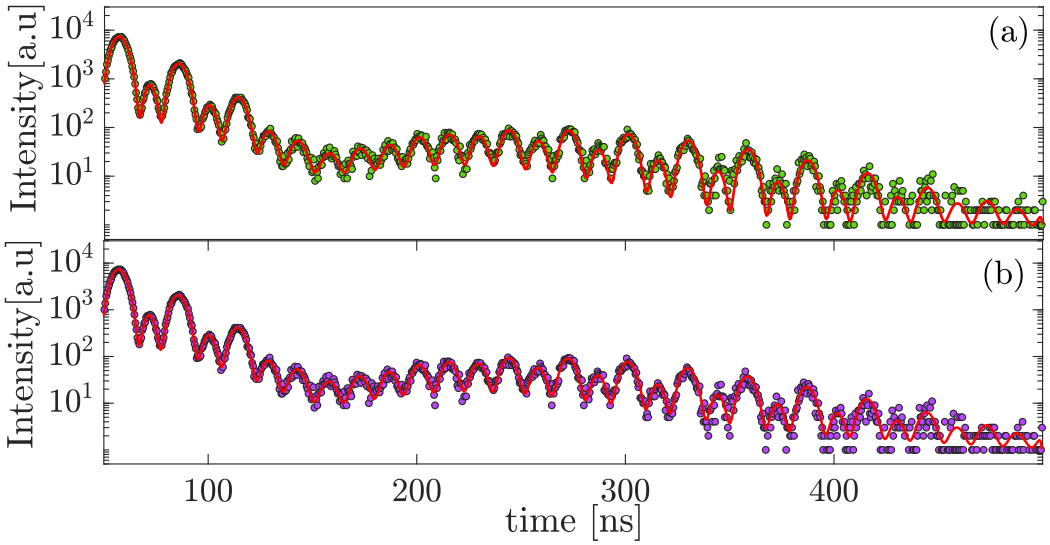

Figure 6.3: (a): Nuclear forward scattering time evolution for the two absorbers (α-^{57}Fe and $[NH_4]_2\ ^{57}Fe[CN]_6$) in cascade. Green dots: experimental data. Red solid line: fit obtained using Eq.3.8 with $N = 3$. (b). Purple dots: experimental data as for (a). Red solid line: fit obtained using Eq.6.3, that is, assuming negligible radiative coupling.

Table 6.2: Parameters of the NFS from the α-^{57}Fe absorber in cascade with the $[NH_4]_2Mg^{57}Fe[CN]_6$ one. The results are from two different fitting procedures: fit(1) refers to Eq. 3.8 with $N = 3$ and fit(2) to Eq. 6.3. χ^2_{red} is the reduced chi-square, $\langle T_{SL}\rangle$ and $w_{T_{SL}}$ are the mean value and the width of the effective thickness distribution for the downstream absorber, respectively. $\hbar\Omega$ is the Zeeman's splitting of the nuclear resonance of α-Fe in units of Γ_0. Γ_D and $\hbar\omega_{IS}$ are the standard deviation of the inhomogeneous broadening and the isomer shift of $[NH_4]_2Mg^{57}Fe[CN]_6$, respectively. Both quantities are expressed in units of Γ_0.

	χ^2_{red}	$\langle T_{SL}\rangle$	$w_{T_{SL}}$	$\hbar\Omega/\Gamma_0$	Γ_D/Γ_0	$\hbar\omega_{IS}/\Gamma_0$
fit(1)	1.27	13.65(6)	3.95(9)	61.849(5)	0.23(2)	1.068(7)
fit(2)	1.28	13.40(6)	4.04(9)	61.846(3)	0.26(1)	1.062(6)

the performed measurements are affected by some systematic error, which unfortunately could not be figured out from the experiment. Nonetheless, it is clear that the analytical description of the NFS data provided by Eq. 6.3 is satisfying and that also in this case the effect of the radiative coupling can be ignored.

6.2 Testing the new set-up on OTP

To fully establish the use of this alternative TDI configuration it is of course required to test it on some archetypal supercooled liquid with an already well-known microscopic dynamics. Ortho-terphenyl (OTP) is for sure one of the best samples for this task.

6.2.1 Experimental details

To maintain OTP in the supercooled state during the long acquisition times required by TDI requires more care during the preparation phase than for the monohydroxyl alcohols. OTP has indeed a great tendency to crystallize especially in the temperature region above T_g which can be accessed by TDI. For this reason it is in fact necessary to reduce as much as possible the number of impurities which may act as nucleation centers. To this aim, the samples here used were obtained starting from a high purity ortho-terphenyl powder ($> 99\%$ pure) from Sigma Aldrich which was additionally purified via vacuum-distillation.
The dynamics of the OTP sample was studied across T_g and a He-flow cryostat was employed to control the temperature as for the TDI measurements on the mono-hydroxyl alcohols. The temperature was controlled with an accuracy of $\pm 0.1\%$. However, instead of a copper sample holder, a Pyrex glass-tube with diamond windows was used (see Fig. 6.4). Glass cells provide indeed less crystallization centers than copper ones. An external cooper holder was then used to fix the glass-tube to the cryostat cold-finger. Concerning the scattering

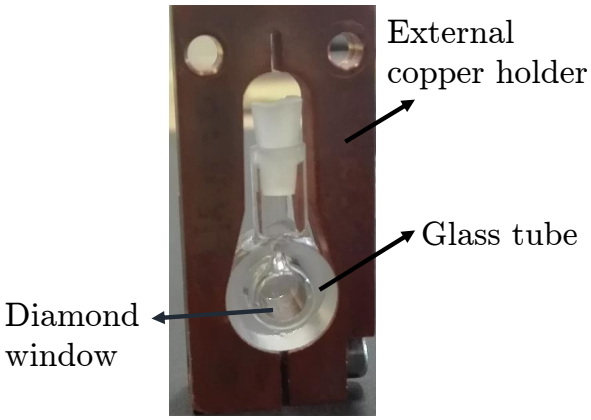

Figure 6.4: Picture of the glass tube cell and of the copper holder used to fix the cell to the cold-finger of the He-flow cryostat.

geometry, the setup was designed in order to have a q-resolution of $\pm 10\%$ at any of the probed q's (see Fig. 6.5). To achieve this resolution, the downstream absorber was illuminated by the scattered photons over an area of $4 \times 10\text{mm}^2$ selected using an appropriate lead mask.

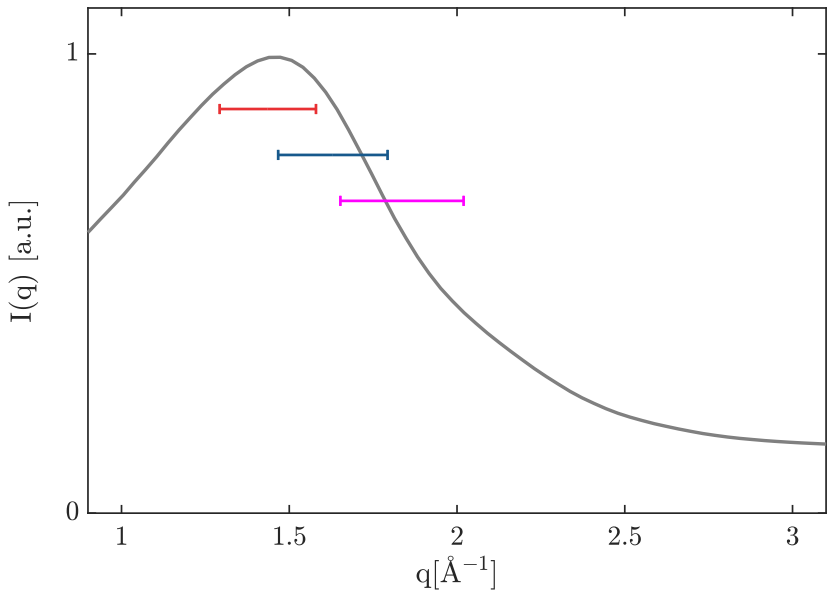

Figure 6.5: Diffuse scattering intensity from OTP at 150.0K. The horizontal bars show the q-ranges over which the TDI beating patterns were measured

6.2.2 Experimental results

Initially the quasi-elastic scattering from OTP at $T = 150.0$K was measured to further calibrate the experimental set-up. In fact at this temperature, much lower than T_g, OTP shows no dynamics in the time-window accessed by TDI, and the intermediate scattering function then simply reduces to a constant, i.e. the non-ergodicity factor f_q. Several issues required indeed to be tested. First of all, during the TDI measurements a much larger area of the reference absorber was illuminated than in the NFS ones. The parameters for the distribution of effective thicknesses of the downstream absorber are therefore expected to be different from the ones in Tab. 6.2 because of the presence of inhomogeneities in the pellet. Furthermore, the cryostat is a source of additional vibrations in the experimental apparatus and consequently it can increase the relative broadening of the probe and reference absorbers.

The measurements were performed at the maximum of the $S(q)$ of OTP ($q_{max} = 14\text{nm}^{-1}$) and two independent data-sets were collected. To describe the time evolution of the beating pattern in presence of the sample Eq. 6.3 requires to be modified according to Eq. 3.19:

$$\begin{aligned} I(t) \quad \propto \quad & 2|G(t,T_\alpha)|^2 + |G(t,T_{SL})F_D(t,\Gamma_D)|^2 \cdot f_{\Delta E} \\ & +4Re\{G(t,T_\alpha)G^*(t,T_S)\}F_D(t,\Gamma_D) \cdot \phi(\mathbf{q},t) \cdot \\ & \cos\left(\frac{\Omega}{2}t\right)\cos\left(\omega_{IS}t\right) + 2\cos\left(\Omega t\right)|G(T_\alpha,t)|^2 \,. \end{aligned} \tag{6.3}$$

The fitting procedure was performed leaving as free parameters the mean value and the width of the thickness distribution of the downstream absorber ($\langle T_{SL}\rangle$,

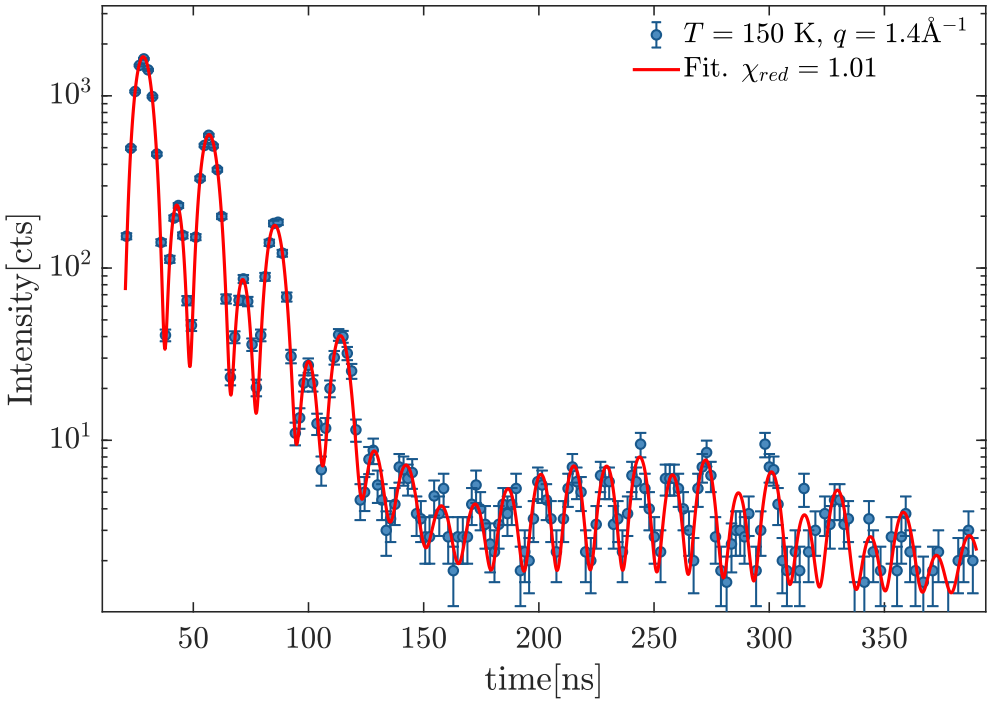

Figure 6.6: Blue dots with errorbar: time-evolution of the TDI beating pattern measured from OTP at a temperature $T = 150.0$K and for a scattering-vector $q = 1.4$Å^{-1}. Red solid-line: fit obtained using Eq. 6.4.

w_{SL}), the inhomogeneous broadening (Γ_D), f_q and $f_{\Delta E}$. For clarity, only one of the two TDI beating patterns collected in the aforementioned conditions (along with the curve obtained from the fitting procedure) is reported in Fig.6.6. The parameters obtained from the two sets were compatible within their uncertainty and their weighted average is reported in Tab. 6.3. As it can be clearly deduced

Table 6.3: Mean value ($\langle T_{SL} \rangle$) and width ($w_{T_{SL}}$) of the effective thickness distribution of the $[NH_4]_2\ ^{57}Fe[CN]_6$ absorber measured over an area of $S = 4 \times 10$ mm^2. Γ_D is the standard deviation of the inhomogeneous broadening for the single-line absorber in units of Γ_0, f_q the non-ergodicity factor of OTP at $q = 14$ nm^{-1} and at a temperature of 150 K. $f_{\Delta E}$ is instead the fraction of the dynamic structure factor of OTP overlapping with the incident SR energy spectrum. All the values here reported are the weigthed average of the results obtained from two data-sets.

$\langle T_{SL} \rangle$	$w_{T_{SL}}$	Γ_D/Γ	f_q	$f_{\Delta E}$
11.6(1)	3.4(3)	0.45(5)	0.854(9)	0.89(2)

from Fig.6.6 and the chi-square of the fit reported in the legend of the figure the model is able to reproduce nicely the experimental data and f_q and $f_{\Delta E}$ were estimated with a statistical accuracy of 1% and 2% respectively. OTP

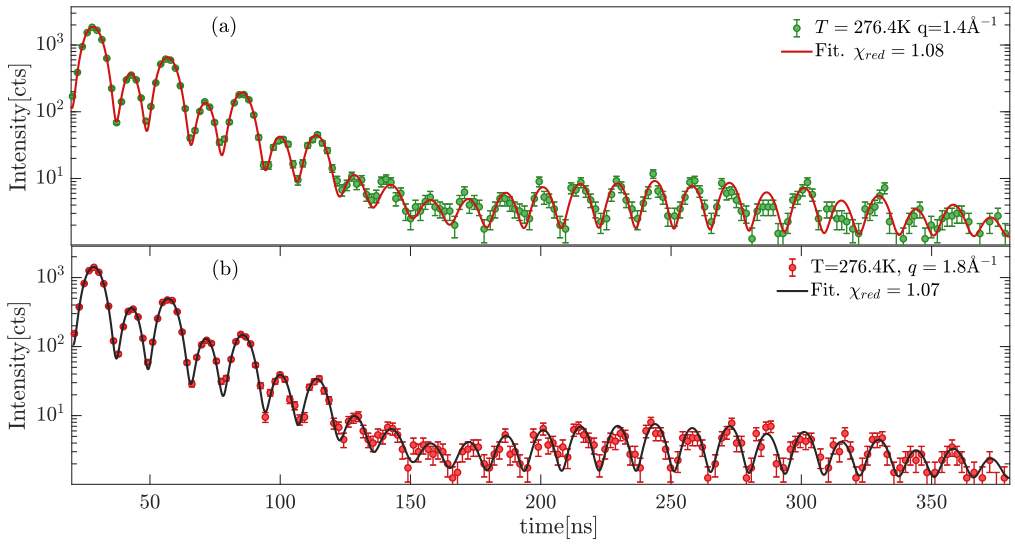

Figure 6.7: (a): time-evolution of the TDI beating pattern measured from OTP at a temperature $T = 276.4$K and for a scattering-vector $q = 1.4$Å^{-1}. Green circles with errorbar: experimental data. Red solid-line: fit obtained using Eq. 6.4. (b): time-evolution of the TDI beating pattern measured from OTP at a temperature $T = 276.4$K and for a scattering-vector $q = 1.8$Å^{-1}. Red circles with errorbar: experimental data. Black solid-line: fit obtained using Eq. 6.4.

was then investigated in the temperature range $[273 - 280]$K, that is below its crossover temperature $T_c = 290$K [56, 61] and for three q-values around the peak of the $S(q)$: 1.4Å^{-1}, 1.6Å^{-1} and 1.8Å^{-1}. In this dynamic range both the α and β_{JG} relaxations are expected to be present and the Kohlrausch-Williams-Watts (KWW) function was again used to model $\phi_q(t)$, in a similar fashion as in Sec.5.2.2. Also in this case the quality of the data was not enough to simultaneously fit the three parameters of the KWW, and β_{KWW} was fixed to 0.6 at each of the probed q's. In this case the De Gennes narrowing at q_{max} was not to accounted for, in order to follow the same procedure as in previous TDI experiments on OTP [11–13, 143] and to be able to directly compare our results with those.
Fig.6.7-(a) reports, as an example, two beating patterns measured at same temperature $T = 276.4$K but at two different q-values: $q = 1.4$Å^{-1} (panel (a)) and $q = 1.8$Å^{-1} (panel (b)). Also in this case the fits performed using Eq.6.4 well describe the time-evolution of the TDI beatings and a $\chi^2 \simeq 1$ was found for all the analysed data-sets. Fig.6.8 shows the $\phi_q(t)$ calculated from the parameters estimated by the fits reported in Fig. 6.6 and in Fig. 6.7 along with the corresponding values of $f_{\Delta E}$. $f_{\Delta E}$ is plotted at $\Delta t_{SR} = 1.8$ps, which corresponds to the time-duration expected for a Fourier-limited X-ray pulse with a bandwidth of $\simeq 0.75$meV. The dynamics of OTP at the ps and sub-ps timescale is dominated by fast relaxation processes [56, 61]. The characteristic time τ_{fast} of these processes is characterized by a weak temperature dependence and the relaxation strength (f_q^{fast}) is large at $q > q_{max}$ and becomes small at

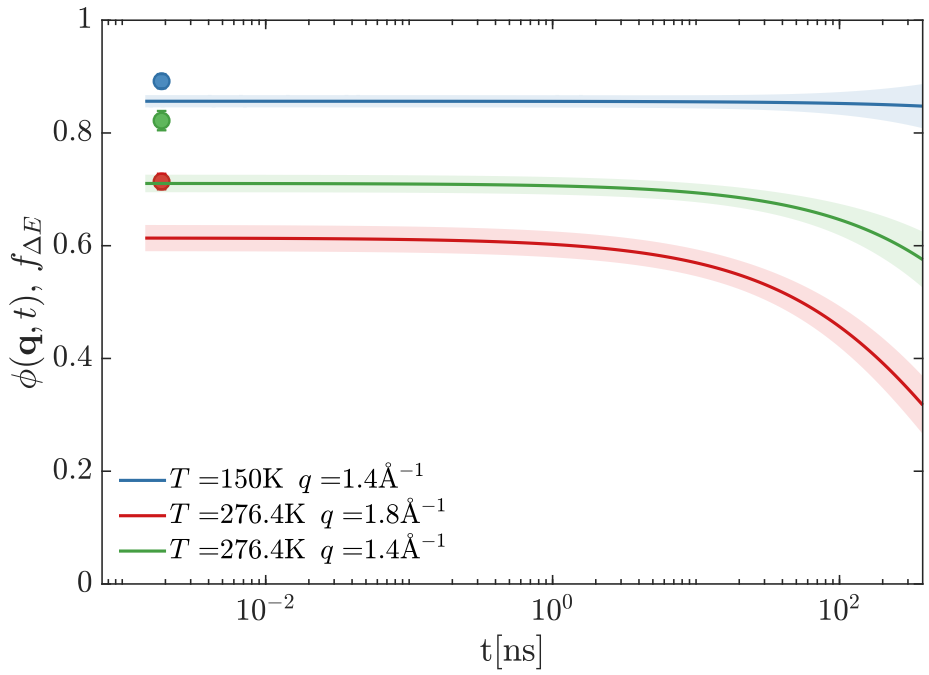

Figure 6.8: Intermediate scattering functions $\phi_{\mathbf{q}}(t)$, calculated from the parameters of the fits reported in Fig.6.6 and Fig.6.7-(a,b). Blue solid line: $T = 150.0$K, $q = 1.4$Å^{-1}; green solid line: $T = 276.4$K, $q = 1.4$Å^{-1}; red solid line $T = 276.4$K, $q = 1.8$Å^{-1}. The areas indicate the 68% confidence intervals. The circles with errorbars are the corresponding $f_{\Delta E}$ values and they are plotted at $\Delta t_{SR} = 1.8$ps, which is the estimated time-duration of the incident SR pulse.

q_{max}. Regarding its T-dependence, f_q^{fast} scales at most linearly with T and approaches zero, in a classical picture, when $T \to 0$ [56, 57]. This is consistent with our results. In fact, $f_{\Delta E}$ is i) always larger than f_q, which is indeed the strength of the much slower relaxations occurring within the time-window of TDI and consequently following the relaxation of the fast processes. In addition, ii) $f_{\Delta E}$ increases on approaching the maximum of the $S(q)$ and iii) for smaller T's. We can also notice that at q_{max} and $T = 150K$, f_q approaches $f_{\Delta E}$. This is explained by the fact that no-decorrelation takes place within the time-interval accessible by TDI and, more in general, after $\Delta t_{SR} \simeq 1.8ps$. Under these conditions the strength of the fast relaxations is indeed expected to be negligible. Conversely, $f_{\Delta E} - f_q$ increases for $T > T_g$, where f_q^{fast} is larger. This scenario is consistent also with what observed for glycerol [14] and corroborates the fact that $f_{\Delta E}$ is sensitive to fast relaxation processes appearing in the $S(q,\omega)$ and occurring within the bandwidth of the incident X-ray pulse.

The average relaxation times $\langle\tau\rangle$, resulting from the beating pattern measured in the T-range [273-277 K] and in the q-range [1.4Å^{-1}-1.8Å^{-1}] are shown in Fig. 6.9 and compared with the ones from the literature[11, 13]. The $\langle\tau\rangle$'s were calculated from the τ values obtained from the fitting procedure, using

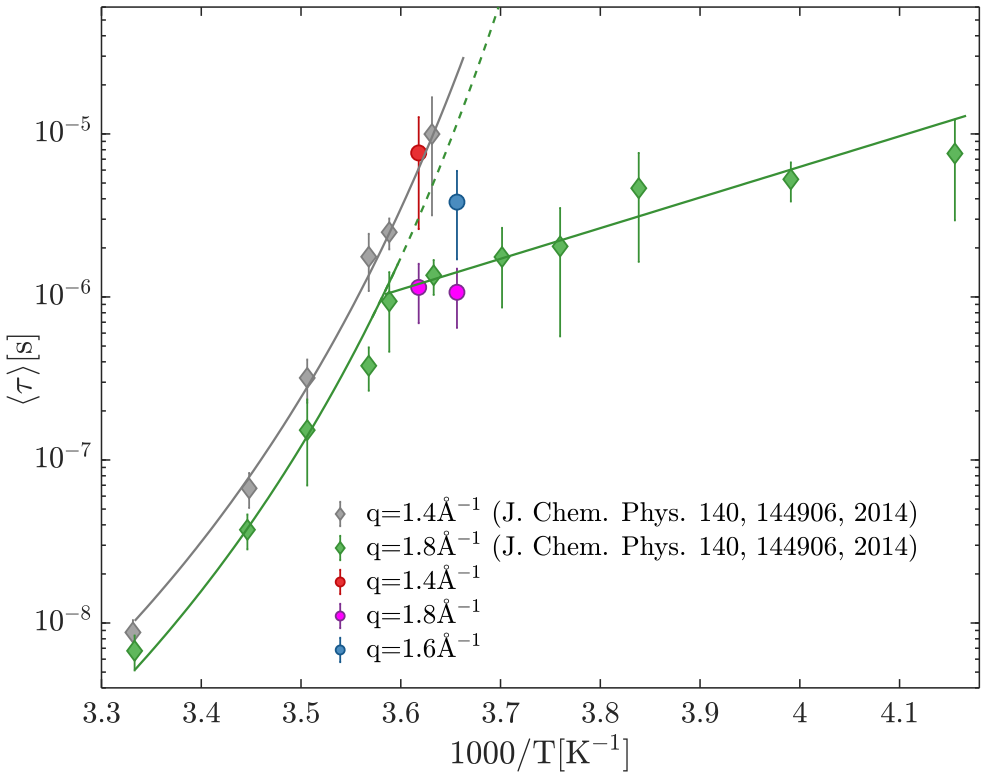

Figure 6.9: T-dependence of the average relaxation time ($\langle\tau\rangle$) measured by TDI at three different exchanged wave-vectors: $q = 1.4$ (red circle), 1.6 (blue circle) and 1.8 Å^{-1} (violet circles). The T-dependence of the OTP relaxation time reported in Ref.[13] *by Kanaya et al.* at $q = 1.4$Å^{-1} (grey diamonds) and $q = 1.8$Å^{-1} (green diamonds) are shown for the sake of comparison. The solid lines are the fits to the TDI data from Ref. [13]. The dashed line is the extrapolation of the T-dependence of the α-relaxation at $q = 1.8$Å^{-1} down to $T = 270$K.

the well-known relation:

$$\langle\tau\rangle = \frac{\tau\Gamma\left(\frac{1}{\beta_{KWW}}\right)}{\beta_{KWW}} \tag{6.4}$$

where Γ is the Euler's Gamma function.
The $\langle\tau\rangle$ obtained at q_{max} (blue circle) can be safely attributed to the structural relaxation according to the τ's reported in Refs. [11, 13] for similar q's and T's. Also the τ's extracted at $q = 1.8$Å^{-1} (orange circles) are consistent with the ones from the literature [13]. Our results indeed corroborate that at this scattering vector and at this temperature TDI probes the β_{JG}-relaxation [13]. For what concerns the τ at $q = 1.6$Å^{-1} (red circle), its T-dependence was not characterized in detail. Nonetheless, it can be reasonably attributed to the β_{JG} relaxation as well. As it can be noticed from Fig. 6.9, the α relaxation at 273 K should be $> 10\mu s$ already at 1.8Å^{-1} and at 1.6Å^{-1}, which is closer to q_{max}, it is expected to be even slower as a consequence of the De-Gennes narrowing,

as suggested by both experiments [56] and simulations [59]. Therefore, since the probed τ is much faster, we can conclude that also at $T = 273$ K and $q = 1.6\text{Å}^{-1}$, the β_{JG} relaxation contributes to the observed dynamics. This result is however not surprising. In fact the q-resolution of our experimental set-up (see Fig. 6.5) is such that the measurement at $q = 1.6\text{Å}^{-1}$ partially covers the q-ranges investigated both at $q = 1.4\text{Å}^{-1}$, where the α-relaxation dominates the microscopic dynamics but is too slow for TDI at $T = 273$K, and at $q = 1.8\text{Å}^{-1}$, where the β_{JG}-relaxation is probed instead.

Finally, Fig. 6.10 reports the relaxation strength relative to the τ's of Fig.

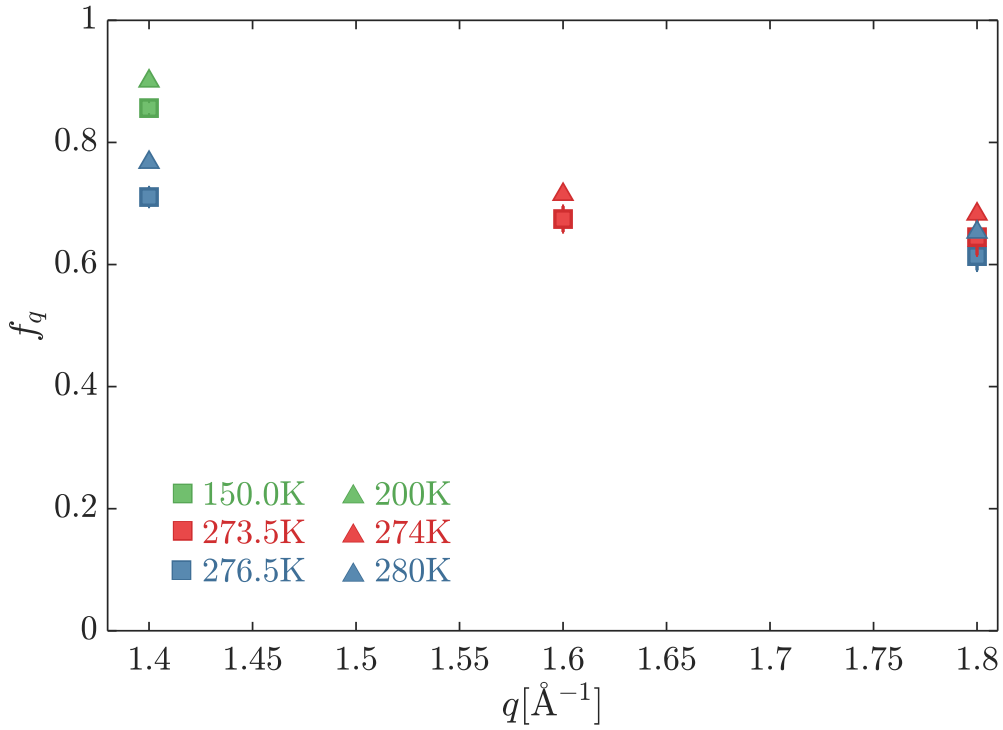

Figure 6.10: q-dependence of the non-ergodicity factor (f_q) of OTP as measured by TDI at several temperatures: 150.0K (green square), 273.5 K (red squares) and 276.4 K (blue squares). The f_q's extracted from neutron inelastic scattering [61] are also reported for the sake of comparison (green, red and blue).

6.9 and to the measurements at $T = 150$ K (TDI beating pattern in Fig.6.6) as a function of q and at several temperatures. The non-ergodicity factors measured by coherent neutron scattering by *Tölle et al.* [61] are also plotted for the sake of comparison. Before proceeding, it is necessary to stress that the characteristic time extracted at each probed q and T is very slow with respect to the time-window directly accessed by TDI. Therefore, the beating patterns do not show a complete decorrelation and, in the event that two relaxation processes were taking place (e.g. α and β_{JG}), TDI would be sensitive only to the faster of the two. So at $q > q_{max}$, where both the α and the β_{JG} processes

contribute to relax density fluctuations, TDI is able to detect only the damping of the QB contrast caused by the faster β_{JG}-relaxation. As a consequence the f_q extracted from our measurements is the total strength accounting for the two relaxation processes (α+β_{JG}). It is also important to remind, as discussed in Ch.5, that f_q shows no discontinuity when the β_{JG} processes separates from the structural one. For all the aforementioned reasons it can be directly compared with the non-ergodicity factor from [61] which was obtained measuring the plateau after the decay of the fast-relaxations.
The f_q's extracted from our TDI measurements, as it can be clearly evicted from Fig. 6.10, fairly agree with the ones from neutron scattering experiments [61]. In fact, they present a consistently similar T and q-dependence: f_q becomes larger on lowering T and on approaching the maximum of the static structure factor with a trend close to the one of the f_q's in [61]. The only inconsistency is in the absolute value of f_q: the values estimated by TDI are systematically smaller ($\simeq 6\%$) than the ones measured by neutron scattering. A likely explanation for this discrepancy can be found if we consider the different q-resolution of the set-up here employed with respect to one used in [61]: neutrons measurements were indeed performed over a range Δq=0.05Å^{-1} [61] whereas for our TDI measurement Δq=0.2Å^{-1}. So the f_q from our measurement are averaged over a larger q-window which comprises the tails of the main peak of the $S(q)$ as well, where the non-ergodicity factor is expected to be smaller.

6.2.3 Take-home message

In this chapter the possibilities offered by multi-line TDI experiments have been investigated and a new scheme, based on three-lines interferograms, has been proposed and tested. The advantages provided by this new approach are many. First of all, as already pointed out in [11, 14, 143], multi-lines set-ups, as the one here described, are intrinsically more efficient than the standard one. In fact, absorbers with multi-lines energy spectra have a larger cross-section for NRS: more channels for resonant scattering are present. Furthermore, as discussed in Sec.6.1, these schemes avoid the use of velocity transducers which are responsible for several issues affecting standard TDI experiments, such as i) the reduction of the effective acquisition time and ii) the introduction of vibrations. An additional advantage is the presence of the unmodulated quantum beats from ^{57}Fe, which allow for a better estimate the QB contrast at longer times, further extending the probed time-window.
However, as clarified from the investigation of OTP shown in the previous paragraph, the main benefit is for sure the possibility of directly measuring relaxation strengths. This information, as widely discussed in Ch. 5, is very interesting, especially for the Johari-Goldstein relaxation: most of the studies carried out up to now have been able to address only its relaxation time. Hence this new set-up has clearly the potentiality to fill this gap and contribute to a more complete understanding of the β_{JG}-process.

Eventually, it is also important to underline that multi-lines set-ups generally present few problems not present in the standard configuration. First of all i) the QB frequency cannot be changed and the approximation of negligible radiative coupling needs to be carefully checked especially when relatively fast dynamics (< 100ns) is probed. In fact, the energy broadening caused by the quasi-elastic scattering from the sample might induce as well a radiative coupling between the resonances of the probe and reference absorbers. In that case the use a velocity transducer might be required [14]. Secondly ii) the data analysis is more cumbersome and its complexity increases with that of the energy spectra of the absorbers. Nonetheless this issue is partially mitigated in the present case as only 3 nuclear resonances are employed. It is clear that such drawbacks are a reasonable price to pay, considered the aforementioned advantages.

Chapter 7

Conclusions

Nuclear γ-resonance time domain interferometry was used to study the Johari-Goldstein relaxation process in 5-methyl-2-hexanol and 1-propanol, two H-bonded liquids displaying a genuine β_{JG}-relaxation. The microscopic density fluctuations of the samples, thanks to the unique dynamic range of TDI, were investigated across the glass-transition region and in a wide range of scattering vectors (q) [9nm^{-1}-40nm^{-1}], spanning from the average inter-molecular distance to the intra-molecular one. These studies were also complemented by dielectric spectroscopy experiments, performed by S. Ccapaccioli and S. Valenti at the University of Pisa, in order to characterize also the re-orientational dynamics and extract the characteristic timescales of the processes.
The measurements here reported show that the β_{JG}-relaxation affects density fluctuations also in mono-alcohols, confirming the previous observations on OTP [11] and PB [13, 103]. Our results demonstrate that the β_{JG}-relaxation decouples from the α-one at a temperature $T_{\alpha\beta}$ which is around 1.2 T_g (1.16 T_g for 5M2H and 1.3 T_g for 1-propanol). Above $T_{\alpha\beta}$ the characteristic time appearing in the TDI spectra shows the characteristic super-Arrhenius behavior expected for the α-process, whereas below $T_{\alpha\beta}$ it is characterized by a milder Arrhenius T-dependence in close agreement with the one found by DS for the Johari-Goldstein relaxation. Intriguingly, in 5M2H and 1-propanol this decoupling does not occur only at q-values corresponding to the intra-molecular length-scale, as previously reported for OTP [11] and PB [13], but also at the peak of the static structure factor, thus at the length-scale characteristic of intermolecular interactions. The temperature dependence of the initial beating pattern contrast (f'_q) was also studied given its strong relationship with the relaxation strength f_q. At most of the probed q-values and at temperatures below $T_{\alpha\beta}$ the timescale of density fluctuations was too slow to observe a complete decorrelation within the time-window directly accessed by TDI. In those cases it was not possible to disentangle the contributions of the α and β_{JG} processes and the extracted f'_q accounted for the the total relaxation strength (α+β_{JG}). Consistently with the results from DS and DDLS [49, 50] the total relaxation strength does not show any discontinuity at $T_{\alpha\beta}$, meaning that when the β_{JG}-relaxation decouples from the α-process the total strength is conserved.

The relaxation strength of the β_{JG}-relaxation could instead be measured in the case of 5M2H. In fact, in the q-range $25\text{nm}^{-1} < q < 40\text{nm}^{-1}$ and for $165\text{K} < T < 181\text{K}$, density fluctuations relax completely within the TDI time-window via the β_{JG}-relaxation while the α-process contribution is negligible (the remaining part of decorrelation is due to the fast process occurring at the ps timescale). At these q and T values we find that, in average, $\simeq 25\%$ of the molecules partecipate to the β_{JG}-process. It is important to point out that, to the best of our knowledge, this is the first time that the relaxation strength of the β_{JG}-relaxation is probed by density fluctuations.
A further characterization of the atomic motions involved in the β_{JG}-process was possible thanks to the study of the q-dependence of the relaxation parameters. In particular it was observed that the τ of the β_{JG}-process displays a strong super-quadratic q-dependence $\tau \propto q^{-4}$ in both samples, similarly to what reported on OTP [11, 12]. The β_{JG}-relaxation has therefore a strongly restricted, sub-diffusive character also in 5M2H and 1-propanol. Concerning the relaxation strength which, we recall, was extracted only in 5M2H and in a limited q-range ($25\text{nm}^{-1} < q < 40\text{nm}^{-1}$), no evident q-dependence was detected.
Finally a detailed comparison between the characteristic timescales provided by TDI and the DS data was performed. In fact the two techniques are sensitive to different degrees of freedom, namely density fluctuations and dipole re-orientations and therefore provide two different points of view on the relaxation process. Interestingly, it was noticed that while the characteristic timescale of the α-relaxation for the density fluctuations is always faster than that appearing in dipole reorientations, a more complex scenario emerges for the β_{JG}-relaxation. In fact density fluctuations within the β_{JG}-process relax slower than reorientations at/close to the peak of the $S(q)$ and faster at larger q's. As a consequence a q-value $q_{DS} > q_{max}$ always exists such that the relaxation time measured by DS ($\tau^{DS}_{\beta_{JG}}(T)$) and TDI ($\tau(q,T)$) match: $\tau^{DS}_{\beta_{JG}}(T) = \tau(q_{DS},T)$. Interestingly, when we applied the same approach to the TDI data available in the literature for OTP [11, 12], which is also a small molecule as 5M2H and 1-propanol, an analogous result was obtained. Concerning polymers we furthermore observed that the same observation holds in simulated systems with reduced intra-molecular torsional barriers [181].
These new insights on the microscopic characteristics of the β_{JG}-process, combined with the information available in literature, are the basis of the microscopic picture for the β_{JG}-relaxation that we could propose.
First of all our results highlight a strong roto-translational coupling within the β_{JG}-process: the center-of-mass dynamics probed by TDI displays the same T-dependence as molecular re-orientations at both the inter and intra-molecular length-scale. Consequently a parallel scenario for re-orientations and translations should be expected. The restricted, sub-diffusive molecular motions characterizing the β_{JG}-relaxations and reflected in the strong super-quadratic q-dependence of τ can be imagined to occur together with the hindered re-orientations ($< 10°$) observed in NMR measurements [107]. The amplitude

(Δr_{JG}) of these local CM re-arrangements is encoded in q_{DS}, which, in view of the roto-translational coupling discussed above, identifies the most probable center-of-mass displacement at $\tau^{DS}_{\beta_{JG}}$. q_{DS} was effectively identified from the q-dependence of $\tau_{\beta_{JG}}$ we measured for 5M2H and 1-propanol and from the ones available in the literature for OTP [11, 12] and used to calculate the mean-squared molecular fluctuation of the molecules undergoing the β_{JG} process, Δr_{JG}. This is possible as the contribution to the intermediate scattering function related to the β_{JG}-relaxation is approximately Gaussian in q around q_{DS} and at $\tau^{DS}_{\beta_{JG}}$.
Consistently with the sub-diffusive behavior of the β_{JG}-relaxation, Δr_{JG} was found to be around 12% of the average inter-molecular distance for 5-methyl-2-hexanol and OTP and 27% in 1-propanol. This result clearly indicates that the β_{JG}-relaxation mainly consists, at $\tau^{DS}_{\beta_{JG}}$, of a rattling motion of very large amplitude within the cage of the nearest neighbors. More precisely, we noticed that the amplitude of such excursions is compatible with the Lindemann criterion for solid (in)stability. In other words such motions are critical in nature and locally responsible for cage-breaking events. Therefore, at/around $\tau_{\beta_{JG}}$, the molecules participating to the β_{JG} process should be considered as un-caged molecules which will then sub-diffuse to even longer distances before the onset of the structural relaxation.
The fraction of molecules participating to the β_{JG} process was estimated to be around 25% for 5-methyl-2-hexanol at $\tau_{\beta_{JG}}$ and, intriguingly, this value is close to the threshold for site-percolation expected for systems with a number of nearest neighbors such as the ones here considered ($z \approx 12$ for 1-propanol and $z \approx 15$ for OTP). This observation implies that the un-caged molecules are connected in a (close to) percolation cluster. It should be stressed that no dynamical correlation is implied by this result which instead provides information about the spatial distribution of the local cage-breaking events.
Clearly this is not the whole story. Our measurements on mono-hydroxyl alcohols have indeed shown that the β_{JG}-relaxation is characterized also by displacements over larger distances as signaled by its presence up to q_{max}, where inter-molecular correlations appear. These longer ranged excursions, as a consequence of the observed roto-translational coupling, should be accompanied by large-angle re-orientations. Such "beyond-the-cage" motions likely occur at a longer timescale than the average cage breaking events and are likely related to the string-like rearrangements hypothesised within the RFOT [35] and observed in simulations on MGs [128, 131]. We can moreover expect such cooperative percolating-like reconfiguring regions to be located within the percolating cluster formed by the un-caged molecules given their higher mobility and the similar topology.
The results obtained in this Thesis thus clarify that within the β_{JG}-relaxation roughly one molecule out of four undergoes a restricted dynamics characterized by displacements of the order of 10% of the average inter-molecular distance. These re-arrangements correspond to local cage-breaking events and the resulting un-caged molecules form a percolating cluster within the sample. At the

same time we also found evidences of larger re-arrangements, occurring at a longer timescale with respect to the cage-breaking events and reaching out at least to the inter-molecular length-scale.

7.1 Future perspectives

A complete microscopic description for the β_{JG}-relaxation, despite the efforts and new results presented in this Thesis, is still to come and more experimental investigations are surely needed.
It would be clearly interesting to directly address the cooperative part of the β_{JG}-relaxation. For what regards the CM dynamics, this implies extending the present investigations towards lower q-values. This is experimentally challenging, since it implies looking at even longer times within the distribution of relaxation times contributing to the β_{JG}-process and in a q-range where we expect its relaxation strength to be small.
A detailed characterization of the microscopic relaxation strength of the β_{JG}-relaxation is also still missing. Even though in this work a first estimate has been provided, its complete T and q dependencies across the static structure factor are still unknown. This information is clearly highly needed, especially at the average inter-molecular distance, in order to shed some light to the microscopic origin of the connection between the α and β_{JG}-relaxation. At the same time, the knowledge of the T-dependence of the relaxation strength would provide further insights on the percolating cluster formed by the "un-caged" molecules and on how this evolves with the temperature.
Another natural prosecution of the studies here reported would be to characterize Δr_{JG} in more systems as a function of both temperature and of the separation between the α and the β_{JG}-relaxation timescales. The results from this work suggest that the separation between the α and the β_{JG}-relaxation plays an important role, but more results in different samples are required to fully understand this issue.
New TDI set-ups based on multi-line absorbers, such as the 3-lines one introduced and tested in this Thesis, can play an important role here. As it has been demonstrated in Ch. 6, these new TDI schemes are intrinsically more efficient and furthermore allow for a direct estimation of the relaxation strength. We recall that this is not possible in standard TDI set-ups with single-line absorbers unless a correction parameters, depending on both the sample properties and the experimental set-up, is also known.
Finally it is also important to point out that, with the advent of X-ray free electron lasers (XFEL), X-rays photon correlation spectroscopy is expected to be able to extend soon its dynamic range to the μs timescale. For instance the new European XFEL in Hamburg (Germany) already allows for repetition rates of 4.5 MHz [187]. XPCS experiments with XFEL radiation could be able soon to contribute to the study of the β_{JG}-relaxation, also thanks to new detection schemes, such as X-ray speckle visibility spectroscopy, able to

overcome the limitations posed by the radiation damage typically severe in XPCS experiments on organic samples [188].

Bibliography

[1] Angell, C. A. Formation of Glasses from Liquids and Biopolymers, *Science* **267**, 1924 (1995).

[2] Debenedetti P. G. & Stillinger, F. H. Supercooled liquids and the glass transition. *Nature* **40**, 259 (2001).

[3] Berthier, L. & Biroli, G. Theoretical perspective on the glass transition and amorphous materials. Rev. Mod. Phys. **83**, 587 (2011).

[4] Ngai, K. L. Relaxation and Diffusion in Complex Systems. *Springer, New York,* (2011).

[5] Johari, G. P. & Goldstein, M. Viscous Liquids and the Glass Transition. II. Secondary Relaxations in Glasses of Rigid Molecules. *J. Chem. Phys.* **53**, 2372 (1970).

[6] Yu, H. B., Shen, X., Wang, Z., Gu, L., Wang, W. H. & Bai, H. Y. Tensile Plasticity in Metallic Glasses with Pronounced β Relaxations. *Phys. Rev. Lett.* **108**, 015504 (2012).

[7] Ngai, K. L., Wang, L.-M., Liu, E. & Wang, W. H. Microscopic dynamics perspective on the relationship between Poisson's ratio and ductility of metallic glasses. *J. Chem. Phys.* **140**, 044511 (2014).

[8] Bhattacharya, S. & Suryanarayanan, R. Local mobility in amorphous pharmaceuticals-characterization and implications on stability. *J. Pharm. Sci.* **98**, 2935 (2009).

[9] Baron, A. Q. R., Franz, H., Meyer, A., Rüffer, R., Chumakov, A. I., Burkel, E. & Petry, W. Quasielastic scattering of synchrotron radiation by time domain interferometry. *Phys. Rev. Lett.* **79**, 2823 (1997).

[10] Röhlsberger, R. Nuclear Condensed Matter Physics with Synchrotron Radiation. Basic Principles, Methodology and Applications. *Springer Tracts Mod. Phys.* **208**, Springer-Verlag Berlin Heidelberg, (2004).

[11] Saito, M., Kitao, S., Kobayashi, Y., Kurokuzu, M., Yoda, Y. & Seto, M. Slow Processes in Supercooled o-Terphenyl: Relaxation and Decoupling. *Phys. Rev. Lett.* **109**, 115705 (2012).

[12] Saito, M., Battistoni, A., Kitao, S., Kobayashi, Y., Kurokuzu, M., Yoda Y. & Seto, M. Slow dynamics of supercooled liquid revealed by Rayleigh scattering of Mössbauer radiation method in time domain. *Hyp. Int.* **226**, 629 (2014).

[13] Kanaya, T., Inoue, R., Saito, M., Seto, M. & Yoda, Y. Relaxation transition in glass-forming polybutadiene as revealed by nuclear resonance X-ray scattering. *J. Chem. Phys.* **140**, 144906 (2014).

[14] Saito, M., Masuda, R., Yoda, Y. & Seto, M. Synchrotron radiation-based quasi-elastic scattering using time-domain interferometry with multi-line gamma rays. *Sci. Rep.* **7**,12558, (2017).

[15] Kauzmann, W. The nature of the glassy state and the behavior of liquids at low temperatures. *Chem. Rev.* **43**, 219 (1948).

[16] Goldstein, M. Viscous Liquids and the Glass Transition: A Potential Energy Barrier Picture. *J. Chem. Phys.* **51**, 3728 (1969).

[17] Stillinger, F. H. A Topographic View of Supercooled Liquids and Glass Formation. *Science* **267**, 1935 (1995).

[18] Heuer, A. Exploring the potential energy landscape of glass-forming systems: from inherent structures via metabasins to macroscopic transport. *J. Phys.: Condens. Matter* **20**, 373101 (2008).

[19] Hodge, I. M. Physical Aging in Polymer Glasses. *Science* **267**, 1945 (1995).

[20] Pérez-Castañeda, T, Jiménez-Riobóo, R. J. & Ramos, M. A. Two-Level Systems and Boson Peak Remain Stable in 110-Million-Year-Old Amber Glass *Phys. Rev. Lett.* **112**, 165901 (2014).

[21] Goldstein, M., Viscous liquids and the glass transition. V. Sources of the excess specific heat of the liquid. *J. Chem. Phys.* **64**, 4767 (1975).

[22] Johari, G. P. Molecular inertial effects in liquids: Poley absorption, collision-induced absorption, low-frequency Raman spectrum and Boson peaks. *J. Non-Cryst. Solids* **307**, 387 (2002).

[23] Martinez, L. M. & Angell, C. A. A thermodynamic connection to the fragility of glass-forming liquids. *Nature* **410**, 663 (2002).

[24] Angell, C. A. & Borick, S. Specific heats C_p, C_v, C_{conf} and energy landscapes of glassforming liquids. *J. Non-Cryst. Solids* **307**, 393 (2002).

[25] Adam G. & Gibbs J. H. On the Temperature Dependence of Cooperative Relaxation Properties in Glass-Forming Liquids. *J. Chem. Phys.* **43**, 139 (1965).

[26] Kirkpatrick, T. R., Thirumalai, D. & Wolynes, P. G. Scaling concepts for the dynamics of viscous liquids near an ideal glassy state. *Phys. Rev. A* **40**, 1045 (1989)

[27] Lubchenko V. & Wolynes, P. G. Theory of structural glasses and supercooled liquids. *Annu. Rev. Phys. Chem.* **58**, 235 (2007).

[28] Biroli G. & Bouchaud J.-P., The Random First-Order Transition Theory of Glasses: A Critical Assessment. *(Wiley-Blackwell, 2012).* Chapt. 2, p. 31.

[29] Lubchenko, V. Theory of the structural glass transition: a pedagogical review. *Adv. in Phys.* **64**, 283 (2015).

[30] Bouchaud, J.-P. Biroli G. On the Adam-Gibbs-Kirkpatrick-Thirumalai-Wolynes scenario for the viscosity increase in glasses. *J. Chem. Phys.* **121**, 7347 (2004);

[31] Ozawa, M., Scalliet, S., Ninarello, A. & Berthier, L. Does the Adam-Gibbs relation hold in simulated supercooled liquids? *J. Chem. Phys.* **151**, 084504 (2019);

[32] Götze, W. Complex Dynamics of Glass-Forming Liquids: A Mode-Coupling Theory *Oxford University Press, Oxford* (2008).

[33] Xia, X. & Wolynes, P. G. Fragilities of liquids predicted from the random first order transition theory of glasses *Proc. Natl. Acad. Sci. U.S.A.* **97**, 2990 (2000).

[34] Stevenson, J. D., Schmalian, J. & Wolynes, P. G. The shapes of cooperatively rearranging regions in glass-forming liquids. *Nature Phys.* **2**, 268 (2006).

[35] Stevenson, J. D. & Wolynes, P. G., A universal origin for secondary relaxations in supercooled liquids and structural glasses. *Nat. Phys.* **6**, 62 (2010).

[36] Wyart, M. Correlations between Vibrational Entropy and Dynamics in Liquids. *Phys. Rev. Lett.* **104**, 095901 (2010)

[37] D. Chandler and J. P. Garrahan, Dynamics on the way to forming glass: Bubbles in space-time,âĂİ Annu. Rev. Phys. Chem. 61, 191âĂŞ217 (2010).

[38] Grest, G. S. & Cohen, M. H., Liquids, glasses, and the glass transition: A free-volume approach. *Advances in Chemical Physics* **48**, 455 (1981).

[39] Gedde, U. W. *Polymer Physics (Chapman and Hall, London, 1995).*

[40] Dyre, J. C. The glass transition and elastic models of glass-forming liquids. *Rev. Mod. Phys.* **78**, 953 (2006).

[41] Kubo, R. Statistical-Mechanical Theory of Irreversible Processes. I. General Theory and Simple Applications to Magnetic and Conduction Problems. *J. Phys. Soc. Jpn.* **12**, 570 (1957).

[42] Boon, J. P. & Yip, S. Molecular Hydrodynamics. *McGraw Hill, New York*, (1980).

[43] Hansen, J.-P. & McDonald, I.R. Theory of Simple Liquids. *Academic, London*, (1986).

[44] Zwanzig, R. Time-correlation functions and transport coefficients in statistical mechanics. *Ann. Rev. Phys. Chem.* **16**, 67 (1965).

[45] Kubo, R. The fluctuation-dissipation theorem. *Rep. Prog. Phys.* **29**, 255 (1966).

[46] Callen, H. B. & Welton, H.B. Irreversibility and generalized noise. *Phys. Rev.* **83**, 34 (1951).

[47] Kremer, F & Loidl, A. The scaling of Relaxation Processes *Springer, Berlin*, (2018).

[48] Gabriel, J., Pabst, F., Helbling, A., Böhmer, T. & Blochowicz, T. The Scaling of Relaxation Processes. *Springer* 203-245, (2018).

[49] Gabriel, J., Pabst, F. & Blochowicz, T. Debye Process and β-Relaxation in 1-Propanol Probed by Dielectric Spectroscopy and Depolarized Dynamic Light Scattering. *J. Phys. Chem. B* **121**, 8847 (2017).

[50] Gabriel, J., Pabst, F., Helbling, A., Böhmer, T. & Blochowicz, T. On the Nature of the Debye-Process in Monohydroxy Alcohols: 5-Methyl-2-Hexanol Investigated by Depolarized Light Scattering and Dielectric Spectroscopy. *Phys. Rev. Lett.* **121**, 035501,(2018).

[51] Van Hove, L. Correlations in Space and Time and Born Approximation Scattering in Systems of Interacting Particle. *Phys. Rev.* **95**, 249 (1954).

[52] Cipelletti, L. & Ramos, L. Slow dynamics in glassy soft matter. *J. Phys. Condens. Matter* **17**, 253 (2005).

[53] Colmenero, J., Alegría, A., Arbe A. & Frick, B. Correlation between Non-Debye Behavior and Q Behavior of the α Relaxation in Glass-Forming Polymeric Systems *Phys. Rev. Lett.* **69**, 478 (1992).

[54] Arbe, A., Colmenero, J. The Scaling of Relaxation Processes. *Springer* 247-245, (2018).

[55] Weeks, E. R. & Weitz, D. A. Subdiffusion and the cage effect studied near the colloidal glass transition. *Chem. Phys.* **284**, 361 (2002).

[56] Tölle A.,Neutron scattering studies of the model glass former orthoterphenyl *Rep. Prog. Phys.* **64**, 1473 (2001).

[57] Sokolov, A. P. and Novikov, V. Fast relaxation in disordered systems: from a double well to a cage. *Phil. Mag.* **84**, 1355, (2004).

[58] Capaccioli, S., Paluch, M., Prevosto, D., Wang & L. -M., Ngai, K. L. Many-body nature of relaxation processes in glass-forming systems. *J. Phys. Chem. Lett.* **3**, 735 (2012).

[59] Sciortino, F., Fabbian, L., Chen, S.-H. & Tartaglia, P. Supercooled water and the kinetic glass transition. II. Collective dynamics. *Phys. Rev. E* **56**, 5397 (1997).

[60] Rinaldi, A., Sciortino, F. & Tartaglia, P. Dynamics in a supercooled molecular liquid: Theory and simulations. *Phys. Rev. E* **63**, 061210 (2001).

[61] Tölle, A., Schober, H., Wuttke, J. & Fujara, F. Coherent dynamic structure factor of orthoterphenyl around the mode coupling crossover temperature T_c. *Phys. Rev. E* **56**, 809 (1997).

[62] Cavagna, A. Supercooled liquids for pedestrians. *Phys. Rep.* **476**, 51 (2009).

[63] Donati, C., Glotzer, S. C., Poole, P. H., Kob W. & Plimpton, S. J. Spatial correlations of mobility and immobility in a glass-forming Lennard-Jones liquid. *Phys. Rev. E* **60**, 3107 (1997).

[64] Berthier, L. Time and length scales in supercooled liquids. *Phys. Rev. E* **69**, 020201(R) (2004).

[65] Vogel M, Rdssler E: Exchange processes in disordered systems studied by solid state 2D NMR. *J. Phys. Chem.* **102**, 2102 (1996).

[66] Tracht, U., Wilhelm, M., Heuer, A., Feng, H., Schmidt-Rohr, K. & Spiess, H. W. Length Scale of Dynamic Heterogeneities at the Glass Transition Determined by Multidimensional Nuclear Magnetic Resonance. *Phys. Rev. Lett.* **81**, 2727 (1998).

[67] Keys, A. S., Abate, A. R., Glotzer, S. C. & Durian, D. J. Measurement of growing dynamical length scales and prediction of the jamming transition in a granular material. *Nat. Phys.* **3**, 260 (2007).

[68] Zondervan, R., Kulzer, F., Berkhout, G. C. G. & Orrit, M. Local viscosity of supercooled glycerol near Tg probed by rotational diffusion of ensembles and single dye molecules *Proc. Natl. Acad. Sci. U.S.A.* **104**, 12628 (2007).

[69] Zhang, Z., Yunker, P. J., Habdas, P. & Yodh, A. G. Cooperative rearrangement regions and dynamical heterogeneities in colloidal glasses with attractive versus repulsive interactions. *Phys. Rev. Lett.* **107**, 20 (2011).

[70] Ediger, M. D. & Harrowell, P. Perspective: Supercooled liquids and glasses. *J. Chem. Phys.* **137**, 080901 (2012).

[71] Zhang, P., Maldonis, J. J., Liu, Z., Schroers J. & Voyles P. M. Spatially heterogeneous dynamics in a metallic glass forming liquid imaged by electron correlation microscopy. *Nat. Comm.* **9**, 1129 (2018).

[72] Maggi, C, Di Leonardo, R., Ruocco, G & Dyre, J. C.,Measurement of the Four-Point Susceptibility of an Out-of-Equilibrium Colloidal Solution of Nanoparticles Using Time-Resolved Light Scattering. *Phys. Rev. Lett.* **109**, 097401 (2012).

[73] Roland, C. M., Hensel-Bielowka, S., Paluch, M. & Casalini, R. Supercooled dynamics of glass-forming liquids and polymers under hydrostatic pressure. *Rep. Prog. Phys.* **68**, 1405 (2005).

[74] Pedersen, U. R., Bailey, N. P., Schroder, T. B., Dyre, J. C. Strong Pressure-Energy Correlations in van der Waals Liquids. *Phys. Rev. Lett.* **100**, 015701 (2008).

[75] Dyre, J. C. Hidden scale invariance in condensed matter. *J. Phys. Chem. B* **118**, 10007 (2014).

[76] Weeks, J. D., Chandler, D., Andersen, H. C. Role of Repulsive Forces in Forming the Equilibrium Structure of Simple Liquids. *J. Chem. Phys.* **54**, 5237 (1971).

[77] Hall, R. W. & Wolynes, P. G. The aperiodic crystal picture and free energy barriers in glasses. *J. Chem. Phys.* **86**, 2943 (1987).

[78] Buchenau, U. & Zorn, R. A relation between fast and slow motions in glassy and liquid selenium. *Europhys. Lett.* **18**, 523 (1992).

[79] Larini, L., Ottochian, A., De Michele, C., Leporini, D. Universal Scaling between Structural Relaxation and Vibrational Dynamics in Glass-Forming Liquids and Polymers. *Nat. Phys.* **4** ,42 (2008).

[80] Pazmino Betancourt, B. A., Hanakata, P. Z., Starr, F. W., Douglas, J. F. Quantitative Relations between Cooperative Motion, Emergent Elasticity, and Free Volume in Model Glass-Forming Polymer Materials. *Proc. Natl. Acad. Sci. U.S.A.* **112**, 2966 (2015).

[81] Dudowicz, J., Freed, K. F. & Douglas, J. F. Generalized entropy theory of polymer glass formation. *Adv. Chem. Phys.* **137**, 125 (2008).

[82] Lindemann, F. A., *Z. Phys.* **11**, 609 (1910).

[83] Gilvarry, J. J., The Lindemann and Grüneisen laws. *Phys. Rev.* 102, 308 (1956).

[84] Stillinger, F. H. & Weber, T. A. Lindemann melting criterion and the Gaussian core model *Phys. Rev. B* **22**, 3790 (1980).

[85] Chakravarty, C., Debenedetti, P. G. & Stillinger, F. H. Lindemann measures for the solid-liquid phase transition, *J. Chem. Phys.* **126**, 204508 (2007);

[86] Dudowicz, J., Freed, K. F. & Douglas, J. F., The Glass Transition Temperature of Polymer Melts. *J. Phys. Chem. B* **109**, 21285 (2005).

[87] Yu, H.-B., Richert, R., Maaß, R. & K. Samwer, K. Unified criterion for temperature-induced and strain-driven glass transitions in metallic glass *Phys. Rev. Lett.* **115**, 135701 (2015).

[88] Greet, R. J. & Turnbull, D. Glass transition in o-terphenyl. *J. Chem. Phys.* **46**, 1243 (1967).

[89] Lewis, L. J. & Wahnström, G. Molecular-dynamics study of supercooled ortho-terphenyl *Phys. Rev. E* **50**, 3865 (1994).

[90] Vogel, M., Doliwa, B., Heuer, A. & Glotzer, S. C., Particle rearrangements during transitions between local minima of the potential energy landscape of a binary Lennard-Jones liquid. *J. Chem. Phys.* **120**, 4404 (2004).

[91] Johari, G. P. & Goldstein, M. Molecular mobility in simple glasses. *J. Phys. Chem.* **74**, 2034 (1970).

[92] Johari, G. P. & Goldstein, M. Viscous liquids and the glass transition. III. Secondary relaxations in aliphatic alcohols and other nonrigid molecules. *J. Chem. Phys.* **55**, 4245 (1971).

[93] Williams, G. & Watts, D. C. NMR Basic Principles and Progress. *Springer: Berlin,* **4**, 271 (1971).

[94] Johari, G. P. Intrinsic mobility of molecular glasses. *J. Chem. Phys.* **58**, 1766 (1973).

[95] Johari, G. P. Glass transition and secondary relaxations in molecular liquids and crystals. *Ann. N. Y. Acad. Sci.* **279**, 117 (1976).

[96] Paluch, M. & Ngai, K. L. Classification of secondary relaxation in glass-formers based on dynamic properties. *J. Chem. Phys.* **120**, 857 (2004).

[97] Ngai, K. L. Relation between some secondary relaxations and the α-relaxations in glass-forming materials according to the coupling model. *J. Chem. Phys.* **109**, 6982-6994, (1998).

[98] Yu, H.-B., Wang, W.-H. & Samwer, K. The β-relaxation in metallic glasses: an overview. *Mater. Today* **16**, 183 (2013).

[99] Hornbøll, L. & Yue, Y. Enthalpy relaxation of hyperquenched glasses and its possible link to α-and β-relaxations. *J. Non-Cryst. Solids* **354**, 350 (2008).

[100] Peng. S.-X., Cheng, Y., Pries, J., Wei, S. & Yu, H.-B. & Wuttig, M. Uncovering β-relaxations in amorphous phase-change materials. *Sci. Adv.* **6**, 726 (2020)

[101] Richter, D., Zorn, R., Farago, B., Frick, B. & Fetters, L. J. Decoupling of time scales of motion in polybutadiene close to the glass transition. *Phys. Rev. Lett.* **68**, 71 (1992).

[102] Fujimori, H., Oguni, M. Correlation index $(T_{g\alpha}$-$T_{g\beta})/T_{g\alpha}$ and activation energy ratio as parameters characterizing the structure of liquid and glass. *Solid State Commun.* **94**, 157 (1995).

[103] Arbe, A., Buchenau, U., Willner, L., Richter, D., Farago, B. & Colmenero, J. Study of the dynamic structure factor in the β-relaxation regime of polybutadiene. *Phys. Rev. Lett.* **76**, 1872 (1996).

[104] Kudlik, A., Benkhof, S., Blochowicz, T., Tschirwitz, C. & Rössler, E. A. The dielectric response of simple organic glass formers. *J. Mol. Struct.* **479**, 201 (1998).

[105] Böhmer, R, Hinze, G., Jörg, T., Qui, F. & H. Sillescu, Dynamical heterogeneity in α-and β-relaxations of glass forming liquids as seen by deuteron NMR. *J. Phys.: Condens. Matter* **12**, A383 (2000).

[106] Richert, R. Spectral selectivity in the slow β-relaxation of a molecular glass. *Europhys. Lett.* **54**, 767 (2001);

[107] Vogel M.& Rössler, E. Slow β process in simple organic glass formers studied by one- and two-dimensional ^2H nuclear magnetic resonance. I. *J. Chem. Phys.* **114**, 5802 (2001).

[108] Johari, G. P. Localized motions of β_{JG}-relaxation and its energy landscape. *J. Non-Cryst. Solids* **307**, 317 (2002).

[109] Duvvuri, K. & Richert, R. Dielectric hole burning in the high frequency wing of supercooled glycerol. *J. Chem. Phys.* **118**, 1356 (2003).

[110] Paluch, M., Roland, C. M., Pawlus, S., Zioło, L. & Ngai K. L. Does the Arrhenius temperature dependence of the Johari-Goldstein relaxation persist above Tg? *Phys. Rev. Lett.* **91**, 115701 (2003).

[111] Ngai, K. L. & Capaccioli, S. Relation between the activation energy of the Johari-Goldstein β-relaxation and T_g of glass formers. Phys. ReV. E **69**, 031501 (2004).

[112] Tanaka, H. Origin of the excess wing and slow β relaxation of glass formers: A unified picture of local orientational fluctuations. *Phys. Rev. E* **69**, 021502 (2004).

[113] Tanaka, H. Two-order-parameter model of the liquid-glass transition. III. Universal patterns of relaxations in glass-forming liquids. *J. Non−Cryst. Solids* **351** 3396 (2005).

[114] Ichitsubo, T., Matsubara, E., Yamamoto, T., Chen, H. S., Nishiyama, N., Saida, J., Anazawa, K. Microstructure of fragile metallic glasses inferred from ultrasound-accelerated crystallization in Pd-based metallic glasses. *Phys. Rev. Lett.* **95**, 245501 (2005).

[115] Böhmer, R, Diezemann, G., Geil, B., Hinze, G., Nowaczyk, A. & Winterlich, M. Correlation of Primary and Secondary Relaxations in a Supercooled Liquid. *Phys. Rev. Lett.* **97**, 13570 (2006).

[116] Richert, R. & Samwer K. Enhanced diffusivity in supercooled liquids. *New J. Phys.* **9**, 36 (2007).

[117] Ichitsubo, T., Matsubara, E. Structural inhomogeneity of metallic glass observed by ultrasonic and inelastic X-ray scattering measurements. *Mater. Sci. Eng. A.* **521**, 236 (2009).

[118] Pronin, A. A., Kondrin, M. V., Lyapin, A. G., Brazhkin, V. V., Volkov, A. A., Lunkenheimer, P. & Loidl, A. Glassy dynamics under superhigh pressure. *Phys. Rev. E* **81**, 041503 (2010).

[119] Goldstein, M., Communications: Comparison of activation barriers for the Johari-Goldstein and alpha relaxations and its implications. *J. Chem. Phys.* **132**, 041104 (2010).

[120] Yu, H. B., Samwer, K., Wu, Y. & Wang, W. H. Correlation between β-relaxation and self-diffusion of the smallest constituting atoms in metallic glasses. *Phys. Rev. Lett.* **109**, 095508 (2012).

[121] Micko, B., Tschirwitz, C. & Rössler, E. A. Secondary relaxation processes in binary glass formers: Emergence of âĂIJislands of rigidityâĂİ. *J. Chem. Phys.* **138**, 154501 (2013).

[122] Yu, H. B., Samwer, K., Wang, W. H. & Bai, H. Y. Chemical influence on β-relaxations and the formation of molecule-like metallic glasses. *Nat. Commun.* **4**, 2204 (2013).

[123] Fragiadakis., D. & Roland, C. M. Dynamic correlations and heterogeneity in the primary and secondary relaxations of a model molecular liquid. *Phys. Rev. E* 89, 052304.

[124] Cicerone, M. T., Zhong, Q. & Tyagi, M. Picosecond Dynamic Heterogeneity, Hopping, and Johari-Goldstein Relaxation in Glass-Forming Liquids. *Phys. Rev. Lett.* **113**, 117801 (2014).

[125] Capaccioli, S., Ngai, K. L., Thayyil, M. S. & Prevosto, D. Coupling of Caged Molecule Dynamics to JG beta-Relaxation: I. *J. Phys. Chem. B* **119**, 8800 (2015).

[126] Ngai, K. L., Capaccioli, S., Prevosto, D., Wang, L.-M. Coupling of Caged Molecule Dynamics to JG beta-Relaxation III: van der Waals Glasses. *J. Phys. Chem. B* **119**, 12519 (2015).

[127] Wang, Z., Ngai, K. L., Wang, W. H., Capaccioli, S. Coupling of caged molecule dynamics to Johari-Goldstein beta-relaxation in metallic glasses. *J. Appl. Phys.* **119**, 024902 (2016).

[128] Yu, H. B., Richert R. & Samwer, K. Structural rearrangements governing Johari-Goldstein relaxations in metallic glasses. *Sci. Adv.* **3**, 1701577 (2017).

[129] Fragiadakis, D. & Roland, C. M. Participation in the Johari−Goldstein process: molecular liquids versus polymers. *Macromolecules*, **50**, 4039 (2017).

[130] Ngai, K. L., Paluch, M. Corroborative evidences of TV^{γ}-scaling of the α-relaxation originating from the primitive relaxation/JG β relaxation. *J. Non-Cryst. Solids* **478**, 1-11 (2017).

[131] Yu, H.-B., Yang, M.-H, Sun, Y., Zhang, F., Liu, J.-B., Wang, C. Z., Ho, K. M., Richert, R. & Samwer, K. Fundamental Link between β Relaxation, Excess Wings, and Cage-Breaking in Metallic Glasses. *J. Phys. Chem. Lett.* **9**, 5877, (2018).

[132] Cicerone, M. T. & Tyagi, M. Metabasin transitions are Johari-Goldstein relaxation events. *J. Chem. Phys.* **146**, 054502 (2017);

[133] Johari, G. P., Source of JG-Relaxation in the Entropy of Glass *J. Phys. Chem. B* **123**, 3010 (2019).

[134] Caporaletti, F., Capaccioli, S., Valenti, S., Mikolasek, M., Chumakov, A. I., Monaco, G., A microscopic look at the Johari-Goldstein relaxation in a hydrogen-bonded glass-former. *Sci. Rep.* **9**, 14319 (2019).

[135] Caporaletti, F., Capaccioli, S., Valenti, S., Mikolasek, M., Chumakov, A. I., Monaco, G. Experimental evidence of the mosaic structure in strongly supercooled molecular liquids. *in preparation* (2020).

[136] Mössbauer. R. Kernresonanzfluoreszenz von Gammastrahlung in ^{191}Ir. *Z. Phys.* **151**, (1958).

[137] Frauenfelder, H., The Mössbauer Effect, A Review with a Collection of Reprints (W.A. Benjamin), New York, (1963).

[138] Smirnov G. V., Coherent effects in resonant diffraction: experiment. *Hyp. Int.* **27**, 203 (1986).

[139] Afanas'ev, A. M. & Kagan, Yu. *Zh. Eksp. Teor. Fiz.* **48**, 327 (1965).

[140] Hannon, J. P. & Trammell, G. T. Mössbauer diffraction. I. Quantum theory of gamma-ray and X-ray optics. *Phys. Rev.* **169**, 315 (1968)

[141] Hannon, J. P., & Trammell, G. T. Coherent excitations of nuclei in crystals by synchrotron radiation pulses. *Phys. B: Condensed Matter*, **159**, 161 (1989).

[142] Smirnov, G. V., General properties of nuclear resonant scattering. *Hyp. Int.* **123**, 31 (1999).

[143] Caporaletti F., Chumakov, A. I., Rüffer, R. & Monaco G., A new experimental scheme for nuclear γ-resonance time-domain interferometry. *Rev. Sci. Instr.* **88**, 105114 (2017);

[144] Kagan, Y., Afanas'ev A. M. & Kohn, V. G. On excitation of isomeric nuclear states in a crystal by synchrotron radiation. *J. Phys. C* **12**, 615 (1979).

[145] Castrignano, S. & Evers, G. Probing quantum dynamical couple correlations with time-domain Interferometry. Phys. Rev. Let. **122**, 025301 (2019)

[146] www.esrf.eu

[147] Jens Als-Nielsen, Des McMorrow. Elements of Modern X-ray Physics. *Wiley* (London), (2011).

[148] Chumakov, A. I., Sergeev, I., Celse, J.-P., Rüffer, R., Lesourd, M., Zhang, L., Sánchez del Río, M. Performance of a silicon monochromator under high heat load. *J. Synchrotron Rad.* **21**, 315 (2014).

[149] Ishikawa, T., Yoda, Y., Izumi, K., Suzuki, C. K., Zhang, X. W., Ando, M. and Kikuta S. Construction of a precision diffractometer for nuclear Bragg scattering at the Photon Factory. *Rev. of Sci. Ins.* **63**, 1015 (1992).

[150] Shvydko, Y. X-Ray Optics High-Energy-Resolution Applications. *Springer* (London), (2004).

[151] Ross, M. Atomic diffusion in glasses studied with coherent X-Rays. *Springer Theses*, (2016).

[152] Baron, A. Q. R., Chumakov, A. I., GrÃijnsteudel, H. F., Grünsteudel, H., Niesen, L and Rüffer, R. Transverse X-Ray Coherence in Nuclear Scattering of Synchrotron Radiation. *Phys. Rev. Lett.* **77**, 4808 (1996).

[153] Böhmer, R. Structure and dynamics of monohydroxy alcohols - Milestones towards their microscopic understanding, 100 years after Debye. *Physics Reports* **545**, 125 (2014).

[154] Debye, P. Polar Molecules. *Chemical Catalog Co.: New York*, (1929).

[155] Ngai, K. -L. & Wang, L. -M. Relations between the structural α-relaxation and the Johari-Goldstein β-Relaxation in two monohydroxyl alcohols: 1-propanol and 5-methyl-2-hexanol. *J. Phys. Chem. B.* **123**, 714 (2019).

[156] Wei, Y. & Sridhar, S. Technique for measuring the frequencyâĂŞdependent complex dielectric constants of liquids up to 20GHz. *Rev. Sci. Instrum.* **60**, 3041 (1989).

[157] Pawlus, S., Paluch, M., Nagaraj, M. & Vij, J. K. Effect of high hydrostatic pressure on the dielectric relaxation in a non-crystallizable monohydroxy alcohol in its supercooled liquid and glassy states. *J. Chem. Phys.* **135**, 084507 (2011).

[158] Jakobsen, B., Maggi, C., Christensen, T. & Dyre, J. C. Investigation of the shear-mechanical and dielectric relaxation processes in two monoalcohols close to the glass transition. *J. Chem. Phys.* **129**, 184502 (2008).

[159] Wendt, H. & Richert, R. Purely mechanical solvation dynamics in supercooled liquids: The $S_0 \leftarrow T_1$ (0-0) transition of naphthalene. *J. Phys. Chem. A* **102**, 5775 (1998).

[160] Huth, H., Wang, L.-M., Schick, C. & Richert, R. Comparing calorimetric and dielectric polarization modes in viscous 2-ethyl-1-hexanol. *J. Chem. Phys.* **126**, 104503 (2007).

[161] Sillrén, P., Matic, A., Karlsson, M., Koza, M., Maccarini M. et al., Liquid 1-propanol studied by neutron scattering, near-infrared, and dielectric spectroscopy. *J. Chem. Phys.* **140**, 124501 (2014).

[162] Scopigno, T., Ruocco, G., Sette, F. and Monaco, G. Is the fragility of a liquid embedded in the properties of its glass? *Science* **302**, 849 (2003).

[163] Scopigno, T., Ruocco G. and Sette, F. Microscopic dynamics in liquid metals: The experimental point of view. *Rev. Mod. Phys.* **77**, 3 (2005).

[164] Scopigno, T., Suck, J.-B., Angelini, R., Albergamo, F. & Ruocco G. High Frequency dynamics in metallic glasses. *Phys. Rev. Lett.* **96**, 135501 (2006)

[165] Benassi, P., Nardone, M., Giugni, A., Baldi, G. & Fontana, A. Collective excitations in liquid and glassy 3-methylpentane. *Phys. Rev. B* **92**, 104203 (2015).

[166] Sillrén, P., Swenson, J., J., Mattsson, D., Bowron, Matic A. The temperature dependent structure of liquid 1-propanol as studied by neutron diffraction and EPSR simulations. *J. Chem. Phys.* **138**, 214501 (2013).

[167] Hansen, C., Stickel, F., Berger, T., Richert, R. & Fischer, E. W. Dynamics of glass-forming liquids. III. Comparing the dielectric α- and β-relaxation of 1-propanol and o-terphenyl. *J. Chem. Phys.* **107**, 1086 (1997).

[168] Andreozzi, L., Faetti M.& Giordano M. Heterogeneities at short and long time scales of the dynamics of a probe molecule in different model glass formers. *Journal of Non-Crystalline Solids*, **352**, 3829 (2006).

[169] Richert, R., On the dielectric susceptibility spectra of supercooled o-terphenyl. *J. Chem. Phys.* **123**, 154502 (2005).

[170] Petzold, N. & Rössler, E. Light scattering study on the glass former o-terphenyl J. Chem. Phys. 133, 124512 (2010);

[171] Mallamace, F., Corsaro, C., Leone, N., Villari, V., Micali, N. & Chen, S.-H. On the ergodicity of supercooled molecular glass-forming liquids at the dynamical arrest: the o-terphenyl case. *Sci. Rep.* **4**, 3747 (2014)

[172] Monaco, G., Masciovecchio, C., Ruocco, G. & Sette, F. Fast Relaxational Dynamics in the o-Terphenyl Glass. *Phys. Rev. Lett.* **82**, 1776 (1998).

[173] Monaco, G., Fioretto, D., Masciovecchio, C., Ruocco, G. & Sette, F., Determination of the Infinite Frequency Sound Velocity in the Glass Former o-Terphenyl. *Phys. Rev. Lett.* **82**, 1776 (1999).

[174] Andrews, J. N. & Ubbelohde, A. R. Melting and crystal structure: the melting parameters of some polyphenyls.*Proc. Roy. Soc.* **A228**, 435 (1955).

[175] Narros, A., Arbe, A., Alvarez, F., Colmenero, J. & Richter, D. Atomic motions in the $\alpha\beta$-merging region of 1,4-polybutadiene: A molecular dynamics simulation study. *J. Chem. Phys.* **128**, 224905 (2008).

[176] Ngai, K. L., Removal of cooperativity in glass-forming materials to reveal the primitive α-relaxation of the coupling model. *J. Phys.: Condens. Matter* **11**, 119 (1999).

[177] Hansen, C. & Richert, R. Dielectric anomalies in the β-relaxation of glassy 1,4-polybutadiene. *Acta Polymer.* **48**, 484 (1997).

[178] Wuttke, J. Laplac-Fourier Transform of the Stretched Exponential Function: Analytic Error Bounds, Double Exponential Transform, and Open-Source Implementation "libkww". *Algorithms* **5**, 604 (2012).

[179] Metzler. R, Klafter, J. The random walk's guide to anomalous diffusion: a fractional dynamics approach. *Phys. Rep.* **339**, 1 (2000).

[180] Mossa, S., Di Leonardo, R., Ruocco, G. & Sampoli, M. Molecular dynamics simulation of the fragile glass-former orthoterphenyl: A flexible molecule model. *Phys. Rev. E* **62**, 612 (2000).

[181] Bedrov, D. & Smith, G. D. Molecular dynamics simulation study of the α- and β-relaxation processes in a realistic model polymer. *Phys. Rev. E* **71**, 050801(R) (2005).

[182] Brostow, W. Radial distribution function peaks and coordination numbers in liquids and amorphous solids. *Chem. Phys. Lett.* **49**, 285 (1977).

[183] Private communication with Dr. Daniel Bowron (daniel.bowron@stfc.ac.uk).

[184] Lorenz, C. D. & Ziff, R. M. Universality of the excess number of clusters and the crossing probability function in three-dimensional percolation. *J. Phys. A: Math. Gen.* **31**, 8147 (1998).

[185] Caporaletti F., Chumakov, A. I., Rüffer, R. & Monaco G. Accessing the non-ergodicity factor of o-terphenyl via multi-line nuclear γ-resonance time-domain interferometry. *Phil. Mag.*, 1(12) (2020);

[186] Saito, M., Seto, M., Kitao, S., Kobayashi, Y., Kurokuzu, M., & Yoda, Y. Improvement of Efficiency of Time-Domain Interferometry Method Using Two Driven Nuclear Absorbers *J.Phys. Soc. Jpn.* **80**, 123001 (2011).

[187] Altarelli, M. et al. (eds). XFEL: The European X-Ray Free-Electron Laser Technical Design Report. Preprint DESY 2006-097 (DESY, 2006) (see also http://xfel.desy.de).

[188] Verwohlt, J., Reiser, M., Randolph, L., Matic, A., Medina, L. A., Madsen, A., Sprung, M., Zozulya, A. & Gutt, C. Low Dose X-Ray Speckle Visibility Spectroscopy Reveals Nanoscale Dynamics in Radiation Sensitive Ionic Liquids. *Phys. Rev. Lett.* **120**, 168001 (2018)

Acknowledgments

I take the opportunity to thank all those who made possible the draft of this PhD thesis and enriched my research with stimulating discussions and insights.
First of all, my deep gratitude goes to my supervisor Prof. Giulio Monaco for giving me the possibility to work on this project and being always ready to help and support me. His guidance during the whole PhD was for me of great inspiration and motivated me to persevere on my work as well as to develop my own scientific ideas and interests. I also thank him for the patient and careful reading and correction of this Thesis.
I want to express my gratitude to Prof. Simone Capaccioli, from the University of Pisa, who strongly contributed to this work with his continuous advice, support and experimental collaboration. I am also grateful for the helpful and stimulating discussions and the careful proofreading of a part of this Thesis.
I thank Sofia Valenti for her help during the synchrotron radiation experiments and for the dielectric spectroscopy characterization of the samples.
I am also grateful to Prof. Kia L. Ngai for the interesting and stimulating thought-provoking discussions on the nature of the β_{JG}-relaxation.
I want to express my gratitude to the beamline staff of ID18 of the European Synchrotron Radiation Facility and in particular to Dr. Aleksandr I. Chumakov for his precious guidance and assistance during the beamtimes and help in the implementation of the experimental set-ups as well. The experiments presented in this work would not have been possible without his collaboration and experience.
A special thanks naturally goes to all the present and former members of the SDSC group in Trento for the nice time spent together and the stimulating discussions, not only of scientific nature, we had together.